# Synthesis of titanium dioxide nanoparticles: phase, morphology and size control

---

A thesis
submitted in partial fulfilment
of the requirements for the Degree
of
Doctor of Philosophy
by
Jan-Yves Ruzicka

---


University of Canterbury
2013

To my parents, for their unwavering faith in my ability to not screw up

and

to Rose, for putting up with the last four years.

"The universe is peeled like an onion, and an onion is all peel."
Umberto Eco, *Focault's Pendulum*

# Abstract

In this work, titanium dioxide ($TiO_2$) was synthesised *via* a number of different methods, with a strong focus on wet chemistry and sol-gel preparations.

Initial studies focussed on a broad survey of synthetic methods, with characterisation by powder X-ray diffractometry (PXRD), scanning and transmission electron microscopy (SEM/TEM), and dynamic light scattering (DLS). A number of these methods produced crystalline nanoparticles of varying sizes, morphologies, and phases.

Further studies were performed on $TiO_2$ synthesised *via* the thermal degradation of peroxotitanic acid. This system was then fine-tuned by the use of fluorine-containing surface modifying agents (SMAs), which allowed for control of particle growth in solution. The obtained materials were characterised as above, as well as by X-ray photoelectron spectroscopy (XPS), employed to examine the electronic structure of the particles' surface. The addition of SMA resulted in the formation of ovoid particles with a large proportion of {010} facets, and the choice of SMA was found to influence the size of the particles.

Further exploration of fluorine-containing SMAs involved the investigation of the use of fluoride-containing carboxylic acids, including mono- and tri-fluorinated acetic acid and three longer-chain perfluorinated carboxylic acids. While acetic acid encouraged the growth of the anatase phase of titania, the highly-acidic environment induced by the use of fluorinated acetic acids resulted in the growth of rutile titania. Longer-chain carboxylic acids were less effective at directing particle growth, and it is posited that this is either due to a micellar effect caused by the acids' hydrophobic long tails, or due to steric effects from the size of the SMA.

Following this, titanium dioxide materials were investigated as supports for atomically-precise gold clusters. In particular, pre-treatment of Aeroxide P-25 titania prior to the deposition of $Au_9$ gold clusters, and the effect of this pre-treatment on gold cluster aggregation, were studied. Analysis was performed using XPS and UV-vis diffuse reflectance spectroscopy to monitor element (gold and phosphorus) oxidation state and material surface plasmon resonance respectively. Aggregation was apparent in all samples, although

support pre-treatment with $H_2SO_4$ or $H_2O_2$ appeared to slow gold cluster aggregation.

Finally, a number of the synthesised titanium dioxide materials were trialled as photocatalysts, using the degradation of the industrial dye Reactive Blue 19 (RB19) under high-intensity broad-spectrum light as a model reaction. Initial studies on this system showed that the extent of photodegradation was affected by the use of buffered solutions, and more notably, by the chemical nature of the buffer. Studies on fluoride-modified $TiO_2$ suggest that the presence of a layer of SMA strongly physisorbed to the material surface negatively affects photocatalytic activity, although even given this layer it appears that the use of $BF_4^-$ as a fluoride source results in a more active catalyst. Of note, the materials trialled show good activity under visible light, being equivalent to or better than the NIST standard Aeroxide P-25. Photocatalytic studies on Au@$TiO_2$ catalysts indicate that the presence of discrete clusters (as determined by XPS) is not a guarantee of activity in photocatalysts, and it is suggested that gold clusters may aggregate under illumination. Further studies also indicate that gold cluster aggregation occurs over time, even in the absence of light.

Table of Contents

# Acknowledgments

A Ph.D. thesis is never undertaken in a vacuum. Foremost, I must thank my supervisors, Dr Vladimir Golovko and Dr Tim Kemmitt, without which I would surely never have completed this task. Vlad has been an unwavering source of stability through thick and thin, and Tim took me in when the 2011 Christchurch earthquake devastated our facilities at the University of Canterbury. Between them my two supervisors have kept me motivated and on-task, even when I felt as if my Ph.D. were doomed to failure. Thanks also go to Dr Christine Rehm and Dr Dennis Mather for supervising my work at AINSE in Sydney.

I also wish to extend my thanks to the members of the Golovko group at University of Canterbury. In particular, thank you to David Anderson for being the senior member of our group, organising the lab and generally showing me the ropes of postgraduate research; to Ida Nuramdhani and Faridah Abu Bakar for working beside me and for both contributing so much to photodegradation studies within the group; and to David and Rohul Adnan for help with gold cluster synthesis.

I wish to express my gratitude to academics and researchers at both the University of Canterbury and at other institutions who have helped me throughout the course of my Ph.D.: A. Prof. Gunther Andersson for constantly providing an unending stream of help and advice regarding XPS fitting and analysis, A. Prof. Greg Metha for lending his expertise in setting up our XPS peak fitting procedure, Drs Bruce Cowie and Lars Anderson at the Australian Synchrotron for their unending help and guidance, Drs Robert Knott and Bridget Ingham for help with SAXS data collection and analysis respectively, Dr Martin Ryan and Campbell McNicoll for powder X-ray diffraction help at Callaghan Innovation, and Dr John Kennedy for opening his laboratory to me following the 2011 earthquakes.

Finally, I must thank the technical staff of the University of Canterbury Department of Chemistry for their never-ending support in creating tools

and gadgets for the group.

I am indebted to the University of Canterbury for its financial support of my thesis through the U.C. Doctoral Scholarship Programme, as well as the Australian Institute of Nuclear Science and Engineering for their contribution through their Postgraduate Research Award.

## Abbreviations used in this thesis

**AEY**: Auger electron yield
**DLS**: Dynamic light scattering
**EM**: Electron microscopy
**EY**: Electron yield
**FFT**: Fast fourier transform
**FWHM**: Full width at half-maximum
**FY**: Fluoresence yield
**HBP**: High binding-energy peak
**HRTEM**: High-resolution transmission electron microscopy
**LBP**: High binding-energy peak
**NEXAFS**: Near-edge X-ray absorption fine structure spectroscopy
**P-25**: Aeroxide P-25 commercially-available $TiO_2$
**PAD**: Plasma arc discharge
**PFBA**: Perfluorobutyric acid
**PFOA**: Perfluorooctanoic acid
**PFPA**: Perfluoropentanoic acid
**PTA**: Peroxotitanic acid
**PXRD**: Powder X-ray diffractometry
**RB-19**: C.I. Reactive Blue 19 industrial dye
**RWP**: Rietveld weight profile reliability.
**SAXS**: Small angle X-ray scattering
**SEM**: Scanning electron microscopy
**SMA**: Surface modifying agent
**TEM**: Transmission electron microscopy
**TEY**: Total electron yield
**TTIP**: Titanium *tert*-isopropoxide
**UV-DRS**: UV-vis diffuse reflectance spectrometry
**XPS**: X-ray photoelectron spectroscopy
**XRD**: X-ray diffractometry

# Chapter I

# Introduction

## *1.1 Overview*

Heterogeneous catalysis has revolutionised industrial chemistry over the past century, such that it is an internationally recognised industry today.[1,2] In recent years, nanoscale materials have seen prominence in use as catalysts, due not only to their high surface area, but also to "quantum effects" that modify behaviour as the dimensions of particles shrink.[2]

Titanium dioxide is an example of a photocatalyst, that is, a material which can convert light to chemical potential energy by exciting electrons in the bulk material. Fujishima and Honda were the first to document this quality in 1972,[3] and it was this publication that sparked the growth of the field known as heterogeneous photocatalysis. While other materials display photocatalytic activity, titanium dioxide remains the most-studied of these due to its chemical stability, low cost, non-toxicity, and accessible band gap.[4] Despite considerable research into the material, progress is still being made in the development of novel titanium dioxide-based catalysts. In particular, current research often focusses on narrowing the band gap of titanium dioxide such that it may absorb more light from ambient sources (*e.g.* sunlight),[5–7] increasing the lifetime of excited electronic states,[7,8] and synthesis of well-defined particles with known surface properties.[6,9–12]

## *1.2 Aim of this work*

The field of titanium dioxide synthesis is broad, encompassing many different synthetic methods, characterisation techniques, and potential applications.[9,12–14] In many cases the properties of the resultant materials can be

tailored to fit the given application, although if the materials are to be considered for industrial use, attention must also be paid to the complexity of synthetic processes, and the ease with which they can be scaled up.

One application of photocatalytic materials (such as $TiO_2$) is in the photodegradation of industrial dye waste, a major contributor to global water pollution.[15,16] A photodegradation system is attractive to both industrial and environmental sectors as it would be relatively simple to implement, cheap to maintain, and chemically benign, especially compared to current techniques.[16,17]However, current $TiO_2$ materials still suffer a number of drawbacks, including poor absorption of visible light[16] and high recombination of charge carriers.[18] Research is still required to make an effective and inexpensive form of $TiO_2$ photocatalyst for this application.

Thus the aim of this work is to synthesise titanium dioxide materials *via* the sol-gel method for potential application in the photocatalytic degradation of industrial dyes. Sol-gel methods have been chosen as they rely on relatively mild conditions compared to other synthetic methods: this allows for reduced cost of synthesis, and the mild conditions also lend themselves well to modification.[19]

This thesis describes the development of a number of sol-gel synthetic methods and their optimisation for visible-light activity. Titanium dioxide is modified by both *in situ* addition of surface modifying agents to direct nanoparticle growth, and by immobilisation of noble metal clusters to aid as electron traps and active sites. These materials are then trialled in the photodegradation of the industrial dye Reactive Blue 19.

Some of this work was carried out at Industrial Research Limited (now Callaghan Innovation) and GNS Science Limited in 2011 due to the effects of the February 2011 Christchurch earthquake. This has been noted at the start of the relevant chapters.

## *1.3 Thesis contributions*

The following publications have resulted from this work:

- T. Kemmitt, N.I. Al-Salim, J. Lian, V.B. Golovko and J.-Y. Ruzicka,

"Transparent, photocatalytic, titania thin films formed at low temperature", *Current Applied Physics* (2013) **13** 1 142–147

Portions of this work have been presented in various forms:

- Poster presentation, "Tuning of nanostructured titanium dioxide for applications in photocatalysis", *Asian Photochemistry Conference 6* (Wellington, NZ, November 2010)
- Poster presentation, "Tuning of nanostructured titanium dioxide for applications in photocatalysis", *MacDiarmid Institute Student Symposium* (Wellington, NZ, November 2010)
- Poster presentation, "Tuning of nanostructured titanium dioxide for applications in photocatalysis", *Pacifichem 2010* (Honolulu, USA, December 2010)
- Poster presentation, "Tuning of nanostructured titanium dioxide for applications in photocatalysis", *Advanced Materials and Nanotechnology 5* (Wellington, NZ, February 2011)
- Poster presentation, "*In-situ* SAXS analysis of $TiO_2$", *Small-Angle Scattering Conference 2012* (Sydney, Australia, November 2012)
- Combined oral-poster presentation, "Modification of titanium dioxide by fluorine-containing surface modifying agents", *Advanced Materials and Nanotechnology 6* (Auckland, NZ, February 2013)
- Oral presentation, "XPS investigations of gold aggregation on titanium dioxide", *MacDiarmid Postgraduate Symposium 2013* (Wellington, NZ, November 2013: Winner of best oral presentation award)

The following papers are currently in preparation following from the work contained in this thesis:

- "Effect of titania surface pre-treatment on deposition and activation of atomically-precise gold clusters"

- "XPS and NEXAFS study of fluorine modified TiO2 nano-ovoids reveals dependence of Ti3+ surface population on the modifying agent."

In addition, the author has contributed to the following papers on work related to, but not directly relevant to, this thesis:

- J.-Y. Ruzicka, D.P. Anderson, S. Gaw and V.B. Golovko, "Platinum-ruthenium nanoparticles: active and selective catalysts for hydrogenation of phenylacetylene", *Australian Journal of Chemistry* (2012) **65** 10 1420–1425

- D. P. Anderson, R. H. Adnan, J. F. Alvino, O. Shipper, B. Donoeva, J.-Y. Ruzicka, H. Al Qahtani, H. H Harris, B. Cowie, J. B. Aitken, V. B. Golovko, G. F. Metha and G. G. Andersson, "Chemically synthesised atomically precise gold clusters deposited and activated on titania. Part II", *Phys. Chem. Chem. Phys.* (2013) **15**, 14806–14813

- M. Z. Ahmad, V. B. Golovko, R. H. Adnan, F. A. Bakar, J.-Y. Ruzicka, D. P Anderson, G. G. Andersson and W. Wlodarski, "Hydrogen sensing using gold nanoclusters supported on tungsten trioxide thin films", *Int. J. Hydrog. Ener.* (2013) **38** 12865–12877

# Chapter II

# Literature Review

## *2.1 The importance of catalysis*

Catalysis describes "a phenomenon by which chemical reactions are accelerated by small quantities of foreign substances".[1] The industrial world that we live in relies on catalysts for its everyday productivity with somewhere between 85–90% of all chemical processes that take place today utilising catalysts in some shape or form.[20] As of 2008 the worldwide trade volume for solid catalysts was estimated to be around USD15 billion per year, and the total value created by these catalysts between USD1.5–15 trillion.[20] Understandably, even small increases in the efficiency of catalysts used in industrial processes may have a large global impact, whether financially (as a result of lowered operating costs) or environmentally (as a result of lowered reaction temperatures and wastes). As the global population continues to increase, the rising demand for materials will ensure that new catalytic processes are continually in demand. As such, it is vital that research continues in this area to uncover new catalysts and processes.

Catalysis can be broadly divided into two categories: **homogeneous catalysis**, in which the catalyst exists in the same phase as the reactant, and **heterogeneous catalysis**, in which the catalyst and reactant exist in different phases. Heterogeneous catalysts are popular candidates for industrial reactions as the differing phases of catalyst and reactant make recovery and recycling of the catalyst much easier. In the case of heterogeneous catalysts immobilised, for example, on the side of a reactor, these concerns disappear completely. However heterogeneous catalysts often suffer in their "atom economy": a very small fraction of the catalyst is located at the surface of the material, and thus a large portion of the catalyst is inaccessible

to the reactant phase.

To address this issue, the vast majority of contemporary catalysts take the form of nanometre-sized particles dispersed on high surface-area supports.[2] This allows for a dramatic increase in the atom economy of such catalysts,[21] but may also result in changes to the catalyst's properties, including its melting point, specific heat, magnetic and optical properties, and surface reactivity. These changes come into effect as the diameter of the particle decreases below the de Broglie wavelength of charge carriers within the material, and the phenomenon is known as the "quantum size effect".[22,23] While the original motivation of nanoscale catalysts was merely to increase their surface area, these materials' size-affected properties were often found to be advantageous for catalysis: for example, while bulk gold is relatively inert, gold nanoparticles demonstrate remarkable catalytic reactivity toward the oxidation of carbon monoxide and other gaseous chemicals.[24]

## *2.2 Photocatalysis*

Photocatalysis is a sub-field of heterogeneous catalysis that utilises light as an energy source. The term "photocatalysis" was first used by Doerffler and Hauffe to describe the oxidation of CO on ZnO under illumination,[25] but it was not until the publication of Fujishima and Honda's work on the photocatalytic water-splitting properties of titanium dioxide in 1972 that the area of heterogeneous photocatalysis attained global academic recognition.[3] Since then the technique of photocatalysis has been employed in a number of fields, the two most active being the photocatalytic breakdown of organic pollutants and energy-related applications stemming from the water-splitting ability of several photocatalytic semiconductors.[8,23]

### *2.2.1 Mechanism of photocatalysis*

In a semiconductor material, the convolution and delocalisation of atomic orbitals leads to the formation of continuous bands of allowed energy states for electrons within the material. In the case of a semiconductor, the highest occupied band (the "valence band") and the lowest unoccupied band (the "conduction band") are separated by a relatively small energy gap referred

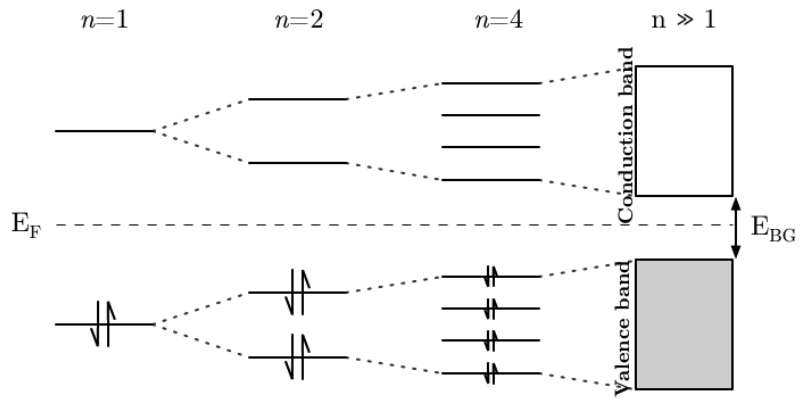


**Figure 2.1.** As a material approaches the bulk, atomic orbitals convolute to form bands. In the case of a semiconductor, the Fermi energy level $E_F$ lies between two bands. The bands are separated by a band gap of energy $E_{BG}$

to as the *band gap* with energy $E_{BG}$. The Fermi energy level of the material lies somewhere within the band gap (Figure 2.1).

If a photon of light with energy $E > E_{BG}$ is absorbed by this semiconductor material, an electron may be promoted from the valence band to the conduction band, simultaneously producing a hole in the valence band. The radiation frequency at which this phenomenon starts to occur is called the absorption threshold.[26] The combination of excited electron and hole are often referred to as an *exciton*. The exciton is free to move around the material, although recombination (*i.e.* relaxation of the electron into the valence band hole) may occur, especially if the material contains a large number of bulk defects. Alternatively, the exciton may migrate to the surface of the material, where it will either recombine or be transferred to electron donors and acceptors if they are available. Thus the electron and hole can be utilised for reduction and oxidation reactions respectively on the semiconductor surface (Figure 2.2).

The propensity for photoexcited electrons and holes to transfer at the surface is influenced by *band bending*, a phenomenon in which band energy levels change as they approach the surface of a material (Figure 2.3). Titanium dioxide tends to exhibit slight downward band-bending, resulting in a high negative surface charge:[27] this in turn makes it an effective photoan-

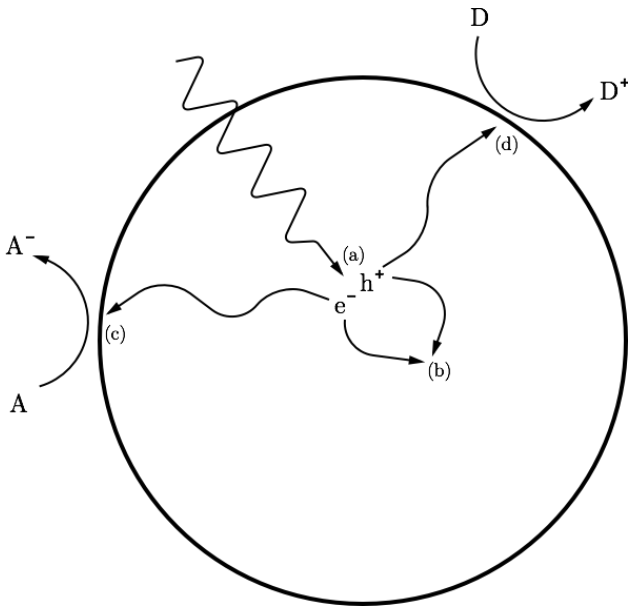


**Figure 2.2.** The mechanism of photocatalysis on a semiconducting material. First, incident radiation excites an electron into the conduction band (a), producing an hole in the process. This electron-hole pair may recombine in the bulk (b) or migrate to the surface of the material, where they react with electron acceptors (c) and electron donors (d).

ode. However, different crystal faces of titanium dioxide (*e.g.* {001}) are also adept at acting as photocathodes, allowing simultaneous oxidation and reduction reactions to occur on the material surface.[28,29]

### *2.2.2 Direct and indirect semiconductors*

The electronic states of a semiconductor material may be further characterised by their *crystal momentum*, most often described as a vector $k$ contained within the Brillouin zone of the crystal lattice.[30] Optical transitions (such as the excitation or relaxation of an electron between bands) must conserve electron momentum: thus, if the electron's momentum changes between bands, a third body (generally a lattice phonon) must also be involved in the transition.

Transitions in which the electron's momentum does not change are referred to as *direct transitions*. If the maximum-energy state in a semiconductor's valence band has the same crystal momentum as the minimal-energy

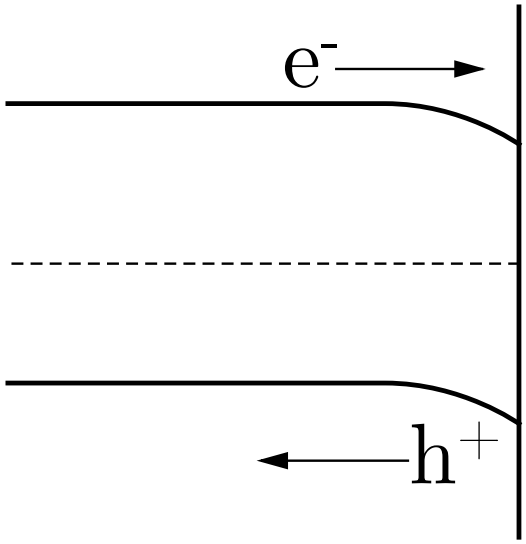


**Figure 2.3.** Band bending is a phenomenon where the electronic structure of a material changes close to the material's surface. This may lead to a charge imbalance, where the surface of the material will be rich in one particular type of charge carrier.

state in its conduction band, such direct transitions occur frequently, and the material is known as a *direct-bandgap semiconductor*. If the valence band maximum and conduction band minimum do not have the same crystal momentum, such direct transitions are forbidden, and the material is known as an *indirect-bandgap semiconductor* (Figure 2.4).

Charge recombination in direct-bandgap semiconductors generally proceeds *via* a process known as direct recombination, in which an electron relaxes from the conduction band to the valence band with no change in momentum. Such a phenomenon is rare in indirect-bandgap semiconductors, as electrons at the bottom of the conduction band do not have the same momentum as holes at the top of the valence band. In such a situation, the electron may relax by simultaneous interaction with a lattice phonon, or it may relax *via* localised energy states caused by lattice defects.[31] These *indirect recombination* processes occur much more rarely than direct recombination: as a result, electron-hole pairs on indirect-bandgap semiconductors exhibit much longer lifetimes than those on direct-bandgap semiconductors.

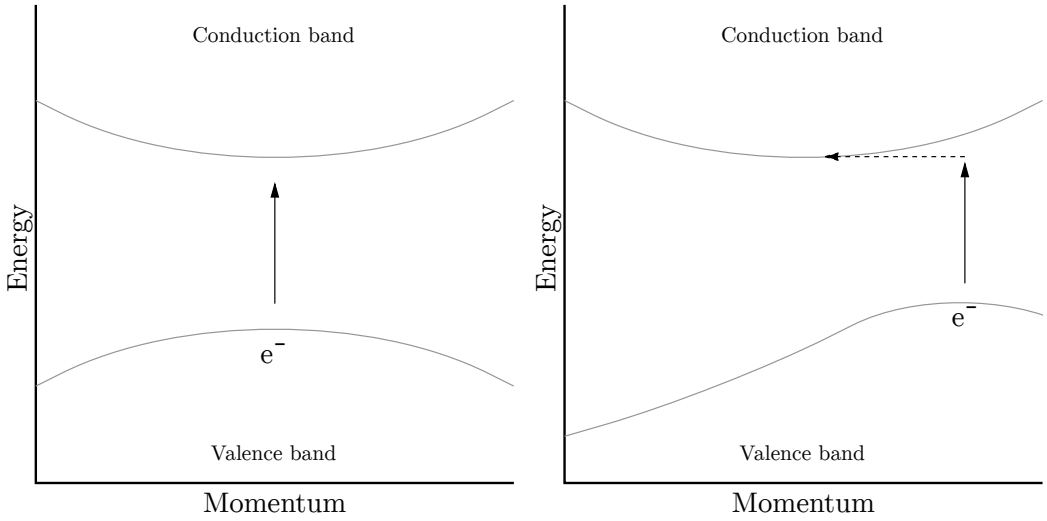


**(a)** Direct-bandgap semiconductor **(b)** Indirect bandgap semiconductor

**Figure 2.4.** The valence band maximum and conduction band minimum coincide in momentum-space for a direct-bandgap semiconductor, while they do not for an indirect-bandgap semiconductor. Transitions in an indirect band gap require a change in momentum, usually supplied by a lattice phonon.

## *2.3 Solar photocatalysis*

The sun is a very attractive light source for photocatalysis, as solar energy is both free to use and globally available. The concept of energy generation *via* photocatalysis relies on the use of solar energy, and it is also useful in non-energetic cases (*e.g.* pollutant degradation), as removing the requirement for a power source makes such systems considerably simpler and more portable. The main requirement for a photocatalyst to harness solar radiation is that its absorption threshold lie within the solar spectrum. While this suggests that the ideal catalyst should have a relatively narrow band-gap and thus a low-energy absorption threshold, it should be noted that as the band gap decreases, two factors diminish the suitability of a narrow band-gap semiconductor as a photocatalyst:

1. Narrow band-gap semiconductors usually exhibit increased electron-hole recombination, lowering efficiency.[32]

2. As the band-gap narrows, excited electrons and holes have redox poten-

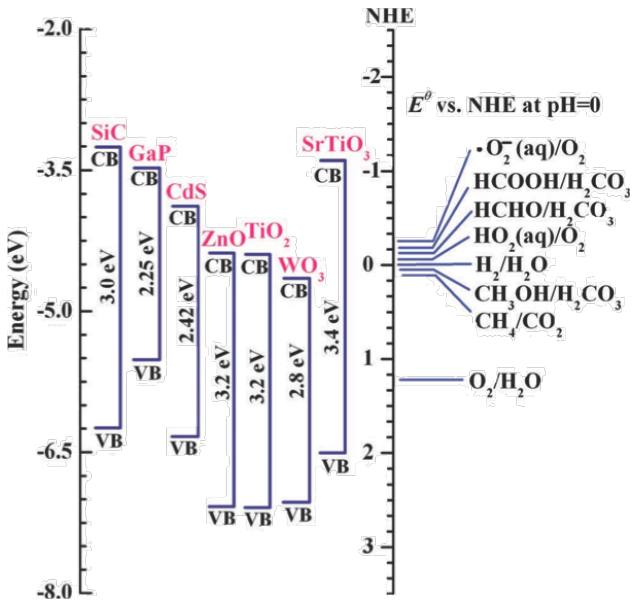


**Figure 2.5.** Comparison of band gaps for semiconductor materials relative to the energy levels of various redox couples in water. A wider band gap allows a wider range of reactions to occur on the material surface. (Tong *et al.*)[32]

tials closer to their Fermi energy. This usually (although not always) means that they less effective catalysts (Figure 2.5).

Thus when selecting or synthesising a solar photocatalyst it is import to balance these concerns against one another. Too wide a band gap and the photocatalyst will not absorb any light, but too narrow and the majority of exciton pairs are lost to recombination or are effectively useless. While recombination may be hindered by modification of the material (as will be discussed later in this chapter), such modifications will by necessity make the system more complex and difficult to synthesise.

## *2.4 Titanium dioxide*

Titanium dioxide, or titania, is a metal oxide semiconductor with the empirical formula $TiO_2$. Like other metal oxides, it is hard, thermally stable and chemically resistant.[23,33] Since the early twentieth century it has been produced commercially as a pigment and whitener,[14] and even then its photocatalytic activity was observed in the form of "chalking", where it would

cause the photodegradation of binders in paint. In the 1960s, Juillet and Teichner observed that titania was photosensitive to daylight,[34] but it was the publication in English of Fujishima and Honda's work on $TiO_2$-based water splitting that popularised its use as a photocatalyst.[3] At the time of writing, titanium dioxide is the most investigated photocatalytic material known,[4,35] and sees use in a number of fields including water splitting, organic pollutant remediation, sensors, and self-cleaning surfaces.[14,35]

Titanium dioxide naturally occurs in three different polymorphs: rutile, anatase and brookite (structure of anatase and rutile shown in Figure 2.6). All three phases are composed of $TiO_6$ octahedra bound in different ways. Rutile is the most thermodynamically stable of the three, being formed by edge-sharing of octahedra to form long chains, while anatase is composed of predominantly point-sharing octahedra and brookite a combination of edge- and point-sharing. Of these, anatase and rutile are the most studied phases for photocatalytic applications.[26] In contrast, brookite is often difficult to synthesise reliably,[8] and is generally photocatalytically inactive;[36] in the interest of brevity, the nature of brookite will not be discussed here.

Rutile is the most common and stable form of $TiO_2$, a direct-bandgap semiconductor with a band gap of 3.0 eV. While this band gap is smaller than that of other titanium dioxide polymorphs, rutile is generally not a suitable candidate for photocatalysis due to its greatly increased rate of electron-hole recombination.[37]

Anatase $TiO_2$ is metastable up to 600–1000°C and thus even though it is technically less stable than rutile it still sees significant use. The band gap of anatase is 3.2 eV and while this limits its activity threshold to UV light, it is still the most popular phase of titania for photocatalytic applications.[4] Anatase is an indirect band-gap semiconductor: this, coupled with its propensity towards hole-trapping on the particle surface,[38] greatly increases the lifetime of photoexcited electron-hole pairs in the material. Excited electrons on anatase ($E^\circ = -0.66$ eV vs. SHE) are sufficiently energetic to participate in the reduction of $H^+$ to hydrogen, while holes ($E^\circ = 2.54$ eV vs. SHE) are able to oxidise water to oxygen,[23,32,39] as well as help in the degradation of a number of organic pollutants.

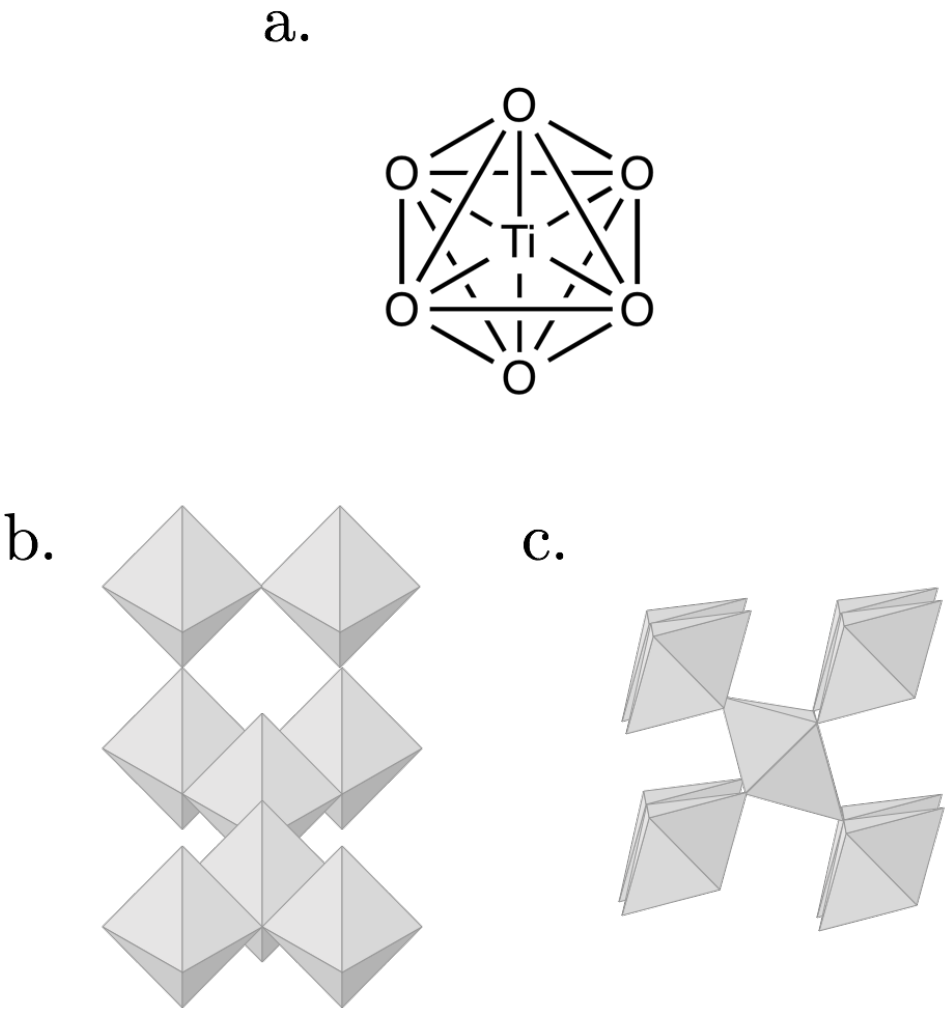


**Figure 2.6.** $TiO_2$ is formed by the arrangement of $TiO_6$ octahedra (a). The two most common polymorphs of $TiO_2$ are anatase (which is formed primarily by point-sharing of octahedra, b) and rutile (formed by edge-sharing, c).

### *2.4.1 Sol-gel synthesis of $TiO_2$*

Nanoscale titanium dioxide may be synthesised by a number of different methods, including sol-gel, micellar and solvothermal synthesis, direct oxidation, chemical or physical vapour deposition, electrodeposition, and microwave synthesis.[9,14] The sol-gel method is generally accepted as the most popular method in current literature:[13] it is a versatile method that provides access to small, well-defined particles even at low temperatures.[13,14] In addition, it is relatively easy to introduce new components to the reaction mixture, which allows for the synthesis of more advanced $TiO_2$-based materials.[19,40]

In a typical sol-gel synthesis, an inorganic precursor $TiR_4$ is dissolved in water or a mixture of solvents. The precursor is rapidly hydrolysed to give $Ti(OH)_xR_{4-x}$, which then undergoes condensation through either substitution or addition reactions to give titanium dioxide.[13,19] While initial studies of $TiO_2$ synthesis tended to use titanium tetrachloride ($TiCl_4$) as a precursor, this resulted in the formation of chloride salts during hydrolysis, which could lead to impurities in the product.[41] Recent synthetic methods have focussed on the use of titanium alkoxides as precursors. These chemicals are relatively inexpensive, pH-neutral, and readily react to give high-purity oxides.[42]

Both halide and alkoxide salts of titanium hydrolyse rapidly in the presence of water: this can result in a lack of control over the shape, size and crystallinity of the end product, and thus several modifications to this method have been made in the literature. The use of acids as peptising agents is relatively popular, especially as the nature of the acid used can influence the properties of the $TiO_2$ material.[14] There has also been significant research into the nonhydrolytic synthesis of $TiO_2$. By replacing the standard hydrolysis-condensation mechanism with an alternative reaction path, the rate of $TiO_2$ formation can be slowed drastically, allowing for far greater control over the end product.[19]

## *2.5 Improving $TiO_2$ activity*

While titanium dioxide is an excellent photocatalyst, two main factors prevent it from being adapted for widespread commercial use.[6]

First, its wide band-gap limits light absorption to the UV ($\lambda \leq 390$nm). Such light makes up approximately 5% of the solar spectrum, limiting the effectiveness of such catalysts under solar irradiation: given the efficiency of current systems, $TiO_2$-based photocatalysts tend not to exceed 1% solar energy conversion.[23,35] By decreasing the band gap sufficiently so the catalyst can absorb visible light, it may be possible to utilise up to 40% of the solar spectrum.[43]

Second, titanium dioxide still exhibits large-scale charge recombination both in the bulk and on its surface. This tends to occur at grain boundaries and bulk or surface defects,[35,44] and can severely limit the photocatalytic activity of the material.

Thus, much research in recent years has been directed at addressing the above problems. Many groups have attempted to lower the band gap of titanium dioxide catalysts by doping (with both metals and non-metals) and surface decoration, or to reduce the recombination rate by providing charge traps, increasing crystallinity or by controlling the size and shape of the particles. In the remainder of this section these methods will be briefly discussed.

### *2.5.1 Doping*

Doping is the practice of adding small quantities of foreign elements to a semiconductor in order to alter is electronic character, generally by creating small bands (mid-gap states) within the band gap. By this method it is possible to alter the photoresponse of a semiconductor, as photons of energy $E < E_{BG}$ can instead excite electrons from the valence band to mid-gap states, or mid-gap states to the conduction band (Figure 2.7). Doping is one of the most extensively-studied methods by which $TiO_2$ has been modified in the literature, and its practice is so wide-spread that its application to any existing or newly-discovered photocatalysts has been described as "inevitable".[43]

Titanium dioxide materials may be doped using a number of methods, including ion implantation, magnetron sputtering, sol-gel modification, and annealing in gas.[45–47] Doping may occur in one of two forms: either substi-

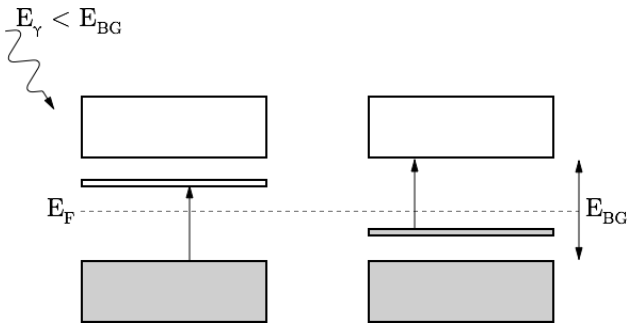


**Figure 2.7.** The addition of dopants can improve the photoresponse of a semiconductor by the introduction of *mid-gap states*. These states allow the material to absorb light of energy $E < E_{BG}$
, either by exciting electrons from the valence band to the mid-gap state (if it lies above the Fermi level) or from the mid-gap state to the conduction band (if it lies below the Fermi level).

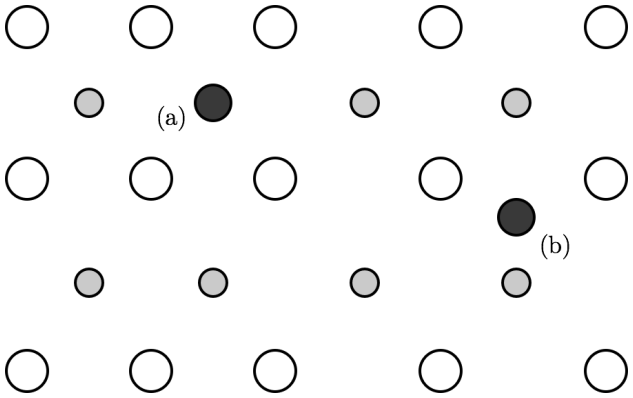


**Figure 2.8.** Dopants may either replace a lattice centre (substitutional doping, a) or simply add to the lattice structure (interstitial doping, b).

tutional, in which the dopant atom replaces a lattice atom, or interstitial, in which it is located between existing lattice atoms (Figure 2.8). While introduction of dopant may increase the photoresponse of the material, it also introduces bulk defects, *i.e.* inconsistencies in the crystal structure, which encourage electron-hole recombination.[32] It is generally observed that photoactivity increases with dopant concentration to a given point, after which activity decreases due to excessive exciton recombination.[7]

$TiO_2$ doping mechanisms can be broadly divided into three groups: cationic doping, anionic doping, and multi-element doping. In addition, "self-doping"

may occur *via* the production of anionic vacancies within the $TiO_2$ lattice.

*Cationic doping*

Cationic dopants replace $Ti^{4+}$ in the crystal lattice, either hybridising with the $TiO_2$ 3*d*-like conduction band or inserting new bands into the bandgap.[32] Cationic doping has been extensively used in attempts to improve the photoresponse of $TiO_2$, with recent reports focussing on the use of alkalai,[7,48,49] transition,[7,50–57] post-transition,[58] and noble metals,[7,59] as well as metalloids,[7,60] carbon[61] (as $C^{4+}$), sulfur[62] (as $S^{6+}$), and rare earths.[63–66] Results depend not only on the type and amount of dopant, but also the method of doping and the reaction being monitored. Such systems are complex and in many cases the properties of the dopant itself must be considered in order to build a comprehensive picture of the doped system: for example, Oropeza *et al.* found that surface doping of $TiO_2$ with Sn(IV) resulted in a slight widening of the band gap; upon reduction to Sn(II) the dopants' electronic nature shifted to give mid-band states lying slightly above the $TiO_2$ valence band, resulting in visible-light activity.[67]

Despite the large body of work on cationic doping of $TiO_2$, these materials tends to suffer from thermal instability and high recombination rates.[68,69] The general lack of success in developing a stable, visible-light active $TiO_2$ photocatalyst by cation doping lead in the 2000s to the investigation of anionic and co-doped $TiO_2$.

*Anionic doping*

In 2001, Asahi *et al.* published their report on the doping of $TiO_2$ using nitrogen.[68] This was a considerable departure from previous studies which had focussed largely on metals as dopants. Asahi instead investigated the theoretical and experimental applicability of carbon, nitrogen, fluorine, phosphorus and sulfur as dopants: importantly, while previous studies had focussed on substituting Ti centres for dopants, this study instead looked at the O centre. The authors concluded that nitrogen was the best of the trialled dopants and increasing the visible light activity of $TiO_2$: sulfur's ionic radius was too large compared to the oxygen atom it would replace, and while carbon and phos-

phorus would more easily occupy the space left by a vacant oxygen centre, the mid-gap states generated by these dopants would in fact occur too *far* into the band gap, making them potent exciton recombination centres. In theoretical calculations, fluorine showed no tendency to add mid-gap states or otherwise narrow the band gap. Experimental investigation found that nitrogen-doped $TiO_2$ was considerably more active at degrading methylene blue than undoped $TiO_2$, and further work showed that this activity was due to substitutionally-doped, rather than interstitially-doped, nitrogen.

Following this paper there has been a considerable amount of interest in the field of anionic $TiO_2$ doping. While the majority of research focusses on the use of nitrogen as a dopant,[70,71] there has also been interest in other anionic dopants, including phosphorus,[72–75] sulfur,[32,76–78] iodine,[79,80] fluorine,[78] and chlorine.[48] While some of these studies have successfully produced materials with an increase visible-light response, this is often due to indirect effects (*e.g.* phosphorus doping may cause oxygen vacancies, which themselves narrow the band gap[72]).

It is interesting to note that nitrogen-doping of rutile $TiO_2$ results in either no change or even a slight widening of the band gap, contrary to what is observed in the case of anatase. It is believed that rutile experiences a more pronounced structural change following substitutional doping of oxygen for nitrogen, which in turn drops the top of the valence band edge. Any increase in photoabsorption due to nitrogen doping in rutile is thus offset by the overall change in the band gap due to structural rearrangement.[69]

*Multi-element doping*

Given the vast array of cationic and anionic dopant materials available, it is natural that research also explore the effect of multiple dopants on $TiO_2$. Two-element doping has been successfully trialled using a combination of two anionic dopants, two cationic dopants, and one of both.[46]

There are a number of ways in which codoping may introduce beneficial synergistic effects. Multiple dopants may co-operatively introduce mid-band gaps, as has been shown with Liu *et al.* on Cr,N-odoped $TiO_2$[51] and Gao *et al.* on N,S-codoped $TiO_2$.[81] In the case of N,S-codoped $TiO_2$, the mid-

gap states introduced by nitrogen (which appear at slightly higher energy than the $TiO_2$ valence band edge) allow access to sulfur 3p orbitals which lie deep in the band gap (and would usually be less accessible). Liu *et al.* offer a similar rationale for the improved performance of Cr,N-codoped $TiO_2$, although they do not offer a thorough theoretical comparison between monodoped and codoped materials. In addition, the use of multiple dopants may encourage charge separation: studies on europium/iron codoped $TiO_2$ have demonstrated reduced electron-hole recombination as the different dopants act as electron (iron) and hole (europium) traps.[7] A similar phenomenon was observed by Niu and coworkers for Fe,S-codoped $TiO_2$.[82]

Extrapolating from this trend, several recent papers have reported the synthesis of *tri*-doped $TiO_2$ materials.[83–87] While some of these materials exhibit good photoresponse, the increasing complexity of their chemical makeup suggests that bulk recombination will quickly become an issue. The benefit of any synergistic effect observed between the dopants must outweigh not only the increase synthetic complexity of the materials, but also any resultant increase in electron-hole recombination.

### *2.5.2 Self-doping*

The production of $Ti^{3+}$-rich $TiO_2$ materials has recently seen interest as an alternative means of extending the photoresponse of $TiO_2$.[88–90] $Ti^{3+}$ is generally a result of the formation of oxygen vacancies in the material, resulting in the production of a localised mid-gap state (attributable to the vacancy, rather than the $Ti^{3+}$) 0.75–1.18 eV below the conduction band edge.[88] Similar to other forms of doping, oxygen vacancies also act as bulk defects,[89] increasing the rate of recombination, and any benefit from doping must be weighed against this.

## *2.6 Surface decoration and composites*

A further way of improving $TiO_2$ photoactivity is to combine it with other nanomaterials. These include metal clusters or atoms, UV- or visible-light-active oxides, and dyes.[46] These materials all modify the photoresponse or activity of the catalyst in some way.

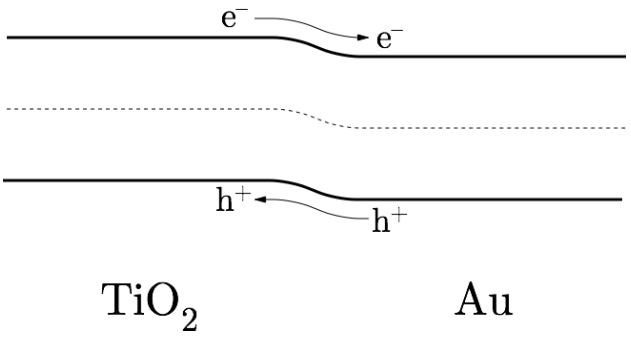


**Figure 2.9.** A heterojunction formed by the deposition of nanoscale gold clusters on the surface of titanium dioxide (band-bending is disregarded for simplicity). Photoexcited electrons are drawn to the gold cluster as its conduction band edge is somewhat lower than that of titanium dioxide, while holes travel in the opposite direction. In this way, electrons and holes are separated and thus cannot recombine.

In many cases, surface decoration or coupling results in the formation of a heterojunction (Figure 2.9),[18,91–95] which in turn drives the separation of electrons and holes within the material. The physical separation of electrons and holes effectively prevents recombination, thus creating a more efficient catalyst.

### *2.6.1 Metal cluster deposition*

Metal oxides have long been used as supports for metal cluster catalysts, to aid in recovery and recycling and to limit aggregation.[24,96] Titanium dioxide is an attractive support for this type of system as it is itself photocatalytically active, and the two catalytic systems (*i.e.* $TiO_2$ support and metal cluster) can interact synergistically.[36] Noble metals (*e.g.* Pt, Pd, Au, Ag, Ir[32]) deposited on the surface of $TiO_2$ act as electron-trapping sites, forming a Schottky junction at the metal/oxide interface (Figure 2.10).[97] In this way photoexcited $TiO_2$ can act as an electron source for these clusters, which in turn effect charge separation for the system, increasing overall catalytic activity.[7,32] Some metal clusters can also alter the photoresponse of the catalyst: gold nanoparticles, for example, display distinctive visible-light absorption due to surface plasmon resonance effects, which can be used to inject electrons into the $TiO_2$ conduction band.[47,98,99]

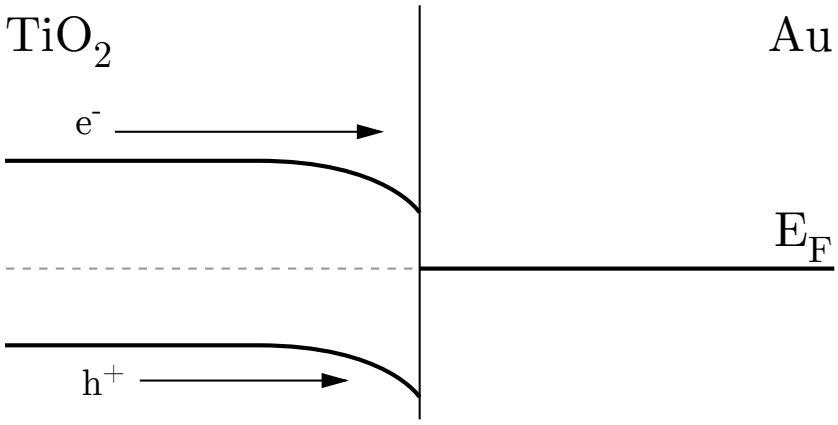


**Figure 2.10.** The deposition of gold nanoparticles on the surface of $TiO_2$ forms a Schottky barrier, reducing charge recombination by separating electrons and holes.

The effect of metal cluster deposition is highly dependent upon particle size, as very small particles exhibit *quantum size effects* which alter their electronic properties.[100,101] For example, below $\sim$ 2 nm gold nanoparticles start to lose their metallic character, affecting charge transfer both from the metal oxide to the gold, and from the gold to substrates adsorbed on the particle surface. Figure 2.11 illustrates how gold particle size alters the ability of said particles to affect reduction of oxygen on the titanium dioxide surface. Bulk gold does not affect this system as the Fermi energy level of bulk gold is lower than the lowest unoccupied orbital of adsorbed oxygen. Very small particles (*e.g.* $Au_1$ or $Au_2$) exhibit high Fermi energy levels which prevent electron transfer from $TiO_2$, also preventing them from aiding in the reduction reaction. Only gold clusters with a Fermi energy level low enough that they can accept electrons from $TiO_2$, but also high enough that they can then donate these electrons to adsorbed oxygen, can affect the reaction. This demonstrates how particle size can have a drastic effect on the catalytic ability of a system.

### *2.6.2 Oxide coupling*

Titanium dioxide nanomaterials can also be coupled to other metal oxides (including other phases of $TiO_2$). The most successful example of this is the commercially-available titanium dioxide photocatalyst, Aeroxide P-

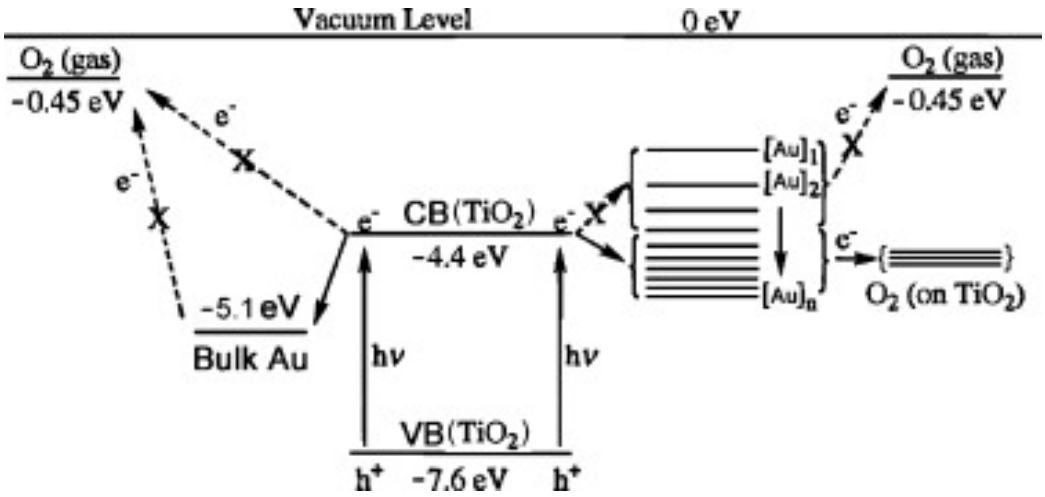


**Figure 2.11.** Gold cluster size drastically affects its electronic character, which in turn affects how it interacts with both the $TiO_2$ support and substrates adsorbed on its surface. (Tian *et al.* )[100]

25 by Evonik. P-25 is a mixed-phase catalyst, being approximately 70:30 anatase:rutile in character, synthesised by flame pyrolysis of $TiCl_4$. Its high activity has been generally attributed to the combination of phases: importantly, the enhanced activity of P-25 is dependent not just on the combination of phases, but the fact that these phases are in physical contact with each other in the material.[94,102]

Several theories have been put forward to explain the enhanced photoactivity of P-25 relative to single-phase $TiO_2$ materials. Initial studies suggested that the rutile phase of titanium dioxide (which, while exhibiting a smaller band-gap than anatase, is generally not as photocatalytically active) acted as an "electron sink", enabling charge separation and thus enhancing the activity of the catalyst (Figure 2.12a).[103] However, the comparatively rapid recombination of charge carriers in rutile-phase $TiO_2$ (as compared to anatase)[38] suggests that transfer of electrons to this phase may not account for the enhanced photoactivity of mixed-phase materials. In 2003, Hurum *et al.* proposed that charge trapping in fact operated by transfer of photoexcited electrons from the rutile phase of $TiO_2$ to lower-energy anatase trapping sites (Figure 2.12b),[37] observing electron transfer from rutile to anatase trapping sites by variable-temperature EPR. This also explains why P-25 titania

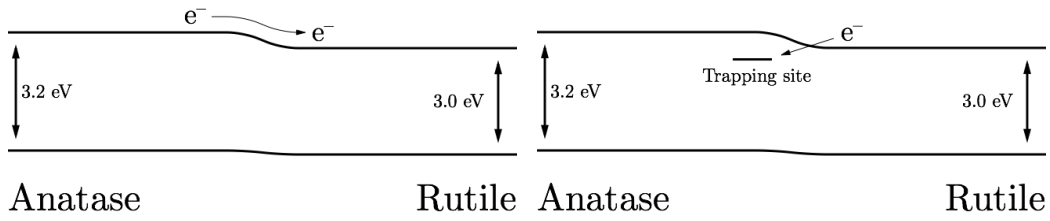


**(a)** Bickley's theory **(b)** Hurum's theory

**Figure 2.12.** Competing theories of P-25 activity. In Bickley's theory the rutile acts as a passive electron trap for photoexcited charges on anatase, while in Hurum's theory, photoexcited electrons on rutile are stabilised by transfer to anatase trapping sites. (Surface band bending is disregarded in these diagrams for simplicity.)

exhibits a slightly narrower band gap than pure-phase anatase $TiO_2$: photoexcited electrons on rutile $TiO_2$ ($E_{BG} = 3.0$ eV) are effectively stabilised by transfer to anatase lattice trapping sites.

Several follow-up papers have reported on the "ideal" ratio of anatase to rutile to capitalise on this effect, but given the variation in these values it appears that the ideal phase ratio is dependent upon the method of synthesis and likely also the application of the material.[104–106] Photoactive brookite-rutile and brookite-anatase catalysts have also been reported, and their activities were found to be greater than equivalent monophasic $TiO_2$ materials. In this case the authors attributed the increased activity of the biphasic materials to increase charge separation.[107]

Titania has also been successfully mixed with a vast number of other semiconductors and metal oxides.[26] These metal oxides may provide increased charge separation by encouraging the transfer of either electrons or holes from one material to another. The presence of metal oxide materials may also alter the $TiO_2$ band gap, either by introduction of mid-gap states or (approaching 1:1 ratios of materials) by hybridisation of band structures.[108,109]

### *2.6.3 Dye sensitisation*

Similar effects to those above can be achieved by the use of a chemisorbed or physisorbed dye. The process of electron- or hole-transfer from dye to catalyst can be incredibly efficient when a monolayer of dye is adsorbed on

the $TiO_2$ surface,[7] and this has been used to great effect in the production of $TiO_2$ solar cells.[110] This method is counterproductive if the material is to be used as a photocatalyst, as the dye will effectively block the surface of the material and will also suffer photodegradation due to the presence of excited electrons and holes on the titania surface.[7]

## *2.7 Inducing crystallinity*

While the sol-gel method is an extremely flexible and mild synthetic technique, its products are all too often either amorphous or poorly crystalline.[13] Calcination (heating) is often employed as a means of inducing or improving crystallinity, although this can also lead to the growth and agglomeration of the nanoparticles.[7,14] Initial heating may induce the transformation of amorphous titania into anatase, but above 600–800°C it will also result in the formation of rutile from anatase.[7,111,112] While calcination is effective at encouraging the crystallisation of amorphous titania, it can also lead to pore collapse,[113,114] reducing the effective surface area of the material.

Hydrothermal or solvothermal treatment (*i.e.* heat-treatment in solution) is also an effective way of inducing crystallinity. In some cases this hydrothermal treatment may be applied during synthesis, while in others it may be used on as-synthesised amorphous (or poorly-crystalline) materials.[111,115,116] This method is generally found to induce crystallinity at lower temperatures than calcination (generally $\leq 250$°C for hydrothermal treatment versus 400–600°C for calcination).[14,114]

The addition of chemicals during synthesis may also encourage synthesis of crystalline $TiO_2$. Classic sol-gel syntheses may employ a number of different acids as catalysts for hydrolysis and condensation reactions;[14] the nature of these acids will also effect the final phase of the $TiO_2$ material. Sulfuric acid and acetic acid, for example, have been demonstrated to induce the formation of anatase $TiO_2$, while nitric or hydrochloric acid promote the rutile phase.[115,117]

## *2.8 Face selectivity*

The structure of crystalline titanium dioxide growing in solution is governed by thermodynamic effects. This can be modelled by the Wulff construction, which assumes that the length of a vector drawn normal to a crystal's face will be proportional to the surface energy of that face.[118] By applying this theorem to anatase titania, it can be determined that absent any other effects, anatase crystals will form truncated octahedral bypyramids, having eight large {101} faces and two small (making up $< 10\%$ of the total surface area) {001} faces.[119] The {101} face of titania has a relatively low surface energy ($\gamma_{\{101\}} = 0.44\text{J m}^{-2}$[119]) and is much less active than the higher-energy {001} face ($\gamma_{\{001\}} = 0.090$ J m$^{-2}$).[120] Therefore to follows that by increasing the relative fraction of the crystal surface made up of {001} faces, one can considerably improve the activity of the resultant catalyst.

It is possible to alter the crystalline shape of a material as it grows by the introduction of surface modifying agents (SMAs). These chemicals preferentially bind to one face of the crystal, limiting growth in that direction. As the crystal grows in other directions, the newly-exposed crystal is immediately occupied by SMA, forcing continual growth of the capped crystal face (Figure 2.13). Carboxylic acids have long been known to bind to titanium dioxide surfaces[121–123] and even form complexes with discrete titanium,[124] and many reports show that they can be used during synthesis to encourage the growth of {001} crystal faces by selective binding.[125–129] Dinh *et al.* , following from preliminary work by Seo and coworkers,[130] have demonstrated the synthesis of tunable $TiO_2$ nanorods using a combination of oleic acid and oleylamine, as the amine group will bind to $TiO_2$ through the {101} face.[131] By altering the concentration one is able to control the rate at which each face grows, and thus the morphology of the final product. Titanium carboxylate centres are quite stable, and the carboxylate groups have been observed remaining in gels even after repeated washing,[132] Some carboxylate SMAs, however, may be removed *via* photodegradation using UV light.[133]

One of the more active fields in recent years has been that of $TiO_2$ morphology modification using fluorine as an SMA. This work started in 2008 with Yang *et al.*'s report on the synthesis of $TiO_2$ nanoparticles with a high

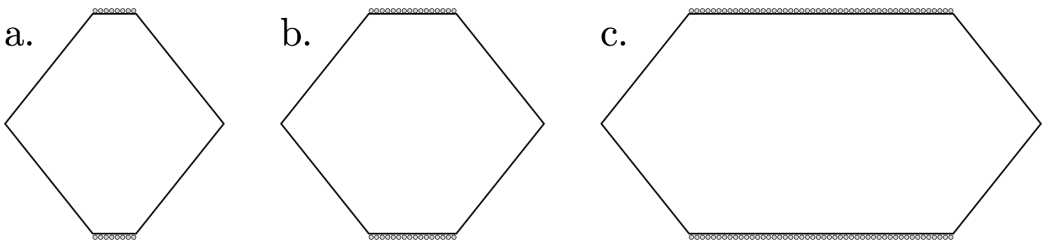


**Figure 2.13.** Surface modifying agents bind preferentially to one or more crystal faces of the growing nanoparticle, limiting growth in that direction and altering the structure of the product.

proportion of {001} faces.[120] This work used hydrofluoric acid as a source of fluorine, which they demonstrated would bind favourably to the {001} face of growing titania nanoparticles. Since the publication of this paper there has been considerable interest in the use of fluorine to control $TiO_2$ growth, with successive groups reporting higher and higher fractions of the $TiO_2$ surface area that are made up of {001} faces.[116,134–150]

A major drawback of this technique is the high toxicity of hydrofluoric acid. Thus several groups have investigated alternative sources of fluorine. Popular sources include fluorinated titanium precursors (generally $TiF_4$)[151,152] and simple salts.[152–157]

## *2.9 Conclusion*

In this chapter the importance of catalysis as a general technique been addressed, and the place of heterogeneous catalysis (and photocatalysis in particular) in the continually developing world has been outlined. Titanium dioxide is an excellent candidate for industrial photocatalytic applications due to its band gap size, chemical stability, non-toxicity, inert nature, and relative cost. Of the known polymorphs of titanium dioxide, anatase is the most commonly-used for photocatalytic applications, and research on the material is vast and wide-ranging.

While titanium dioxide is an excellent candidate for photocatalytic applications, it still suffers drawbacks, namely its limited absorption profile and high exciton recombination rate. Numerous attempts have been made in the literature to rectify these problems, including doping (using both anionic and

cationic dopants), coupling with other semiconductor materials, decoration with metal clusters, increasing crystallinity *via* calcination or solvothermal methods, and use of surface modifying agents to alter its overall shape and thus reactivity. While these techniques have succeeded in creating catalysts that are either more active under visible light or more efficient in their use of photoexcited electrons and holes, they also introduce more problems. While doping can narrow the band-gap of the material, it invariably leads to bulk defects that encourage recombination and can also reduce the catalyst's oxidising or reducing ability. Noble-metal-decorated $TiO_2$ still suffers aggregation effects which severely limit its recyclability, and SMA modification often introduces toxic chemicals or time- and resource-consuming additional steps to the synthesis process. Despite forty years of research into the synthesis of titanium dioxide as a photocatalyst, the industry standard against which materials are compared is still synthesised by flame pyrolysis of $TiCl_4$ in the absence of modifying materials. There thus exists a strong motivation for researchers to continue work in this field.

# Chapter III

# Synthetic and characterisation methods

## *3.1 Introduction*

This chapter describes general experimental procedures used throughout this thesis, including synthetic methods and characterisation techniques. If a technique is only used in one chapter of this thesis, discussion of the experimental setup will be described in the relevant chapter.

## *3.2 X-ray diffraction*

Powder X-ray Diffraction (PXRD) was performed at the University of Canterbury using two different X-ray diffractometers: originally a Bruker APEXII CCD area detector using Mo $K_\alpha$ radiation and a graphite monochromator, and following this an Agilent Technologies SuperNova X-ray diffractometer using Cu $K_\alpha$ radiation. Original data was collected in two dimensions, and was integrated (see Appendix A) to give values of intensity versus $Q$. Data collected using the SuperNova was already integrated. In both cases, baseline removal was performed using polynomial fitting. All data was collected at room temperature.

For analysis the APEXII, powders were finely ground before being placed in a glass melting point tube. This tube was mounted in the machine and subjected to a thirty- or sixty-second exposure, while being rotated by 360° in the $\phi$ axis. It was found that exposures longer than this overloaded individual pixels on the CCD.

For analysis using the SuperNova, powders were finely ground, mixed with a perfluorinated oil and placed on the end of a glass capillary. This capillary was mounted and manually centred, then analysed for ten minutes

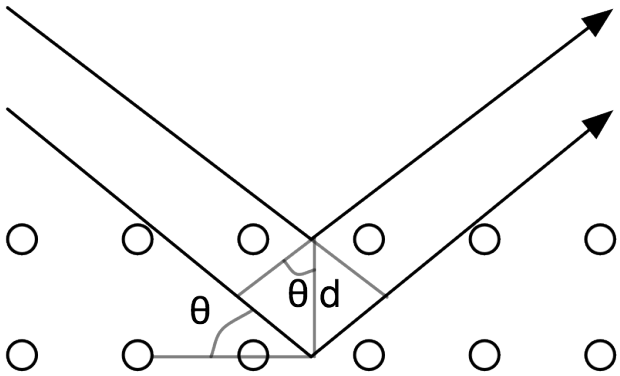


**Figure 3.1.** Two photons diffracting from parallel crystal planes.

while rotating in the $\phi$ axis.

Anatase and rutile concentrations were determined by analysis of the anatase (101) and rutile (110) primary peaks, using an empirical formula developed by Spurr and coworkers:[158]

$$f = \frac{1}{1 + 1.265\frac{I_R}{I_A}} \tag{3.1}$$

where $f$ is the weight fraction of anatase, and $I_R$ and $I_A$ the intensities of the anatase and rutile primary peaks.

Grain size is estimated using the Scherrer equation. Given a beam of X-rays (wavelength $\lambda$) incident on a crystal lattice of spacing $d$ at an angle of $\theta$ to the incident beam, reflected X-rays will be observed diffracted from the crystal at an angle of $2\theta$ to the transmitted beam (3.1). If two photons are reflected off planes adjacent to one another, one photon will travel a slightly longer distance than the other. This difference, referred to as the *path difference*, can be written as:

$$p = 2d \sin\theta \tag{3.2}$$

It follows that if the two photons reflect instead off of two crystal planes $n$ planes apart, the total path difference will be $p_n = np_1$. If the path difference between two photons is a multiple of $\lambda$, they will *constructively interfere*, resulting in increased intensity at this angle $2\theta$. If, however, two photons are reflected with a path difference of $(n + 0.5)\lambda$, they will be exactly out

of phase and will cancel each other out, leading to *destructive interference*. If we assume an infinite lattice, this is guaranteed for all $p \neq n\lambda$. For example, if $p = 1.1\lambda$ it follows that every reflection will be cancelled out by the corresponding reflection for $n = 5$ ($p_5 = 5.5\lambda$).

As the dimensions of the crystal decrease, it follows that reflected photos with path differences close to $n\lambda$ will start to show intensity. For example, if $p = 1.001\lambda$ the corresponding out-of-phase reflection will occur for $n = 500$, $p_n = 500.5$. As the crystal size decreases, the number of crystal planes will decrease and less and less reflected photons will be cancelled out. This reveals itself as a broadening of the diffraction rings, and is most noticeable for crystals less than $1\mu$m in size.

The relationship between peak broadening and crystal size was determined by Paul Scherrer in 1918 and is now represented in the Scherrer equation:[159]

$$L = \frac{K\lambda}{\beta \cos(\theta)} \tag{3.3}$$

where $L$ is the linear dimension of the crystalline domain, $K$ a numerical constant (assumed to be 0.93), $\lambda$ the wavelength of incident radiation, $\beta$ the full-width at half maximum of the diffraction peak, and $\theta$ the diffraction angle. Scherrer's original estimation of the constant $K$ was:

$$\begin{aligned} K &= 2\left(ln\frac{2}{\pi}\right)^{\frac{1}{2}} && (3.4)\\ &= 0.93 && (3.5) \end{aligned}$$

Later researchers arrived at different values for the constant $K$, based on different approximation methods and different methods of measuring the value $\beta$.[159] For most applications the value $K$ can be approximated to 0.9.[160]

The value $\beta$ can be artificially inflated by properties of the measurement instrument, and to arrive at a correct value of particle size such *instrumental broadening* should be taken into account:

$$\beta_{\text{actual}} = \beta - \beta_i \tag{3.6}$$

Instrumental broadening contributions to $\beta$ were determined using a $LaB_6$ standard for work performed at the Australian Synchrotron and Callaghan Innovation. Due to the absence of an appropriate standard at the University of Canterbury, instrumental broadening was approximated by use of P-25 "Aeroxide" commercial titania as a secondary standard. A sample of P-25 was measured by PXRD at Callaghan Innovation, and peak widths were measured, accounting for instrumental broadening using the $LaB_6$ standard available there. A sample of the same batch of P-25 was then measured by PXRD at the University of Canterbury, and the peak widths compared against those obtained at Callaghan Innovation. Instrumental broadening was assigned to each peak such that the corrected width for each peak matched the correct width of the corresponding peak measured at Callaghan Innovation.

## *3.3 Electron microscopy*

Scanning electron microscopy (SEM) was conducted on samples using a JEOL 7000F FE-SEM. The working distance was varied between 10 mm and 4 mm to give the best image, while voltage was usually kept around 10 kV and current around 9 (arbitrary units for current). SEM samples were prepared by adding a sample of analyte ($\sim$10 mg) to ethanol ($\sim$ 1 mL) and sonicating until fully dispersed. A drop of sample was then placed on a silicon slide (approximate dimensions 5 $\times$ 5 mm) and left to dry.

Transmission electron microscopy (TEM) was conducted using a Philips CM-200 TEM. Apertures and lenses were aligned at the start of each session. TEM samples were prepared as for SEM samples above, but were immobilised on a 300-mesh copper TEM grid coated with heavy carbon/Formvar film (unless otherwise stated).

Particle size analysis was performed using the ImageJ image analysis software.[161] Particles were modelled as ellipses, with ellipse fit parameters (major and minor axes) used for all particle size and anisotropy calculations.

### *3.3.1 TEM particle fringing*

When an electron beam is diffracted by a sample, it will change phase slightly. The interference of diffracted and non-diffracted electron beams results in a

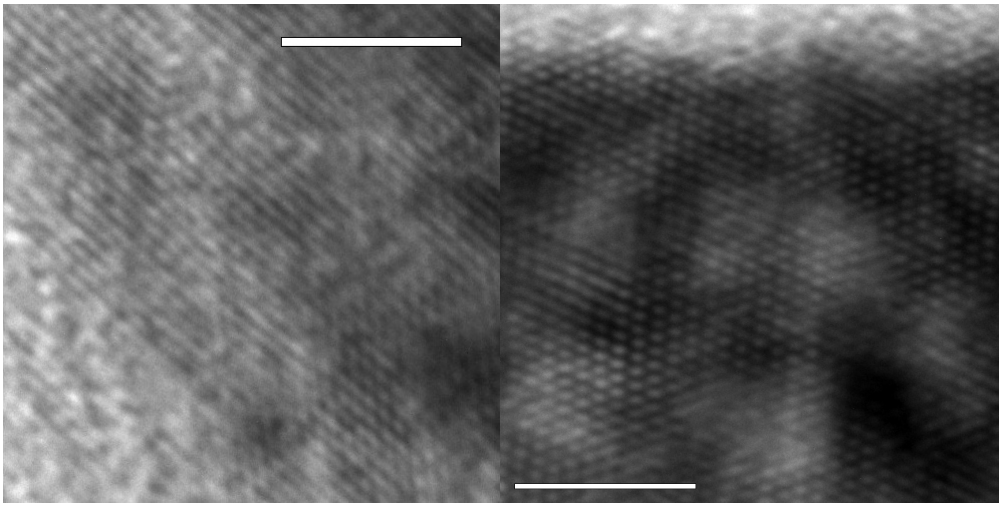

**(a)** Fringing **(b)** Structure image

**Figure 3.2.** Examples of fringing and structure images in TEM, both artefacts of the phase contrast phenomenon. Scale bars indicate 5 nm.

phenomenon called "phase contrast". Phase contrast typically manifests as a speckled pattern in the background of images, but in the case of crystalline samples, it may result in fringing (see Figure 3.2a). Fringing occurs due to the interaction of the electron beam with the ordered atomic lattice of the crystalline material, and results in a series of alternating bright and dark lines which are a function of the inter-lattice spacing. By analysing these fringes and comparing them against literature data it is possible to discern the phase and orientation of crystalline nanoparticles.[162]

When fringing occurs due to two different Miller indices of the nanocrystal, the resultant pattern is known as a "structure image" (Figure 3.2b), and the resulting pattern may also aid in phase identification by analysis of the angle between the two fringing patterns.[162]

TEM fringing was monitored using the software package ImageJ.[163] Images that showed evidence of fringing were first calibrated using scale bars, and then cropped such that only the fringing sections of the image were evident. The images were then subject to Fast Fourier Transform (FFT) processing. Fringing lines, being periodic functions, were represented by bright spots in the FFT image of the micrograph, and their period was de-

termined by measuring the radius of these bright spots in reciprocal space. The angle between fringing lines could be determined by measuring the angle between bright spots in reciprocal space. For titanium dioxide phase and alignment identification, fringing distances were compared against literature sources (see Section 3.2).

## *3.4 Dynamic light scattering*

Dynamic light scattering (DLS) measurements were made on a Microtrak Zetatrak DLS instrument. Zeta potentials were also recorded using the instrument. All blanks were performed using Milli-Q distilled water. Samples were dispersed in Milli-Q water and sonicated until homogeneous. Concentration was generally higher than 10 g $L^{-1}$ (as used for SEM and TEM samples), modified based on the loading index as reported by the DLS apparatus. In general, low concentrations were favoured to prevent or mitigate aggregation. If particle sizes appeared unusually large (compared against EM particle sizing), repeated were performed. Particles were analysed for three runs of sixty seconds each. It was generally possible to determine when aggregation had taken place by comparing particle size distributions for the same sample over a number of measurement sessions.

Zeta potential measurements often required a higher concentration than particle size measurements. In this case, separate measurements were taken for particle size and zeta potential, to limit aggregation in particle size measurements.

Particles with low (close to zero) zeta potentials exhibited aggregation in solution, evidenced as a discrepancy between particle size as determined by SEM and as determined by DLS. In some cases this could be countered by diluting the colloidal solution, however it was sometimes impossible to find a concentration above the detection limit of the machine at which particles did not aggregate.

## *3.5 UV-vis DRS*

UV-vis diffuse reflectance spectroscopy (UV-vis DRS) was performed on a Cary 4040 Spectrometer, fitted with a Research & Industrial Instruments

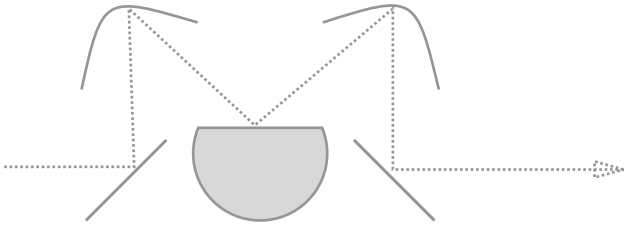

**Figure 3.3.** Standard UV-vis DRS setup. The incident beam is directed onto the sample *via* a combination of plane and parabolic mirrors, while the diffuse reflection is collected by another parabolic mirror onto the right-most plane mirror, which reflects it into the detector.

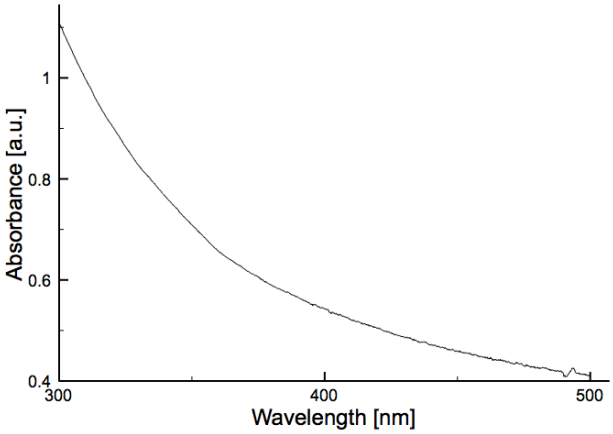


**Figure 3.4.** Absorbance profile of the UV-vis DRS apparatus, measured using a galvanometer mirror as a target.

Company TR-5 ATR unit (setup shown in Figure 3.3). The sample is placed in the sample holder and illuminated with the incident light beam. Light reflected by the sample is collected by the right hand parabolic mirror and focussed onto the right-hand plane mirror, which then illuminates the detector. Due to the reflection profile of the mirrors (see Figure 3.4), data could only be collected between 300–600 nm. At wavelengths shorter than this, absorbance due to the mirrors of the apparatus prevented accurate measurement.

Data was collected for all samples from 300–600 nm in absorbance mode, at a rate of 500 nm $min^{-1}$ with a slit width of 2 nm. At least seven duplicates of each spectrum were taken. In all cases a baseline (calculated using a

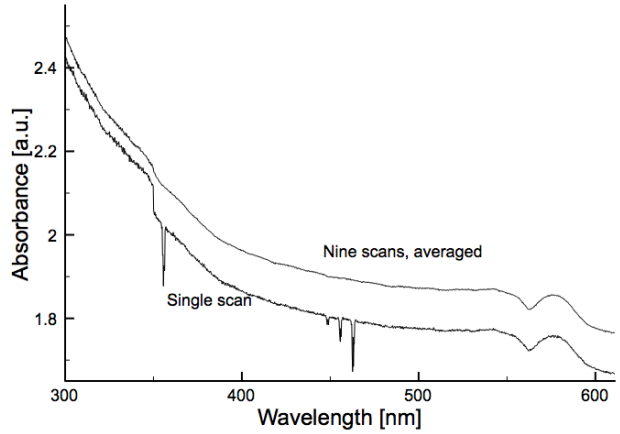


**Figure 3.5.** UV-vis DRS analysis. The bottom trace shows a single UV-vis DRS measurement, with characteristic intermittent spikes. The top trace (offset for clarity) shows a composite of nine separate measurements on the same sample, averaged as described in the body text.

cleaned galvanometer mirror, profile measured five times and averaged) was subtracted from the data. It was found that samples displayed intermittent downward spikes in absorbance (see Figure 3.5). It is thought that these may be due to secondary reflections from non-blacked sections of the UV-vis DRS apparatus. Since these features did not repeatedly occur, it was possible to remove them from the data set.

Data was processed in the following manner. All sequential duplicates of each spectrum were combined, giving a number of values of absorbance at each wavelength. From these the relative deviation of each data point from the mean was found by:

$$\delta_i \equiv \frac{\left|\mathrm{A}_i - \overline{\mathrm{A}}\right|}{\overline{\mathrm{A}}} \tag{3.7}$$

For a set of seven points the value $\delta_{\max}$ is defined as the largest $\delta_i$ value in the set. If $\delta_{\max} > 0.01$, the point with the highest $\delta_i$ was removed from the set and the $\delta_i$ values recalculated. This process was repeated until $\delta_{\max} \leq 0.01$ for this particular wavelength. If this process resulted in only one point for a given wavelength, all seven points were used regardless.

As a result of this process, each wavelength would have anywhere between two and seven absorbance values. The mean of these values was then used as

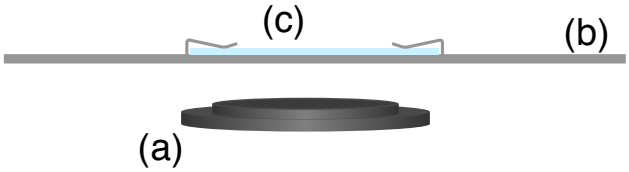


**Figure 3.6.** Sample preparation method for UV-vis DRS using the Agilent UV-vis DRS sphere. Powdered sample is placed in the holder (a) and pressed to form a loose pellet. The sample holder is inserted into the plate (b) such that the sample is pressed against the attached quartz window (c). The sample plate can then be placed into the machine.

the absorbance. In general, the region between ∼350 nm and 600 nm showed very little noise, with repeated measurements further reducing any instrumental noise. The region of 300–350 nm, however, exhibited considerable noise. This is likely due to a combination of two factors: first, the mirrors' decreasing reflectivity in this region, and second, the titanium dioxide samples absorbing light in this region, providing less signal and thus increasing overall uncertainty.

In early 2013, the Department of Chemistry purchased a UV-vis DRS sphere for this spectrometer. Due to the improved signal of this machine compared to the previous setup, it was used for all subsequent measurements. Due to the vertical alignment of the samples, it was required that a quartz window be placed in front of the sample in order to prevent powdered sample falling into the machine (see Figure 3.6). Samples were manually pressed onto a sample holder, which was then attached to the sample plate while horizontal. The quartz window was attached, keeping the powder pellet in place, and the whole plate was then inserted into the machine.

### *3.5.1 Kubelka-Munk band gap determination*

The optical absorption coefficient $\alpha$ of a semiconductor around the band-gap can be modelled by the equation:[164–166]

$$\alpha = B\frac{(h\nu - E_g)^{m/2}}{h\nu} \tag{3.8}$$

where $B$ is a constant, $h\nu$ is the energy of the incident radiation, $E_g$ is the

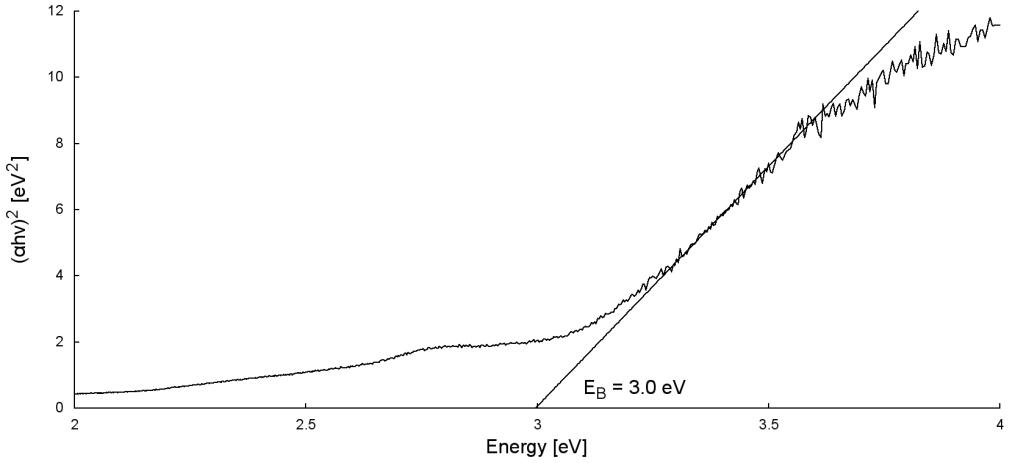


**Figure 3.7.** A typical modified Kubelka-Munk plot. The band gap is determined by extending the linear portion of this graph to $(\alpha h\nu)^2 = 0$.

energy of the band gap, and $m$ is a constant set to 1 for direct transitions.[165] UV-vis DRS allows a measure of the optical absorption of a sample as a function of radiation energy, and thus by using this data it is possible to approximate the band gap. A plot of $(\alpha h\nu)^2$ against $hv$ (a modified Kubelka-Munk plot[166]) reveals a distinctive "kinked" shape (see Figure 3.7). By extending the linear portion of this graph to $(\alpha h\nu)^2 = 0$ it is possible to find the direct band gap, as when $h\nu = E_g$, $\alpha = 0$.

## *3.6 XPS*

X-ray Photoelectron Spectroscopy (XPS) was carried out at the Australian Synchrotron Soft X-ray Beamline. X-ray energy was determined on a case-by-case basis in order to achieve the best cross-section for the elements to be analysed, while also ensuring that peaks of interest did not overlap Auger peaks or other phenomena.

Samples were generally prepared by dispersion in water followed by deposition on a small (3 mm × 5 mm) doped silicon wafer. These wafers were then affixed to stainless steel discs by conducting carbon tape: their small size allowed for up to twelve samples on a single disc, allowing for fast analysis and high throughput.

XPS signals were normalised using the adventitious carbon peak (284.8

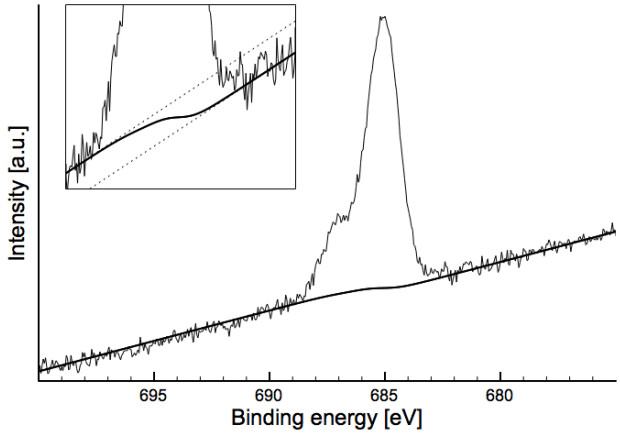


**Figure 3.8.** Sample XPS peak (here the F 1s XPS peak) on a changing background. The background is modelled by a combination of linear and Shirley functions. Inset: the effect of the Shirley function on the background under the peak.

eV).[167] Background was approximated using a Shirley's approximation.[168] If this did not prove sufficient (*e.g.* if the background signal before and after the peak was not "flat"), the background was simulated using a combination of a linear function and Shirley background function (see Figure 3.8).[169] The background (as a function of the binding energy $E_B$) could thus be modelled:

$$B(E_B) = mE_B + k_1 + (k_2 - k_1)\frac{\sum_{E=0}^{E_B} I(E)}{\sum_{E=0}^{\infty} I(E)} \tag{3.9}$$

where $m$ is the slope of the linear background and $k_1$ and $k_2$ are constants for the Shirley background, determined by fitting to the pre- and post-edge signal. $I(E)$ indicates the intensity of the fitted peak at a given energy $E$.

Signals were modelled using a pseudo-Voigt function with 30% Lorentzian character and 70% Gaussian character. Peak fitting was performed using non-linear least squares fitting. Relative concentrations were determined using the elemental cross-sections and anisotropy factors collated by Yeh and Lindau.[170]

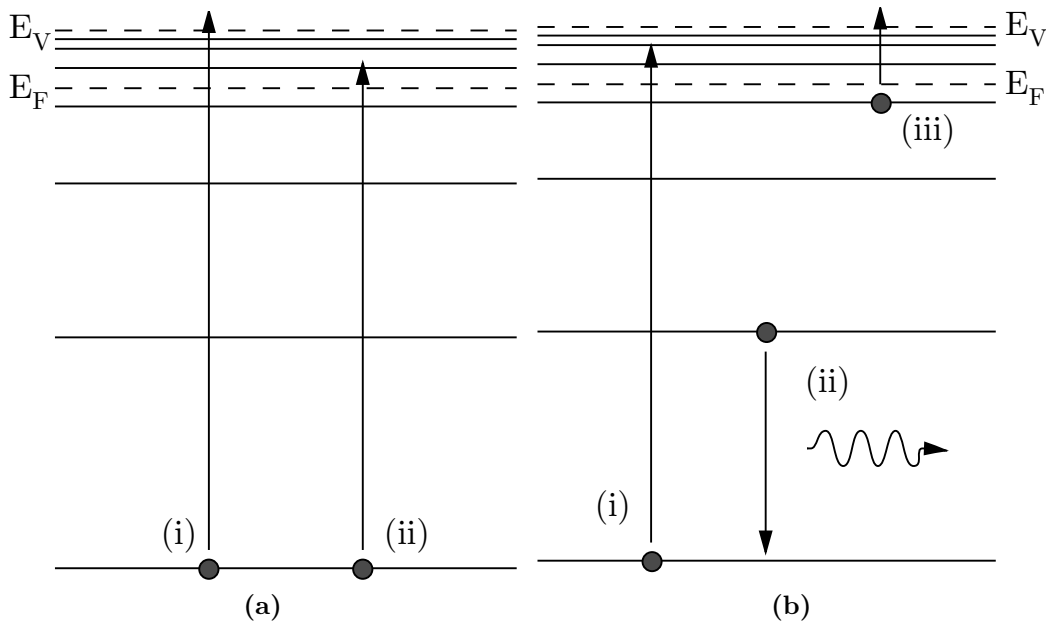


**Figure 3.9.** Electron excitation and emission in (a) XPS and (b) NEXAFS. In XPS, incident radiation ionises core electrons (a i) to above the vacuum energy $E_V$, allowing them to escape. Core electrons excited into bound states (such as unoccupied orbitals above the Fermi energy $E_F$, a ii) are not detected. In NEXAFS, the excitation energy is varied to select purely bound-state excitation (b i). Excitation to bound states allows secondary electrons to relax to the ground state, giving off energy either radiatively (b ii) or by releasing valence-band "Auger" electrons (b iii).

## *3.7 NEXAFS*

XPS gives detailed information about the electronic and chemical state of a sample, but is limited in that it will only detect absorption events that lead to ionisation (*i.e.* emission of a photoelectron, see Figure 3.9a). Excitation to bound states (such as unoccupied orbitals above the Fermi energy) may lead to secondary electron emission (so-called "Auger electrons"), but these do not provide any additional information in XPS.

Near-Edge X-ray Absorption Fine Structure (NEXAFS) spectroscopy is a technique related to XPS in which the *incident* X-ray energy, rather than the detection energy, is varied. By varying the incident X-ray energy across a known absorption edge, it is possible to selectively excite electrons from

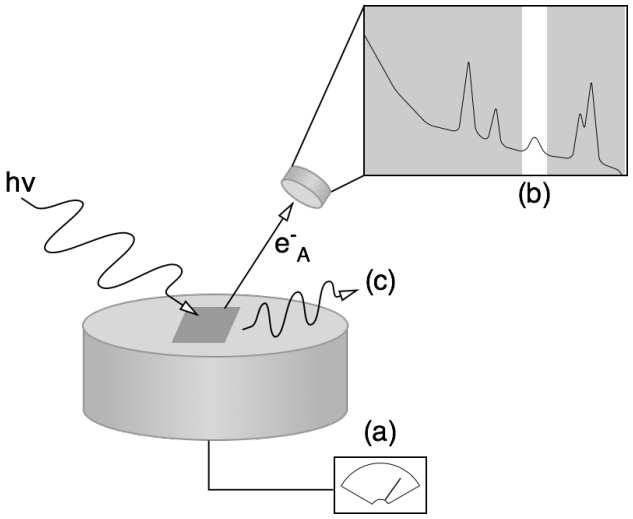


**Figure 3.10.** Methods of NEXAFS detection. Spectra were collected by Total Electron Yield (a), Auger Electron Yield (b), and Fluorescence Yield (c) methods, as described in the main text.

one state to another. By observing a number of phenomena related to the excitation of the core electron (including the emission of Auger electrons and photons, Figure 3.9b), it is possible to measure the fine structure of the element in question.[169]

NEXAFS studies reported here used three means of detection (Figure 3.10):

- **Total Electron Yield (TEY)**, determined by measuring the current flow of electrons to the sample holder, replenishing electrons lost via Auger radiation.
- **Auger Electron Yield (AEY)**, determined by observing electron radiation from the sample at the energy for a given Auger peak (since $E_{kin}$ for Auger electrons is independent of incident radiation energy).
- **Fluorescence Yield (FY)**, determined by observing photons emitted as a result of Auger electron release.

NEXAFS spectra were normalised by the following method:

1. Linear background was determined by fitting of the pre-edge, and applied to the spectrum.

2. The spectrum was normalised such that the post-edge was approximately unity.

### *3.7.1 NEXAFS spectroscopy on $TiO_2$*

Titanium dioxide NEXAFS studies generally focus on the Ti $L_{2,3}$ edge, in which electrons are excited from the Ti 2p orbital. In the case of $Ti^{4+}$, excitation generally occurs to the unoccupied Ti 3p orbital (Figure 3.11a). In the case of octahedral coordination around the Ti atom (as is the case in $TiO_2$), the originating Ti 2p orbital is split due to spin-orbit coupling to give $2p_{1/2}$ and $2p_{3/2}$ atomic orbitals, while the destination Ti 3p orbital is split due to ligand-field interactions to give $e_g$ and $t_{2g}$ orbitals.[171] This combination of orbital splittings means that there are *four* possible transitions that may be observed in NEXAFS (Figure 3.11b): these are generally divided into the $L_2$ (from Ti $2p_{1/2}$) and $L_3$ (from Ti $2p_{3/2}$) series.[172] A typical NEXAFS spectrum for the Ti 2p edge (with transitions labelled) is shown in Figure 3.11c.

The $e_g$ peaks are actually both combinations of two peaks,[172] as can be seen in the shoulder this peaks exhibits in Figure 3.11. The relative intensity of these two peaks can be used as a measure of the phase of the studied material: in the case of anatase, the lower-energy $L_3e_g$ peak is more intense, whereas for rutile the higher-energy peak is more intense. In the case of brookite the peaks tend to be approximately the same intensity.[172] The reason for this splitting was until recently a matter of debate, however in 2010 Cheynet *et al.* demonstrated using electron energy-loss spectroscopy not only that the $L_3e_g$ peak was actually composed of *four* different subpeaks (two for anatase and two for rutile), but also that the variation in peak intensities is due to long-range band structure effects.[173]

It may be that bulk doping of $TiO_2$ is detectable by NEXAFS spectroscopy. Chen *et al.* have reported a change in the $L_2$ splitting of the Ti $L_{2,3}$ NEXAFS spectrum due to N doping,[174] attributing this effect to the change in the Ti ligand field due to the introduction of substitutional nitrogen. However a number of other publications exploring NEXAFS spectroscopy of doped $TiO_2$ have not commented on a change in the NEXAFS peak splitting due to doping,[175–179] reinforcing the fact that this phenomenon

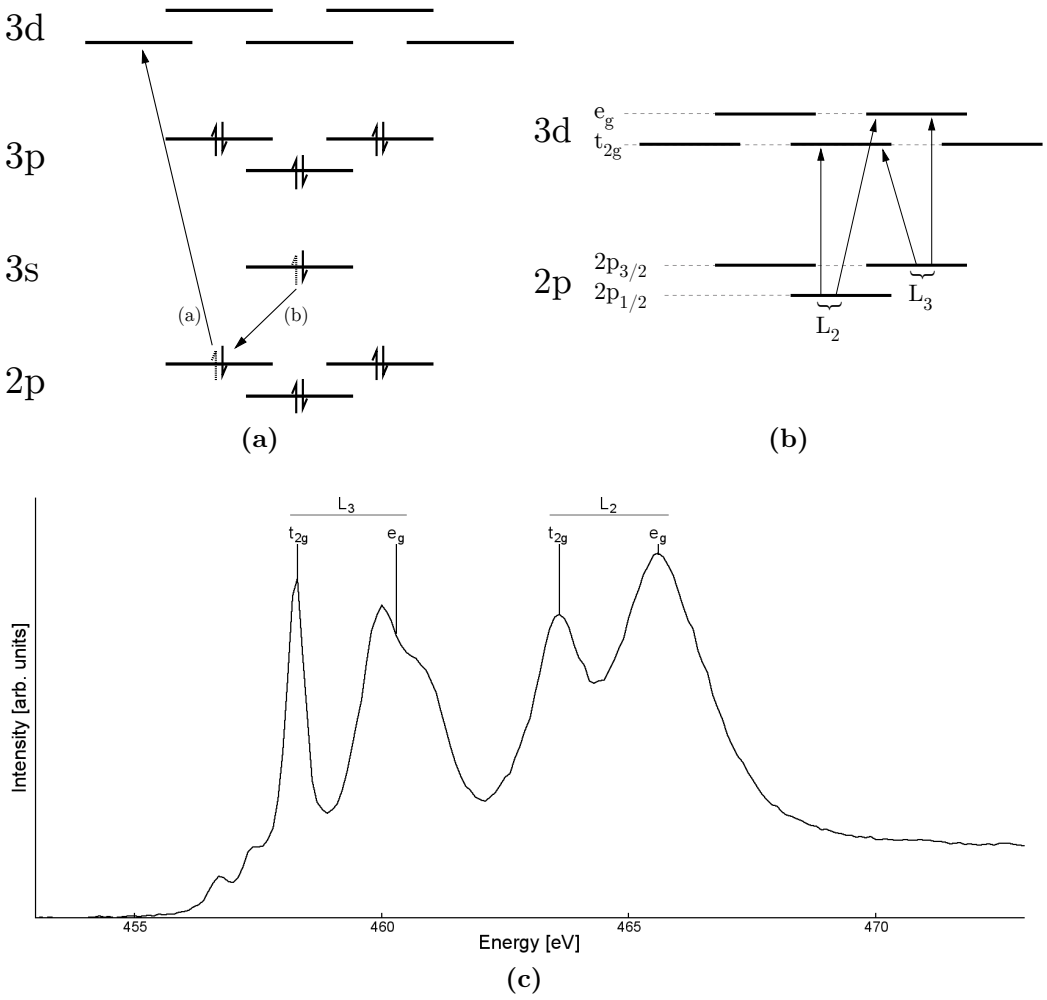


**Figure 3.11.** Ti 2p NEXAFS focusses on excitation of electrons in the Ti 2p orbital, generally to the unoccupied 3d orbital (a). Due to spin-orbit coupling and ligand-field interactions, this leads to four possible transitions (b), which can be seen in a typical NEXAFS spectrum of $TiO_2$ (c).

is relatively weak when compared to the effect of *e.g.* titania phase on the NEXAFS spectrum.

# Chapter IV

# Differing methods of $TiO_2$ synthesis

A goal of this project was to evaluate several methods of $TiO_2$ synthesis before focussing on one in particular. This chapter details several avenues of research that were explored during this project, but for which insufficient analysis was performed to warrant its own chapter. A number of these projects were performed at other locations immediately after the Christchurch 2011 earthquake, including the work on oxalic acid synthesis (performed at Industrial Research Limited, now Callaghan Innovation) and arc discharge synthesis (performed at GNS Science), and *in situ* SAXS analysis of $TiO_2$ (performed at ANSTO, Sydney).

## *4.1 Synthesis of titanium dioxide by sol-gel synthesis in the presence of oxalic acid*

### *4.1.1 Introduction*

Carboxylic acids have long been used as surface modifying agents (SMAs) in the synthesis of $TiO_2$, and their binding to the $TiO_2$ surface has been the subject of much study.[4] Oxalic acid, the smallest dicarboxylic acid (Figure 4.1a) binds strongly to the titanium dioxide surface (favouring anatase over rutile), generally as the oxalate ($O_2C_2O_2^{2-}$) anion, with oxygen atoms binding to adjacent Ti sites (Figure 4.1b) and affecting growth of both anatase and rutile phases.[180]

Despite the suitability of oxalic acid as an SMA, there is a scarcity of literature on its use as an SMA.[181,182] While carboxylic acids have been dismissed by some due to their intense affinity for the $TiO_2$ surface[183] (which can make SMA removal difficult without resorting to harsh conditions), oxalic acid is easily degraded by combined UV/$TiO_2$ treatment.[146] Thus the oxalic

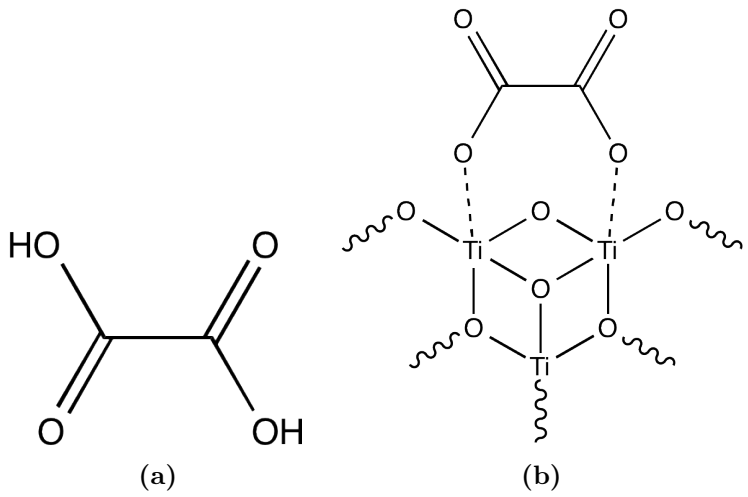


**Figure 4.1.** (a) The structure of oxalic acid; (b) Binding of the oxalate ion to the $TiO_2$ surface.

acid/$TiO_2$ system has an "in-built" cleaning mechanism, allowing for strict control over the synthetic environment but also allowing the production of $TiO_2$ whose surface is free of residual SMA.

In this study, titanium dioxide particles were synthesised by a combination hydrolytic/thermolytic technique in the presence of oxalic acid and ammonium fluoride as surface modifying agents (SMAs). The resultant materials were analysed by powder X-ray diffraction to monitor the particle phase and crystallite size during the reaction. The effect of oxalic acid and ammonium fluoride concentrations, as well as heating temperature and time, on these properties, is reported.

### *4.1.2 Experimental*

Titanium isopropoxide (TTIP, Lancaster Synthesis), oxalic acid dihydrate (AR grade, Ajax Chemicals), and ammonium fluoride were used as received.

In a typical procedure, oxalic acid dihydrate (3.15 g, 25 mmol) is dissolved with heating (30°C) and stirring in ethanol (23 g, 500 mmol). Once the oxalic acid is fully dissolved, titanium isopropoxide (14.2 g, 50 mmol) is added. Upon addition, the titanium precursor produces a white titanium oxalate slurry. This slurry is thoroughly stirred and to this is added distilled water

(180 mL, 10 mol). The resulting white opaque solution is stirred vigorously at 60°C for approximately one hour, over which time the opaque white solution becomes translucent as the titanium oxalate network decomposes to give a colloid of titanium oxide nanoparticles. The colloid is removed from heat when no further clarification of the solution occurs.

The above synthetic method produces titania in an environment of 0.5 mole equivalents of oxalic acid (compared to titanium). A second batch of titania was also synthesised using 0.4 mole equivalents (2.52 g, 20 mmol) of oxalic acid. These will be referred to as $TiO_2$-0.5Ox and $TiO_2$-0.4Ox respectively.

Both batches of titania were heat-treated with fluoride post-synthesis at 95°C. An amount of anhydrous ammonium fluoride was added to samples of each batch, and 7 mL of colloidal solution was placed in an 8 mL heat- and pressure-resistant glass vial with a PTFE seal. Samples were heated for 1, 2, 3 and 4 days. Fluoride amounts added to $TiO_2$-0.5Ox were 0.1, 0.25, 0.5, 1 and 2 mole equivalents (compared to titanium), and the samples will be referred to as $TiO_2$-0.5Ox-0.1F, $TiO_2$-0.5Ox- 0.25F, *etc.*. Fluoride amounts added to $TiO_2$-0.4Ox were 0.1, 0.25, 0.5, and 1. In all cases, equivalent materials were synthesised in the absence of fluoride, and these will be referred to as $TiO_2$-0.4Ox-0F *etc.*.

A second set of experiments were performed at 180°C. These were heated using teflon-lined stainless steel pressure vessels. For these samples the oxalic acid ratio was fixed at 0.5 mole equivalents, while the fluoride ratio was set to 0, 0.1, 0.25 and 0.5 mole equivalents. Samples were taken after heating for 2 and 4 days. These samples were be referred to as $TiO_2$-180.

Once withdrawn from heating, liquid samples were placed in crystallising dishes and exposed to UV light for at least 48 hours. This had the dual effects of removing the water/ethanol solute and also causing the degradation of oxalic acid, catalysed by the titanium dioxide nanoparticles. The resulting powders were mixed to ensure full exposure and placed under UV light for a further 24 hours.

It was found that even temperatures of 95°C were in some cases able to break the seal of the glass vials, leading to escape of solvent. Due to time constraints, only a select few experiments could be repeated. Sufficient data

was collected to perform analysis, as detailed below.

### *4.1.3 Characterisation*

Samples were characterised by SEM using a JEOL JSM-6500F field emission scanning electron microscope. Samples were prepared by diluting one-hundredfold and placing a drop of sample on a silicon chip, then letting the solute evaporate. PXRD was performed using a Philips PW3700 series diffractometer using Co-$K_\alpha$ radiation ($\lambda$ = 1.7889 Å), and data analysed using the TOPAS analysis software package.

### *4.1.4 Results*

PXRD results are displayed in Table 4.1. The majority of samples were anatase in nature, although the exact fraction of anatase varied depending on heating time, temperature, and ratio of both oxalic acid and fluoride in solution.

The anatase fraction of each sample is shown in Figure 4.2. It can be seen that for $TiO_2$-0.5Ox, the majority of the sample is anatase even in the absence of fluoride, while the addition of even a small amount of fluoride encourages the growth of anatase. This has been previously reported in other sol-gel systems in the literature[153] and it is believed that the strong affinity of fluoride for $TiO_2$ surfaces[120] allows the same mechanism to occur here. The system exhibits entirely anatase character until the concentration of fluoride exceeds that of titanium: at this point, the minority phases observed are not rutile or brookite but oxammite ($(NH_4)_2C_2O_4 \cdot H_2O$) and two forms of ammonium titanium fluoride ($NH_4TiF_5$ and $NH_4TiF_6$).[184]

When the oxalic acid ratio is reduced (Figure 4.2b), traces of rutile start to appear in low-fluoride ([F]/[Ti] $\leq$ 0.5) samples. These measurements suggest that the population of rutile slowly grows over time with heat treatment unless other factors (such as the presence of SMAs such as fluoride or oxalate) interfere. The low anatase fraction of $TiO_2$-0.4Ox-1F is again due to the presence of oxammite and ammonium titanium fluorides.

An increase in temperature (Figure 4.2c) results in a dramatic increase in the rate of conversion of anatase to rutile. Without the influence of fluoride,

**Table 4.1.** Oxalic acid $TiO_2$ PXRD data.

| [F]/[Ti] | Time [days] | Anatase Fraction | Anatase Size [nm] | Rutile Fraction | Rutile Size [nm] | Oxammite Fraction | Oxammite Size [nm] | $(NH_4)_2TiF_5$ Fraction | $(NH_4)_2TiF_5$ Size [nm] | $(NH_4)_2TiF_6$ Fraction | $(NH_4)_2TiF_6$ Size [nm] |
|---|---|---|---|---|---|---|---|---|---|---|---|
| **$TiO_2$-0.4Ox** | | | | | | | | | | | |
| 0 | 3 | 97.9% | 6.5 | 2.1% | 33.9 | | | | | | |
| | 4 | 95.2% | 6.2 | 4.8% | 35.0 | | | | | | |
| | 5 | 96.7% | 6.4 | 3.3% | 40.2 | | | | | | |
| 0.1 | 3 | 99.4% | 7.7 | 0.6% | 78.4 | | | | | | |
| | 4 | 99.1% | 8.1 | 0.9% | 28.4 | | | | | | |
| 0.25 | 3 | 100.0% | 9.3 | | | | | | | | |
| | 4 | 100.0% | 9.6 | | | | | | | | |
| 0.5 | 2 | 100.0% | 6.9 | | | | | | | | |
| | 3 | 100.0% | 8.1 | | | | | | | | |
| | 4 | 97.2% | 8.3 | | | | | | | 2.8% | 54.5 |
| 1 | 2 | 69.2% | 5.6 | | | 20.1% | 121.0 | 4.9% | 137.7 | 5.7% | 29.2 |
| | 4 | 69.9% | 6.9 | | | 13.8% | 116.9 | 7.5% | 30.3 | 8.8% | 15.0 |
| **$TiO_2$-0.5Ox** | | | | | | | | | | | |
| 0 | 4 | 93.9% | 6.2 | 6.1% | 34.4 | | | | | | |
| 0.1 | 2 | 100.0% | 7.1 | | | | | | | | |
| | 3 | 100.0% | 7.8 | | | | | | | | |
| | 4 | 100.0% | 8.4 | | | | | | | | |
| 0.25 | 1 | 100.0% | 7.1 | | | | | | | | |
| | 2 | 100.0% | 8.1 | | | | | | | | |
| | 3 | 100.0% | 9.2 | | | | | | | | |
| | 4 | 100.0% | 9.8 | | | | | | | | |
| 0.5 | 1 | 100.0% | 7.2 | | | | | | | | |
| | 2 | 100.0% | 8.6 | | | | | | | | |
| | 3 | 100.0% | 8.7 | | | | | | | | |
| | 4 | 100.0% | 10.4 | | | | | | | | |
| 1 | 2 | 60.3% | 6.8 | | | 18.5% | 39.1 | 15.5% | 20.5 | 5.7% | 37.8 |
| | 3 | 68.5% | 7.4 | | | 20.9% | 54.1 | 5.7% | 26.9 | 4.9% | 44.8 |
| | 4 | 65.4% | 6.3 | | | 18.3% | 53.8 | 10.8% | 35.4 | 5.6% | 23.2 |
| 2 | 1 | 56.7% | 5.4 | | | 17.8% | 119.8 | 19.1% | 77.8 | 6.4% | 27.9 |
| | 4 | 96.3% | 8.9 | | | | | | | | |
| **$TiO_2$-180** | | | | | | | | | | | |
| 0 | 2 | 76.8% | 14.8 | 23.2% | 81.7 | | | | | | |
| | 4 | 13.0% | 14.5 | 87.0% | 78.1 | | | | | | |
| 0.1 | 2 | 100.0% | 16.8 | | | | | | | | |
| | 4 | 95.0% | 17.6 | 5.0% | 44.3 | | | | | | |
| 0.25 | 2 | 100.0% | 16.6 | | | | | | | | |
| | 4 | 100.0% | 16.6 | | | | | | | | |
| 0.5 | 2 | 100.0% | 15.7 | | | | | | | | |
| | 4 | 100.0% | 16.7 | | | | | | | | |

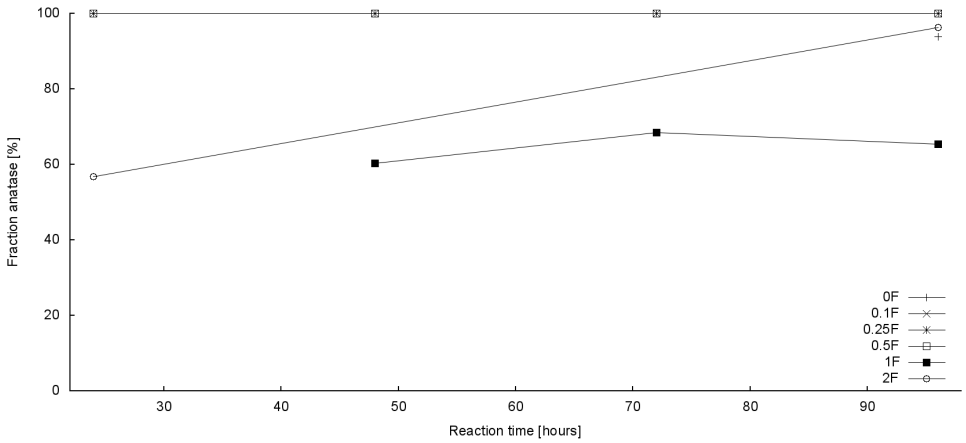


**(a)** $TiO_2$-0.5Ox

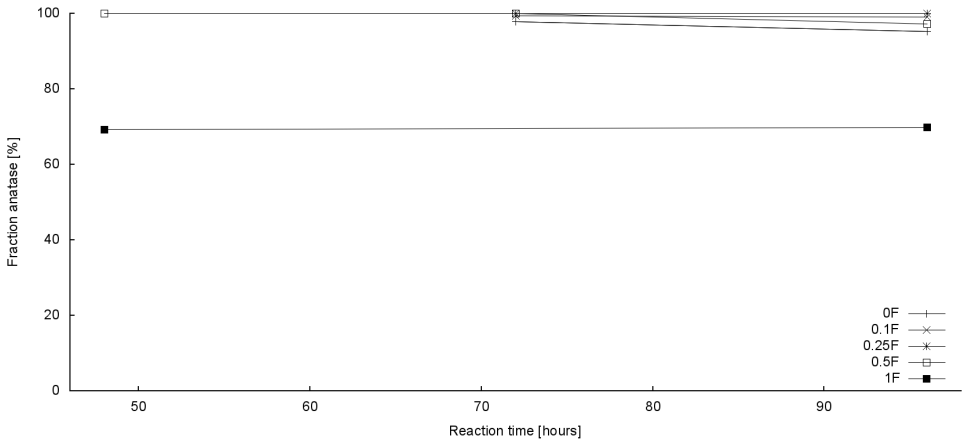


**(b)** $TiO_2$-0.4Ox

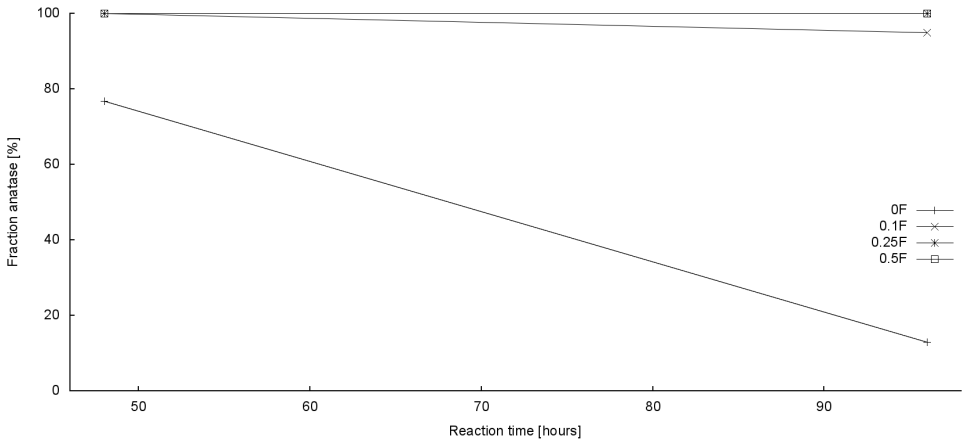


**(c)** $TiO_2$-180

**Figure 4.2.** Anatase fraction (as determined by PXRD) for oxalic acid-modified $TiO_2$.

after four days of heating the sample has almost entirely transformed to the rutile phase. Once again it is observed that even 0.1 mole equivalents of fluoride severely retards this process, resulting in only 5% rutile character. This demonstrates that fluoride is effective at suppressing the growth of rutile, even at relatively high synthesis temperatures.

Anatase particle size as a function of oxalic acid and fluoride concentration, heating temperature and time is shown in Figure 4.3. As is expected, thermal treatment in solution results in slow particle growth, with larger particles observed when heating was performed at a higher temperature. Samples synthesised in the presence of excess ([F]/[Ti] $\geq$ 1) fluoride showed erratic particle growth behaviour: this may be due to the formation of oxammite and ammonium titanium fluorides in solution. The drop in anatase particle size for those samples heated at 180°C (Figure 4.3c) may be due to the (relatively) rapid formation of rutile in these systems.

An overall comparison of anatase crystallite size can be made after four days (96 hours) of heating, as shown in Figure 4.4. As concentration of fluoride in solution increases, so too does the anatase particle size. If the presence of fluoride in solution encourages the growth of anatase it makes sense that increasing the concentration of fluoride in solution then increases the rate at which anatase particles will grow. However, after a given fluoride concentration ([F]/[Ti] = 1 for $TiO_2$-0.5Ox) the anatase crystal size decreases. The reason for this drop is unknown, but may be connected with the formation of oxammite and ammonium titanium fluorides as described previously. This trend is also apparent in $TiO_2$-0.4Ox, but of particular interest the anatase crystallite size "peak" occurs at only [F]/[Ti] = 0.25. Further, the crystal sizes for the range [F]/[Ti] $\leq$ 0.25 appear similar between $TiO_2$-0.4Ox and $TiO_2$-0.5Ox. This suggests that:

- Anatase crystallite size is dependent on fluoride concentration, but not directly on oxalate concentration

- However, the presence of oxalate in solution increases the threshold fluoride concentration beyond which anatase crystallite size starts to decrease.

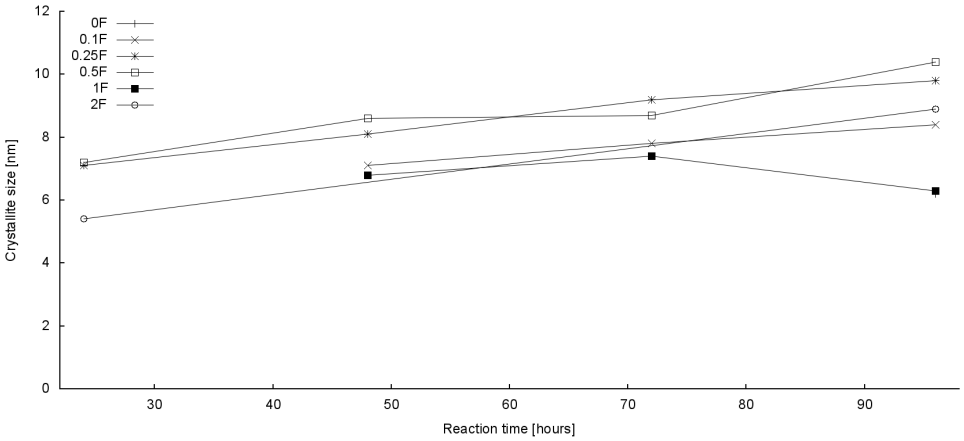


**(a)** $TiO_2$-0.5Ox

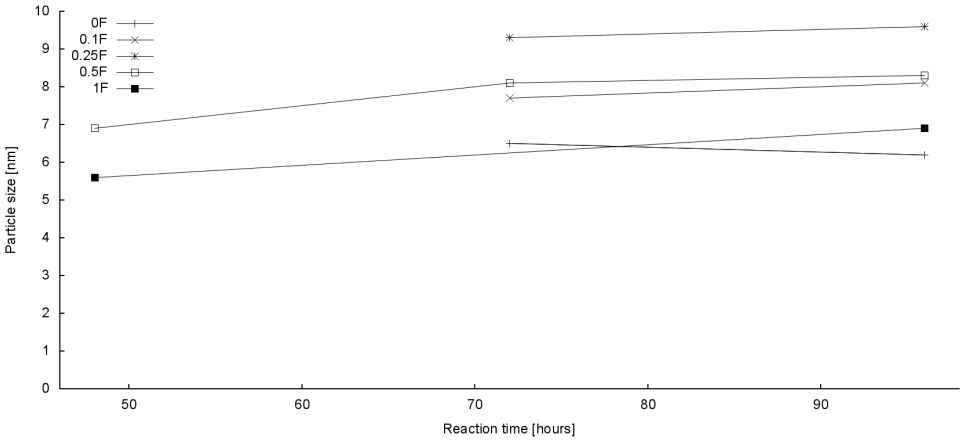


**(b)** $TiO_2$-0.4Ox

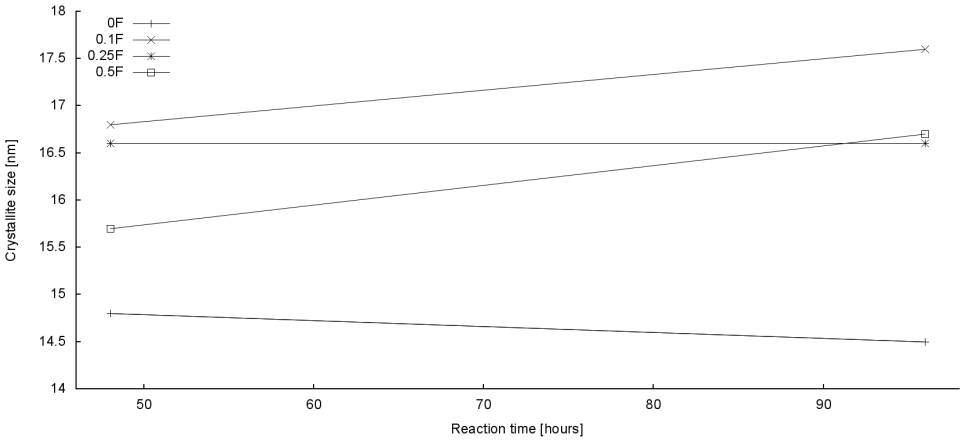


**(c)** $TiO_2$-180

**Figure 4.3.** Anatase particle size (as determined by PXRD) for oxalic acid-modified $TiO_2$.

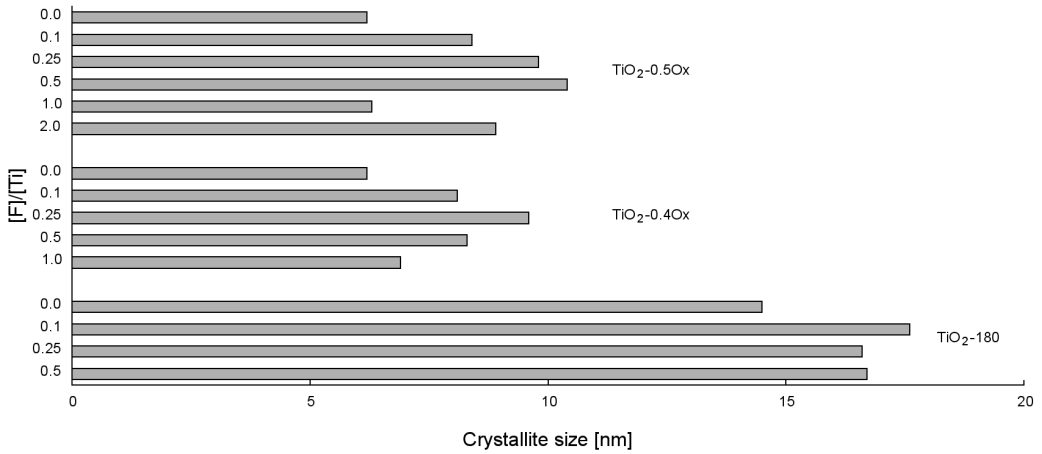


**Figure 4.4.** Comparison of oxalic acid $TiO_2$ crystallite size after 96 hours of heating, as determined by PXRD.

The exact mechanism by which oxalic acid inhibits the effects of excess fluoride is unknown.

### *4.1.5 Conclusion*

Titanium dioxide nanoparticles were synthesised in the presence of oxalic acid and ammonium fluoride by a combination hydrolysis/thermolysis technique. Titanium dioxide/oxalic acid sol was first synthesised by addition of titanium isopropoxide to a solution of oxalic acid, and this sol was then heated in the presence of ammonium fluoride.

PXRD analysis of samples extracted during the heating process indicate that both oxalic acid and ammonium fluoride encourage the growth of anatase over rutile $TiO_2$, although fluoride appears to have a more pronounced effect in this regard. Growth of rutile occurs upon heating, although this effect is countered by the addition of sufficient fluoride to the solution. Addition of excess ammonium fluoride leads to the formation of oxammite and ammonium titanium fluoride phases, to the detriment of anatase growth. Raising the heating temperature results in a much more rapid growth of rutile, although the final phase composition appears to depend not on temperature but on concentration of SMAs.

Anatase particles were found to grow steadily under heating, however

their rate of growth is heavily dependent upon the concentration of fluoride. At low concentrations, fluoride appears to encourage particle growth, however beyond a peak fluoride concentration, more fluoride was found to be detrimental to particle growth. The presence of oxalic acid in solution appeared to prevent the onset of this phenomenon.

The work in this section represents an initial investigation of the properties of oxalic acid- and fluoride-modified $TiO_2$. While the current data shed some light on the properties of the $TiO_2$ particles as they grow in solution, more work is required in order to determine the exact mechanism by which, for example, fluoride affects the growth of these particles. In addition, while phase and crystal size are explored in this section, there has been no attempt to determine the shape of these particles (*e.g.* by electron microscopy), nor if the use of fluorine- or nitrogen-containing SMAs has resulted in surface of bulk doping. Future studies may explore the mechanism of particle formation and growth in more detail, may further characterise the end products, or may also explore applications of these materials in areas such as photodegradation or photocatalysis.

## *4.2 Synthesis of $TiO_2$ using benzyl alcohol*

### *4.2.1 Introduction*

Sol-gel titanium dioxide synthesis largely relies on the hydrolysis of a titanium precursor upon exposure to water:

$$TiR_4 + xH_2O \longrightarrow Ti(OH)_xR_{4-x} + xHR \tag{4.1}$$

However there are additionally a number a non-hydrolytic condensation processes by which titanium dioxide can form.[19] Of note, these reactions tend to be considerably slower than their hydrolytic equivalents, which allows finer control of the product.[19,185] An example of a non-hydrolytic condensation reaction is that of benzyl alcohol with titanium alkoxide, which proceeds by way of alcohol elimination (see Scheme 4.1).[186]

The non-hydrolytic synthesis of titanium dioxide in benzyl alcohol was studied extensively by Niederberger *et al.* in the 2000s,[186–191] but it appears

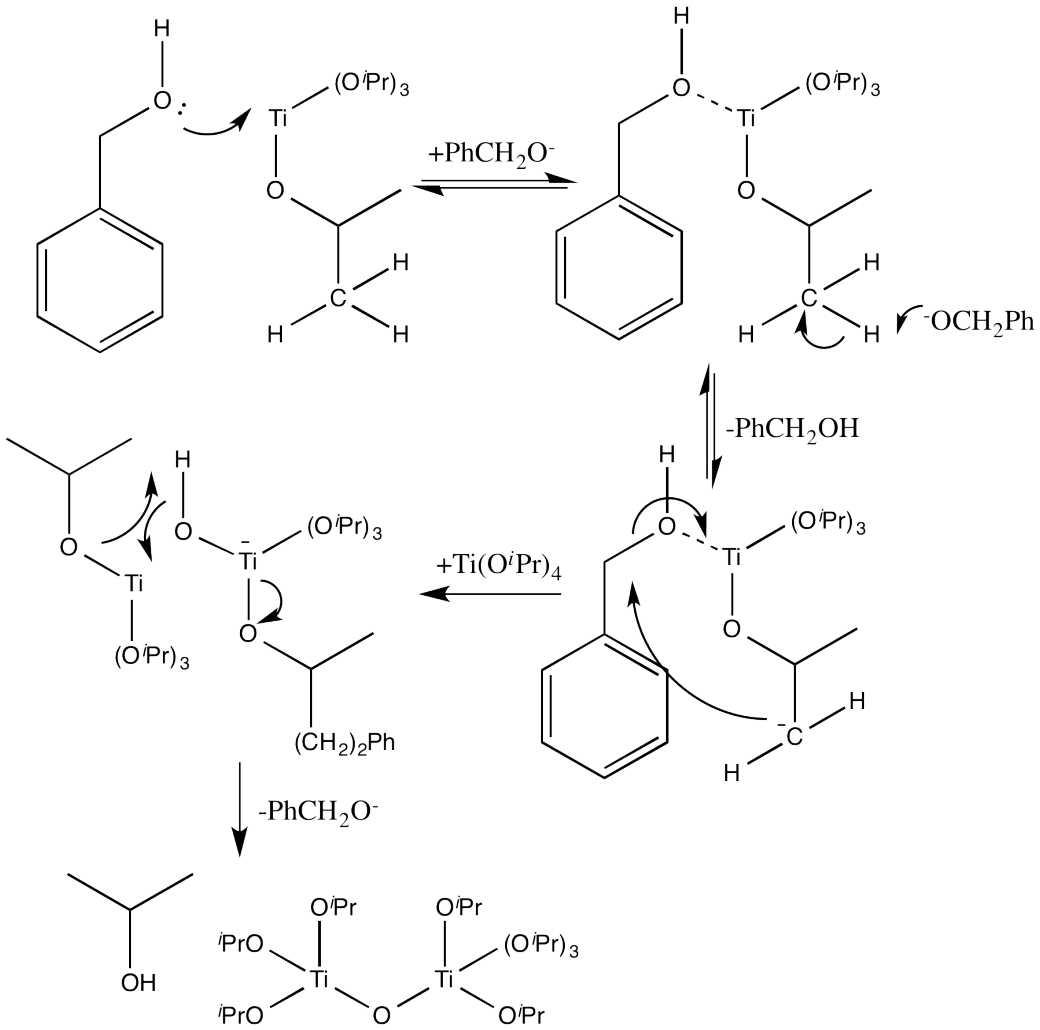


**Scheme 4.1.** The formation of titanium dioxide *via* alcohol elimination.

only recently to have gained popularity outside of his group. In 2007, Zhu *et al.* published a similar synthesis using ultrasound irradiation,[192] and this is (to our knowledge) the first mention of the technique in the literature by another group. Since then a number of other groups have reported similar syntheses,[183,193–200] although the field is still subdued compared to other areas of titanium dioxide synthesis.

One drawback of non-hydrolytic synthesis methods is that their products are generally very limited in shape and crystallinity unless a surface modifying agent (SMA) is used. Carboxylic acids are often used as SMAs, due to their affinity for the $TiO_2$ surface, but this can be a drawback as the extent of their binding can lead to restriction of crystal growth.[183] In 2008, Wu *et al.* demonstrated the synthesis of $TiO_2$ using the benzyl alcohol method, using a small amount of supplementary water in combination with oleylamine as SMAs. They successfully demonstrated that the addition of water allowed for the synthesis of nanoparticles with high-energy ({001} and {010}) crystal faces. Of note, $TiO_2$ synthesised in the absence of water demonstrated considerably different shape and crystallinity than those synthesised in its presence. While further literature has expanded on this synthetic method,[131,200,201] there has to date been no more comprehensive investigation of synthesis using the oleylamine/water system.

In the following section we report the synthesis of $TiO_2$ first following, and then expanding upon, Wu's method. Of particular note we explore the effect of pressure and stirring on the properties of the products of the reaction, which were investigated by PXRD and electron microscopy. Following from this we further investigate synthesis of $TiO_2$ using the benzyl alcohol method under reflux conditions. The effect of both oleylamine and water upon $TiO_2$ shape, size and crystallinity are investigated.

### *4.2.2 Experimental*

Titanium dioxide was synthesised based on a method described by Wu *et al.*,[183] expanded to explore the effect of pressure, stirring, and surface modifying agents on the synthetic procedure. The various experimental procedures are outlined below.

*Heating under pressure*

Samples synthesised using this method will be denoted: "p-$TiO_2$".

Benzyl alcohol (20.88 g, 192.4 mmol), oleylamine (6.50 g, 24.32 mmol) and Milli-Q water (0.400 g, 22.2 mmol) were added to a 90 mL capacity teflon-lined pressure vessel (Parr pressure vessel details here). Following this, titanium isopropoxide (TTIP, 0.937 g, 3.296 mmol) was added, resulting in a milky-white solution characteristic of hyrolysed titanium precursor. The solution was stirred for ten minutes, before being sealed and heated (with stirring) to 180°C for 24 hours. After reaction the reaction mixture had turned an opaque orange-yellow colour.

The reaction mixture was brought to room temperature and flocculated by the addition of ethanol (20 mL). Upon standing for approximately five minutes a white-yellow precipitate appeared, leaving a yellow solute. The precipitate was recovered by centrifugation (5000 RPM, 5 minutes), and washed three times by dispersal in chloroform (10 mL) with agitation, addition of ethanol (15 mL) and centrifugation (as above).

This reaction was also performed without water, following the syntheses reported by Wu *et al.*. The synthesis performed with water will be denoted "p-$TiO_2$−OA−$H_2O$" and that performed without water "p-$TiO_2$−OA".

*Heating under reflux conditions*

Samples synthesised using this method will be denoted: "r-$TiO_2$".

A similar mixture of reagents to those listed above ($n_{TiO_2}$ = 824 $\mu$mol, molar ratios between reagents remained constant) were combined in the same order as listed above in a 20 mL round bottom flask. This mixture was stirred for ten minutes, before being heated to 180°C for 24 hours under reflux conditions. After approximately six hours, the mixture was observed to turn opaque yellow.

Following the reaction, the product was recovered and purified as above.

Four different syntheses were performed under these conditions, to explore the effect of surface modifying agent on the synthesis:

- As written: r-$TiO_2$−OA−$H_2O$

- Without water: r-$TiO_2$−OA
- Without oleylamine: r-$TiO_2$−$H_2O$
- Without either water or oleylamine: r-$TiO_2$−None

*Heating under pressure, no stirring*

Samples synthesised using this method will be denoted: "o-$TiO_2$".

The same mixture of reagents as previously reported ($n_{TiO_2}$ = 1.650 mmol, molar ratios between reagents remained constant) was combined in a round-bottom flask and stirred for ten minutes. Following this the mixture was transferred to a 45 mL capacity, teflon-lined stainless-steel pressure vessel (built in-house), which was then sealed and heated in a synthetic oven to 180°C for 24 hours (no stirring). Following the reaction, the product was recovered and purified as above.

*Characterisation*

Samples were analysed by PXRD using an Agilent SuperNova XRD with a copper $K_\alpha$ source, and data processed using the TOPAS powder diffraction software package. TEM images were acquired as discussed in Chapter 3.

### *4.2.3 Results*

PXRD results are shown in Figure 4.5, with phase composition and Scherrer crystallite sizes reported in Table 4.2. Broadening due to small crystallite size (especially in the case of rutile) resulted in the overlap of the anatase and rutile primary peaks: in a number of cases, the rutile phase is evident only as a small shoulder on the anatase primary peak. All samples exhibited almost entirely anatase character, as has been previously reported.[187,189] However, those samples synthesised by reflux showed a broad scattering peak symptomatic of considerable amorphous character, suggesting that the product was only partially crystalline. Due to the nature of the diffraction setup, it is impossible to determine the fraction of $TiO_2$ that is crystalline.

Samples synthesised in the presence of oleylamine, but without the addition of water, showed large and distinctive (002) diffraction peaks under

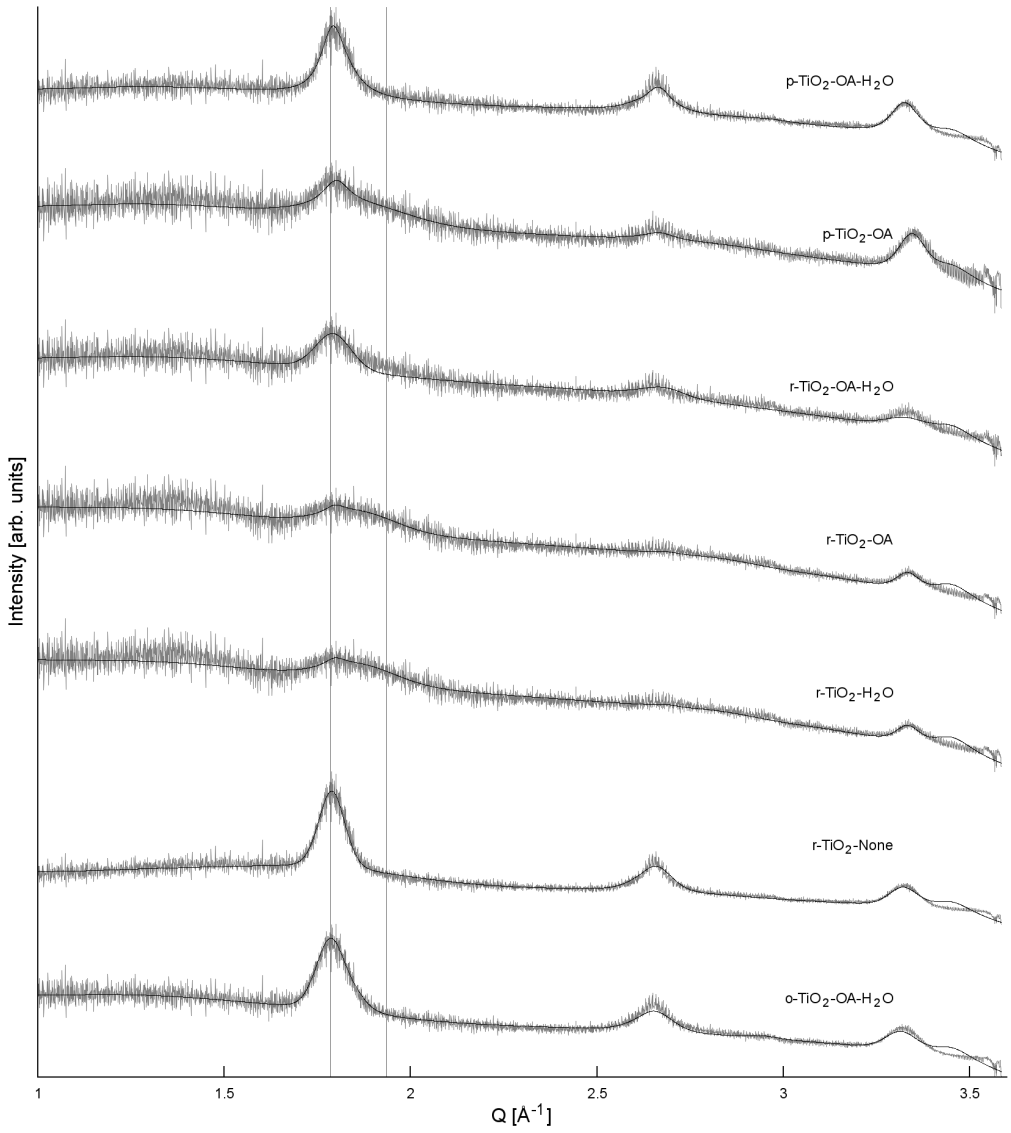


**Figure 4.5.** PXRD data for $TiO_2$ synthesised in benzyl alcohol. Raw data is shown in grey, fitted peaks in black. The grey vertical lines indicate expected peak positions for anatase ((101) face, $Q = 1.78$ Å$^{-1}$) and rutile ((110) face, $Q = 1.94$ Å$^{-1}$).

**Table 4.2.** Benzyl alcohol $TiO_2$ phase composition and Scherrer crystallite size.

| Sample | Phase | Fraction | Crystallite size [nm] |
|---|---|---|---|
| p−$TiO_2$−OA−$H_2O$ | Anatase | 96% | 11.9 |
| | Rutile | 4% | 6.5 |
| p−$TiO_2$−OA | Anatase | 90% | 9.3 |
| | Rutile | 10% | 11.5 |
| o−$TiO_2$−OA−$H_2O$ | Anatase | 98% | 10.6 |
| | Rutile | 2% | 13.8 |
| r−$TiO_2$−OA−$H_2O$ | Anatase | 92% | 10.5 |
| | Rutile | 8% | 13.2 |
| r−$TiO_2$−OA | Anatase | 93% | 7.7 |
| | Rutile | 7% | 6.8 |
| r−$TiO_2$−$H_2O$ | Anatase | 98% | 13.9 |
| | Rutile | 2% | – |
| r−$TiO_2$−None | Anatase | 94% | 12.1 |
| | Rutile | 6% | 0.5 |

PXRD (Figure 4.6). This correlates well with Wu's report, which showed that the exclusion of water results in "sheets" of $TiO_2$ with exposed (100) crystal faces (Figure 4.7).[183] On the other hand, water caps the (101) and ($\bar{1}$01) crystal faces of $TiO_2$, resulting in distinctive rhomboid particles: while the (002) peak is present, it is less dominant than the (101) peak.

$TiO_2$ synthesised without stirring (o−$TiO_2$) showed considerable crystallinity coupled with a much smaller anatase (200) peak than equivalent materials synthesised with stirring. While this observation suggests that stirring during the reaction encourages the growth of nanosheets, it must also be noted that the mechanism of heating (synthesis oven for o−$TiO_2$, heated pressure reactor for p−$TiO_2$) may also have an effect on synthesis. For example, it is anticipated that a slight temperature gradient may be established in the pressure reactor due to the heating setup, which would not exist in oven synthesis.

Surprisingly, $TiO_2$ synthesised by reflux in the absence of any SMAs (r−$TiO_2$−None) shows considerable crystallinity, coupled with a very low

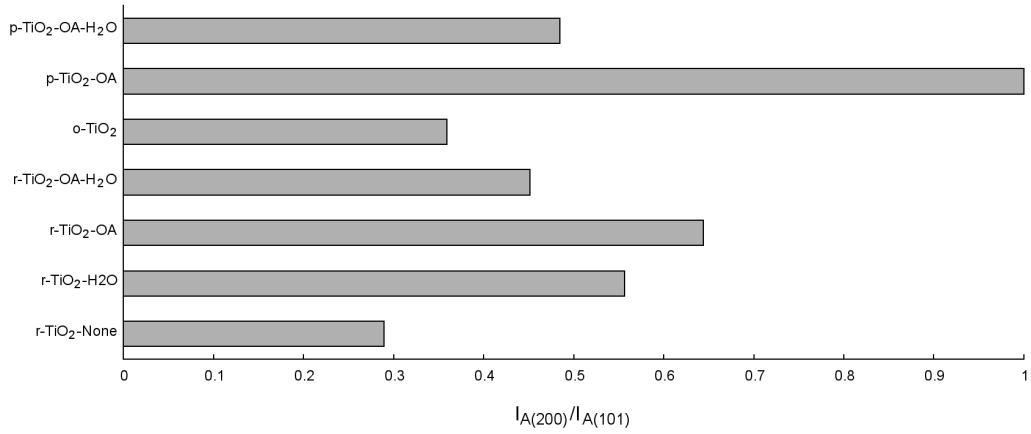


**Figure 4.6.** Ratio of peak intensities of the anatase (200) and (101) peaks.

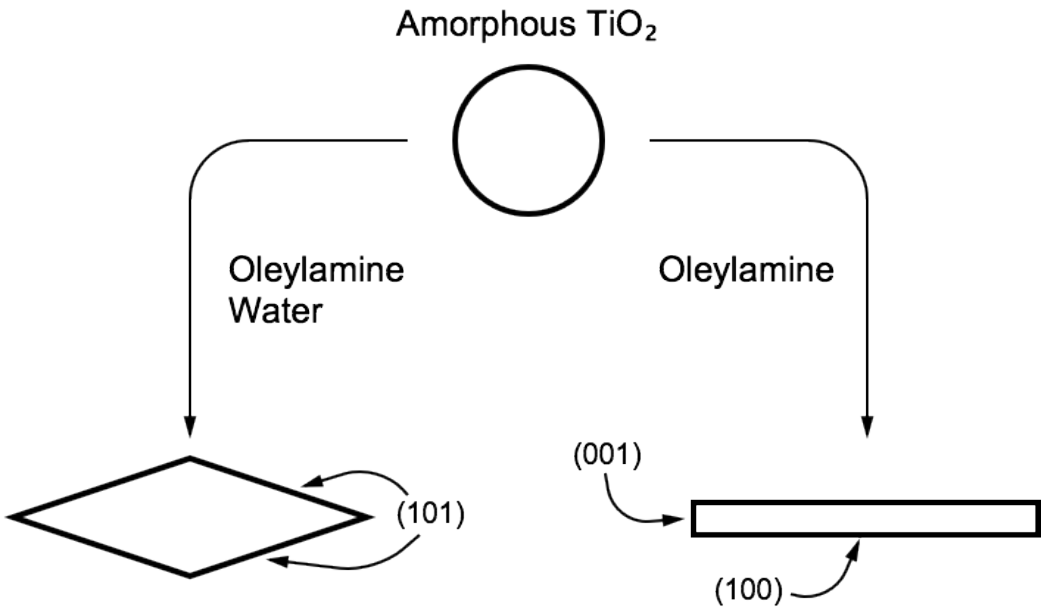


**Figure 4.7.** The effect of surface modifying agent on particle growth. Oleylamine will preferentially bind to the (100) face, encouraging growth in the (001) direction and producing long nanosheets. Water binds to the (101) and ($\bar{1}$01) faces, resulting in rhomboid nanoparticles.

anatase (200) peak compared to other samples. This suggests that under these conditions the presence of SMAs may in fact hinder crystallinity.

*Electron microscopy*

$TiO_2$ particles were analysed by transmission electron microscopy. Nanoparticles were not observed for r−$TiO_2$−OA, but in all other cases they were observed. The crystallinity and purity of these products were dependent upon the conditions trialled. For example, both p-series and o-series $TiO_2$ appears much purer than the majority of r-series $TiO_2$ materials, which appear to exhibit substantial amorphous bodies in which particle are embedded (Figure 4.8c–e). This correlates well with PXRD data (Figure 4.5). While r−$TiO_2$−None did not exhibit these amorphous masses (again in agreement with TEM), the particles appeared considerably less monodisperse and well-formed than those synthesised in the presence of SMA.

r−$TiO_2$−OA appeared to consist entirely of large ($d \geq 1\mu$m) aggregates which exhibited striations under high magnification: these are believed to be anatase $TiO_2$ nanosheets. These were not observed in p−$TiO_2$−OA, however Wu *et al.* also reported difficulty observing these materials without further post-processing.[183] PXRD analysis (above) suggests that these nanosheets do exist, as the relatively high anatase (200) peak for p−$TiO_2$−OA cannot be explained by the particles observed here by TEM. It may be that while anatase nanosheets form under both conditions discussed here, they only form the densely laminated structures observed by Wu *et al.* under higher-pressure conditions. Of interest, r−$TiO_2$−OA−$H_2O$ exhibited these laminar patterns, suggesting that nanosheets formed under reflux conditions even when water was present in solution. This is likely due to loss of water during the reaction, a result of the high temperature (180°C) to which the solvent was heated. The ratio of anatase (200) to (101) PXRD peaks suggests that the water *does* have an effect on the system prior to loss, however. Of note, neither r−$TiO_2$−$H_2O$ or r−$TiO_2$−None exhibited evidence of nanosheet formation, confirming the fact that oleylamine was required in solution to allow nanosheet formation.

High-resolution TEM analysis of particles confirmed that they were simi-

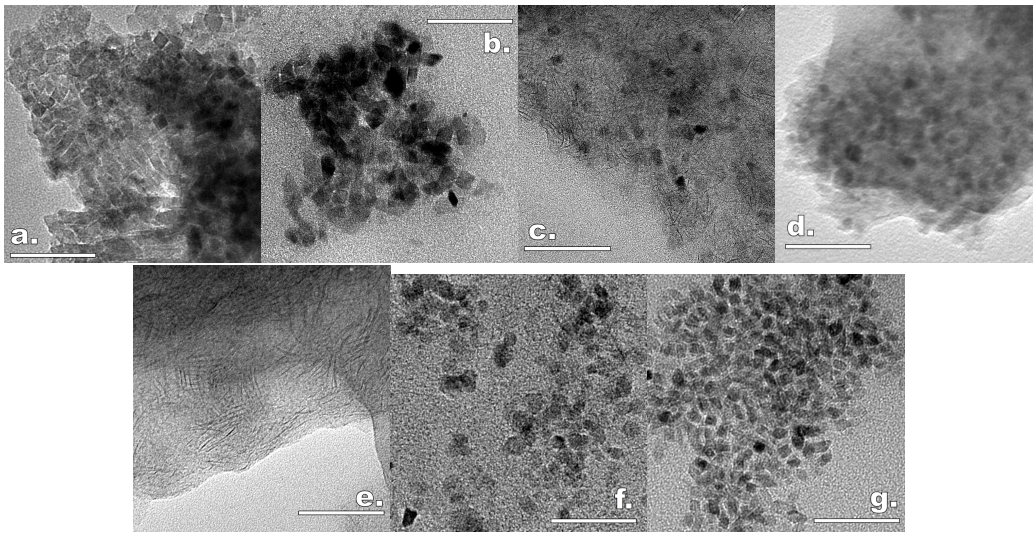


**Figure 4.8.** Low-resolution TEM images of benzyl alcohol $TiO_2$ nanoparticles: (a) p−$TiO_2$−OA−$H_2O$, (b) p−$TiO_2$−OA, (c) r−$TiO_2$−OA−$H_2O$, (d) r−$TiO_2$−OA, (e) r−$TiO_2$−$H_2O$, (f) r−$TiO_2$−None, (g) o−$TiO_2$−OA−$H_2O$. Scale bar indicates 50 nm.

lar in shape to those reported by Wu *et al.* (Figure 4.9), with strong anatase (101) fringing patterns. Such particles were observed even for p−$TiO_2$−OA. It is doubtful that this is due to trace water (*e.g.* impurities in reactants) as particles were not observed for r−$TiO_2$−OA. Wu *et al.* reported the synthesis of rhombic anatase nanoparticles even under anhydrous conditions at temperatures exceeding 200°C,[183] so the formation of these particles may be due to peculiarities of the experimental setup.

### *4.2.4 Conclusion*

$TiO_2$ nanoparticles were synthesised by a non-hydrolytic method in benzyl alcohol, using oleylamine and water as surface modifying agents (SMAs). The results of Wu *et al.*[183] were replicated, with particle shape, size and crystallinity analysed by powder X-ray diffraction and transmission electron microscopy. In the presence of both SMAs, rhomboid anatase nanoparticles with exposed (101) faces were formed, while use of oleylamine as the sole SMA resulted in anatase nanosheets with marked (200) PXRD peaks.

The method of heating and influence of both oleylamine and water as

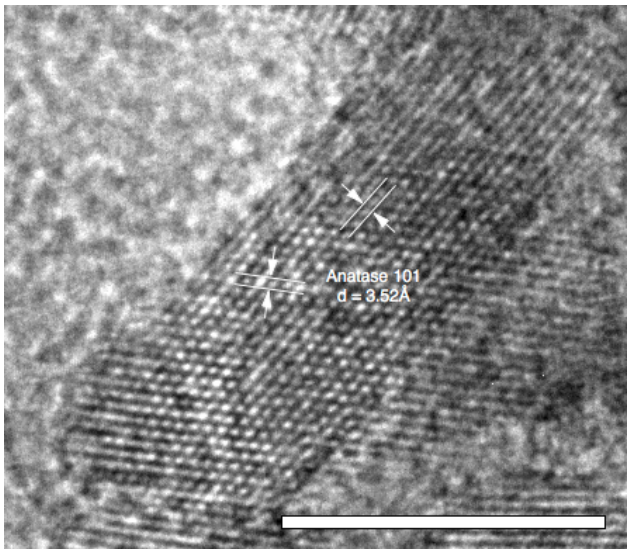


**Figure 4.9.** High-resolution TEM image of $TiO_2$ particle, with anatase (101) crystal faces marked. Scale bar indicates 10 nm.

SMAs were further investigated. It was found that reflux synthesis may allow for the loss of water during synthesis, resulting in nanosheet formation in all cases where oleylamine was present. In the absence of any SMA, reflux in benzyl alcohol results in small, poorly-formed anatase nanoparticles. In addition, it was found that synthesis in pressure vessels kept in a synthetic oven was preferable to synthesised in a heated pressure reactor for the formation of rhomboid anatase nanoparticles.

As with other studies described in this chapter, the described investigation into the synthesis of $TiO_2$ in benzyl alcohol may be used as the basis of further research in the group. In particular, future investigation may determine which particular aspect of oven synthesis (*e.g.* stirring, temperature gradient, other) allows for more crystalline particles than those synthesise in a pressure reactor. This study has thus far restricted its investigation to those SMAs discussed by Wu *et al.* : however the technique is flexible and it is entirely possible that it could be modified to include new and different SMAs which allow for selective growth of specified $TiO_2$ crystal faces. The controlled nature of the synthetic process suggests that it would be promising for such future studies.

## *4.3 Synthesis of titanium dioxide by arc discharge*

### *4.3.1 Introduction*

Arc discharge (also referred to as plasma arc discharge or PAD) has been studied since the 1920s,[202] but saw popularity when it was found in 1991[203] that the technique could be used to synthesise carbon nanotubes (CNTs). The high temperatures involved in arc discharge result in fewer structural defects as compared to other methods of CNT fabrication.[204] Since this discovery, the field of arc discharge synthesis has broadened considerably to include nanoparticle synthesis. To date, arc discharge has been used to synthesise nanoparticles of $MoS_2$, CuO, $Cu_2O$, Ag, Au, $WO_3$, $TiO_2$ and ZnO.[205]

In PAD synthesis a plasma is formed by applying a large voltage between two electrodes. Electrons from the cathode are forced to "jump" the gap to the anode, consequently heating the intervening air until eventually it becomes hot enough to form a plasma of cations and free electrons. Since the plasma is a much more conductive medium than air, once a plasma is formed it can be maintained with a lot lower potential than was required to form it.

The presence of plasma around the electrodes will result in gradual erosion, especially at the anode, which is subject to constant bombardment of high-energy electrons due to the maintenance of the current. This results in the ejection of particles or fragments of the electrode material into the plasma. Cluster formation may then occur as the ejected species collides, either with other ejected species or with the "carrier gas" (*i.e.* the gas making up the plasma). Eventually, these species are ejected from the plasma arc, where they will experience a rapid drop in temperature. At this point the particles stop growing.

A number of factors influence the growth and crystallinity of the particles produced by PAD. The most commonly studied include the type and pressure of the carrier gas, and the current of the circuit. The type of gas is important not just because it can be used as a cluster "building block" (*e.g.* oxygen gas used to form metal oxides[206]), but also because its intrinsic properties dictate the environment in which clusters form, and thus the clusters' properties. For

example, the addition of hydrogen gas has been shown to favour rutile over anatase in the PAD synthesis of $TiO_2$.[207,208] Carrier gas pressure also has a significant effect. Banerjee *et al.* demonstrated in 2010 that the phase of $TiO_2$ produced by PAD could be systematically altered by changing the pressure of the argon/oxygen gas mixture used in this synthesis (although this is still indirectly attributed to the pressure of oxygen in the chamber). Meanwhile, Tanaka *et al.* have reported that increasing the pressure of the carrier gas resulted in a decrease in particle size, and theorised that this was due to the increase in the number of collisions between the $TiO_2$ particles and the gas. Finally, the current of the plasma determines the number of electrons impacting the anode and thus the rate of particle production and ejection. A higher current generally results in a higher concentration of clusters in the plasma arc and a concomitant increase in particle size.[205,209,210]

In this preliminary study, titanium dioxide was synthesised by plasma arc discharge using a custom-built arc discharge apparatus. A number of factors were varied, specifically the carrier gas type and pressure, and plasma current, and the effects of these variations on particle size and crystallinity were investigated by powder X-ray diffraction, dynamic light scattering, and electron microscopy of the resultant particles.

### *4.3.2 Experimental*

This work was performed at GNS Science in Lower Hutt, Wellington. Titanium dioxide was synthesised by arc discharge using a custom setup assembled at GNS Science Limited (see Figure 4.10). A plasma arc is established between a titanium metal rod anode and a graphite block cathode in an isolated chamber. A stainless steel shield is placed around the electrode setup to catch titanium dioxide powder produced in the plasma arc.

In a typical experiment, air was first removed from the chamber by vacuum pump. The required atmosphere was then let into the chamber. A voltage of 100V was applied to the system, and the gap between anode and cathode narrowed until a plasma arc formed. At this point the voltage was reduced to approximately 10V, giving a constant current.

The plasma arc was maintained for 3 minutes. After this time, the elec-

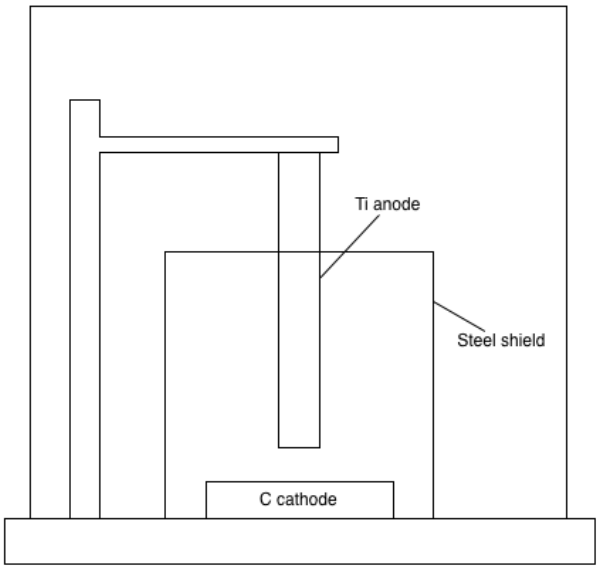


**Figure 4.10.** Schematic of the arc discharge setup.

tronic potential was removed and the chamber was left for 30 minutes. This allowed the atmosphere in the chamber to cool and also let airborne titanium dioxide settle before collection.

Titanium dioxide powder was collected from the inner surface of the stainless steel shield by brushing into a collection vessel.

Following the establishment of conditions that would produce an appreciable yield, five different samples were synthesised by this method to gauge the effect of atmosphere type and pressure, and plasma current. The different conditions are shown in Table 4.3. $TiO_2$-60-300R is a repeat of $TiO_2$-60-300, however marks on the stainless steel shield suggest that rather than arcing to the carbon cathode the plasma arced to the shield itself.

### *4.3.3 Characterisation*

Samples were analysed by PXRD using a Bruker D8 ADVANCE powder X-ray diffractometer with a Cobalt $K_\alpha$ source ($\lambda$ = 1.7902 Å). Anatase and rutile primary peaks were modelled by pseudo-Voigt peaks, and fit by non-linear least squares fitting. Phase composition was determined by Spurr's equation,[158] and grain size was estimated using the Scherrer equation.[159]

**Table 4.3.** Synthesis conditions used in the creation of $TiO_2$ by the arc discharge method.

| Code | Current [A] | Pressure [Torr] | Gas |
|---|---|---|---|
| $TiO_2$-40-300 | 40 | 300 | Air |
| $TiO_2$-60-300 | 60 | 300 | Air |
| $TiO_2$-60-300R[1] | 60 | 300 | Air |
| $TiO_2$-60-300He | 60 | 300 | Helium |
| $TiO_2$-60-760 | 60 | 760 | Air |

[1] Same conditions as $TiO_2$-60-300, see main text.

Scanning electron microscopy was performed using a JEOL 7000F FE-SEM, and transmission electron microscopy using a Philips CM-200 TEM. Particle size in solution was determined by dynamic light scattering. For further information on sample preparation and operating conditions, see Chapter 3.

### *4.3.4 Results*

SEM images of particles are shown in Figure 4.11. All samples were comprised of polydisperse spheres, ranging from 5–10 nm to several $\mu$m in diameter (Figure 4.12). Such shapes are common in arc discharge synthesis,,[207,208,211] and is attributed to the high temperature of synthesis.[208] Due to the limited resolution of the SEM instrument, smaller particles ($d < 10$ nm) were difficult to discern: these could however be observed under TEM. While particle aggregation is expected during the deposition-evaporation process used in SEM sample preparation, in several cases it was observed that particles were embedded in or decorated with what is believed to be amorphous titanium dioxide (see *e.g.* Figure 4.11b). This is believed to be a result of the synthesis method.

SEM and DLS particle sizing data are shown in Figure 4.13. It should be stressed that due to the limits in SEM resolution, SEM particle sizing data is expected to be skewed slightly high. Particles display minimal anisotropy, and particle size tends to fit one of two distributions:

- A pseudo-log-normal distribution, in which a considerable population

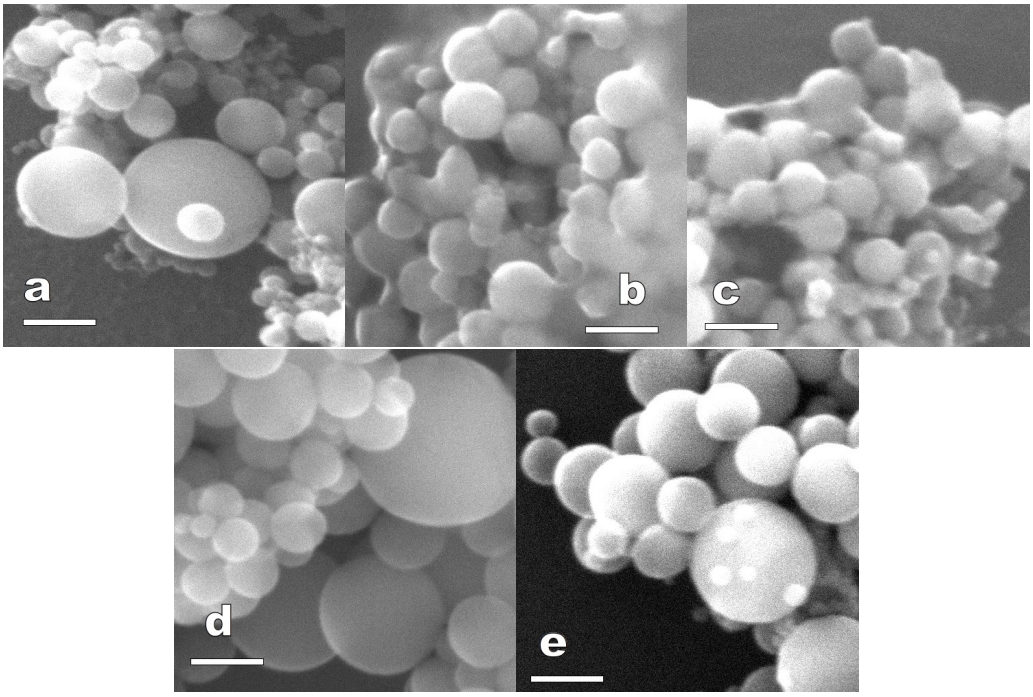


**Figure 4.11.** SEM images of: a) $TiO_2$-60-300, b) $TiO_2$-60-300R, c) $TiO_2$-60-300He, d) $TiO_2$-40-300, e) $TiO_2$-60-760. Scale bar in all cases is 100 nm.

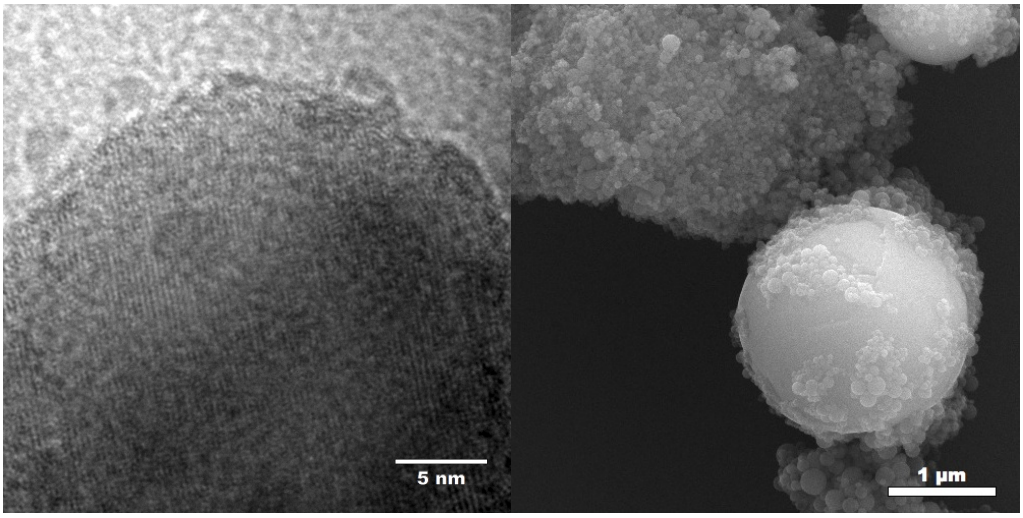


**Figure 4.12.** An example of the two extremes of $TiO_2$ particle size observed: a TEM image of sub-10 nm particles (left) and SEM image of a particle several microns in diameter (right).

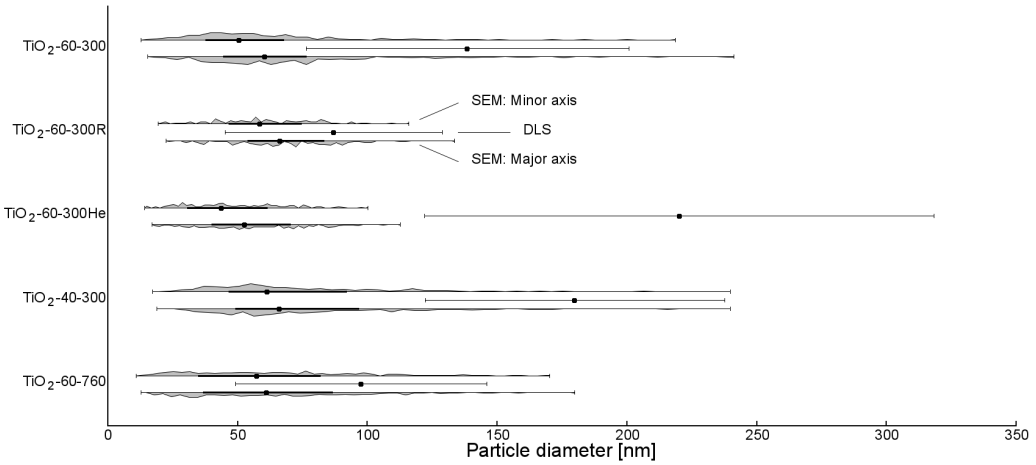


**Figure 4.13.** SEM (minor and major axes) and DLS particle sizing data for arc discharge $TiO_2$. Circles indicate the median size, thick lines the range of the upper and lower quartile, and thin lines the range of the sample. Area graphs indicate relative frequency of particle sizes for SEM sizing.

of particles is accompanied by a long "tail" at higher diameter (*e.g.* $TiO_2$-60-300, $TiO_2$-40-300, $TiO_2$-60-760), and

- a pseudo-normal distribution, lacking the long tail at higher diameter (*e.g.* $TiO_2$-60-300R, $TiO_2$-60-300He).

DLS particle sizing data indicate uniformly higher particle size than SEM particle counting. This is believed to be due to particle aggregation in solution.

PXRD data are shown in Figure 4.14. Peaks are fitted using two pseudo-Voigt functions (see Figure 4.15 for an example fitting and residual), and phase composition and crystallite size were calculated using Spurr's formula[158] and Scherrer's equation[159] respectively. Data are presented in Table 4.4. It is noted that crystallite size approximates particle size as determined by SEM particle sizing, indicative of single-crystalline particles. This is confirmed by HRTEM fringing analysis of particles (see Figure 4.16). No other phase than $TiO_2$ is observed, even for the supposedly oxygen-poor $TiO_2$-60-300He. This indicates that despite attempts to remove atmosphere from the chamber, oxygen was still present during synthesis.

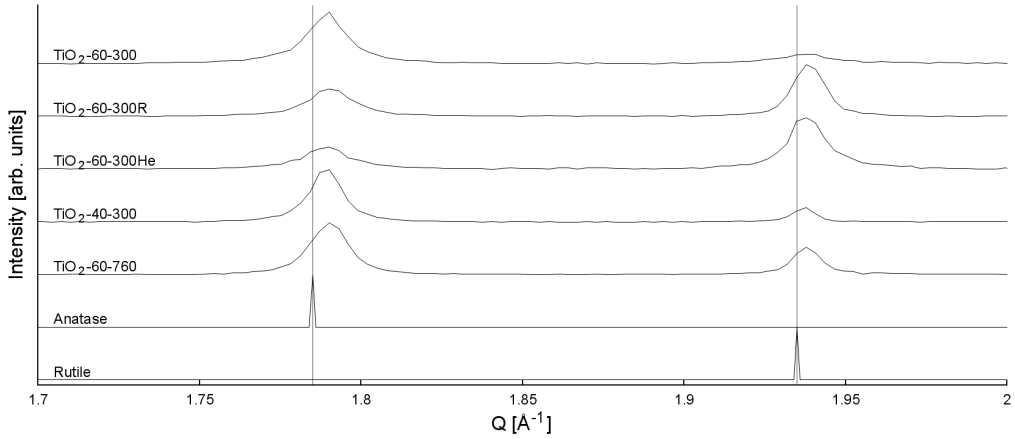


**Figure 4.14.** PXRD data for arc discharge-synthesised $TiO_2$, shown alongside theoretical peaks for anatse, rutile and brookite $TiO_2$.

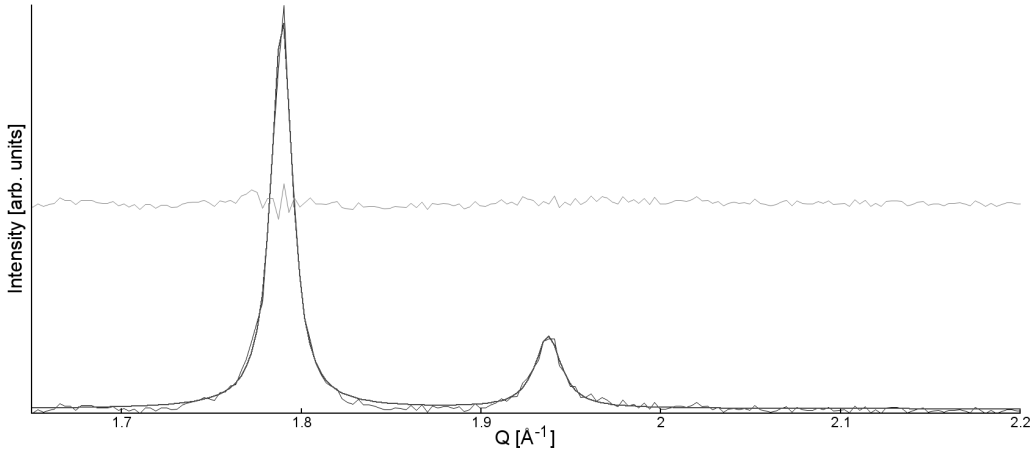


**Figure 4.15.** A typical PXRD fitting (here for $TiO_2$-60-300). Residual is shown in grey.

**Table 4.4.** Phase composition and Scherrer crystallite size for arc discharge-synthesised $TiO_2$.

| Sample | Phase | Fraction | Crystallite size [nm] |
|---|---|---|---|
| $TiO_2$-60-300 | Anatase | 77% | 68.22 |
| | Rutile | 23% | 54.33 |
| $TiO_2$-60-300R | Anatase | 37% | 62.93 |
| | Rutile | 63% | 93.78 |
| $TiO_2$-60-300He | Anatase | 29% | 62.83 |
| | Rutile | 71% | 78.33 |
| $TiO_2$-40-300 | Anatase | 82% | 88.66 |
| | Rutile | 18% | 137.75 |
| $TiO_2$-60-760 | Anatase | 67% | 75.34 |
| | Rutile | 33% | 103.33 |

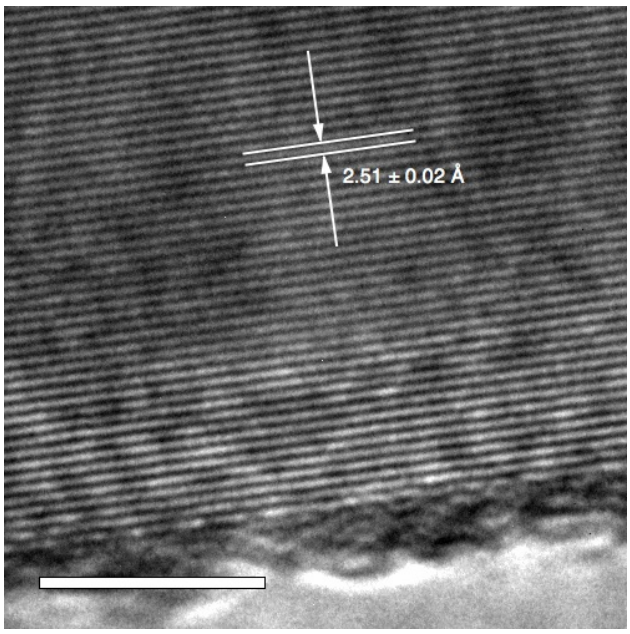


**Figure 4.16.** HRTEM image of $TiO_2$-60-300He, showing crystal lattice fringing. In this case the fringing is due to the Rutile (101) crystal face ($d = 2.49$ Å). Scale bar indicates 5 nm.

Anatase was the majority phase for $TiO_2$-60-300, $TiO_2$-40-300, and $TiO_2$-60-760. Of note, these samples also exhibited a log-normal size distribution by SEM particle sizing. $TiO_2$-60-300R and $TiO_2$-60-300He, whose particle size distributions more resembled normal distributions, were mainly ($\sim 80\%$) rutile.

### *4.3.5 Discussion*

The materials produced in this study appear to fall into two main groups:

- Mainly anatase, with a log-normal size distribution ($TiO_2$-60-300, $TiO_2$-40-300, $TiO_2$-60-760), and
- mainly rutile, with a normal size distribution ($TiO_2$-60-300R, $TiO_2$-60-300He).

Barborini *et al.* have previously reported that as PAD-synthesised $TiO_2$ grows, it preferentially adopts anatase form.[22] Given the high temperature conditions of the plasma arc, it is reasonable to assume that if there is some drive for larger particles to form anatase, their crystalline will rearrange to form this new structure. Given the lack of observed particles above $d = 100nm$ for rutile samples, it is assumed that the majority of anatase reported in PXRD is due to these larger particles.

This phenomenon suggests that in the case of $TiO_2$-60-300R (where the plasma arc grounded on the stainless steel shield) and $TiO_2$-60-300He, some mechanism of the system either slows the growth of $TiO_2$ particles, or reduces the amount of time in which the particles can grow. If the plasma arc grounds on the shield rather than the cathode, it follows that the arc will be shorter and thus the volume occupied by the plasma (*i.e.* the volume in which particle growth is possible) will shrink. Particles will leave this space in the chamber sooner, resulting in less growth and thus a more monodisperse sample.[209,212] As helium has a high thermal conductivity compared to atmospheric gasses[213] it will allow $TiO_2$ particles to cool much faster, reducing the growing time and thus producing smaller, more monodisperse particles. The use of helium is also likely to encourage the growth of rutile by providing

an oxygen-poor environment:[208] it should be noted that the highest rutile fraction was recorded for $TiO_2$-60-300He.

By comparison of $TiO_2$-40-300 and $TiO_2$-60-300, it can be seen that decreasing the current of the plasma encourages the growth of larger crystallites, which may also explain the slightly higher proportion of anatase reported by PXRD analysis. While SEM particle sizing shows that $TiO_2$-40-300 particles are slightly larger than $TiO_2$-60-300 particles, the difference is not as marked as reported by PXRD. This illustrates the danger of relying purely on non-representative techniques such as electron microscopy for characterisation. It is interesting that DLS particle sizing also reports larger particle sizes for $TiO_2$-40-300, even though in both case mean DLS particle sizes lie well above the median particle size as determined by SEM sizing. Previous literature has reported that increasing the current of the plasma arc results in an increase in particle size and polydispersity,[205,209,210] as the use of higher current results in faster ablation of the anode, resulting in a higher concentration of metal in the plasma arc and thus faster growth. The reason for this discrepancy is unknown.

By comparison of $TiO_2$-60-760 with $TiO_2$-60-300 it is found that increasing the pressure of the chamber results in a slightly lower anatase content and smaller particles as observed by SEM and DLS, although interestingly PXRD Scherrer particle sizing suggests that the crystallites are larger. It has previously been reported by Tanaka *et al.* that increasing the pressure of the atmosphere results in the synthesis of smaller particles.[206] An increase in the atmospheric pressure results in a decrease in the mole fraction of $TiO_2$ particles in the plasma arc, which effectively reduces the chances of two $TiO_2$ particles colliding and merging. As a result, a larger number of smaller $TiO_2$ particles are produced by the method. PAD-$TiO_2$ synthesised in low-oxygen environments has demonstrated a tendancy towards formation of rutile over anatase,[208] and therefore one might expect that increasing the pressure (and thus the availability of oxygen) may favour the formation of anatase. However, the presence of a sizeable proportion of anatase at 300 Torr suggests that in neither of these reactions is the concentration of oxygen low enough to influence the product crystallinity.

### *4.3.6 Conclusion*

$TiO_2$ nanoparticles were synthesised by plasma arc discharge (PAD) using a variety of conditions, using an in-house apparatus at GNS Science. By varying conditions, the effects of current, pressure, and type of gas on particle size and morphology were investigated. In addition, due to arcing from the stainless steel shield used to catch powder, it was possible to investigate the effect of reduced plasma arc volume. It was found that both reduction of the plasma arc volume and use of helium as a carrier gas resulted in mainly rutile particles with a smaller, narrower size distribution, confirming previous literature. Increasing the pressure of carrier gas resulted in smaller particles, while decreasing the current produced slightly larger particles, in stark contrast with established literature.

## *4.4 Small angle X-ray scattering studies on $TiO_2$ formation*

*This work was conducted at the Australian Nuclear Science and Technology Organisation, Lucas Heights, Sydney, and was funded by an AINSE PGRA scholarship.*

### *4.4.1 Introduction*

The study of small-angle X-ray scattering can be thought of as a corollary of X-ray diffraction at small angles, and thus the observation of larger-scale features in the material. As such is it useful for observing the periodic structures found in, for example, proteins or higher polymers.[214] Soon after the discovery of the small-angle scattering phenomenon in 1930[215] it was found that ensembles of nanoscale particles (including powders[216] and colloids[215]) would systematically scatter X-rays to give patterns which were derived from the properties of the system. Guiner and Fournet have since established that this scattering phenomenon will occur for any system exhibiting "heterogeneities in the matter...having dimensions from several tens to several hundred times the X-ray wavelength."[214] Given that the characteristic wavelength of most laboratory X-ray sources (*e.g.* Cu $K_\alpha$, $\lambda = 1.54$ Å) is on the order of Ångstroms, it follows that the small-angle X-ray scattering (SAXS)

technique is appropriate for the measurement of particles with dimensions ranging from ∼1–100 nm. This, combined with the ability to perform SAXS analysis of particles in solution, makes the technique ideal for the *in situ* characterisation of sol-gel synthesised nanoparticles even during synthesis.

Time-resolved SAXS on metal oxide nanoparticle synthesis has been widely used in the literature to monitor particle growth and evolution.[198,217–223] This technique is generally performed using a synchrotron source,[198,219,221–223] as such facilities provide a much higher intensity X-ray beam, providing more accurate measurement at shorter time scales. These studies are also possible using laboratory sources,[217,218,220] although this requires higher exposure times and thus inevitably provides less accurate data, especially in rapidly-changing systems.

In this section, two different sol-gel syntheses of $TiO_2$ were analysed by *in situ* small angle X-ray scattering. In the first method, titanium dioxide was synthesised by hydrolysis in ethanol, a rapid reaction that leads to the formation of amorphous spherical nanoparticles; in the second method, $TiO_2$ was synthesised *via* the thermal degradation of peroxotitanic acid, a much more gradual process that produces crystalline needle-shaped particles. SAXS analysis was performed periodically over the course of the synthesis, with data analysed using the Igor/Irena software package. Using these data, the formation kinetics of the two systems are discussed.

### *4.4.2 Experimental*

#### *Synthesis*

Titanium dioxide was synthesised by two methods: hydrolysis in ethanol (e-$TiO_2$) and thermal degradation of peroxotitanic acid (p-$TiO_2$).

e-$TiO_2$ was synthesised in the following manner. Water (3.38 g, 187.8 mmol) was added to anhydrous ethanol (25 mL) under a nitrogen atmosphere and the solution heated to 30°C with stirring. Following this, titanium isopropoxide (TTIP, 1.78 g, 6.26 mmol) was added to anhydrous ethanol (25 mL) and the solution then added *via* syringe to the water-ethanol solution. Addition of TTIP to ethanol before addition to solution allowed the titanium precursor to disperse, preventing excessive inhomogeneity upon addition.

p-$TiO_2$ was synthesised in the following manner. Titanium isopropoxide (1.78 g, 6.26 mmol) was added to ethanol (15 mL), followed by water (75 mL). The resulting white slurry of amorphous $TiO_2$ was stirred for ten minutes, before being centrifuged (3000 RPM, 10 minutes). The white precipitate was washed twice with water (50 mL), being recovered each time by further centrifugation (as above). The washed precipitate was then redispersed in water (50 mL), and 30% w/w hydrogen peroxide (7.10 g, 62.6 mmol) was added with stirring. The solution immediately turned a characteristic yellow-orange as titanium peroxide bonds formed, and over the following half hour became transparent. After an hour of stirring, the solution was heated to 100°C under reflux conditions.

*Characterisation*

Samples where characterised *ex situ* (after reaction for 24 hours) by scanning electron microscopy and powder X-ray diffraction (using an Agilent SuperNova X-ray diffractometer). For details on characterisation techniques, see Chapter 3.

Both solutions were characterised by small angle X-ray scattering (SAXS) using a Bruker Nanostar SAXS instrument with a rotating anode Cu $K_\alpha$ source. A 2D CCD detector was used with a resolution of 68 $\mu$m and a camera length of 1070 mm. The beamstop gave a theoretical $Q_{\min}$ of $\sim$ 0.008 $Å^{-1}$, although this was found to be closer to 0.01 Å$-1$ in practice. SAXS analysis was performed at the Bragg Institute, Sydney.

Samples were mounted in 2mm quartz capillaries (Charles Supper Company), which were stoppered with wax to prevent solute evaporation. Before each experiment, solvent blanks were run (50 mL ethanol/1.78 mL water for e-$TiO_2$, pure water for p-$TiO_2$) for each capillary to be used. Capillaries were marked so that during analysis the correct solvent blank could be subtracted from each measurement: preliminary experiments demonstrated that the differences in scattering profiles between capillaries were significant compared to the signal from the sample.

To perform a measurement, sample (1 mL) was withdrawn from the reaction vessel and placed in a capillary, which was then immersed in ice water

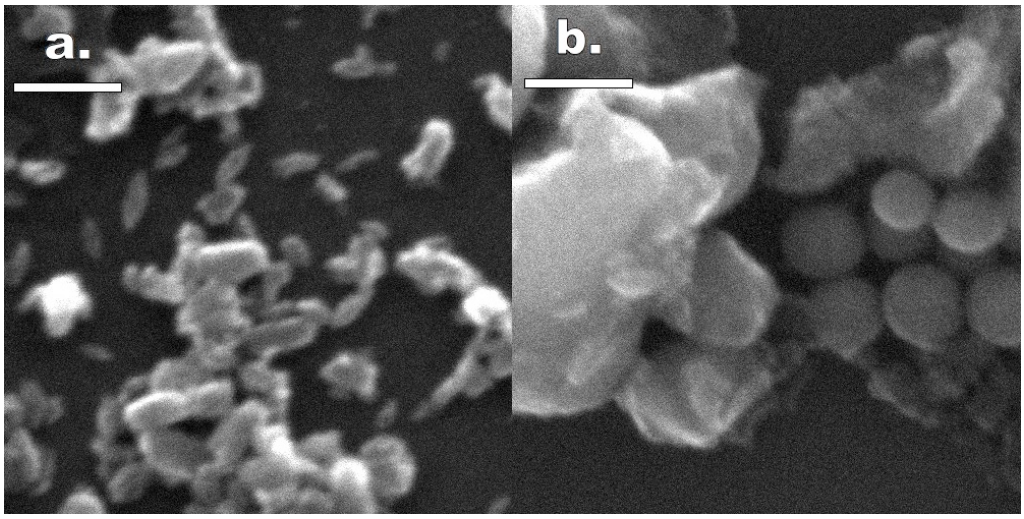


**Figure 4.17.** SEM images of (a) p-$TiO_2$, and (b) e-$TiO_2$. Scale bars indicate 100 nm.

to slow the hydrolysis or degradation reaction as much as was possible. The capillary was then sealed with wax before being inserted into the machine. Measurement time was 30 minutes. Measurements are denoted *e.g.* "p-$TiO_2$-30" to indicate a measurement of the p-$TiO_2$ system after 30 minutes. $t = 0$ for e$TiO_2$ was defined as the point of titanium precursor addition, while for p-$TiO_2$ it was defined as the point at which heating began. Detector signal was integrated over 360°, and the appropriate solvent background subtracted from the signal before processing.

### *4.4.3 Results*

SEM images show that e-$TiO_2$ particles are spherical and somewhat polydisperse, ranging from 50 nm to sizeable fractions of a micron in diameter. p-$TiO_2$, however, forms much more monodisperse, needle-like particles (see Figure 4.17). PXRD analysis showed that e-$TiO_2$ was amorphous, while p-$TiO_2$ showed evidence of anatase, rutile and brookite phases (Figure 4.18).

A typical SAXS pattern is shown in Figure 4.19. Spectra were analysed using the Irena package in Igor Pro.[224]

e-$TiO_2$ samples (Figure 4.20) demonstrated evidence of large scattering bodies, but even at $t = 30$ minutes these particles were too large for the

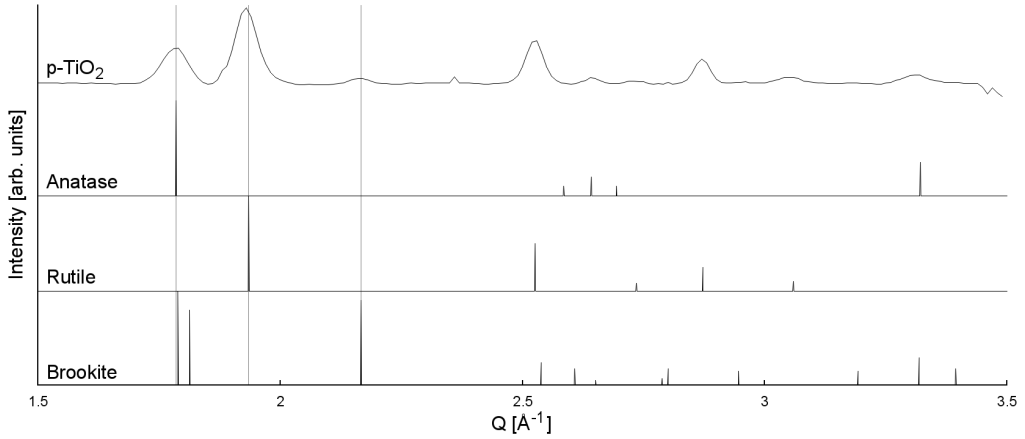


**Figure 4.18.** PXRD plot of p-$TiO_2$, shown alongside theoretical PXRD patterns for anatase, rutile and brookite $TiO_2$.

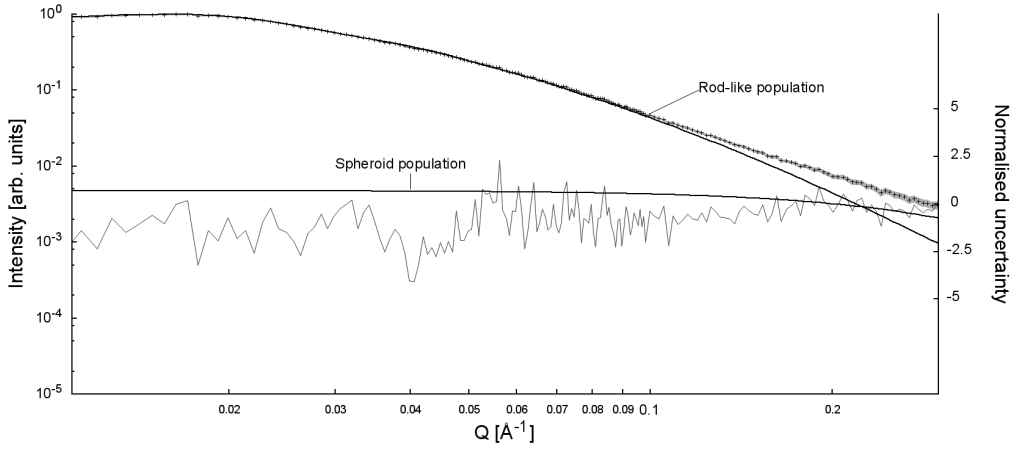


**Figure 4.19.** A typical SAXS pattern and data fitting (shown here: p-$TiO_2$ at $t = 0:00$ hr). Points show experimental data, shaded area shows instrumental uncertainty. Solid black line indicates populations of rod-like and spheroid particles, and grey line shows normalised uncertainty, given by (Actual − Model)/Uncertainty.

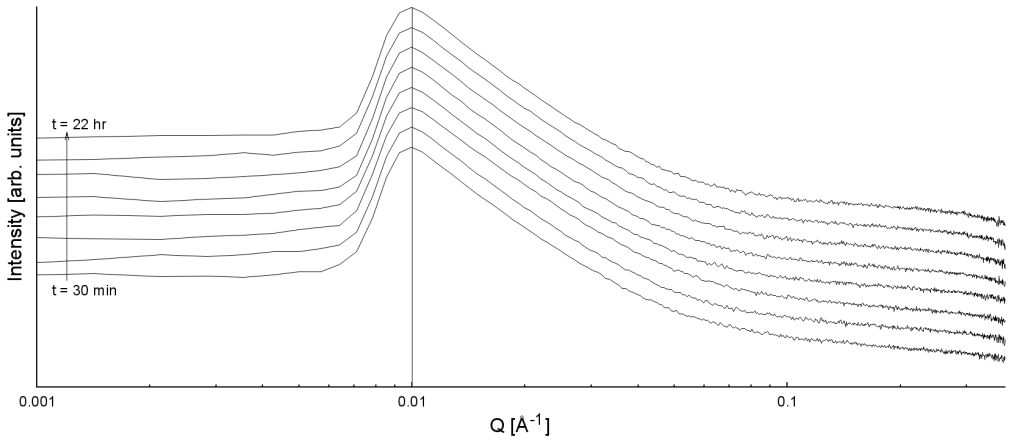


**Figure 4.20.** SAXS patterns of e-$TiO_2$ over the course of the reaction (no background subtraction applied). Data is offset for ease of comparison. The line at 0.01 Å$^{-1}$ indicates the start of the beamstop regime.

allowed Q-range of the SAXS instrument. Scattering data relevant to sizing information was effectively hidden by the beam-stop of the instrument, effectively inhibiting data fitting and size or shape determination.

p-$TiO_2$ samples were initially modelled using a spheroid form factor, but this was found not to match SAXS data, especially at high Q. It was found that the data were best modelled using a combination of a unified rod and additional spheroid form factor (Figure 4.22). The unified rod form factor uses Beaucage's unified method[225] to model rod-like particles in solution, while the spheroid form factor accurately models spherical or near-spherical particles. An additional hard sphere structure factor is included at low-Q to model a slight drop-off observed in the unified rod form factor of samples (Figure 4.21). Size regimes were modelled using log-normal distributions. Relevant fitting data is given in Table 4.5.

Of interest, while the population responsible for the rod-like form factor continually exhibit large mean sizes, the spheroid population volume is consistently larger, indicating that these particles make up the majority of the $TiO_2$ material. It it believed that the rod-like form factor is caused by particularly large $TiO_2$ needles, while the spheroid form factor is caused by much smaller particles which, while elongated, are closer to spheroid in nature. As

**Table 4.5.** SAXS fitting data for p-$TiO_2$. Hard sphere structure factor was applied to the unified rod form factor. Volumes given in arbitrary units.

| Time | Unified Rod | | | | Spheroid | | Hard sphere | |
|---|---|---|---|---|---|---|---|---|
| | Aspect ratio | Volume | Mean radius [Å] | Std. dev. | Volume | Mean radius [Å] | Radius [Å] | Volume |
| 0:00 | 7.11 | 0.63 | 31.46 | 0.73 | 2.38 | 3.47 | 142.24 | 0.076 |
| 1:46 | 6.81 | 0.20 | 229.28 | 0.35 | 0.45 | 15.06 | 376.67 | 0.039 |
| 2:30 | 6.85 | 0.18 | 288.97 | 0.24 | 0.22 | 26.93 | 334.74 | 0.039 |
| 3:00 | 4.01 | 0.10 | 316.20 | 0.20 | 0.22 | 32.26 | 325.16 | 0.056 |
| 4:00 | 3.99 | 0.13 | 322.30 | 0.21 | 0.35 | 28.63 | 332.60 | 0.066 |
| 7:00 | 3.40 | 0.0012 | 311.85 | 0.13 | 0.0056 | 26.53 | 355.67 | 0.038 |
| 18:00 | 3.62 | 0.00061 | 281.74 | 0.27 | 0.0060 | 16.90 | 344.39 | 0.13 |
| 20:00 | 3.69 | 0.0038 | 299.90 | 0.19 | 0.02 | 30.14 | 317.27 | 0.084 |
| 22:00 | 2.79 | 0.00038 | 293.49 | 0.26 | 0.0028 | 30.07 | – | 0 |
| 24:00 | 3.06 | 0.086 | 242.33 | 0.34 | 0.40 | 18.13 | 334.81 | 0.032 |

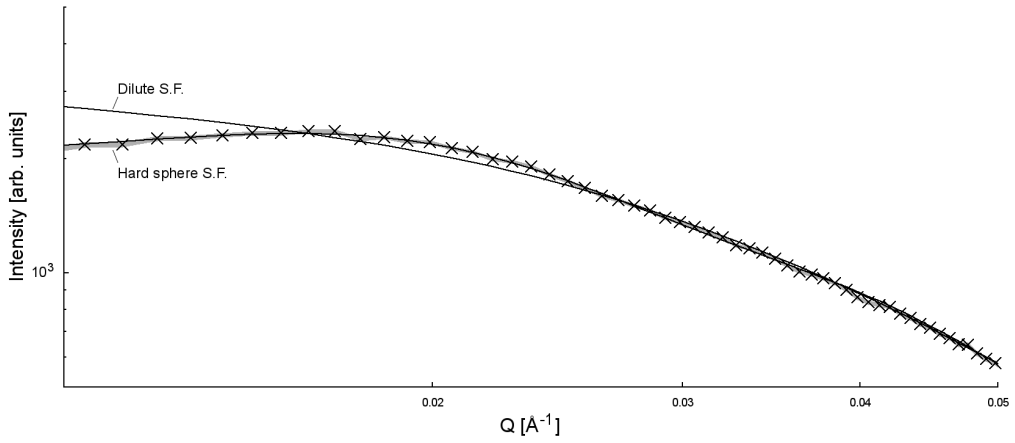


**Figure 4.21.** Low-Q intensity values of a typical SAXS pattern (shown here: p-$TiO_2$ at $t = 0:00$ hr), modelled using a dilute (*i.e.* assuming no inter-particle interaction) and a hard sphere structure factor.

particles grow larger (and thus more rod-like) they begin to precipitate from solution, thus the low volume of rod-like particles.

Measurements after $t = 18$ hours show a marked drop in intensity. As the graphs in Figure 4.22 are plotted using log scales, uncertainty becomes more prominent as overall intensity decreases. The decrease in intensity also leads to uncertainty in the parameters used to fit these data, although uncertainty in these parameters cannot readily be determined due to the complex nature of the fitting equation.

The parameters described in Table 4.5 are:

- **Aspect ratio**: The ratio of rod length to diameter.
- **Volume**: The relative contribution of each factor to the overall signal.
- **Mean radius**: The mean of the log-normal particle size distribution for each population.
- **Std. dev.**: Standard deviation of the size distribution. The standard deviation for the spheroid form factor was constrained to 0.5.
- **Hard sphere radius**: Distance between particles as dictated by hard sphere interaction. This was greater than the mean particle size in all

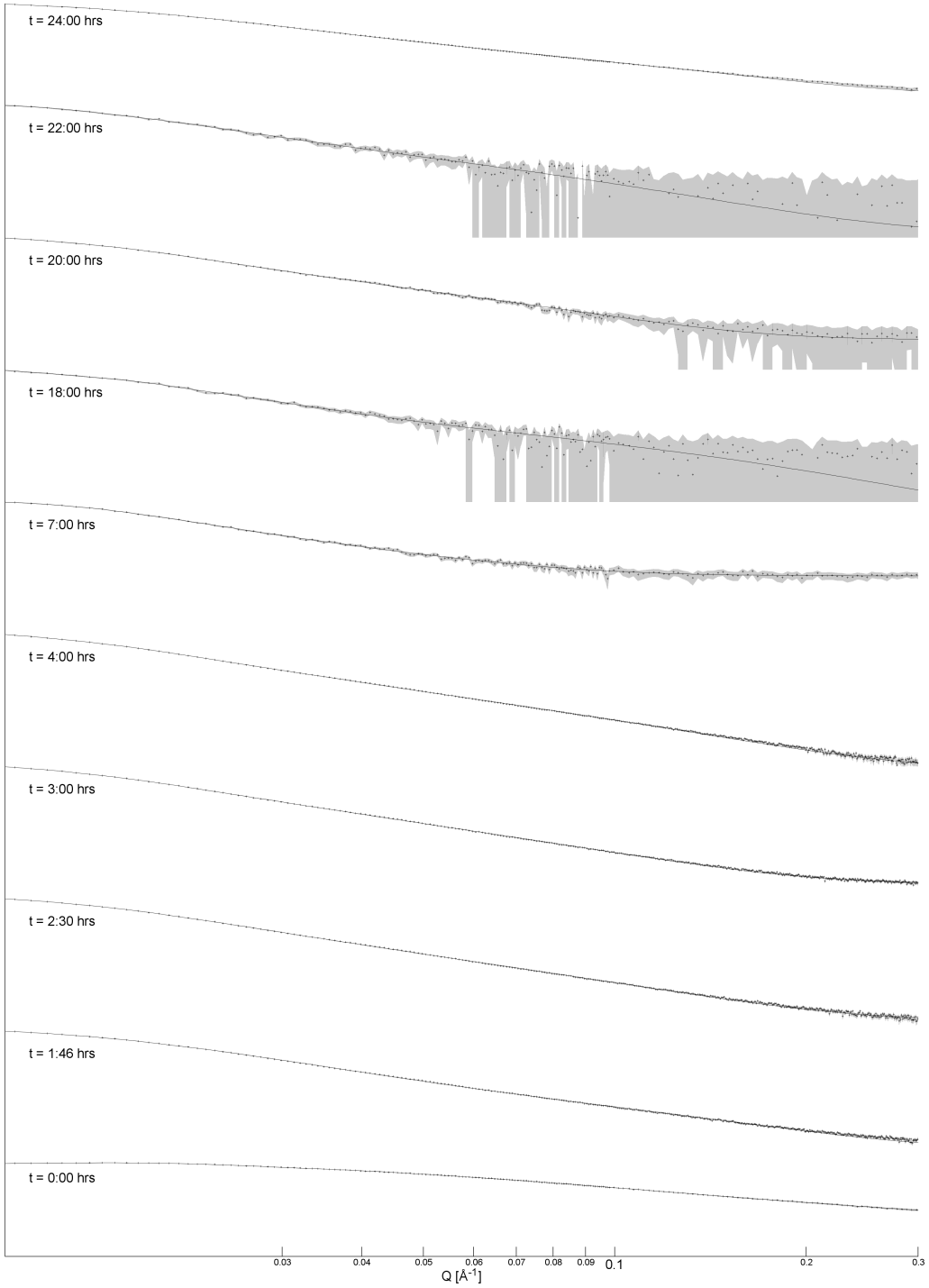


**Figure 4.22.** SAXS data and fitting curves for all p-$TiO_2$ samples. Shaded region indicates uncertainty, points indicate raw data, lines indicate fitted curves.

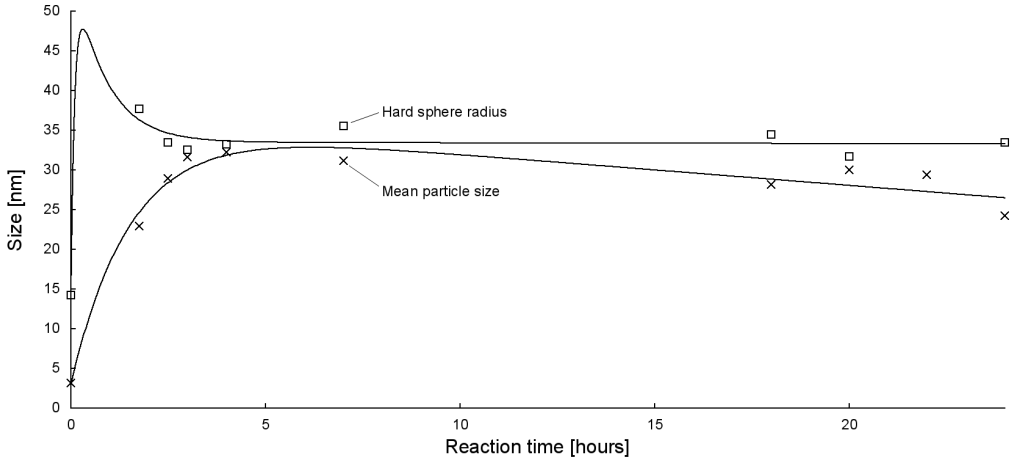


**Figure 4.23.** Mean particle size and hard sphere radius evolution with reaction time for p$-TiO_2$
. Solid lines show proposed growth mechanism.

cases, which is to be expected given their elongated nature.

Patterns are clearly apparent in the growth of mean particle size and hard sphere radius (Figure 4.23), as well as particle aspect ratio (Figure 4.24). When aspect ratio is large (early in the reaction), the hard sphere radius is considerably larger than the mean particle size. As the aspect ratio decreases and particles become slightly more spherical, hard sphere radius begins to approach particle size. This may also indicate aggregation of particles in solution. The early peak in hard sphere radius shown in Figure 4.23 is only indirectly supported by data, in this case by the steady and asymptotic decrease in hard sphere size in the domain $1{:}46 < t < 4$.

Patterns are also seen in both rod and spheroid volume fraction (Figure 4.25) and rod standard deviation (Figure 4.26) as the reaction proceeds. Volume fraction of both spheroid and rod populations decreases drastically in the first 3–4 hours of the reaction as numerous small particles aggregate, reducing the overall concentration of particles in solution. The populations of these two form factors appear to be closely linked: for example, when the volume fraction of the rod form factor lies above the line of best fit (*e.g.* $t = 4$ hours, $t = 24$ hours), so does that of the spheroid form factor. The high initial standard deviation rapidly decreases over the first three hours,

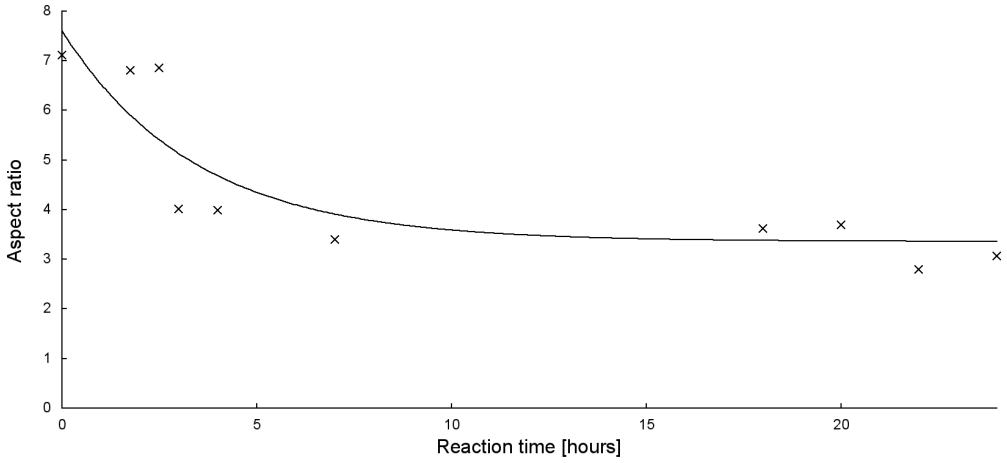


**Figure 4.24.** Particle aspect ratio evolution with reaction time for p$-TiO_2$ . Solid line shows proposed aspect ratio evolution mechanism.

but then starts to rise over the course of the reaction. The reason for this rise is unknown, as mechanisms such as Ostwald ripening would be expected to reduce the standard deviation of particle size.

It is proposed that synthesis be divided into two stages: a preliminary "rapid-growth" stage at $0 < t < 3$ hours, and a subsequent "ripening" stage at $t > 3$ hours. The rapid-growth stage is characterised first by the formation of a polydisperse ensemble of small needle-like nanoparticles with dimensions $d < 5$ nm. These particles grow by hydrolysis and condensation as the surrounding peroxotitanic sol decays, becoming less needle-like and more monodisperse as growth continues. By $t = 3$ hours growth has stabilised with mean particle size of $d \approx 30$ nm and an aspect ratio of $\sim 3.5$. At this point peroxotitanic acid precursor has decayed completely. During the remainder of the reaction, a slight decrease in mean particle size is observed. This is believed to be due to the formation of larger particles by Ostwald ripening, which subsequently precipitate from solution due to their size and hence are not measured.

### *4.4.4 Conclusion*

Titanium dioxide was synthesised *via* two different methods: by rapid hydrolysis in ethanol (e-$TiO_2$), and by thermal degradation of peroxotitanic

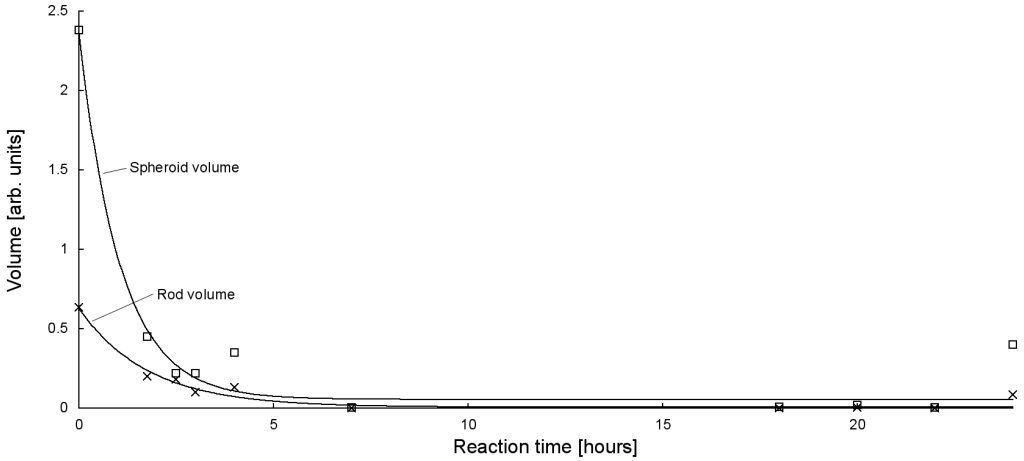


**Figure 4.25.** Form factor volume fraction evolution with reaction time for p−$TiO_2$

.

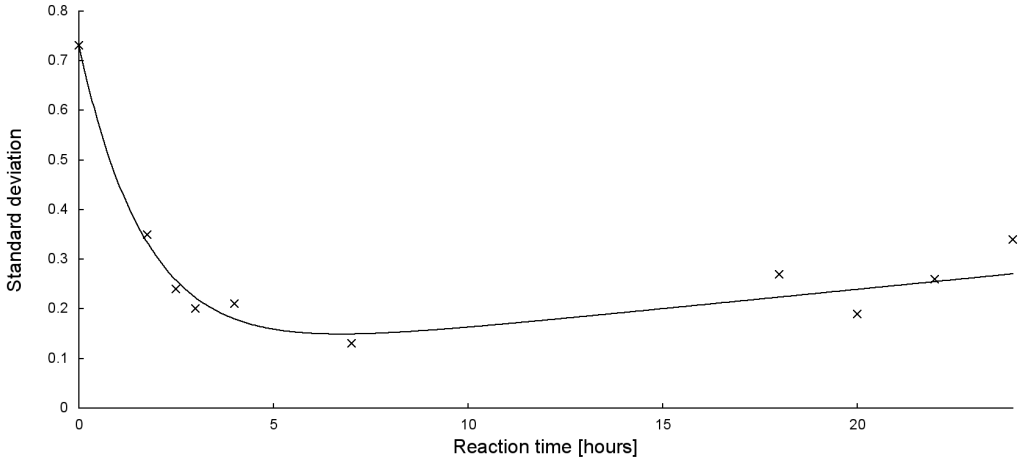


**Figure 4.26.** Rod size standard deviation evolution with reaction time for p−$TiO_2$

.

acid (p-$TiO_2$). Both systems were monitored during the reaction by small-angle X-ray scattering and data analysed using the Irena/Igor application. Even after half an hour, e-$TiO_2$ was already too large to properly analyse using the given instrument setup, reinforcing the rapidity of particle growth under hydrolysis. p-$TiO_2$ synthesis occurred in two well-defined stages: a first in which particles grew as a result of the breakdown of the peroxotitanic acid sol, and a second in which particle growth was halted by the lack of reactant in solution, but particle size and dispersity still changed due to as-yet unidentified processes.

While these studies have provided an in-depth description of the $TiO_2$ system during synthesis, they have essentially been limited by the nature of the instrument used. Bench systems like the one used in this report are considerably less intense than synchrotron SAXS facilities, which are seeing increased use in time-resolved studies.[198,219,221–223] The intensity of a synchrotron source allows for scan times an order of magnitude (or more) shorter than those required by bench sources, providing much finer temporal resolution (and thus more frequent sampling) than was possible in these studies. For example, the growth of e-$TiO_2$ was impossible in this study as it took place on a timescale shorter than the measurement period. Use of a synchrotron source would allow not only for comparison of these two techniques, but would also provide greater insight into the action of $TiO_2$ centres during the first, "growth" phase of p-$TiO_2$.

# Chapter V

# Modification of titanium dioxide nanoparticles by fluoride-containing surface modifying agents

## *5.1 Introduction*

In 2008 Gao Lu and coworkers demonstrated[120] that by addition of hydrofluoric acid to $TiF_4$ aqueous solution, followed by heating to 180°C, they were able to synthesise well-formed, highly-crystalline anatase $TiO_2$ nanoparticles with a high degree of the usually rare high-energy {001} facets. Their results were backed up with theoretical calculations which demonstrated the affinity between fluoride and the {001} face of titania. Importantly, it was found that fluoride would bind more readily to the {001} than the low-energy and relatively abundant {101} face of titania, a trend very rarely observed. Binding of fluoride to the {001} face prevents growth along this axis, resulting in nanoparticles with a high fraction of {001} faces as compared to those grown in the absence of fluoride (see Figure 5.1). In this way the fluoride acts as a *surface modifying agent* during titanium dioxide growth.

Lu's work inspired a number of groups,[116,134,135,137,138,140–150,226–228] who were able to modify conditions to optimise high-energy facet formation and even drive synthesis towards the growth of higher-energy faces of titanium dioxide (*e.g.* {110}[137]) in small quantities. While Lu *et al.* were initially able to achieve 47% {001} faces, further work by the group showed that synthesis in 2-propanol increased the yield of {001} faces to 64%. Over the following years the yield of {001} has steadily increased, until in 2012 Diana Mars and coworkers reported the synthesis of anatase thin films on gold that exhibited up to 98% {001} facets.[152]

While these catalysts may show enhanced catalytic ability, the vast majority of these works focus on the use of the toxic and highly dangerous hy-

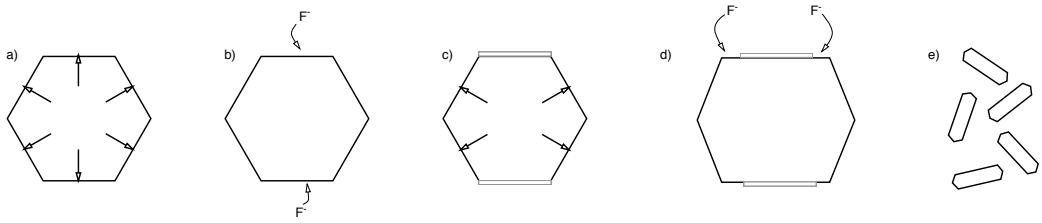


**Figure 5.1.** The growth of titanium dioxide crystals under sol-gel conditions. Undisturbed, crystals will form in the most thermodynamically-favourable state, as determined by the crystal's Wulff construction[118](a); however surface modifying agents (here shown as fluoride, $F^-$) can adsorb onto the growing crystal surface (b), preventing growth. If the SMA preferentially adsorbs onto one face (c), crystal growth in one or more directions is retarded, resulting in a change in shape for the growing crystal. As the crystal grows, more SMA may form on the surface, futher directing the shape of the particle (d) and thus the shape of the overall catalyst (e).

drofluoric acid as a fluorine source. Some researchers (notably Yu *et al.*[136]) have shown similar results using ionic liquids, which are considerably more complex than the relatively simple fluoride sources used previously. Only very recently have researchers focussed on simpler and less toxic sources of fluorine or fluorine-containing species.[151–156]

In this chapter we present a study of the effect of a number of fluorine-containing salts ($NH_4F$, $NH_4BF_4$, $NH_4PF_6$, $NBu_4F$, $NBu_4BF_4$, $NBu_4PF_6$) on the synthesis of crystalline titanium dioxide nanoparticles *via* the thermal degradation of peroxotitanic acid under mild conditions. We have purposefully selected a wide range of fluorine-containing surface modifying agents to gauge the effect not only of the fluorine source ($F^-$, $BF_4^-$, $PF_6^-$) but also of the cation ($NH_4^+$, $NBu_4^+$) on the formation of titanium dioxide. While some of these salts (*i.e.* $NH_4F$,[153,154,157] $NH_4BF_4$[155]) have seen previous use in literature, the majority of the modifying agents used in this study had not been tested previously until the publication of this study.

## *5.2 Experimental*

### *5.2.1 Synthesis*

Titanium isopropoxide (98%, Merck), ammonium tetrafluoroborate, ammonium hexafluorophosphate, tetrabutylammonium hexafluorophosphate (Sigma), ammonium fluoride (BDH), tetrbutylammonium fluoride (1M in THF, Acros Organics), and tetrabutylammonium tetrafluoroborate (Strem) were all used as supplied, without further purification. P-25 titania "Aeroxide" was manufactured by Evonik Degussa GmbH. Titania particles are 80:20 anatase to rutile phase, with a quoted average particle size of 30 nm and surface area of 50 $m^2$ $g^{-1}$.

Titanium dioxide was synthesised by the thermal degradation of peroxotitanic acid.[42] Titanium isopropoxide precursor (1.78 g, 6.27 mmol) was dissolved in ethanol (5 mL) in a 50 mL round-bottom flask with stirring. To the solution was added Milli-Q water (25 mL), resulting in the rapid hydrolysis of titanium isopropoxide to produce hydrated titanium dioxide, in the form of an opaque white precipitate. The mixture was magnetically stirred (600 rpm) for a further ten minutes to ensure complete hydrolysis, and the precipitate was then centrifuged (5 min at 5000 rpm) and washed several times with Milli-Q water (by repeated redispersion using Vortex agitator followed by centrifugation as before) to remove ethanol and isopropanol formed during hydrolysis.

The titanium dioxide powder was redispersed in water (50 mL) and combined with fluoride salt. The following salts were used: ammonium fluoride ($NH_4F$), ammonium tetrafluoroborate ($NH_4BF_4$), ammonium hexafluorophosphate ($NH_4PF_6$), tetrabutylammonium fluoride ($NBu_4F$), tetrabutylammonium tetrafluoroborate ($NBu_4BF_4$), and tetrabutylammonium hexafluorophospate ($NBu_4PF_6$). Salts were added in a 1:1 molar ratio with titanium (assuming complete hydrolysis and retention of the solid material during washing). Hydrogen peroxide (4.26 g 50% w/w, 62.63 mmol) was then added dropwise with rapid stirring. Following this addition, the previously opaque white solution immediately turned yellow and became transparent over the course of approximately thirty minutes as the peroxotitanic acid sol formed. The solution was stirred for one hour after the addition of hydrogen

peroxide, before being heated to 100°C with stirring. Heating was maintained for twenty-four hours, during which the transparent yellow solution produced an opaque white or white-yellow solid.

The precipitate was removed from solution by centrifugation and washed several times with water. For those catalysts modified by tetrabutylammonium salts, the precipitate was then washed twice with acetonitrile to remove excess tetrabutylammonium salt, followed by a further two washes with water. Powders were dried under vacuum to remove remaining solvent.

### *5.2.2 Characterisation*

Dried products were analysed by powder X-ray diffraction (PXRD) at the Australian Synchrotron. Samples were prepared by packing finely ground dried $TiO_2$ powder in 0.3 mm quartz glass capillary tubes (ultrasound was used to pack the powder down to the bottom of the tubes). The capillary tubes were irradiated for 180 seconds and continuously rotated during the measurement. Data were collected with a Mythen detector spanning 80° in $2\theta$. Analysis was performed using Topas 4.2 (Bruker ASX). A Rietveld refinement of a NIST standard $LaB_6$ 660b was used to determine the incident photons wavelength (0.688650 Å) and instrument profile parameters. A Chebyshev $5^{th}$ degree polynomial was used to model material scattering and instrumental background. Structural files of anatase, rutile and brookite were fitted to the PXRD patterns using the Topas analysis program, allowing refinement of crystallite size (Lorentzian and Gaussian), strain (Lorentzian and Gaussian), Ti occupancy, thermal parameters, scale, preferential orientation and lattice parameters. In the case of anisotropic crystallites displaying preferential orientation, two phases of the same lattice parameters, thermal parameters and Ti occupancies were fitted with independently refining degrees of preferential orientation and crystallite size. Crystallite sizes were determined by the average weighted breadth of a Double-Voigt fit.[229]

Surface area measurements were performed by BET analysis of $N_2$ adsorption on the samples, using a Micrometrics ASAP2010. Samples were degassed for three hours at 300°C under 3 $\mu$m Hg of vacuum.

Scanning electron microscopy (SEM) and transmission electron microscopy

(TEM) images were obtained using a Jeol 7000F FE-SEM and Philips CM-200 TEM respectively. Dynamic light scattering (DLS) and zeta potential measurements were performed using a Microtrac Zetatrac dynamic light scattering instrument. For further details see Chapter 3.

The materials were analysed by X-ray photoelectron spectroscopy (XPS) and near-edge X-ray absorption fine-edge structure (NEXAFS) spectroscopy on the soft X-ray beamline at the Australian Synchrotron.[230] Samples were dispersed in ethanol and drop-coated onto a silicon wafer prior to measurement.

All XPS measurements were performed using an excitation energy of 825 eV and a pass energy of 10 eV. Data was collected using a SPECS Phoibos 150 hemispherical energy analyser. The background was fitted using a Shirley approximation for all peaks, with pre- and post-peak background simulated using a simple straight-line equation. Binding energies were normalised using the adventitious carbon peak located at 285 eV (assumed to be the most intense C peak when more than one was observed), and intensities were normalised against titanium. In all cases, energy correction was minimal, indicating little to no charging of the material.

NEXAFS was carried out using the same apparatus on the Ti $L_{2,3}$ edge, with an excitation energy ranging from 450 to 485 eV and a pass energy of 50 eV. Total and Auger Electron Yield (TEY and AEY) as well as Fluorescence Yield (FY) spectra were collected for all samples.

## *5.3 Results*

### *5.3.1 Particle sizing*

As-prepared materials were characterised by scanning electron microscopy (SEM) and dynamic light scattering (DLS) to determine particle size. A minimum of 200 particles were analysed for each sample for SEM particle size counting. Particle sizes are showin in Figure 5.2, sample SEM images of particles are shown in Figure 5.3 (for comparison SEM image of titania synthesised in the absence of SMA, see Figure 5.4).

All products were found to be ovoid nanoparticles, with a mean anisotropy (calculated by SEM particle sizing) of 0.40–0.49. DLS data generally agreed

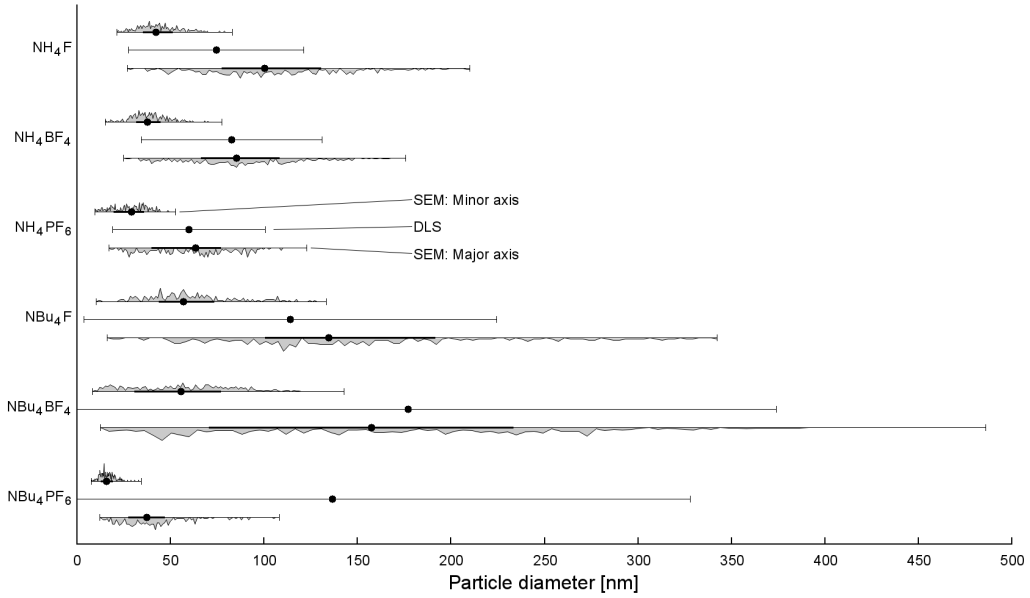


**Figure 5.2.** Particle diameter measured along the major and minor axes, as well as average particle diameter measured by DLS. For SEM particle sizing, the thin line indicates the full range of particles counted, the thick line the upper and lower quartiles, and the central dot the median value. Area graphs show distribution of particle sizes within this continuum. For DLS the dot indicates the number-mean particle size and the error bars the 95% confidence interval.

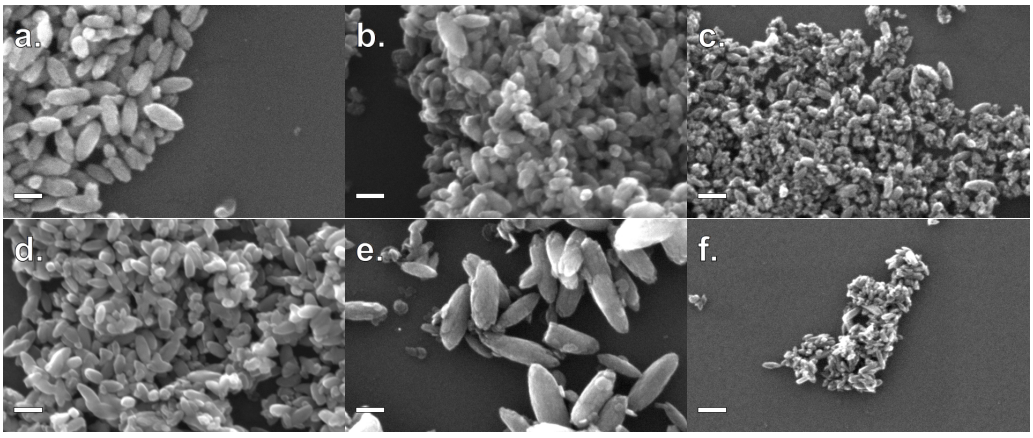


**Figure 5.3.** SEM images of $TiO_2$ modified by: (a) $NH_4F$; (b) $NH_4BF_4$; (c) $NH_4PF_6$; (d) $NBu_4F$; (e) $NBu_4BF_4$; (f) $NBu_4PF_6$. All scale bars are 100 nm.

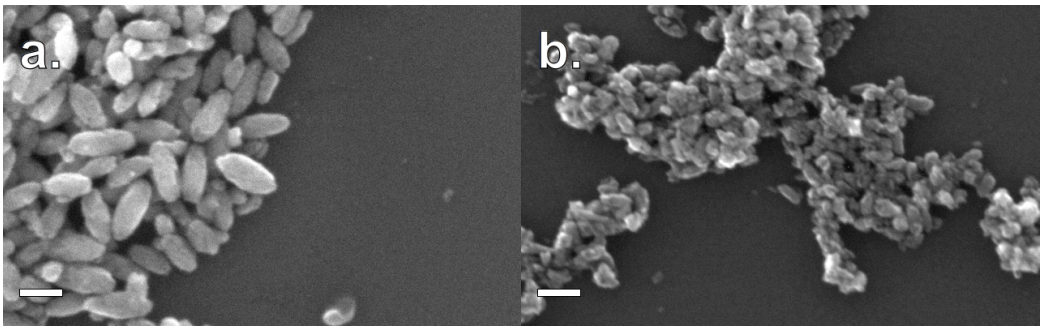


**Figure 5.4.** SEM image of $TiO_2$ synthesised by thermal degradation of peroxotitanic acid, both in the presence of $NH_4F$ SMA (a) in the absence of any SMA (b). Scale bars indicate 100 nm.

with SEM particle sizes, except for $NBu_4PF_6$-modified $TiO_2$. The presence of $NBu_4PF_6$ on the surface of the particles likely encourages their aggregation in solution, giving rise to a much larger apparent size by DLS.

While particles synthesised in the presence of $F^-$ and $BF_4^-$ appear to have approximately the same size, particles synthesised in the presence of $PF_6^-$ are much smaller. Of note, there appears to be a considerable difference in size between $NH_4BF_4$- and $NBu_4BF_4$-modified $TiO_2$. Specifically, particles synthesised in the presence of $NBu_4$-containing SMAs are much more polydisperse. This indicates that particle size is dependent not only on the anionic group, but also on the cationic group of the SMA.

### *5.3.2 Surface area measurements*

Surface area measurements (BET isotherm) are shown in Figure 5.5, and tabulated in Table 5.1. All samples exhibited type 4 isotherms, with some small hysteresis suggesting larger pores (see Figure 5.6), which may also be evident under HRTEM analysis (Figure 5.7). It is postulated that these pores may be caused by the evolution of oxygen as the peroxotitanic acid gel slowly degrades under heating. $NH_4^+$-modified $TiO_2$ materials show hysteresis for the range $0.7 < P/P_0 < 1$, suggesting a relatively narrow pore size distribution, while $NBu_4^+$-modifed $TiO_2$ materials exhibit hysteresis loops down to much lower pressures, indicative of a wider range of pore sizes down to a much smaller size.[231] $NBu_4BF_4{-}TiO_2$ exhibits a significantly different adsorption

**Table 5.1.** Surface area and porosity data for fluorine-modified $TiO_2$ materials.

| SMA | BET surface area [$m^2$ $g^{-1}$] | Avg. pore diameter [nm] |
|---|---|---|
| $NH_4F$ | 56.26 | 23.5 |
| $NH_4BF_4$ | 46.99 | 34.2 |
| $NH_4PF_6$ | 157.28 | 12.8 |
| $NBu_4F$ | 40.22 | 7.8 |
| $NBu_4BF_4$ | 22.58 | 31.5 |
| $NBu_4PF_6$ | 99.15 | 14.9 |

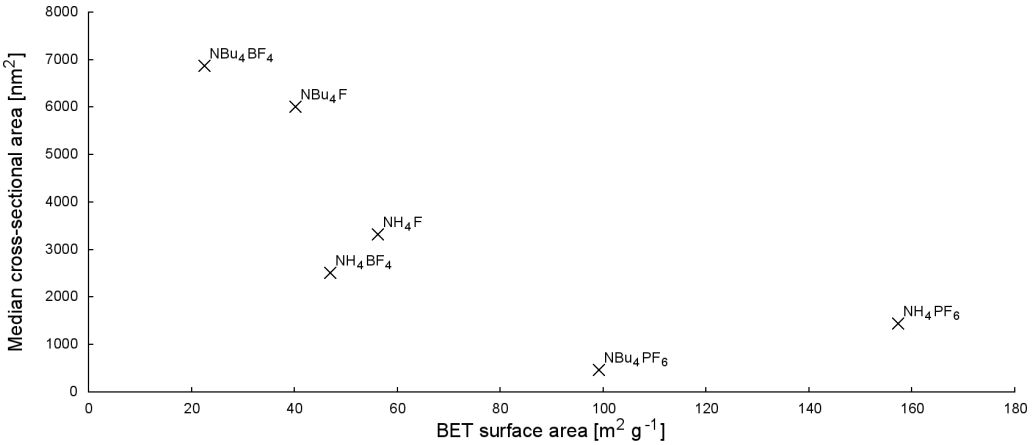


**Figure 5.5.** BET surface areas for $TiO_2$ modified by different fluoride-containing SMAs. These values are plotted against median cross-sectional area for these particles, as calculated using SEM particle-sizing data. It can be seen that there is a weak ($p < 0.1$) correlation between cross-sectional area and surface area.

curve to the other samples, and this may be due to the adsorption of SMA on the material surface, effectively reducing its surface area.[232]

### *5.3.3 Crystallinity*

High-quality PXRD patterns were collected at the Powder Diffraction beamline at the Australian Synchrotron. PXRD analysis showed that all products were crystalline, and generally formed the anatase phase of titania (Figure 5.8): in fact, materials synthesised in the presence of $NH_4^+$-containing surface modifying agents showed no rutile or brookite content. Titanium dioxide synthesised by a similar manner in the absence of fluoride ions (marked "No

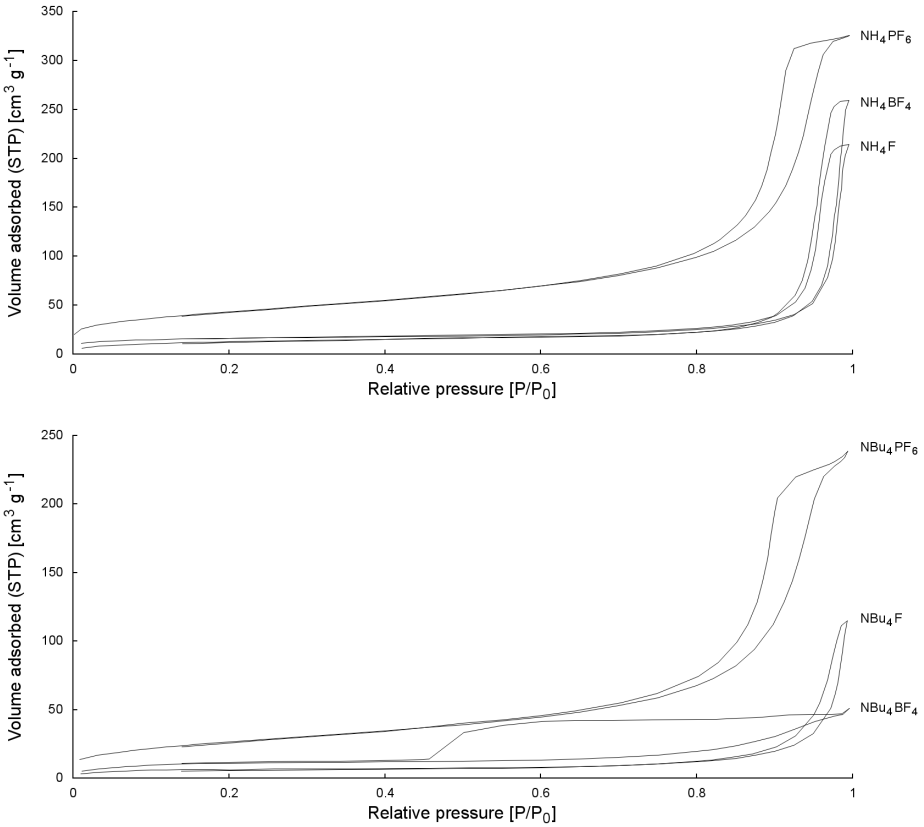


**Figure 5.6.** Raw gas adsorption isotherms for fluoride-modified $TiO_2$.

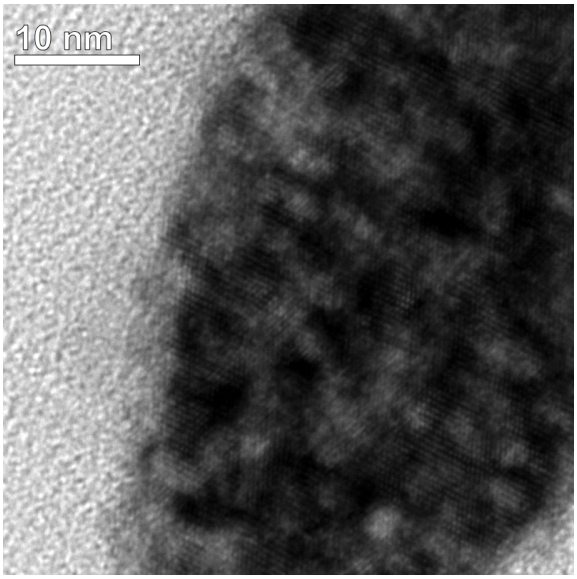


**Figure 5.7.** A high-resolution TEM image of $NH_4F$-modified $TiO_2$ shows possible evidence of irregular pores.

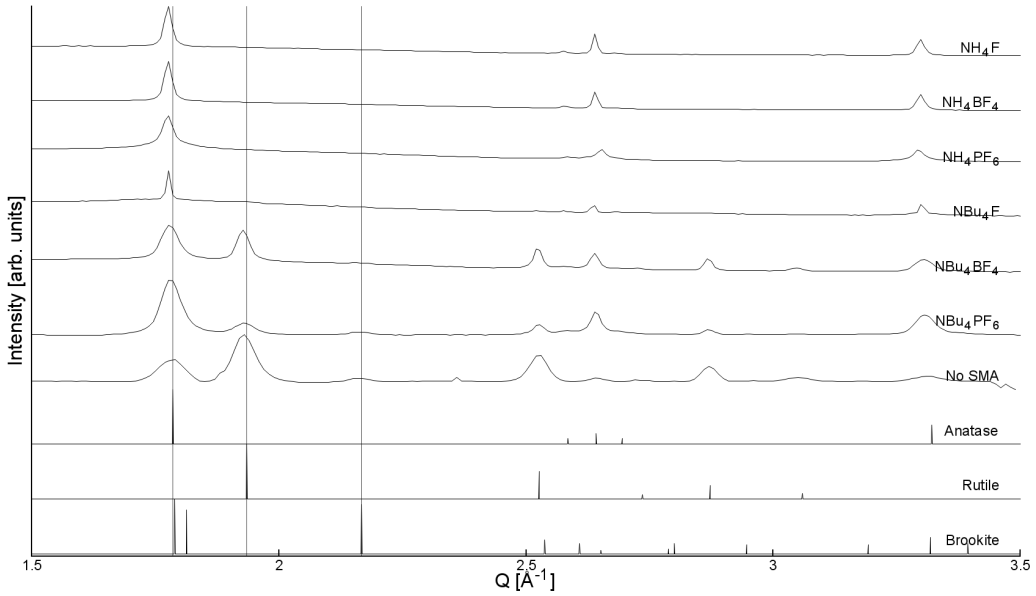


**Figure 5.8.** PXRD diffraction patterns for $TiO_2$ modified with fluoride salts, alongside theoretical peaks for anatase, rutile and brookite $TiO_2$.

SMA") forms a roughly 28:72 mixture of anatase and rutile. Yu and coworkers[233] have previously observed this effect, and argued that the presence of fluoride may either prevent phases other than anatase from forming (due to preferential binding) or may encourage the phase transformation to anatase. For $NBu_4^+$-SMA-modified materials, rutile and even brookite were observed (see Table 5.2 for exact amounts). If it is assumed that phase selectivity is due to the presence of SMA, the presence of these phases suggests that in the case of $NBu_4^+$-SMAs, the anion is not as influential in the formation of the nanoparticle.

The titanium occupancy was allowed to vary during the Rietveld refinement, which is a common technique to determine phase composition.[234] In most cases the titanium occupancy of the materials was less than one, *i.e.* the crystal lattice was titanium deficient. Titanium-deficient titanium dioxide has previously been attributed to the presence of $OH^-$ ions within the bulk.[235] Given the use of $H_2O_2$ in the synthesis of the products reported here, it is feasible that $OH^-$ groups would be trapped within the lattice, resulting in a lower-than-expected titanium occupancy. The titanium occupancy

**Table 5.2.** The weights of phases and crystallite dimensions as calculated from a Rietveld refinement fitting anatase, brookite and rutile phases for each SMA. Percentage weight of phases was determined by the Rietveld refinement and size was calculated from a volume weighted mean column height of a Double-Voigt fit.[229] Error indicates 99% C.I.

| | Anatase | | | Rutile | | Brookite | |
|---|---|---|---|---|---|---|---|
| SMA | Fraction [%] | Dimensions [nm] | | Fraction [%] | Dimensions [nm] | Fraction [%] | Dimensions [nm] |
| $NH_4F$ | 100 | 28.7±1.3 × 119±12 | | | | | |
| $NH_4BF_4$ | 100 | 27.2±1.2 × 90±9 | | | | | |
| $NH_4PF_6$ | 49±4 | 19.8±0.7* | | | | | |
| | 51±4 | 3.3±0.2* | | | | | |
| $NBu_4F$ | 76±3 | 70±8 × 200±30 | | 24±3 | 13±2* | | |
| $NBu_4BF_4$ | 48.5±1.6 | 11.8±0.7 × 40±3 | | 43.6±1.0 | 16.8±0.6 × 38.3±1.4 | 7.9±0.9 | 8.8±1.2* |
| $NBu_4PF_6$ | 57.2±1.4 | 10.9±0.5 × 34.1±1.7 | | 22.4±1.1 | 8.2±0.8 × 20.9±0.8 | 20.5±0.9 | 6.8±0.4* |

*Sample is isotropic in shape.

within the anatase phase was approximately 0.82 for all $NH_4^+$-SMA-modified products and 0.89 for $NBu_4^+-TiO_2$. The small difference in Ti deficiencies between the two cation types of SMAs suggests the Ti deficiency is only partially dependent on the SMA but mostly due to the peroxo-titanic acid hydrothermal synthesis. Rutile in $NBu_4BF_4-TiO_2$ and $NBu_4PF_6-TiO_2$ exhibited titanium occupancy of 0.88: very similar to the majority of anatase phase crystallites, suggesting again that deficiencies in Ti are related to synthesis conditions rather than the SMA.

Size and microstrain analysis of the PXRD data by Rietveld refinement (Figure 5.9, see experimental for details) shows that a majority of the products are anisotropic in shape. All samples except $NH_4PF_6-TiO_2$ show preferential orientation for both anatase and rutile in the [001] direction, and are also anisotropically elongated in this direction. Additionally, the anatase (004) peak is both larger and narrower than expected from shape- and direction-isotropic modelling of a population of the same crystallite size. These peak profiles are best explained by rod-like crystallites oriented along the [001] direction. The larger area is explained by the preferred orientation, and the sharper line profile is explained by increased crystallinity along the major planes of the rod (see Figure 5.10). As can be seen in Table 5.2 the addition of SMA produced anatase crystallites that were elongated in the [001] direction for all cases except $NH_4PF_6-TiO_2$. The dimensions observed in SEM and those calculated from PXRD data largely agree. The exception is $NBu_4BF_4-TiO_2$, whose ovoid particles (observed in SEM) have dimensions far larger than those determined by PXRD. It is likely that the observed particles are made of a number smaller crystallites aggregated in an ordered fashion.

For $NH_4PF_6-TiO_2$, the PXRD data was best modelled by two isotropic (in shape and direction) anatase populations, one population of diameter $\sim$3.3 nm and another larger population of diameter 19.8 nm. The larger anatase population showed no preferred crystallite orientation, although in SEM the larger particles appeared elongated (Figure 5.3C). The aggregation of smaller particles around the larger particles could have prevented them from preferentially orienting, or alternatively the observed particles may not be single crystallites. The rutile phase titania also showed rod-like character

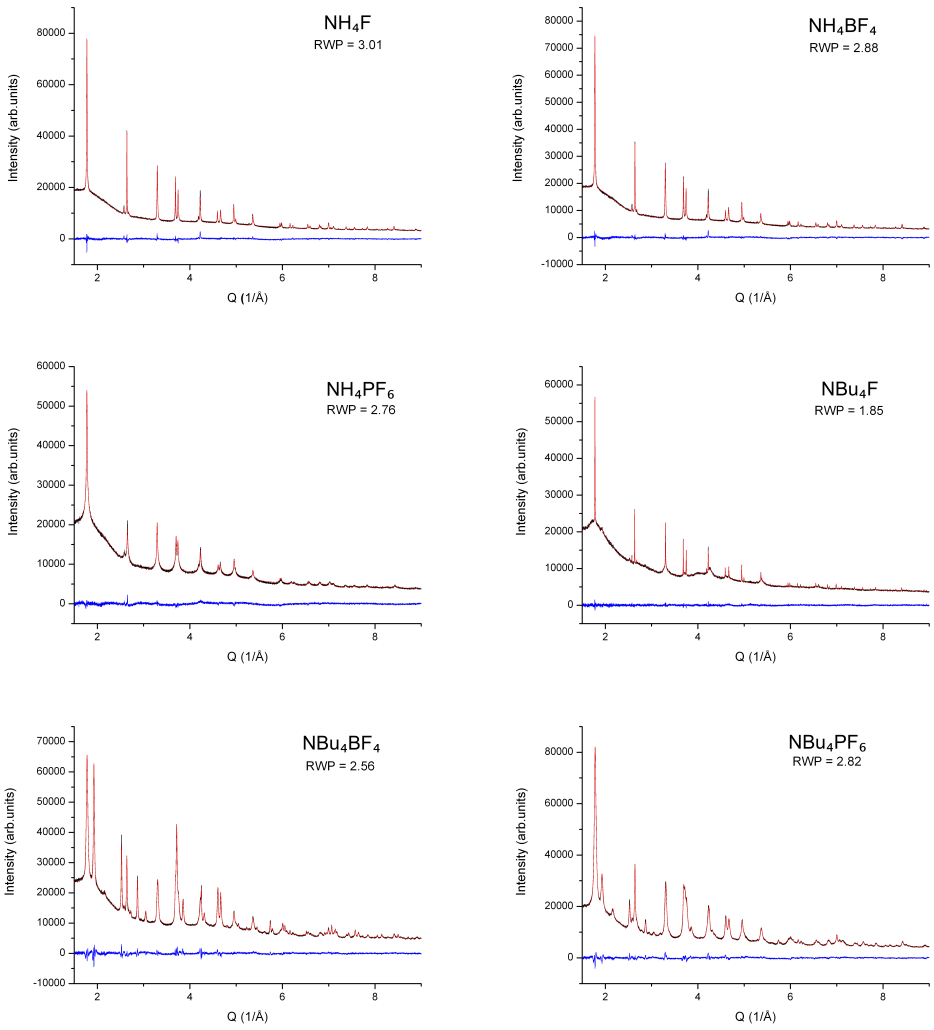


**Figure 5.9.** XRD data fitting and Rietveld refinement for SMA-modified $TiO_2$. Experimental data shown in black, fitting in red and residual in blue. Here "RWP" refers to the Rietveld weight profile reliability.[236]

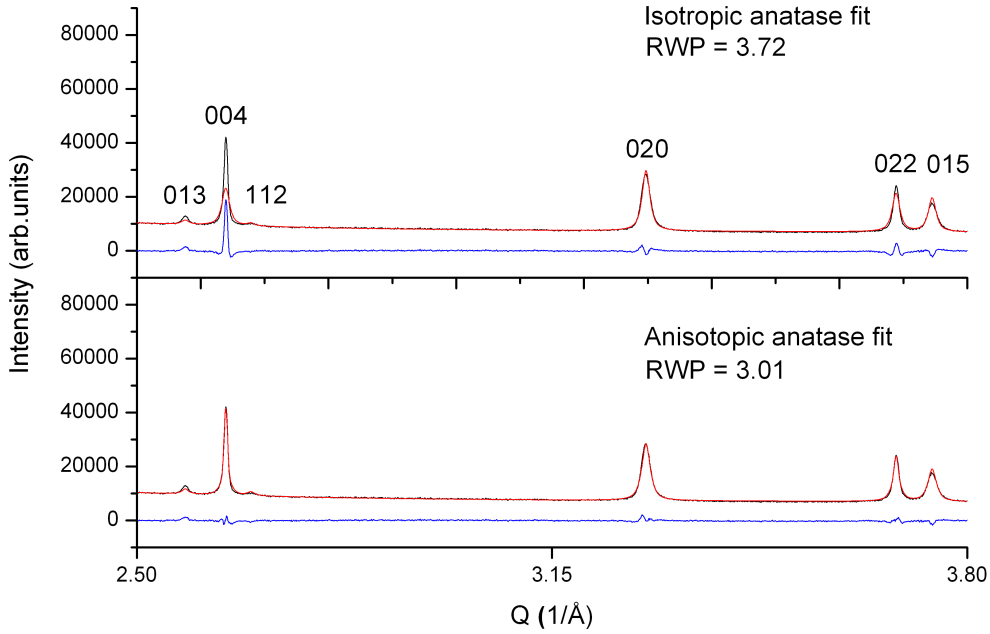


**Figure 5.10.** Isotropic and anisotropic XRD fits for $NH_4FTiO_2$. The residual (blue) is considerably noisier for the isotropic fit, which indicates that the crystals are anisotropic.

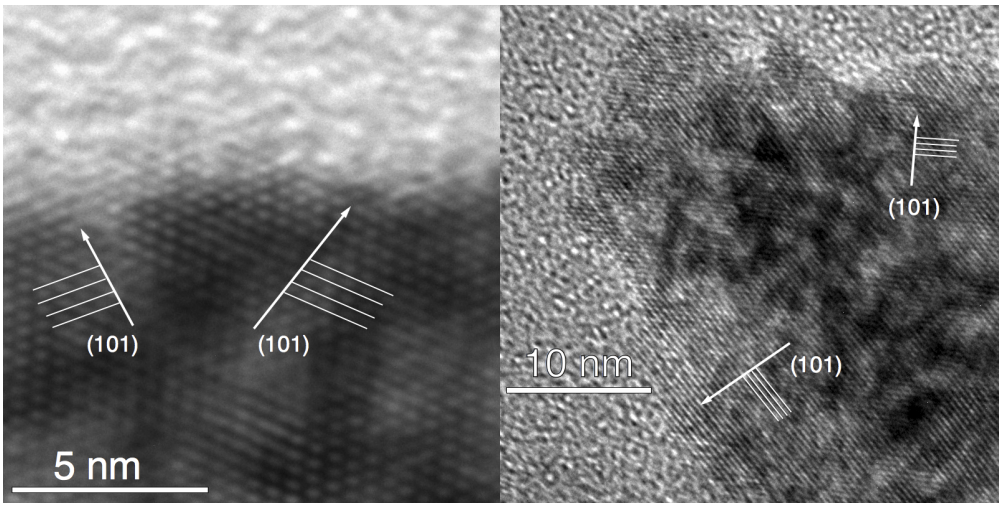


**Figure 5.11.** HRTEM fringing from the (101) face of fluorine-modified $TiO_2$ proceeds at ∼45° to the long edge of the nanoparticle. (Shown here: TEM image of $NH_4F{-}TiO_2$.)

and exhibited preferential orientation (however, for $NBu_4F{-}TiO_2$ particle shape could not be determined due to the lack of definition in rutile peaks). This rod-like form is typical of rutile grown in an acidic environment.[237,238]

HRTEM studies further confirmed the particle size and shape model developed based on SEM and PXRD data, demonstrating strong fringing patterns (Figure 5.11) indicative of crystalline material. Ovoid particles exhibited strong fringing indicative of the [101] plane, at approximately 45° to their long edge, suggesting that their shape was dictated by the growth of specific crystal faces. Based on this data, it is proposed that the (010) face is located on the long edge of the nanoparticle (Figure 5.12).[239] It should be noted that many smaller particles do not follow this pattern: these particles appear more regularly in products synthesised using $NBu_4$-containing SMAs.

### *5.3.4 Electron spectroscopy studies*

X-ray photoelectron spectroscopy (XPS) was performed at the soft X-ray beamline of the Australian Synchrotron. Survey scans (see Figure 5.13) showed evidence of carbon, titanium, oxygen, nitrogen, fluorine, and silicon (from the wafer), with boron and phosphorus observed for $BF_4^-$- and $PF_6^-$-modified materials (Figure 5.14). High-resolution XPS was performed

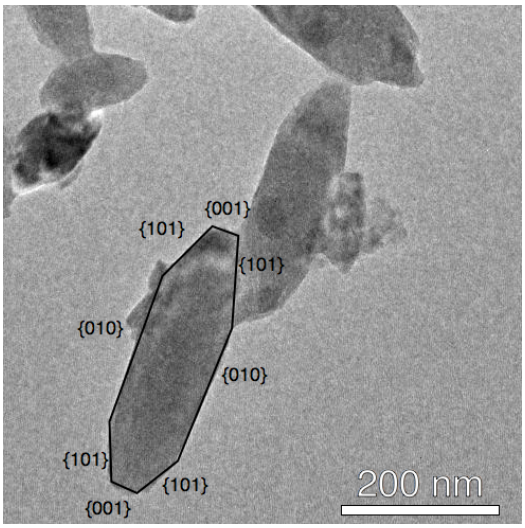


**Figure 5.12.** The proposed structure of nanocrystalline $TiO_2$. (Shown here: $NBu_4F{-}TiO_2$.)

on the fluorine 1s, titanium 2p, nitrogen 1s, oxygen 1s and carbon 1s peaks, as well as the phosphorus 2p peak for $PF_6^-$-modified samples. Peak positions, intensities, and peak full widths at half maximum (FWHMs) are tabulated in Tables 5.3 and 5.4.

Two oxygen 1s peaks were observed (see Figure 5.15 for a typical O 1*s* XP spectrum). The peak at $\sim$ 532.5 eV was assigned to surface Ti−O−H, while the one at $\sim$ 530 eV were assigned to Ti−O−Ti.[146] In all cases the Ti:O ratio by XPS was approximately 1:2, suggesting that any deviation in occupancy levels in the bulk did not continue to the surface of the material.

The presence of fluoride was confirmed by XPS (Figure 5.16). Two peaks were observed at 687–688 eV (A) and 684–685 eV (B). All samples exhibited this double-peak feature, despite being washed several times with distilled water (and additionally with acetonitrile for tetrabutylammonium salt-modified samples), indicating that the SMA was strongly bound to the surface. While fluorine peaks in the region of peak A have previously been attributed to surface lattice fluoride (Ti−F−Ti),[155,240–243] it was found that this peak could be removed by treatment with KOH solution (1 M, one hour: Figure 5.16). This suggests that the fluoride species is more likely to be surface-bound. Additionally, a small carbon XPS peak (see Figure 5.17) is

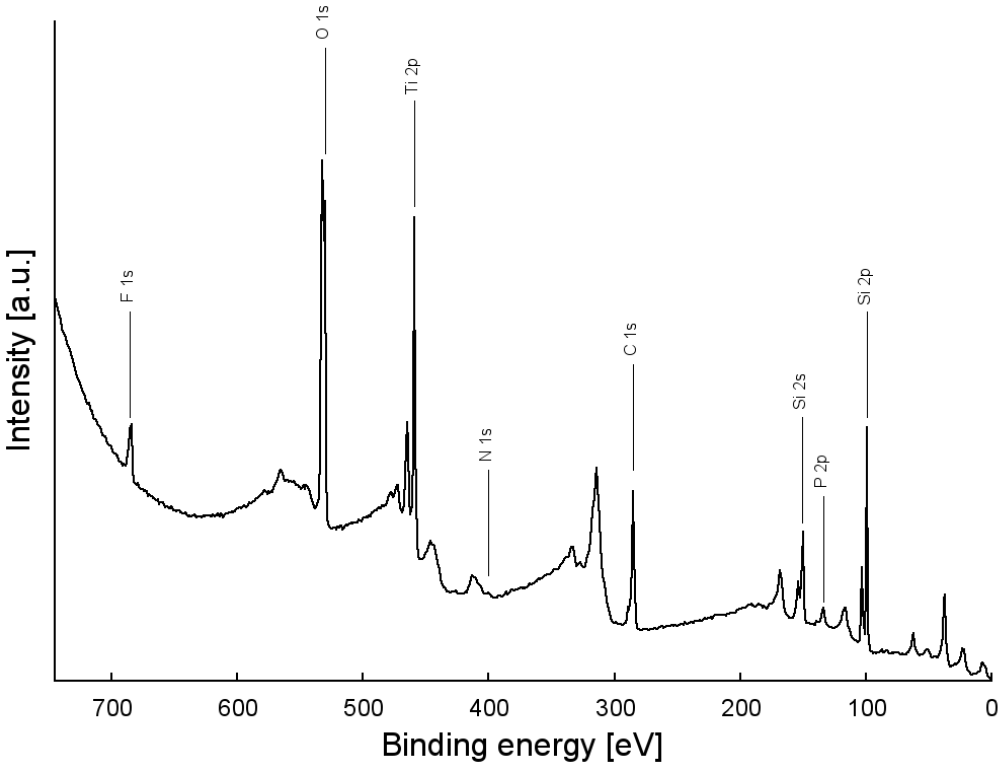


**Figure 5.13.** Survey XP spectrum for a typical sample (here: $NH_4PF_6$−$TiO_2$. Photoelectron peaks are marked: unmarked peaks are auger peaks.

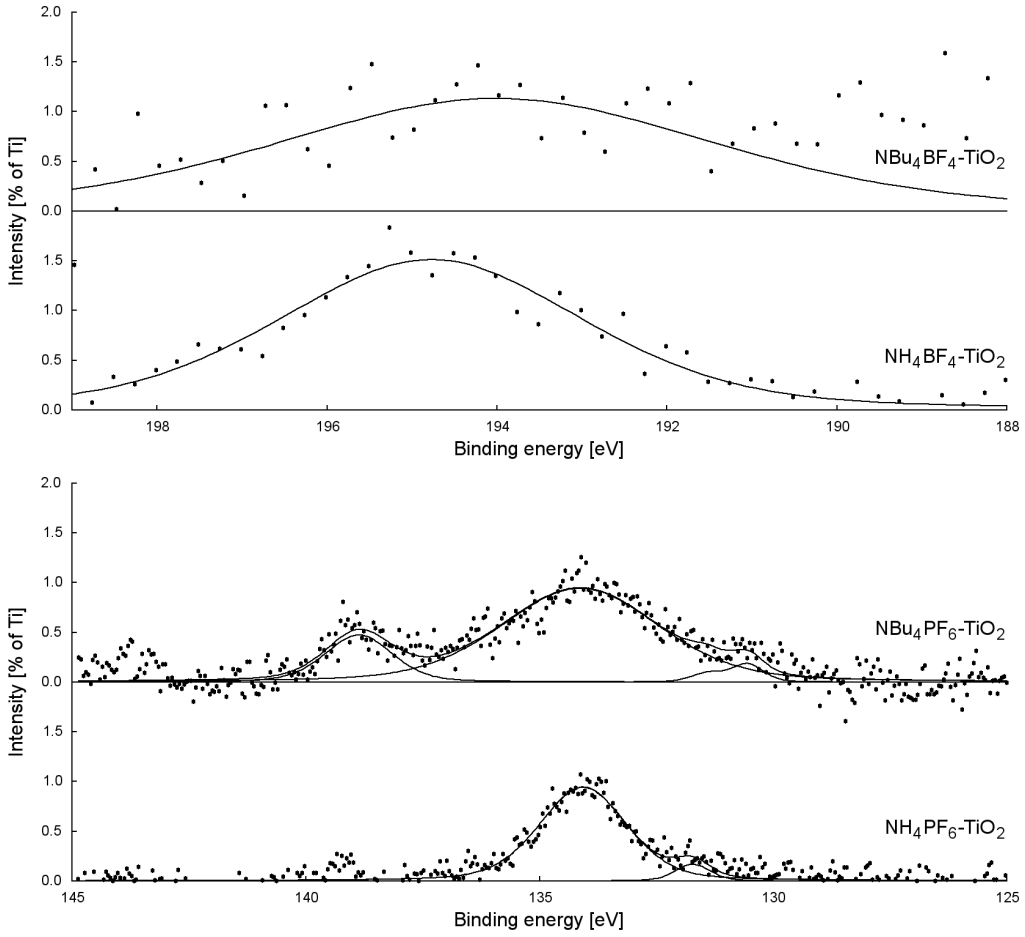


**Figure 5.14.** B 1s and P 2p XPS peaks for $BF_4^-$- and $PF_6^-$-modified $TiO_2$ materials.

**Table 5.3.** XPS fitting data for $NH_4^+$-SMA-modified $TiO_2$ materials.

| **$NH_4F-TiO_2$** | | | | | |
|---|---|---|---|---|---|
| Element | # | $E_B$ [eV] | Intensity | FWHM [eV] | Abundance [%] |
| Ti 2p | 1 | 459.21 | 74511 | 1.05 | 4.11 |
| Ti 2p | 2 | 458.01 | 4882 | 1.34 | 0.27 |
| C 1s | 1 | 285 | 24280 | 1.42 | 9.64 |
| C 1s | 2 | 286.22 | 8375 | 2.15 | 3.33 |
| C 1s | 3 | 289.28 | 1901 | 1.4 | 0.76 |
| F 1s | 1 | 684.77 | 5879 | 1.55 | 0.58 |
| F 1s | 2 | 686.81 | 3596 | 1.99 | 0.36 |
| N 1s | 1 | 400.4 | 2895 | 2.99 | 0.68 |
| N 1s | 2 | 400.25 | 459 | 0.94 | 0.11 |
| Si 2p | 1 | 99.11 | 20400 | 0.48 | 7.5 |
| Si 2p | 2 | 103.08 | 13865 | 1.43 | 5.1 |
| Si 2p | 3 | 99.93 | 828 | 0.89 | 0.3 |
| O 1s | 1 | 530.59 | 106229 | 1.23 | 15.98 |
| O 1s | 2 | 532.64 | 340752 | 1.65 | 51.27 |
| **$NH_4BF_4-TiO_2$** | | | | | |
| Element | # | $E_B$ [eV] | Intensity | FWHM [eV] | Abundance [%] |
| Ti 2p | 1 | 459.34 | 179764 | 1.1 | 13.69 |
| Ti 2p | 2 | 457.92 | 7453 | 1.25 | 0.57 |
| C 1s | 1 | 285 | 18819 | 1.49 | 10.32 |
| C 1s | 2 | 286.21 | 9703 | 2.31 | 5.32 |
| C 1s | 3 | 289.24 | 3819 | 1.7 | 2.09 |
| F 1s | 1 | 684.86 | 15328 | 1.51 | 2.1 |
| F 1s | 2 | 686.73 | 4799 | 1.8 | 0.66 |
| N 1s | 1 | 400.34 | 1552 | 1.26 | 0.51 |
| N 1s | 2 | 399.32 | 236 | 0.86 | 0.08 |
| Si 2p | 1 | 98.88 | 200 | 0.48 | 0.1 |
| Si 2p | 2 | 102.85 | 550 | 1.43 | 0.28 |
| Si 2p | 3 | 102.39 | 78 | 1.11 | 0.04 |
| O 1s | 1 | 530.62 | 202620 | 1.14 | 42.09 |
| O 1s | 2 | 531.97 | 106684 | 2.36 | 22.16 |
| **$NH_4PF_6-TiO_2$** | | | | | |
| Element | # | $E_B$ [eV] | Intensity | FWHM [eV] | Abundance [%] |
| Ti 2p | 1 | 459.18 | 149500 | 1.06 | 8.82 |
| Ti 2p | 2 | 457.79 | 4268 | 0.9 | 0.25 |
| C 1s | 1 | 285 | 28555 | 1.62 | 12.13 |
| C 1s | 2 | 286.72 | 2944 | 1.19 | 1.25 |
| C 1s | 3 | 289.26 | 2790 | 1.41 | 1.19 |
| F 1s | 1 | 684.65 | 16461 | 1.56 | 1.75 |
| F 1s | 2 | 686.76 | 5459 | 1.89 | 0.58 |
| N 1s | 1 | 400.23 | 1622 | 1.25 | 0.41 |
| N 1s | 2 | 399.73 | 1005 | 3.64 | 0.25 |
| Si 2p | 1 | 99 | 13523 | 0.46 | 5.32 |
| Si 2p | 2 | 102.98 | 7654 | 1.35 | 3.01 |
| Si 2p | 3 | 99.64 | 1156 | 1.03 | 0.45 |
| O 1s | 1 | 530.32 | 117686 | 1.02 | 18.94 |
| O 1s | 2 | 532.48 | 201666 | 1.69 | 32.45 |
| O 1s | 3 | 530.9 | 77182 | 1.31 | 12.42 |
| P 2p | 1 | 133.7 | 2481 | 1.88 | 0.68 |
| P 2p | 2 | 131.03 | 368 | 1.01 | 0.1 |

**Table 5.4.** XPS fitting data for $NBu_4^+$-SMA-modified $TiO_2$ materials.

| **$NBu_4F-TiO_2$** | | | | | |
|---|---|---|---|---|---|
| Element | # | $E_B$ [eV] | Intensity | FWHM [eV] | Abundance [%] |
| Ti 2p | 1 | 458.97 | 178707 | 1.04 | 10.6 |
| Ti 2p | 2 | 457.69 | 12923 | 1.21 | 0.77 |
| C 1s | 1 | 285 | 47974 | 1.54 | 20.48 |
| C 1s | 2 | 286.13 | 23811 | 1.87 | 10.17 |
| F 1s | 1 | 684.67 | 7865 | 1.49 | 0.84 |
| F 1s | 2 | 687.03 | 7159 | 1.79 | 0.76 |
| N 1s | 1 | 402.02 | 5026 | 1.3 | 1.28 |
| N 1s | 2 | 400.44 | 5717 | 2.64 | 1.45 |
| Si 2p | 1 | 98.84 | 490 | 0.28 | 0.19 |
| Si 2p | 2 | 102.99 | 2516 | 1.56 | 0.99 |
| Si 2p | 3 | 99.03 | 3348 | 0.47 | 1.32 |
| O 1s | 1 | 530.19 | 38842 | 0.89 | 6.28 |
| O 1s | 2 | 532.4 | 67113 | 1.61 | 10.85 |
| O 1s | 3 | 530.64 | 210239 | 1.2 | 34 |
| **$NBu_4BF_4-TiO_2$** | | | | | |
| Element | # | $E_B$ [eV] | Intensity | FWHM [eV] | Abundance [%] |
| Ti 2p | 1 | 459.18 | 125831 | 1.09 | 5.78 |
| Ti 2p | 2 | 457.83 | 6797 | 1.25 | 0.31 |
| C 1s | 1 | 285 | 40311 | 1.43 | 13.34 |
| C 1s | 2 | 286.21 | 17784 | 2.09 | 5.89 |
| C 1s | 3 | 289.22 | 2632 | 1.25 | 0.87 |
| F 1s | 1 | 684.74 | 23942 | 1.61 | 1.98 |
| F 1s | 2 | 686.86 | 10237 | 2.04 | 0.85 |
| N 1s | 1 | 402.16 | 1302 | 1.22 | 0.26 |
| N 1s | 2 | 400.14 | 2152 | 2.03 | 0.42 |
| Si 2p | 1 | 99.11 | 22905 | 0.39 | 7.02 |
| Si 2p | 2 | 103.15 | 20274 | 1.43 | 6.21 |
| Si 2p | 3 | 99.27 | 11096 | 0.5 | 3.4 |
| O 1s | 1 | 530.44 | 106793 | 1.05 | 13.39 |
| O 1s | 2 | 532.74 | 267302 | 1.57 | 33.51 |
| O 1s | 3 | 531.13 | 54036 | 1.34 | 6.77 |
| **$NBu_4PF_6-TiO_2$** | | | | | |
| Element | # | $E_B$ [eV] | Intensity | FWHM [eV] | Abundance [%] |
| Ti 2p | 1 | 459.03 | 137399 | 1.02 | 7.03 |
| Ti 2p | 2 | 457.72 | 3592 | 0.94 | 0.18 |
| C 1s | 1 | 285 | 41540 | 1.5 | 15.3 |
| C 1s | 2 | 286.46 | 9029 | 1.79 | 3.33 |
| C 1s | 3 | 289.17 | 4901 | 1.23 | 1.81 |
| F 1s | 1 | 684.55 | 13037 | 1.66 | 1.2 |
| F 1s | 2 | 686.79 | 9728 | 1.82 | 0.9 |
| N 1s | 1 | 400.03 | 1663 | 1.73 | 0.36 |
| Si | 1 | 99 | 21071 | 0.38 | 7.19 |
| Si | 2 | 102.98 | 16245 | 1.43 | 5.54 |
| Si | 3 | 99.14 | 8956 | 0.49 | 3.06 |
| O 1s | 1 | 530.24 | 123176 | 1.05 | 17.19 |
| O 1s | 2 | 532.56 | 201380 | 1.56 | 28.1 |
| O 1s | 3 | 530.94 | 53814 | 1.37 | 7.51 |
| P 2p | 1 | 133.8 | 4265 | 3.83 | 1.01 |
| P 2p | 2 | 138.55 | 981 | 1.61 | 0.23 |
| P 2p | 3 | 130.49 | 246 | 0.8 | 0.06 |

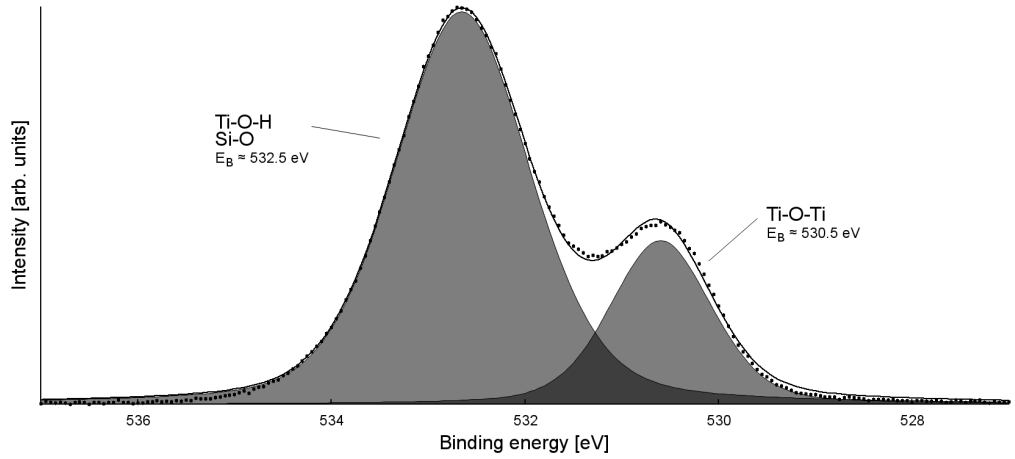


**Figure 5.15.** Typical O 1s XPS peak and assignments. Experimental data shown as filled circles, theoretical data shown as lines. The peak at 532.5 eV is attributable to both surface oxygen on $TiO_2$ and lattice oxygen in $SiO_2$, a result of the silicon wafer the samples are deposited on.

observed to disappear after KOH treatment: this peak may be attributable to fluorocarbon species.[244] Peak B is assigned to surface-bound, chemisorbed Ti−F) groups. Of particular note, this treatment appeared not to remove chemisorbed Ti−F (peak B), despite previous findings in the literature.[116,146] The reason for the stability of this species even under basic conditions is as yet unknown.

Analysis of the titanium XPS signal (see Figure 5.18 for fitting) shows a characteristic peak at 459 eV attributed to $Ti^{4+}$, with a smaller peak around 457.7–458 eV due to $Ti^{3+}$. In all cases, the $Ti^{3+}$ content for SMA-modified $TiO_2$ (as a function of total Ti content, see Figure 5.19) was greater than for P-25. This is likely due to the effect of the surface-bound fluoride, which has been previously shown[233] to encourage $Ti^{3+}$ formation. In addition, there is an apparent correlation between both anionic and cationic group of the SMA, and the abundance of $Ti^{3+}$ in the material (*i.e.* $F^- > BF_4^- > PF_6^-$; $NBu_4^+ > NH_4^+$). The presence of these $Ti^{3+}$ centres may improve visible light activity through the creation of localised mid-gap states,[88,245] aiding in the visible-light activity of the materials.

NEXAFS analysis was performed on the Ti $L_{2,3}$ transition using Auger and Total Electron Yield (AEY and TEY) and Fluorescence Yield (FY)

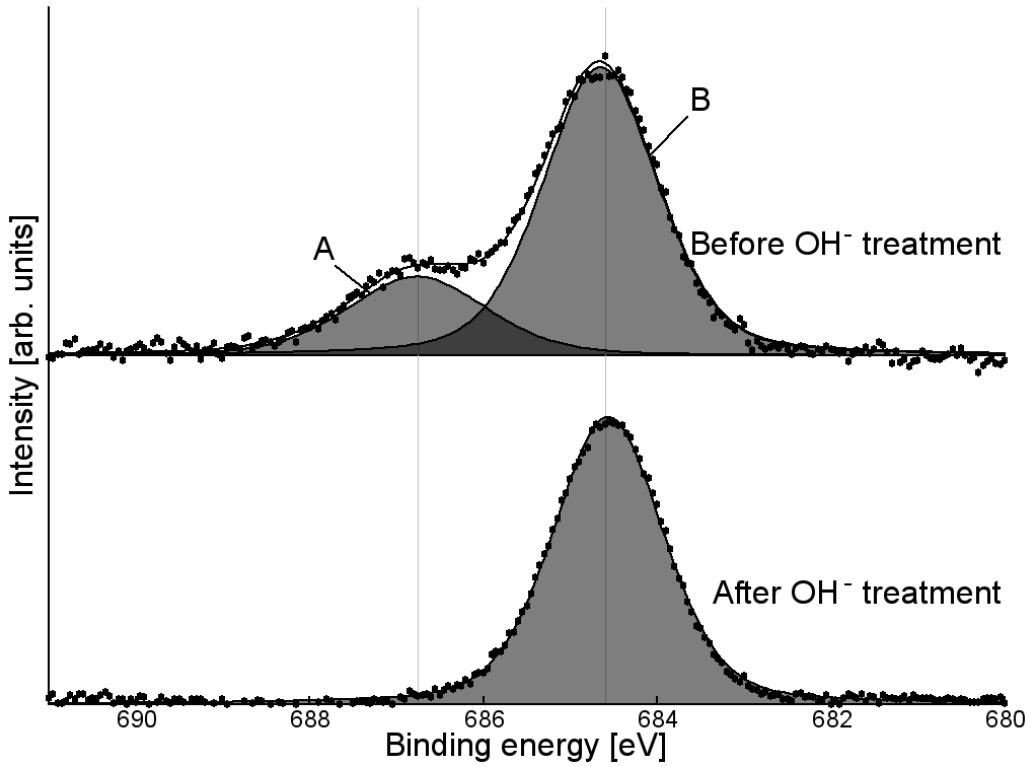


**Figure 5.16.** F 1s XPS peak for $NH_4PF_6$-modified $TiO_2$, before and after washing with KOH. Grey signal shows raw data, with Shirley baseline removed.

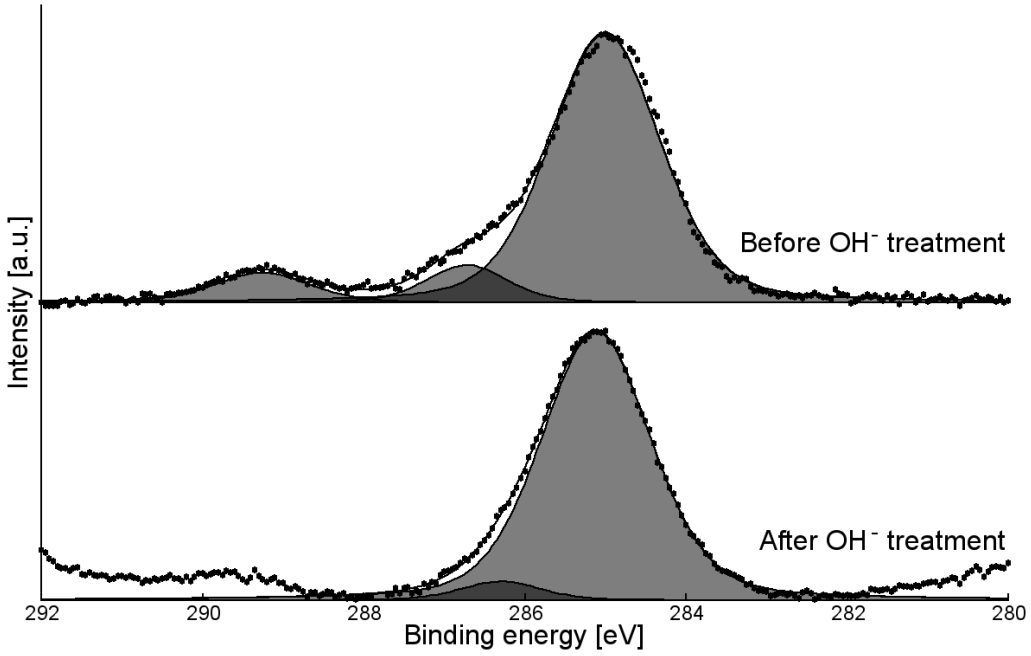


**Figure 5.17.** C 1s XPS peaks for $NH_4PF_6$ before and after KOH treatment.

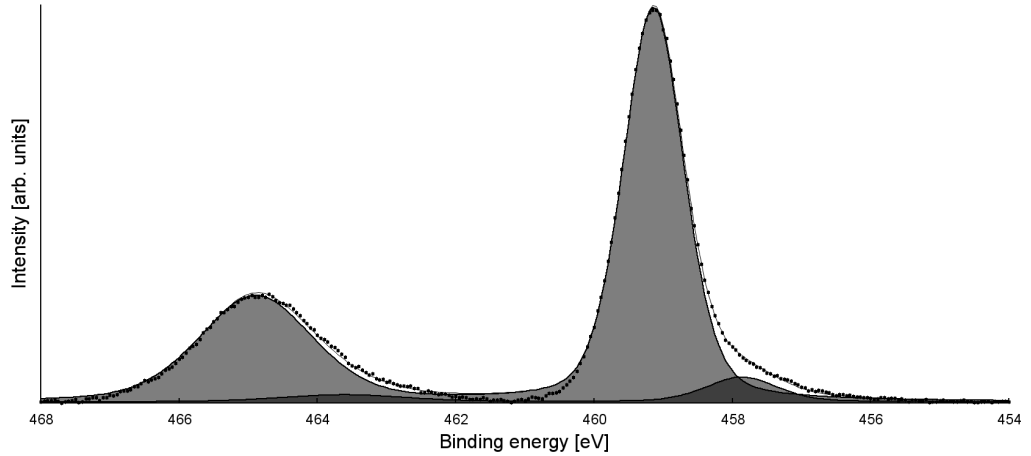


**Figure 5.18.** A typical Ti 2p XPS peak (shown here, that for $NBu_4F{-}TiO_2$). Fitting curves are shown for $Ti^{4+}$ and $Ti^{3+}$. Experimental data is shown as filled circles.

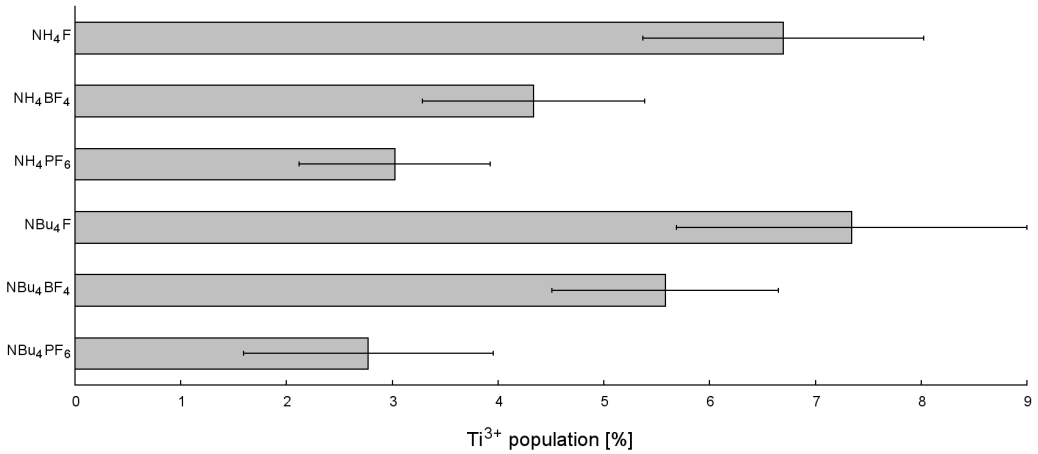


**Figure 5.19.** $Ti^{3+}$ content (as a percentage of total Ti content) for each product. Error bars show 95% C.I.

**Table 5.5.** NEXAFS peak assignments.

| Peak | Assignment |
|---|---|
| A | Satellite peak |
| B | Satellite peak |
| C | $t_{2g}$ $L_3$ |
| D | $e_g$ $L_3$ |
| E | $e_g$ $L_3$ |
| F | $t_{2g}$ $L_2$ |
| G | $e_g$ $L_2$ |

measurements (Figure 5.20). The AEY spectrum was found to be the most well-defined, with TEY and FY exhibiting a lower signal-to-noise ratio. In a majority of cases the edge displays a characteristic shape, with auxiliary peaks marked *A* and *B* and main peaks *C*–*G* (see Figure 5.21 for peak positions, and Table 5.5 for assignments).

The ratio between the peaks *D* and *E* is strongly dependent on the crystal phase of the titanium dioxide material, due to long-range structural effects.[173] Anatase materials exhibit a strong *D* and somewhat weaker *E* peak, while rutile displays the converse. It can be seen that for $NH_4^+$-SMA-modified $TiO_2$ the low-energy peak *C* is significantly more intense, and the high-energy peak *D* is apparent only as a shoulder. For $NBu_4F$- and $NBu_4PF_6$-modified

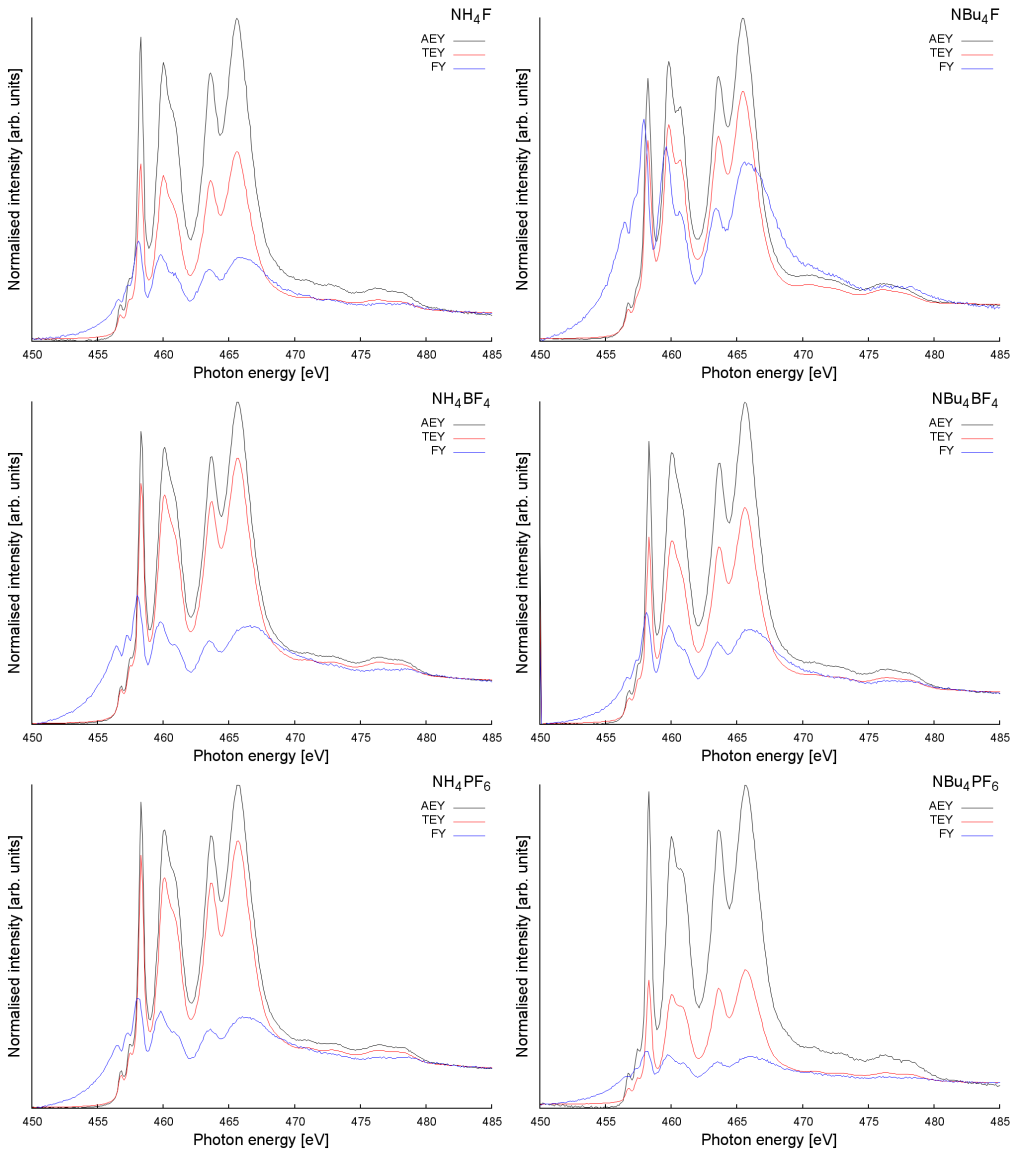


**Figure 5.20.** NEXAFS AEY, TEY and FY spectra for fluoride-modified $TiO_2$ materials.

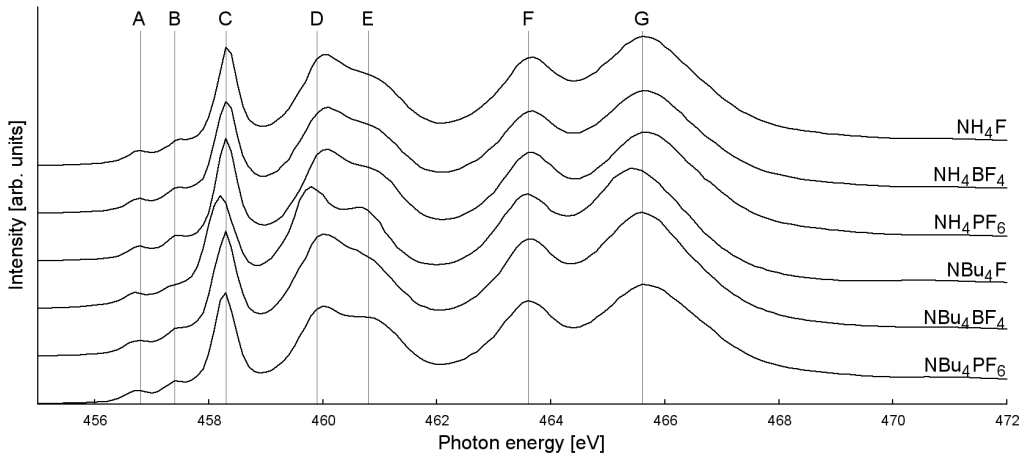


**Figure 5.21.** Comparison of AEY NEXAFS spectra for fluoride-modified $TiO_2$ samples, with peaks labelled.

$TiO_2$, the high-energy peak is more apparent: this is a result of the presence of significant quantities of rutile in the material, which correlates with the PXRD findings above.

The presence of $Ti^{3+}$ also affects the Ti $L_{2,3}$ NEXAFS edge in a number of ways:

- Peak $C$ shifts to a higher energy (up to ∼0.2 eV), while peak $G$ shifts down in binding energy.[246]
- The relative intensities $I_C/I_D$ and $I_F/I_G$ decrease.[175]
- A small shoulder-peak occurs at ∼462.5 eV, on the low-energy side of peak $F$[175]

Electron yield NEXAFS is generally sensitive to only the top 50 Ångstroms of the material, while fluorescence yield measurements may penetrate at far at 500–1000 Ångstroms into the bulk.[169,171] It is therefore tempting to use these techniques to analyse the $Ti^{3+}$ content of the materials at different distances from the particle surface; however NEXAFS also suffers from an overabsorption or "self-absorption" effect in which the intensity of given peaks may vary depending on the penetration depth of the technique.[247,248] While this rules out the use of relative intensities as a measure of relative $Ti^{3+}$ content, peak energies are unaffected by overabsorption effects.

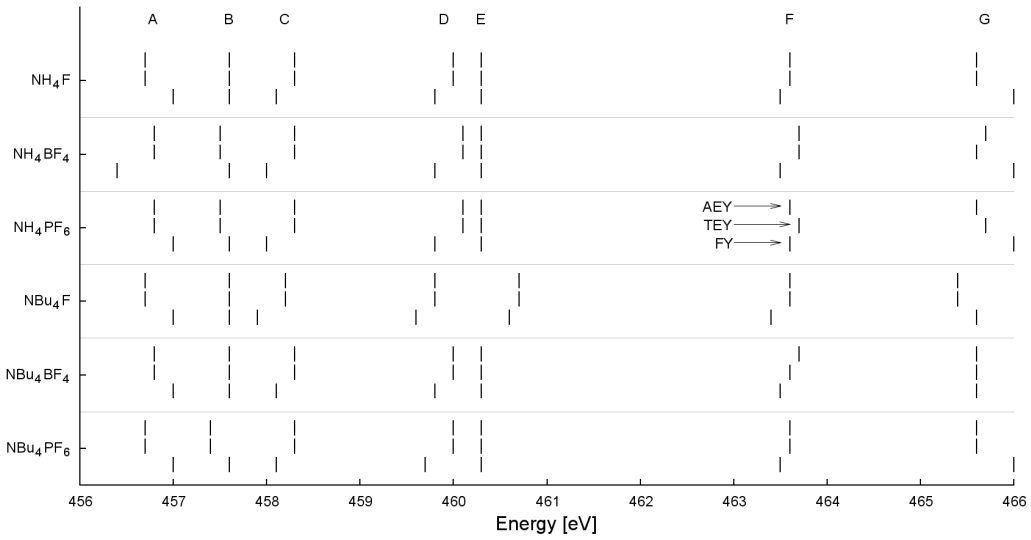


**Figure 5.22.** Relative energy positions of NEXAFS peaks for fluoride-modified $TiO_2$. Lines indicate, from top to bottom in each series, AEY, TEY and FY data.

By comparing the energies of NEXAFS peaks using different techniques (Figure 5.22), it can be seen that AEY and TEY techniques give very similar values, as is to be expected, as they are both electron yield techniques. However, the FY technique results in a slight shift in energies of NEXAFS peaks. It can be seen that for all samples, the peak *C* is shifted to a slightly (0.2–0.3 eV) higher energy for EY NEXAFS than for FY NEXAFS, while for the majority of samples (except for $NBu_4BF{-}TiO_2$) the *G* peak is shifted to a lower (0.2–0.4 eV) energy for EY NEXAFS than FY NEXAFS. In both cases, electron-yield NEXAFS techniques (which are more surface-sensitive than fluorescence-yield techniques) indicate phenomena that suggest the presence of $Ti^{3+}$: this in turn suggests that $Ti^{3+}$ in the material is situated preferentially at the surface. No peak is observed at ∼462.5 eV for any sample, indicating that even if $Ti^{3+}$ exists preferentially the surface of the particle, it still only exists in small amounts relative to the total Ti population.

### *5.3.5 Surface charge*

The majority of fluoride-modified materials show a negative zeta potential, the two exceptions being $NBu_4BF_4$- and $NBu_4PF_6$-modified $TiO_2$ (zeta po-

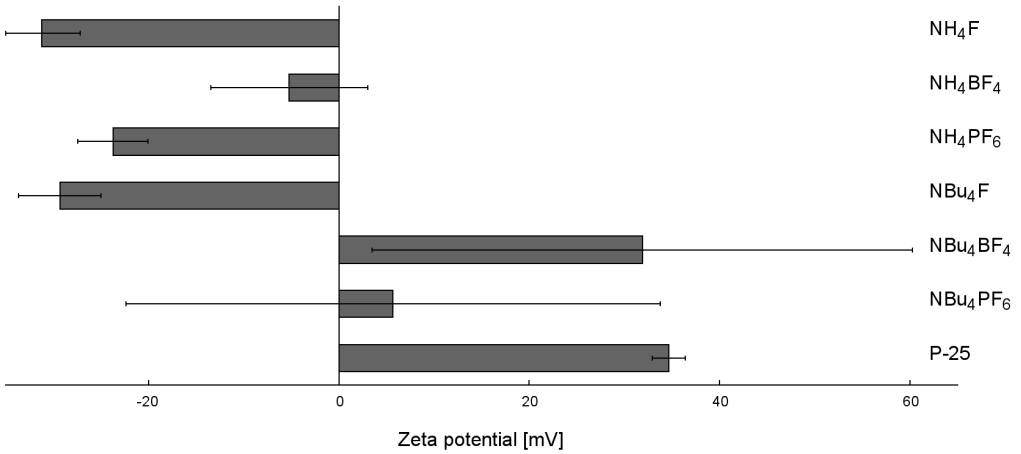


**Figure 5.23.** Zeta potentials for fluoride-modified $TiO_2$ as compared to P-25. Error bars indicate 95% CI.

tential measurements shown in Figure 5.23). In contrast, $TiO_2$ synthesised in the absence of SMA shows a positive zeta potential. It is expected that the fluoride-containing anion of the SMA, which is bound to the surface, is responsible for the change in zeta potential. The variation in zeta potential between materials suggests that not all SMAs are equal in their ability to influence the surface of the material.

There is no correlation between XPS measurements of fluoride intensity (normalised by total Ti signal) and zeta potential. This may be due to the differing preparation methods and media for the two techniques (*i.e.* measurement in solution at atmospheric pressure as opposed to measurement of the solid under UHV conditions).

### *5.3.6 Mechanism of growth*

The above results demonstrate that the choice of SMA heavily influences particle size, crystallinity, surface area and electronic structure of the product. In solution, fluoride ($F^-$) will bind strongly to titanium, forming Ti−F. The presence of fluoride bound to titanium during synthesis encourages the growth of anatase (as opposed to rutile) titania:[233] this suggests that those materials that exhibit rutile and brookite character are exposed to lower concentrations of fluoride during synthesis. Pure anatase materials exhibited a

much larger (004) PXRD peak than predicted by the spherical particle model, which correlated with SEM and TEM observations of anisotropy. This further suggests that the SMA is responsible for alterations in both particle size and particle phase.

XPS studies show that fluoride is chemically bound to the $TiO_2$ surface as Ti−F, not as Ti−$BF_4$ or Ti−$PF_6$. Previous reports are inconclusive on the nature of $BF_4^-$-SMA modification: Zhou and coworkers recently reported that $TiO_2$ synthesised in acidic $NaBF_4$ solution was modified by the $BF_4^-$ ion, citing evidence of Ti−B−F species in B XPS;[156] other groups have reported that $NaBF_4$ dissociates to give surface Ti−F as an SMA.[155,249] It is posited that in the synthetic method outlined in this report, $BF_4^-$ decomposes to give free fluoride in addition to boric acid (here "≡ Ti" represents surface-bound titanium):

$$\begin{aligned} \equiv \mathrm{Ti{-}OH} + \mathrm{BF_4^-} &\longrightarrow \equiv \mathrm{Ti{-}F} + \mathrm{BF_3} + \mathrm{OH^-} \\ \mathrm{BF_3} + 3\,\mathrm{H_2O} &\longrightarrow 3\,\mathrm{H^+} + 3\,\mathrm{F^-} + \mathrm{H_3BO_3} \end{aligned}$$

$PF_6^-$ has been reported to decay in a similar manner to give $F^-$.[250] We therefore propose a similar mechanism for $PF_6^-$ in solution:

$$\begin{aligned} \equiv \mathrm{Ti{-}OH} + \mathrm{PF_6^-} &\longrightarrow \equiv \mathrm{Ti{-}F} + \mathrm{PF_5} + \mathrm{OH^-} \\ \mathrm{PF_5} + 4\,\mathrm{H_2O} &\longrightarrow 5\,\mathrm{H^+} + 5\,\mathrm{F^-} + \mathrm{H_3PO_4} \end{aligned}$$

This mechanism is schematically illustrated in Figure 5.24. An increase in temperature accelerates the decomposition of $BF_4^-$, especially near the boiling point of the solvent.[251] Previously titanium dioxide was synthesised in the presence of $BF_4^-$ at 130°C, allowing for the facile production of $F^-$.[155] It appears that in the synthetic method reported here, the release of $F^-$ is kinetically controlled by the lower temperature of the reaction. If the rate of fluoride formation is significantly slower than the rate of titanium dioxide condensation, the early-stage formation of titanium dioxide will take place in an effectively "fluoride-free" environment.

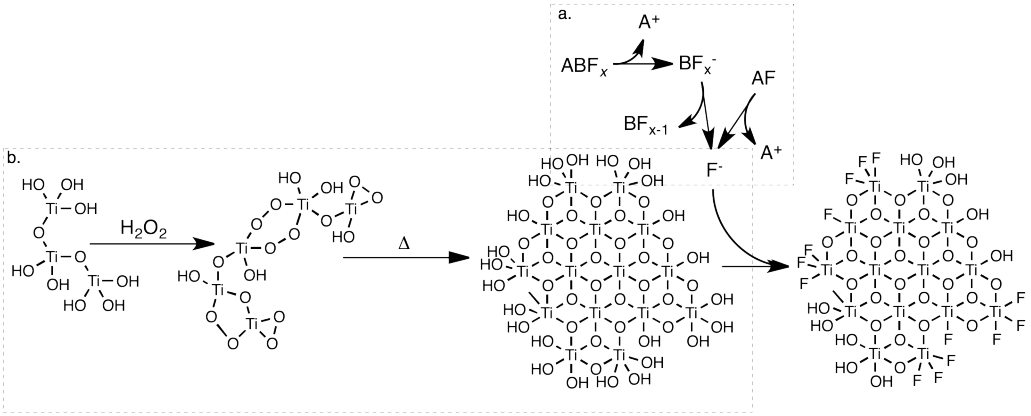


**Figure 5.24.** A proposed mechanism for the formation of fluoride-modified $TiO_2$ in solution. $F^-$ is formed by the dissolution (and hydrolysis) of fluoride salts (a), while nuclei of titanium dioxide simultaneously form by the breakdown of peroxotitanic acid (b). $F^-$ will then chemisorb to the surface of titanium dioxide, dictating its growth.

The presence of rutile and brookite in some materials suggests that during the initial stage of titania formation there is insufficient free fluoride present in solution to ensure complete anatase formation. Non-anatase content appears to increase as anion and cation mass increase. This suggests that $PF_6^-$ decays at a slower rate than $BF_4^-$, and that the presence of $NBu_4^+$ as a cation similarly retards the rate of decay.

## *5.4 Conclusion*

Titanium dioxide nanoparticles were synthesised by thermal degradation of peroxotitanic acid in the presence of a number of non-toxic, fluoride-containing, surface-modifying agents (SMAs). The chemical nature of both the anion and cation comprising each SMA affects the properties of the synthesised titania. Overall, the particles were highly crystalline with a high $Ti^{3+}$ population and residual Ti−F species at the surface. Additional fluoride-containing species were observed on the surface of the particles: treatment with KOH solution was found to remove these species, chemisorbed Ti−F proved surprisingly resistant to removal *via* this method.

The choice of SMA was found to influence particle shape and size. $F^-$-

and $BF_4^-$-containing SMAs resulted in the formation of monodisperse, ovoid nanoparticles with exposed (010) and (101) faces, while $PF_6^-$-containing SMAs systematically favoured formation of much smaller $TiO_2$ particles, resulting in an increased surface area.

Synchrotron XPS and NEXAFS studies provide the first evidence that *surface-bound* $Ti^{3+}$ content can be systematically controlled by the choice of SMA. These techniques also reveal two novel trends on the effect of both cations and anions on the abundance of $Ti^{3+}$ (*i.e.* $F^- > BF_4- > PF_6^-$; $NBu_4^+ > NH_4^+$). We expect that these properties will lead to increased visible-light activity for the materials due to the creation of intra-band energy levels.

# Chapter VI

# Modification of titanium dioxide by fluoride-containing carboxylic acids

## *6.1 Introduction*

It has been known for some time that acetic acid will readily bind to titanium or its oxide in solution, replacing hydroxy groups on the particle surface,[121–123] but it was the work of Livage *et al.* in 1987 that pioneered its use in titania synthesis.[252] They found that acetic acid will readily chelate to the titanium centre, displacing alkoxy groups (*e.g.* O$^i$Pr, OEt, OMe: Scheme 6.1) and forming a stable compound that resisted hydrolysis, in stark comparison to unmodified titanium alkoxides.[253] This paved the way for further work exploring the synthesis of titanium dioxide using acetic acid[125,129,254–267] as well as other carboxylic acids,[126,127,268–271] as surface modifying agents (SMAs).

While early work focussed on the use of acetic acid, a number of more recent papers[130,272] have followed the work of Weller *et al.* , who in 2003 reported the synthesis of $TiO_2$ using oleic acid as a surface modifying agent,[126] demonstrating that longer-chain carboxylic acids are viable candidates for $TiO_2$ surface modification. The passivating effect of oleic acid can be seen in the requirement for heat treatment of the titanium-oleic acid mixture at

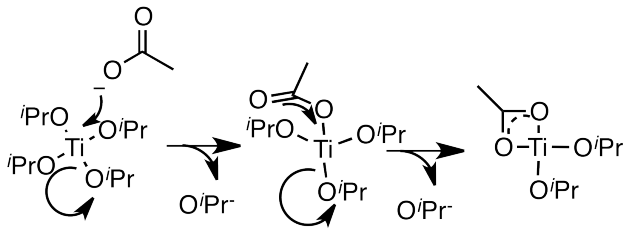


**Scheme 6.1.** Acetic acid will readily form a stable, bidentate bond with titanium.

80°C, and the use of amine to further catalyse the reaction: even under optimal conditions, titanium dioxide particle formation took place on the order of hours, rather than seconds or minutes. Meanwhile, Li and coworkers showed that it was possible to synthesise anatase titania using linoleic acid as an SMA.[127] Of note, they found that the same technique *failed* to give a product when linoleic acid was substituted for valeric or acetic acid, although they did not provide a mechanistic reason why short-chain carboxylic acids would prevent particle formation in this case. Regardless, their findings demonstrated that the chain length of carboxylic acid SMAs plays an important role in the synthesis of $TiO_2$.

It has previously been shown that fluoride-containing alcohols coordinated to titanium through the ROH group may chelate through a weak fluoride-titanium bond.[273] The extent to which this occurs depends on how easily the fluorine can find itself in a coordinating position. While this behaviour has been generalised to include any neutral Lewis base,[132,274] fluorine-containing alcohols tend to be more electron-withdrawing in nature: thus a fluoroalcohol binding through the ROH group withdraws electron density from the Ti centre of the particle, which in turn provides a more attractive target for the chelating F centre.

While this phenomenon has been explored for a number of chelating ligands (including chloroacetic acids[275]), to our knowledge there has been no attempt to synthesise titanium dioxide in the presence of fluorine-containing carboxylic acids. It is expected that the carboxyl group of these SMAs would bind strongly to titania as usual, but the fluoride-modified "tail" of the acid may also provide a chelating effect, thus altering the behaviour of the SMA and possibly the nature of the resultant $TiO_2$ nanomaterials. It is important that the effect of tail length is also studied, as a longer fluorine-containing tail may allow for greater SMA flexibility and more effective coordination to the particle surface.

In this chapter, we investigated the effect of a number of fluorine-containing carboxylic acids on the properties of $TiO_2$ synthesised in their presence. These carboxylic acid surface modifying agents (SMAs) included acetic acid, its di- and trifluoro-substituted analogues, and three long-chain perfluorinated carboxylic acids: perfluorobutyric acid (PFBA), perfluoropentanoic

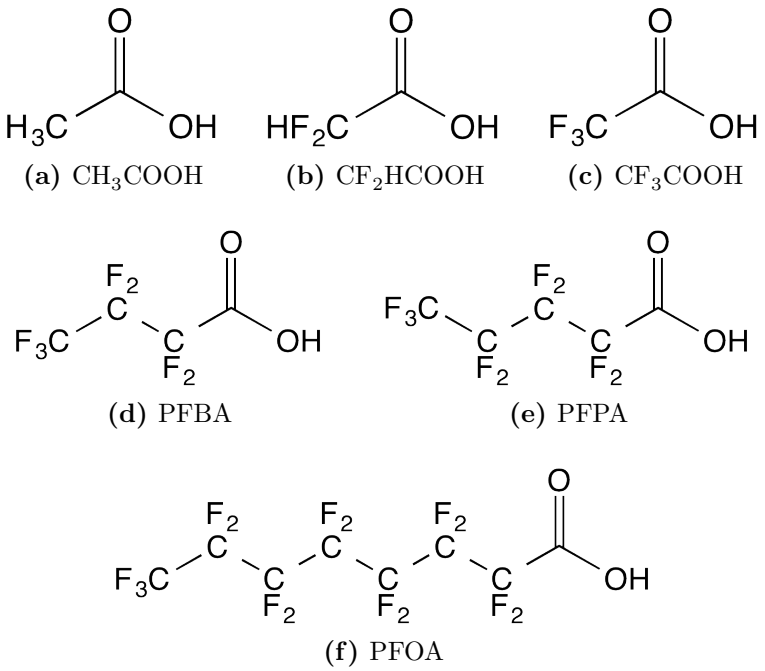


**Figure 6.1.** The surface modifying agents used in this chapter.

acid (PFPA), and perfluorooctanoic acid (PFOA) (Figure 6.1). In addition, two different synthetic methods were trialled. In the standard method (similar to that outlined in Chapter 5), amorphous titanium dioxide was first formed by hydrolysis of titanium isopropoxide prior to SMA addition. In the direct-addition method, SMA was added directly to titanium isopropoxide, allowing the formation of the titanium carboxylate complex prior to initial nucleation.

The effect of these variables was studied by X-ray diffraction (XRD), scanning electron microscopy (SEM), dynamic light scattering (DLS), and zeta potential measurements. Using these techniques it was possible to determine the phase, size, shape, and surface charge of the particles, and from these infer how SMA type and addition method affects the outcome of th synthesis.

## *6.2 Experimental*

Titanium *tert*-isopropoxide ($\geq$ 98%, Acros), acetic acid (99.8%, BDH), difluoroacetic acid (95%, Aldrich), trifluoroacetic acid (95%, Aldrich), perfluorbutyric acid (99%, Acros), perfluorpentanoic acid (97%, Acros), and perfluorooctanoic acid (96%, Aldrich) were all used as supplied.

Carboxylic acid-modified titanium dioxide particles were synthesised through one of two different methods.

In the first method (referred to as the "standard" method), titanium *tert*-isopropoxide (1.78 g, 6.26 mmol) was added to EtOH (5 mL) with stirring, followed by distilled water (25 mL). Upon addition of water, the solution rapidly changed colour to opaque white as amorphous titanium dioxide was formed. The mixture was stirred rapidly for ten minutes, and then centrifuged to remove solvent. The precipitate was washed twice with distilled water before being redispersed in distilled water (50 mL) in a 250 mL round-bottom flask. To this was added carboxylic acid in a 1:1 molar ratio with the titanium (assuming no losses during hydrolysis and washing), followed by hydrogen peroxide (4.26 g of 50% w/w solution, 62.6 mmol). Due to the acidic nature of the SMA, the solution tended to turn a deep orange-red colour, which has been previously observed for the formation of peroxotitanic acid at low pH.[276,277] The solution was stirred for one hour and then heated under reflux for 24 hours. Following this, the solution was cooled to room temperature, andthe precipitate was recovered by centrifugation and washed three times with distilled water. Finally, the powder was washed with methanol and dried under reduced pressure in a vacuum dessicator. Particles synthesised using the standard addition method will be referred to in the text as $sTiO_2$.

In the second method (referred to as the "direct addition" method), titanium *tert*-isopropoxide (1.78 g, 6.26 mmol) was added to a solution of anhydrous isopropanol (5 mL) and carboxylic acid (6.26 mmol). Following this, a solution of hydrogen peroxide (4.26 g of 50% w/w solution, 62.6 mmol) in distilled water (50 mL) was added with stirring. The mixture turned red, again indicative of the formation of peroxotitanic acid in acidic solution. After stirring for an hour, the solution was heated under reflux for 24 hours.

Following this, the precipitate was cooled, recovered, washed and dried as for the standard method of synthesis. Particles synthesised using the direct addition method will be referred to in the text as $dTiO_2$.

Samples were analysed by powder X-ray diffraction using an Agilent SuperNova X-ray diffractometer with a Cu $K_\alpha$ source, as well as scanning electron microscopy using a JEOL 7000F FE-SEM and DLS using a Microtrack Zetatrack light scattering instrument. For further details of instrument setup, see Chapter 3. Scherrer particle sizing was performed using XRD information, however these data have not been corrected for instrumental broadening. This means that reported absolute crystal sizes will be smaller than actual crystallite sizes; this data has been reported here as a means of comparing *relative* crystallite sizes.

## *6.3 Results*

### *6.3.1 Standard method*

PXRD analysis of samples is shown in Figure 6.3. $CH_3COOH{-}sTiO_2$ is observed to be a mixture of anatase and rutile titania. By application of Spurr's equation[158] to the peaks (fitted using a pseudo-Voigt distribution, Table 6.1) it was found that $CH_3COOH{-}sTiO_2$ was made up of approximately 82% anatase and 18% rutile material. This is in contrast with $TiO_2$ synthesised in the absence of SMA, which was only 29% anatase. $CH_3COOH$ has previously been reported in the literature to preferentially encourage the formation of anatase over rutile.[128] The use of fluoride-modified SMAs favoured the synthesis of rutile, which is presumed to be due to their more acidic nature.[278] Trace amounts of anatase are observed for $CF_2HCOOH{-}sTiO_2$ and $PFBA{-}sTiO_2$, but not for $CF_3COOH{-}sTiO_2$ or $PFOA{-}sTiO_2$. Additionally, $PFBA{-}sTiO_2$ exhibited a broad peak at $Q \approx 0.9\text{Å}^{-1}$ (removed in Figure 6.3 due to baseline fitting, see Figure 6.4 for comparison of raw data), indicative of a considerable fraction of amorphous material (presumed to be either residual SMA or titania).[126] Unfortunately, the fraction of amorphous material could not be estimated.

Scherrer crystallite sizing was performed on all samples, however these measurements have not been corrected for instrumental broadening, which

**Table 6.1.** Percentage phases of $sTiO_2$ synthesised using carboxylic acid SMAs. "None" indicates no SMA was used.

| SMA | % Anatase | % Rutile | $pK_a$ |
|---|---|---|---|
| None | 29 | 71 | - |
| $CH_3COOH$ | 82 | 18 | 4.76 |
| $CF_2HCOOH$ | 7 | 93 | $1.2^{279}$ |
| $CF_3COOH$ | - | 100 | $-0.3^{279}$ |
| PFBA | 7 | 93 | 0.4* |
| PFPA | - | 100 | Unknown |
| PFOA | - | 100 | $1.01–3.8^{280}$ |

* Based on SPARC theoretical $pK_a$[279]

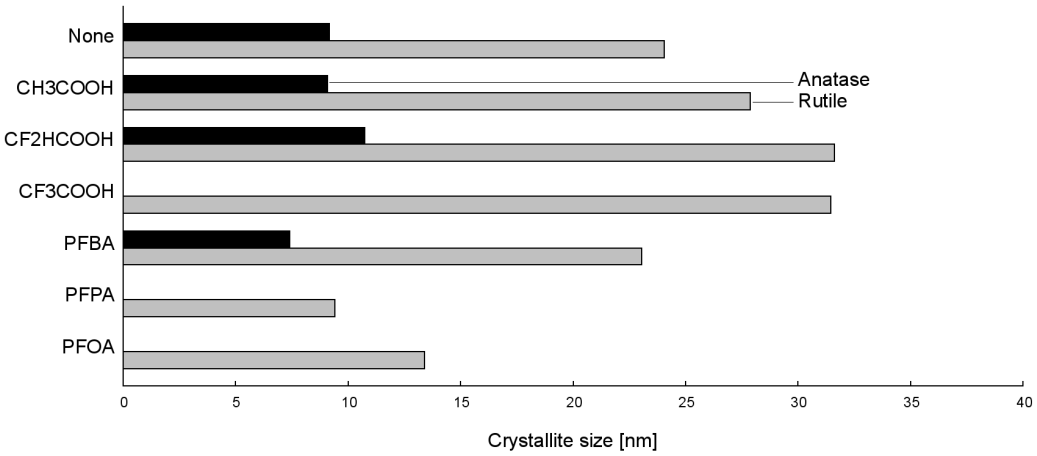


**Figure 6.2.** Scherrer crystallite sizes for $sTiO_2$ materials.

is assumed to be constant over all samples. Scherrer crystal sizes are reported in Figure 6.2. It can be seen that while the addition of acetic acid affects the relative proportions of anatase and rutile synthesised, it has little effect on the crystallite size, slightly encouraging rutile growth. In comparison, larger anatase and rutile particles were obtained when $CF_2HCOOH$ and $CF_3COOH$ were used as SMAs. Longer-chain acids have less of an obvious effect on crystallite size, although PFPA and PFOA both appear to limit crystal growth.

Representative SEM images of samples are shown in Figure 6.5. Particle sizing was performed on at least 200 particles, and particle sizes are shown

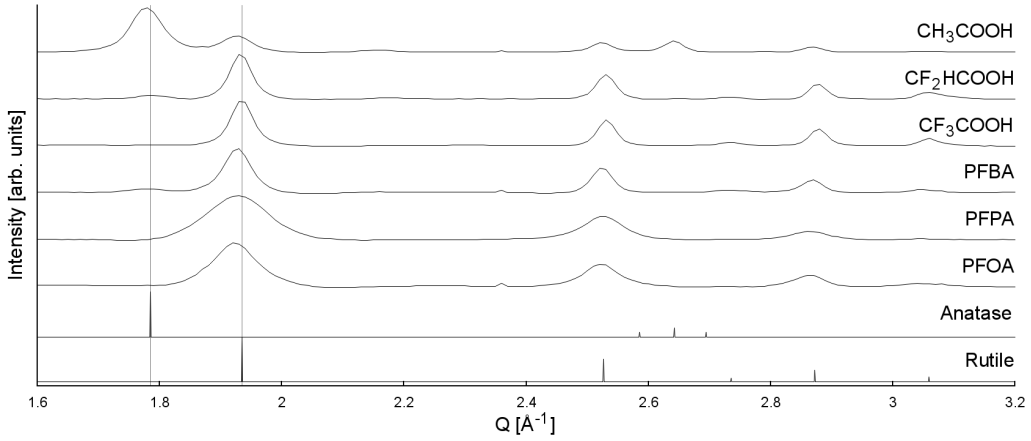


**Figure 6.3.** PXRD for $sTiO_2$ synthesised using carboxylic acid SMAs, alongside theoretical peak positions for anatase and rutile $TiO_2$.

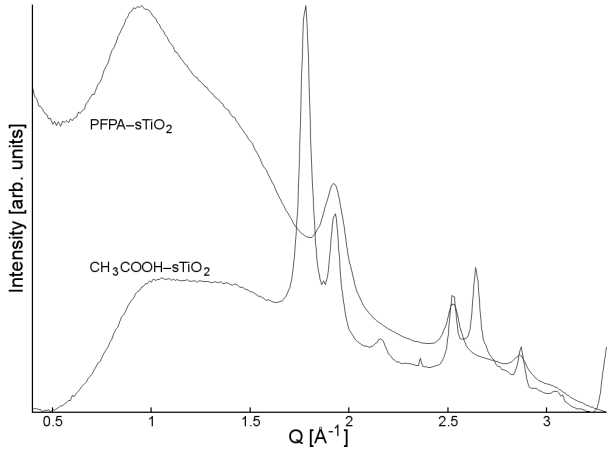


**Figure 6.4.** Comparison of PXRD raw peaks of PFPA−$sTiO_2$ and $CF_3COOH$−$sTiO_2$. The broad peak at $Q = 0.9\text{Å}^{-1}$ is caused by scattering from amorphous material.

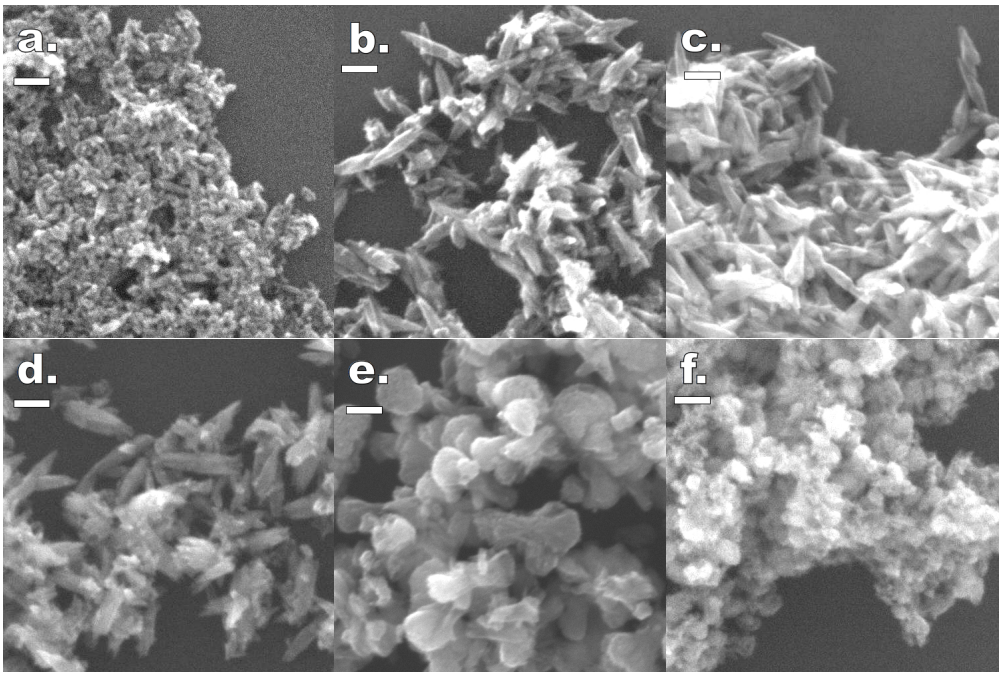


**Figure 6.5.** SEM images of $sTiO_2$ modified with $CH_3COOH$ (a), $CF_2HCOOH$ (b), $CF_3COOH$ (c), PFBA (d), PFPA (e) and PFOA (f). Scale bars correspond to 100 nm.

in Figure 6.6.

$CH_3COOH{-}sTiO_2$ forms small, somewhat elongated particles with an anisotropy ($d_{min}/d_{max}$) of 0.40 ($\pm$ 0.19). Substituting this SMA for a fluorinated equivalent (either $CF_2HCOOH$ or $CF_3COOH$) results in significantly larger, more elongated particles (anisotropy is 0.25 $\pm$ 0.14 for $CF_2HCOOH{-}sTiO_2$, 0.23 $\pm$ 0.10 for $CF_3COOH{-}sTiO_2$). The use of $CF_3COOH$ results in slightly more needle-like (*i.e.* more anisotropic) particles, and while the largest observed $CF_3COOH{-}sTiO_2$ particles are larger than any for $CF_2HCOOH{-}sTiO_2$, the very similar median and interquartile range values suggest that differences in particle major axis diameter are minimal between the two products.

Perfluorobutyric acid (PFBA), with a fluoride tail considerably longer than that of trifluoroacetic acid, appears to give a similar product to those obtained using fluorinated acetic acids. PFOA-modified $sTiO_2$ is rutile, much like $PFBA{-}sTiO_2$, however, the particles are considerably smaller and some-

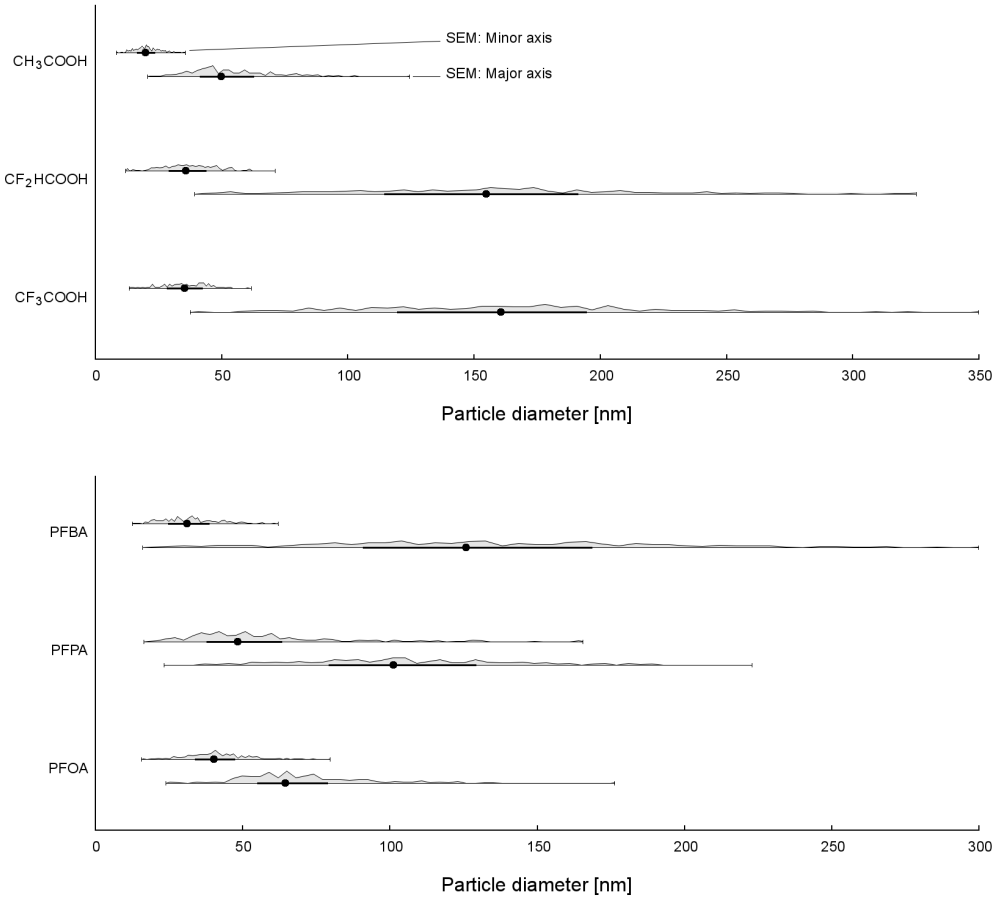


**Figure 6.6.** Dimensions of surface-modified $sTiO_2$, determined by SEM particle sizing. Circle shows median value, thick line shows upper and lower quartile, while thin lines show entire range. Relative frequency is shown as area plots.

what less needle-like than other crystalline materials reported here. However, PFPA−$sTiO_2$ appears drastically different to other materials under SEM, appearing to consist of quasi-spherical particles of diameter $\sim$ 70 nm. This sample also showed significant amorphous material under PXRD, and it may be that the presence of excessive SMA causes the structure observed under SEM. It is unknown why PFPA demonstrates such behaviour as an SMA, while PFOA and PFBA do not.

By examining $CF_3COOH$−$sTiO_2$, PFBA−$sTiO_2$ and PFOA−$sTiO_2$, one can observe that longer tail length is possibly linked to loss of control over particle size and morphology. This can also be seen by comparison of particle sizing data in Figure 6.6, particularly in the range of both minor and major axis diameter. It may be that longer-chain perfluorinated carboxylic acids form a micellar system, due to their long hydrophobic tails combined with their hydrophilic carboxylic heads. Such phenomena have previously been observed for long-tail carboxylic acids in water.[126] Formation of a micellar system would drastically change the shape of the $TiO_2$ particles synthesised within it, and this would explain why we see such a drastic change in particle morphology when PFBA and PFOA are used as SMAs. Alternatively, as tail length increases, steric effects may prevent a high concentration of SMA at the particle surface, limiting its ability to affect particle size.[281]

Dynamic light scattering (DLS) was performed on samples dispersed in water to determine their average hydrodynamic radius, and to confirm the above SEM particle sizing measurements (see Figure 6.7). A number of samples were found to aggregate readily in water, as evidenced by considerably larger particle size than was found by SEM particle counting and by a large deviation in particle sizes. $CH_3COOH$−$sTiO_2$, as well as all long-chain carboxylic acid samples, showed considerable aggregation in water, even at very low concentrations. In contrast, $CF_2HCOOH$−$sTiO_2$ and $CF_3HCOOH$−$sTiO_2$ show considerably narrower size distributions centred between the median minor and major axis diameters, indicative of well-dispersed particles in solution.

The zeta potentials of $sTiO_2$ materials are shown in Figure 6.8. Also shown is the zeta potential for titanium dioxide synthesised by the standard method in the absence of SMA. $CH_3COOH$−$sTiO_2$ has a zeta potential close

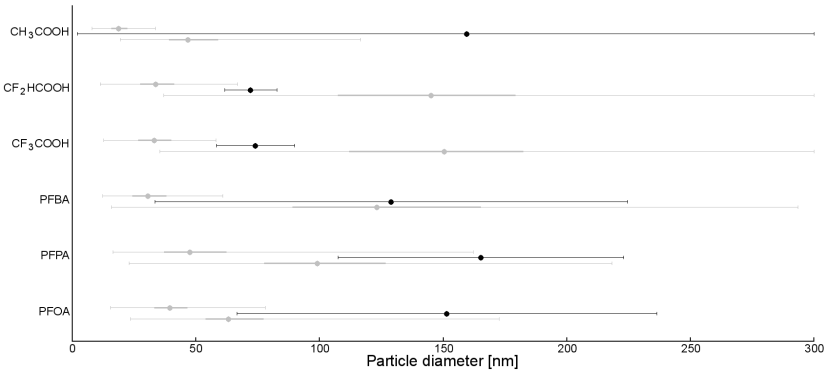


**Figure 6.7.** Dynamic light scattering (DLS) particle sizing data for surface-modified $sTiO_2$. In grey, SEM particle sizing data for the same materials. For DLS, the point indicates the number mean particle diameter and the error bars indicate one standard deviation. For SEM data, the point indicates the median value, the thick line the inter-quartile range, and the error bars the range of values.

to zero, which explains the extensive aggregation observed during DLS. This is attributed to the presence of negatively-charged acetate ions on the surface of the material. The use of di- and trifluoroacetic acid as SMA results in a material with a zeta potential much closer to that of unmodified titania: this suggests that the negative charge of the surface fluoroacetate ions is somehow negated.

A similar effect is observed for PFBA-modified $sTiO_2$, however PFPA$-sTiO_2$ shows a considerable negative zeta potential, indicative of negative charge on the surface of the particle. This is consistent with previous observations that PFPA$-sTiO_2$ appears to maintain a thick layer of SMA on its surface. Disregarding this data point, the progression of zeta potentials for $CH_3COOH-sTiO_2$, PFBA$-sTiO_2$, and PFOA$-sTiO_2$ suggests that for perfluorinated carboxylic acid SMAs, surface charge decreases with increasing tail length.

### *6.3.2 Direct addition method*

By addition of titanium isopropoxide to acetic acid prior to hydrolysis, the complex $Ti(O^iPr)_{4-x}(OAc)_x$ is allowed to form.[124,252] This complex is more stable than titanium isopropoxide, and hydrolysis will thus proceed at a much slower pace, even bound up in the peroxotitanic acid gel. The slower

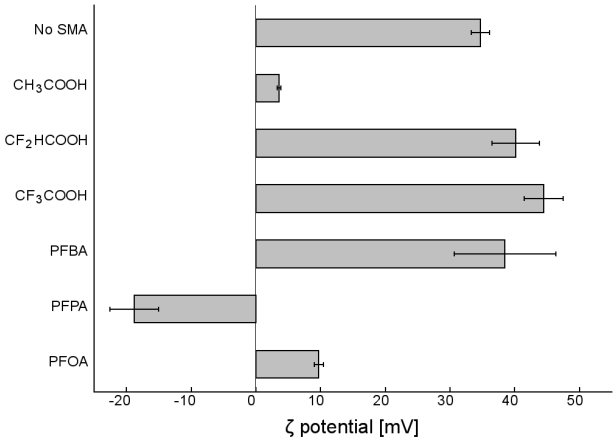


**Figure 6.8.** Zeta potential measurements for carboxylic acid-modified $sTiO_2$. Error bars show 95% C.I.

rate of hydrolysis allows for greater control over the synthesis of the titania particles, and it is expected that the formation of such species will alter the shape, size, and/or phase of the resultant particles. The proposed schematic mechanism of synthesis, showing various stages of the synthetic process for both direct and standard methods, is shown in Scheme 6.2.

Of particular interest, NMR studies (in $CDCl_3$) of the material obtained from the mixture of a 1:1 ratio of titanium alkoxide and acetic acid demonstrate that under such conditions, the complex $Ti(OR)_2OAc$ (with acetate acting as a bidentate ligand) is formed, rather than a mixture of unsubstituted, monosubstituted and disubstituted titanium alkoxide.[128,256]

PXRD analysis of $dTiO_2$ samples is shown in Figure 6.10, with phase fractions tabulated in Table 6.2. $CH_3COOH{-}dTiO_2$ exhibits considerably less anatase than the equivalent $sTiO_2$. This is counter to what has previously been reported by Chang *et al.*,[129] who observed almost entirely anatase from a similar method and cited the retardation of hydrolysis as the cause. In the cited study, a molar acid:titanium ratio of 3:1 was used, and it may be that a 1:1 ratio as used here is insufficient to achieve this effect.

Scherrer particle sizing on $dTiO_2$ materials, compared to equivalent studies for $sTiO_2$, are shown in Figure 6.9. It is generally observed that $dTiO_2$ crystals are slightly larger than their $sTiO_2$ counterparts: this trend is par-

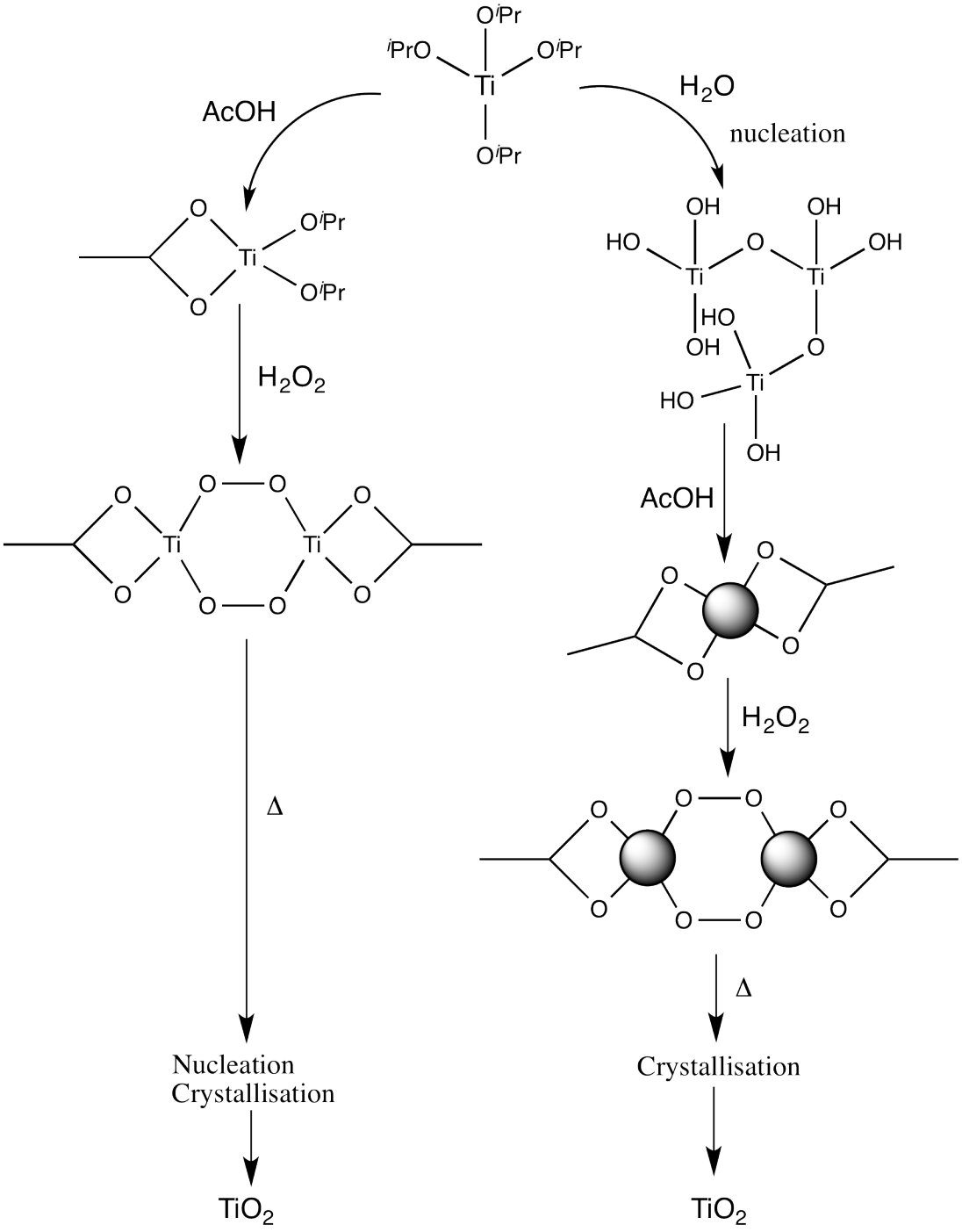


**Scheme 6.2.** An outline of the synthetic process, following both the direct addition (left) and standard (right) synthetic methods. Using the standard method, nucleation occurs rapidly after the addition of water, producing small, amorphous particles (shown here as grey spheres). Under the direct addition method, nucleation only occurs after hydrogen peroxide addition, in the heating stage.

**Table 6.2.** Percentage phases of $dTiO_2$ synthesised using carboxylic acid SMAs.

| SMA | % Anatase | % Rutile | $pK_a$ |
|---|---|---|---|
| $CH_3COOH$ | 40 | 60 | 4.76 |
| $CF_2HCOOH$ | 15 | 85 | $1.2^{279}$ |
| $CF_3COOH$ | 10 | 90 | $-0.3^{279}$ |
| PFBA | 0 | 100 | 0.4* |
| PFPA | 0 | 100 | Unknown |
| PFOA | 0 | 100 | $1.01–3.8^{280}$ |

* Based on SPARC theoretical $pK_a$ [279]

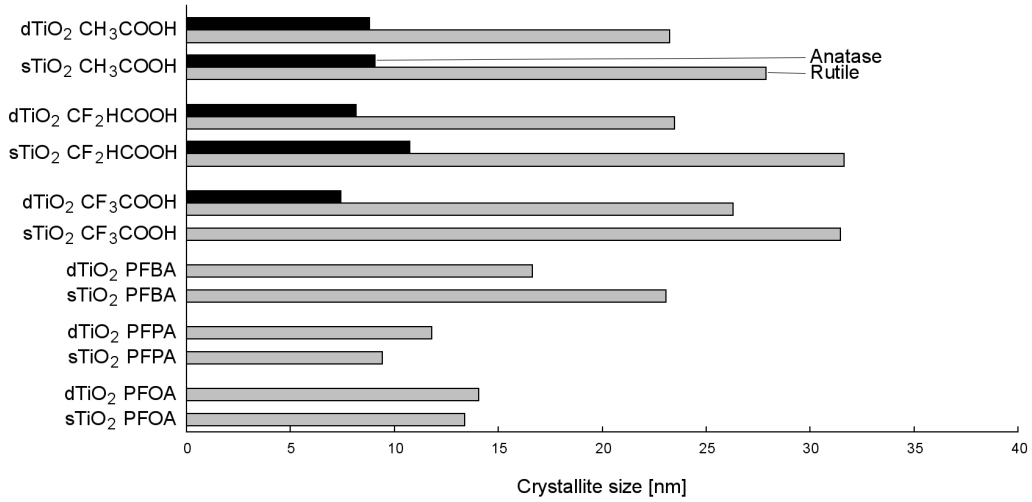


**Figure 6.9.** Scherrer crystallite sizes for $dTiO_2$ materials. Equivalent $sTiO_2$ materials are included as a comparison.

ticularly noticeable for $CF_2HCOOH$-, $CF_3COOH$-, and PFBA- modified materials. PFPA- and PFOA-modified materials both exhibit smaller crystallite sizes than equivalent $sTiO_2$ materials.

It is interesting that $CH_3COOH$–$sTiO_2$ (synthesised *via* the standard method) produces a much higher fraction of anatase than $CH_3COOH$–$dTiO_2$. Given the assertion in the literature[127,128,130,257] that acetic acid tends to encourage the formation of anatase $TiO_2$, this suggests that the effect of $CH_3COOH$ is somehow lessened in the case of the direct addition method. One reason for this could be the time of addition and the availability of Ti centres. If amorphous $TiO_2$ is allowed to form before SMA is added, the

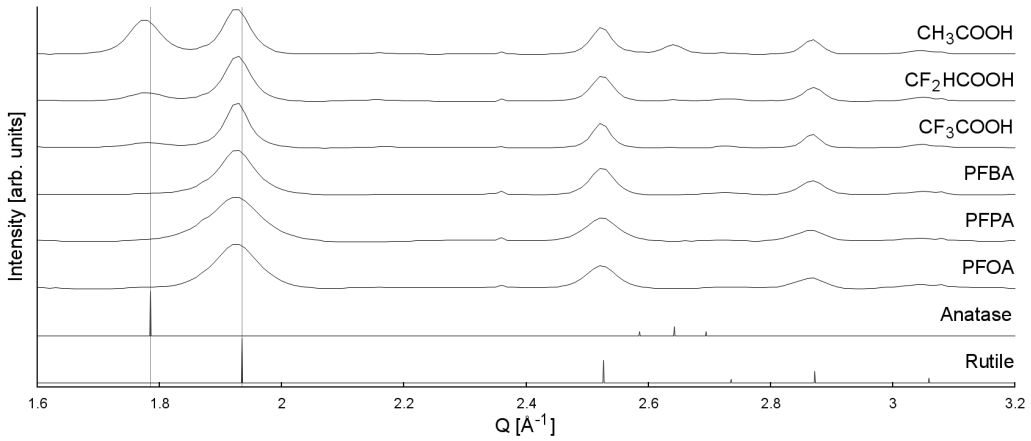


**Figure 6.10.** PXRD for $dTiO_2$ synthesised using carboxylic acid SMAs, alongside theoretical peak positions for anatase and rutile $TiO_2$.

majority of Ti will be in sub-surface positions on the particles, and inaccessible to SMA. As a result, the apparent SMA:Ti ratio will be much higher than 1:1. In the case of direct addition, SMA is added to titanium alkoxide solution prior to particle formation, and as a result the apparent SMA:Ti ratio is 1:1.

A small but significant anatase fraction is present in both $CF_2HCOOH$- and $CF_3COOH$-modified $dTiO_2$. Contrary to what was observed for $CH_3COOH$, in this case the direct method appears to *promote* the formation of anatase. This may be due to increased Ti-SMA binding affinity, a result of the strongly acidic nature of these fluorine-modified acetic acids.

No anatase phase is observed for $dTiO_2$ modified by long-chain perfluorinated carboxylic acids. Use of PFBA, PFPA and PFOA as SMAs in the direct method results in all cases in effectively pure rutile. Since the $pK_a$ of these acids decreases as chain length increases,[279] it may be that the decreasing pH of the solution overrides any influence of the coordinating carboxylate group on particle crystallinity.

SEM images of $dTiO_2$ materials are shown in Figure 6.11, and detailed particle sizing and morphology analysis based on SEM images (at least 200 particles observed; compared against SEM particle sizing data for $sTiO_2$) are shown in Figure 6.12.

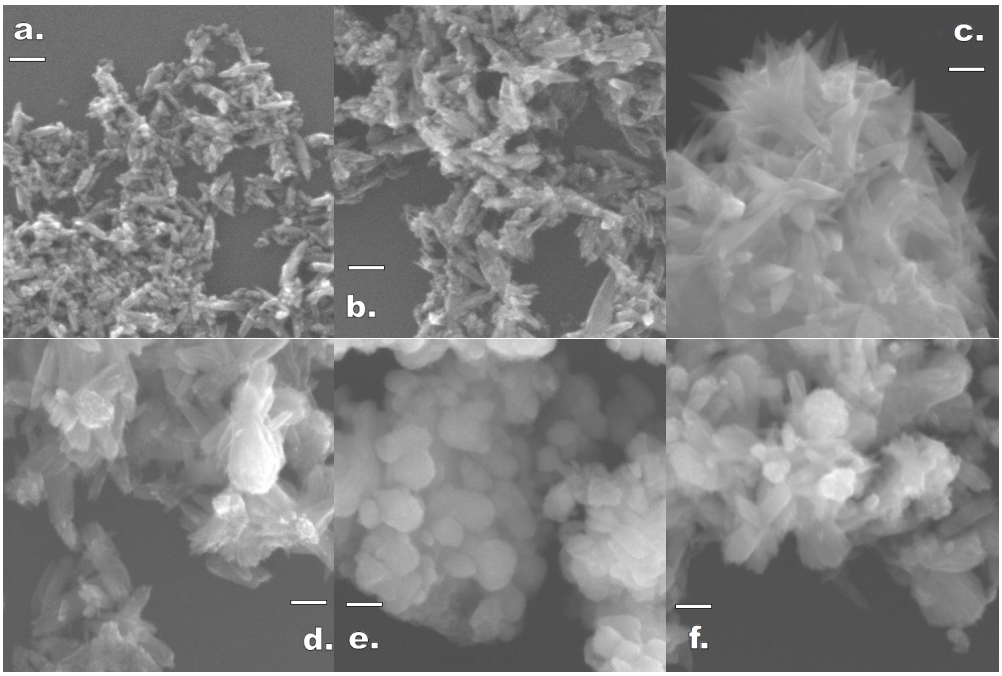


**Figure 6.11.** SEM images of $dTiO_2$ modified with $CH_3COOH$ (a), $CF_2HCOOH$ (b), $CF_3COOH$ (c), PFBA (d), PFPA (e) and PFOA (f). Scale bars correspond to 100 nm.

$CH_3COOH{-}dTiO_2$ appears larger and more polydisperse than $CH_3COOH{-}sTiO_2$. The difference in size may be due to the different methods of nucleation of the two synthetic methods. In the standard method, initial nucleation occurs when titanium isopropoxide is added to water, with rapid hydrolysis producing numerous $Ti(OH)_4$ centres. In comparison, the formation of $Ti(OAc)_x(O^iPr)_y$ centre by direct addition of acetic acid limits hydrolysis, and as a result nucleation "shifts" to the breakdown of the peroxotitanic acid sol. This breakdown and subsequent nucleation occur much more slowly, and less centres of nucleation will form as a result. With less nucleation centres, individual particles will be larger. $CH_3COOH{-}dTiO_2$ is also considerably more anisotropic than $CH_3COOH{-}sTiO_2$: this is likely due to the larger proportion of rutile, which preferentially forms needle-like shapes.[238]

Choice of synthetic method appears to have little effect on the size of $CF_2HCOOH{-}TiO_2$ and $CF_3COOH{-}TiO_2$ particles. In contrast, the influ-

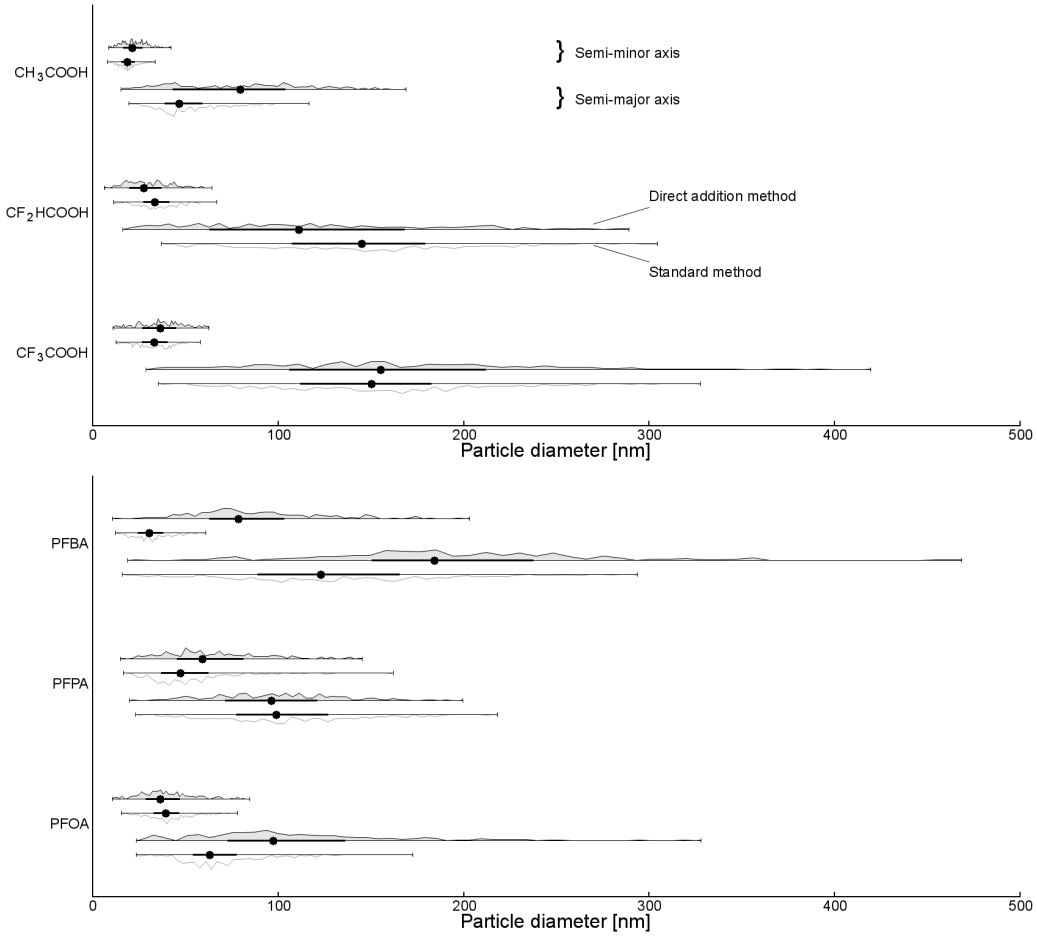


**Figure 6.12.** SEM particle sizing comparison of $sTiO_2$ and $dTiO_2$. Circle shows median value, thick lines show upper and lower quartile, and thin lines show entire range. Relative frequency is shown as area plots.

ence of long-chain perfluorinated carboxylic acids appears dependent on addition order. PFBA−$dTiO_2$ appears to lose some of its characteristic shape as compared to PFBA−$sTiO_2$, resulting in polydisperse, less well-shaped particles. This can be seen in the increase in particle's diameter, particularly the minor axis, which is also considerably more polydisperse under the direct-addition regime. While PFPA−$TiO_2$ seems largely unaffected by the direct addition method (suggesting that SMA remains in this sample as it does for PFPA−$sTiO_2$), PFOA−$TiO_2$ appears much less uniform when synthesised by direct addition. These results are consistent with those reported previously in this chapter on powder X-ray diffraction data, *i.e.* that the direct addition method of synthesis tends to offer less control over the final phase and size of the material.

DLS particle sizing data are shown in Figure 6.13, and zeta potential data in Figure 6.14. DLS measurements for $CH_3COOH$−$dTiO_2$ suggest that less aggregation occurs for this sample than for $CH_3COOH$−$sTiO_2$, although the zeta potential for $CH_3COOH$−$dTiO_2$ is only slightly more positive. DLS data for $CF_2HCOOH$−$dTiO_2$ and $CF_3COOH$−$dTiO_2$ are larger than expected based on SEM particle sizing, suggesting either that aggregation occurs or that median SEM particle size is somewhat smaller than the actual median particle size. While PFBA−$dTiO_2$ shows little evidence of aggregation, it appears that PFPA− and PFOA−$dTiO_2$ both suffer aggregation in solution, which may be related to the size and long tail of the SMA.

All fluoride surface-modified $dTiO_2$ materials (except for PFOA−$dTiO_2$) consistently exhibit zeta potentials of around 10 mV. This is in contrast to $sTiO_2$ materials, which displayed zeta potentials approaching 40 mV, and suggests either that any charge neutralisation mechanisms as discussed earlier are inhibited, or that less SMA ends up on the surface of the particles. PFOA−$dTiO_2$ displays a slightly negative zeta potential, which is closer in character to PFPA−$sTiO_2$ than any other material reported in this study.

### *6.3.3 Reducing the SMA:Ti ratio*

Studies thus far have focussed on maintaining a 1:1 molar ratio of SMA to Ti. In order to investigate the effect of SMA concentration on $TiO_2$

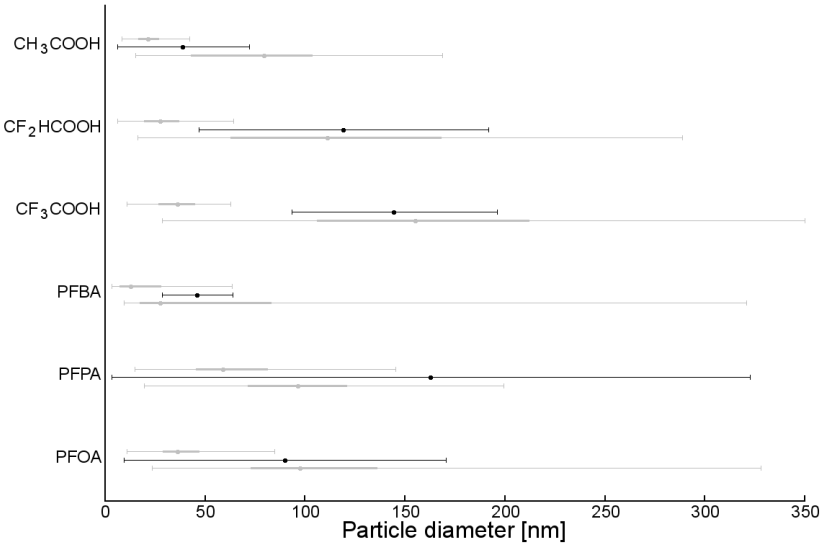


**Figure 6.13.** Dynamic light scattering (DLS) particle sizing data for surface-modified $dTiO_2$. In grey, SEM particle sizing data for the same materials. For DLS, the point indicates the number mean particle diameter and the error bars indicate one standard deviation. For SEM data, the point indicates the median value, the thick line the inter-quartile range, and the error bars the range of values.

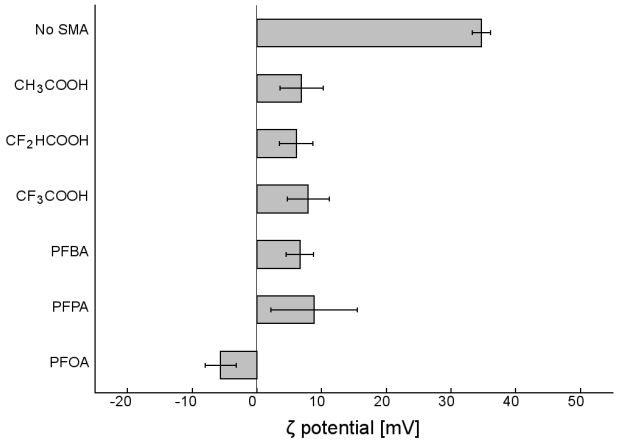


**Figure 6.14.** Zeta potential measurements for surface-modified $dTiO_2$. Error bars show 95% C.I.

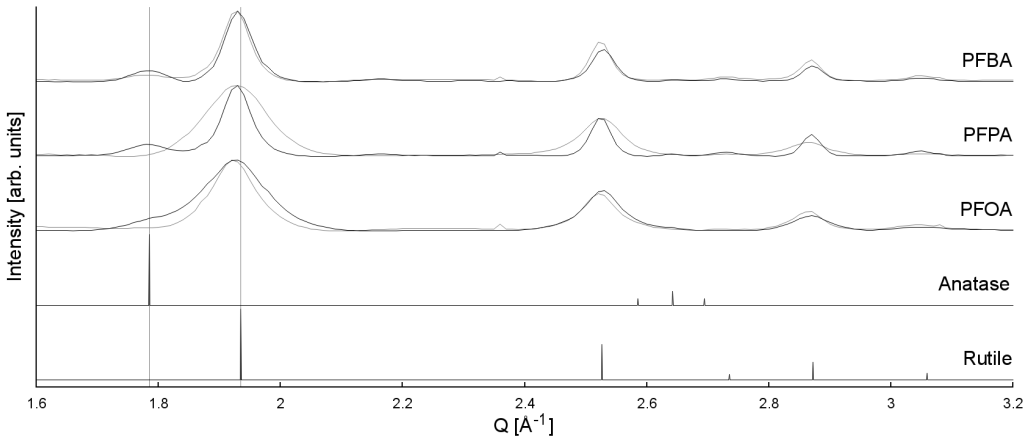


**Figure 6.15.** PXRD pattern for 0.1−$sTiO_2$. In grey, the PXRD pattern for $sTiO_2$ using a 1:1 SMA:Ti ratio.

**Table 6.3.** Phases of surface-modified 0.1−$sTiO_2$.

| SMA | % Anatase | % Rutile |
|---|---|---|
| PFBA | 11 | 89 |
| PFPA | 14 | 86 |
| PFOA | 6 | 94 |

phase, morphology, and size, three materials (PFBA−$TiO_2$, PFPA−$TiO_2$, and PFOA−$TiO_2$) were synthesised using the standard method with a SMA:Ti ratio of 0.1:1. These materials' phase, shape, size and surface charge were analysed by PXRD, SEM, DLS, and zeta-potential measurements. Materials synthesised in this method will be referred to as *e.g.* 0.1PFBA−$sTiO_2$ in the text.

PXRD patterns are shown in Figure 6.15, compared against those of $sTiO_2$ synthesised using a 1:1 molar ratio of SMA:Ti (phase compositions are shown in Table 6.3). 0.1−$sTiO_2$ samples show significantly higher anatase content than equivalent samples prepared using a 1:1 SMA:Ti ratio, indicating that the presence of fluoride-containing SMAs encourages the formation of rutile over anatase.

Analysis of Scherrer crystallite sizes (Figure 6.16) indicates that reducing the SMA concentration results in considerably larger rutile crystallites in the case of PFPA−$sTiO_2$ and slightly smaller rutile crystallites for PFOA−$TiO_2$,

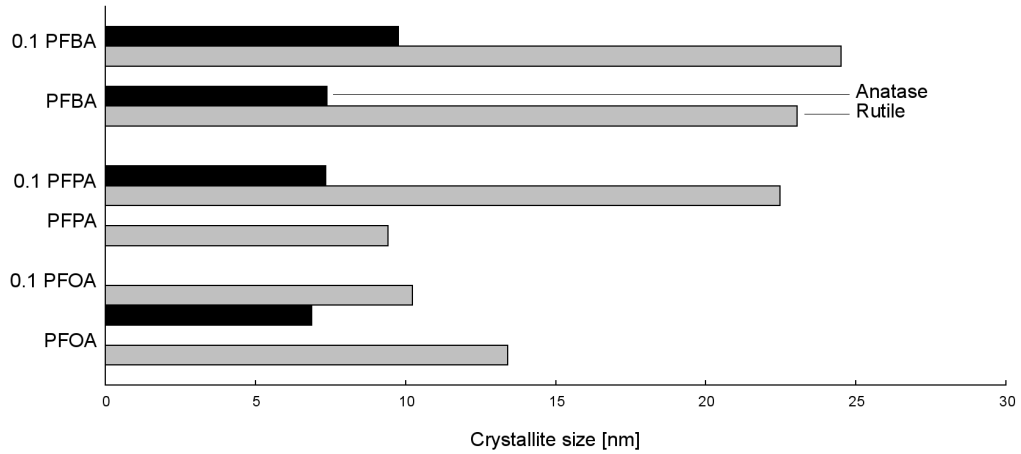


**Figure 6.16.** Scherrer crystallite sizes for 0.1−$sTiO_2$ materials. Equivalent $sTiO_2$ materials are included as a comparison.

while crystallite size stayed approximately constant for PFBA−$TiO_2$.

Representative SEM images are shown in Figure 6.17, and particle sizing analysis based on counting at least 200 particles from SEM images is shown in 6.18. All particles take on the familiar lozenge shape as has previously been shown in this chapter, although these samples seem somewhat more well-defined than their 1:1 counterparts. Of particular note, 0.1PFPA−$sTiO_2$ appears a more regular lozenge shape than the spherical particles reported for PFPA−$sTiO_2$: this adds further credence to the possibility that this phenomenon for PFPA−$sTiO_2$ and PFPA−$dTiO_2$ is due to the presence of excess SMA on the particle surface. Both 0.1PFBA− and 0.1PFPA−$sTiO_2$ appear much closer in shape to $CH_3COOH$−$sTiO_2$ than any other $sTiO_2$ products, which suggests that at the molar ratio of 0.1:1 the effect of SMA on particle shape is reduced considerably. 0.1PFOA−$sTiO_2$ resembles PFBA−$sTiO_2$, exhibiting long needles rather than the lozenges observed for other 0.1−$sTiO_2$ products. The greater $pK_a$ of this SMA may encourage growth of these particles even at lower SMA concentrations, explaining both particle shape and size under SEM and the above observations on PFOA−$sTiO_2$ crystallite size.

It can be seen that for 0.1PFBA− and 0.1PFPA−$TiO_2$ particle size decreases considerably as the amount of SMA decreases, while 0.1PFOA−$TiO_2$ becomes both longer and thinner. The combination of increasing crystallite

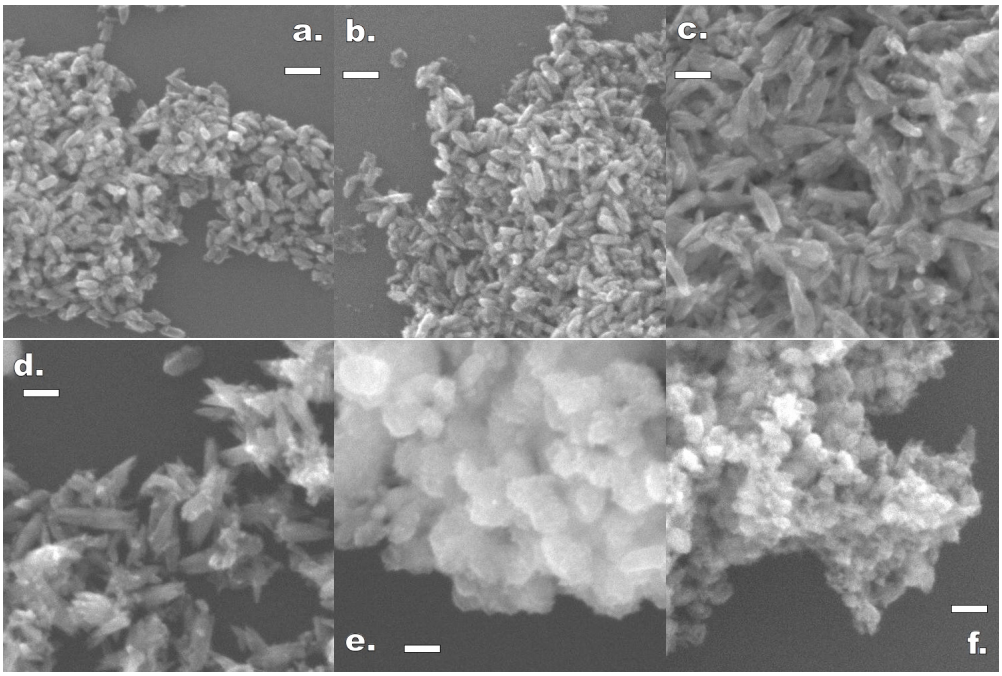


**Figure 6.17.** SEM images of $TiO_2$ synthesised by the standard method, modified by long-chain perfluorinated carboxylic acids using a 1:10 SMA:Ti ratio: (a) PFBA, (b) PFPA, (c) PFOA. Shown for comparison are equivalent material synthesised using a 1:1 SMA:Ti ratio: (d) PFBA, (e) PFPA, (c) PFOA. Scale bars correspond to 100 nm.

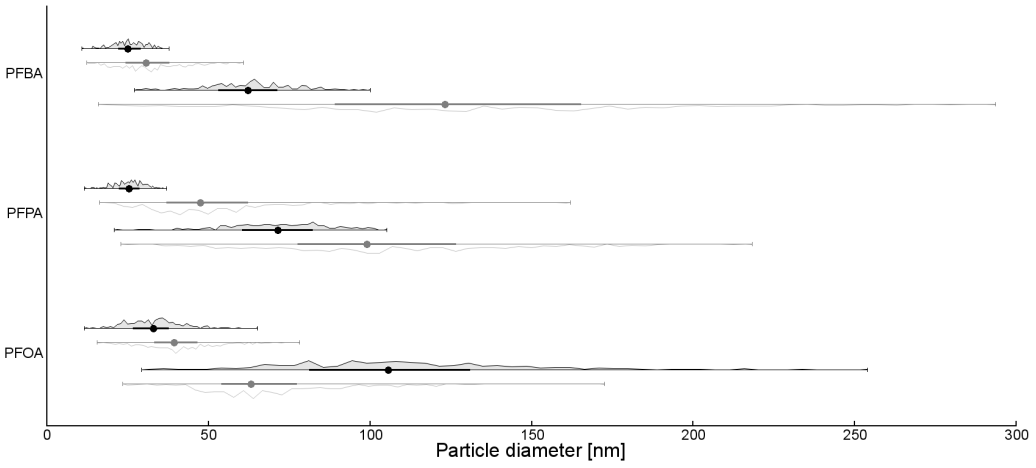


**Figure 6.18.** SEM particle sizing for surface-modified 0.1−$sTiO_2$. Circle shows median value, thick line shows upper and lower quartile, while thin lines show entire range. Relative frequency is shown as area plots. Data is compared against that for 1:1 SMA:Ti $sTiO_2$ (in grey).

size and decreasing particle size (as determined by PXRD and SEM/DLS respectively) for 0.1PFPA−s$TiO_2$ suggest that the nature of this material has changed significantly from a spherical or irregular polycrystalline aggregate to a more well-controlled monocrystalline lozenge shape. This further suggests that an excess of long-chain fluorinated SMA is actually detrimental to the synthesis of well-formed particles. The decrease in 0.1PFOA−$TiO_2$ crystallite size may be attributed to the narrowing of the particle, which would decrease the length dimension of the particle in at least one crystalline direction. Other XRD peaks (*e.g.* the rutile [101] peak at $Q = 2.52$ Å$^{-1}$) in Figure 6.15 do not show the same drastic broadening as is exhibited by the rutile [110] peak ($Q = 1.94$ Å$^{-1}$), which correlates with this.

DLS and zeta potential graphs for these samples are shown in Figures 6.19 and 6.20 respectively. All samples exhibited significant aggregation that prevented particle sizing *via* DLS (even when the analyte loading was reduced to just above the detection limit), and this can be attributed to their uniformly low zeta potentials ($\sim 8$ mV, see Figure 6.14). It is to be expected that as the concentration of SMA (and thus the degree of surface coverage of $TiO_2$ particles) decreases, the effect of each SMA on zeta potential will decrease. It is interesting, however, that the zeta potential gravitates to around 8 mV, and not $\sim 40$ mV (the zeta potential of unmodified $TiO_2$).

Comparison of the above data with those presented in Section 6.3.1 reveals several interesting facts. First, the use of fluorinated carboxylic acid SMAs encourages the growth of rutile over anatase in the formation of $TiO_2$ particles. By reducing the concentration of SMA it is revealed that the presence of these compounds also changes the overall crystallite size: this may due to the reduced ability of SMAs to control particle growth at lower SMAs. The reduction of SMA concentration also resulted in more well-defined particles (as determined by SEM): of particular note, PFPA−$TiO_2$, which under both standard and direct synthesis methods appeared spherical and poorly-defined under SEM, exhibited typical crystallite properties when the concentration of SMA was reduced. The overall range of particle sizes generally decreased, and this may once again be linked to the reduced effect of SMA on particle size, shape and crystallinity.

These observations suggest that while these fluorine-containing carboxylic

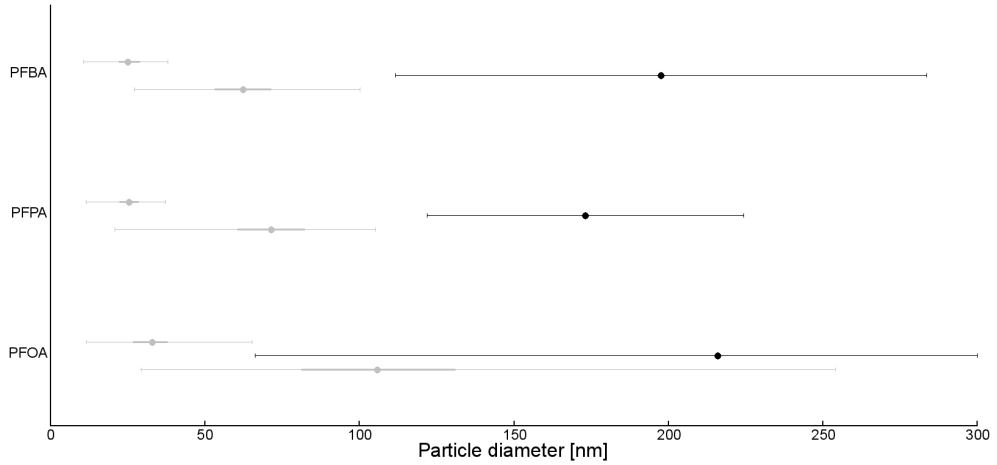


**Figure 6.19.** DLS particle sizing for standard-method $TiO_2$ modified by long-chain perfluorinated carboxylic acids using a 1:10 SMA:Ti ratio. In grey, particle sizing data (minor and major axis diameter) obtained by particle sizing on SEM images.

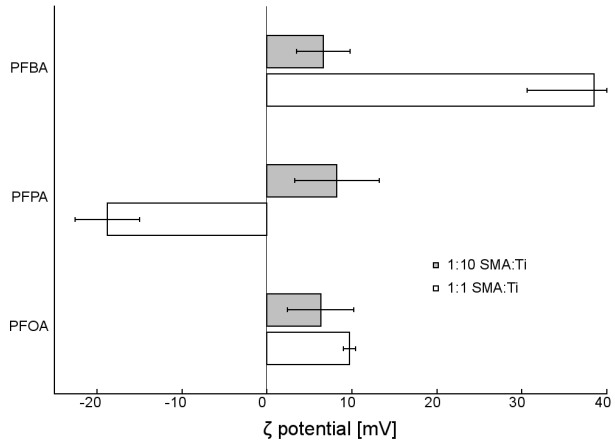


**Figure 6.20.** In grey, zeta potential measurements for standard-method $TiO_2$ modified by long-chain perfluorinated carboxylic acids using a 1:10 SMA:Ti ratio. In white, zeta potential data for the 1:1 ratio equivalent materials.

acid SMAs have a marked effect on $TiO_2$ particle size, shape and crystallinity, Overall trends in these properties may easily be "masked" by excess SMA, which can obscure particle size, alter surface charge, encourage aggregation, and create noise in PXRD patterns.

## *6.4 Conclusion*

In this chapter, we explored the synthesis of $TiO_2$ nanoparticles *via* the thermal degradation of peroxotitanic acid (PTA), as modified by a number of fluorine-containing carboxylic acids. Two methods were used to synthesise these materials: in the first, surface modifying agent (SMA) was added to amorphous titania before PTA formation (standard method), and in the second, SMA was added to titanium precursor prior to hydrolysis to form a titanium-acetate compound, which was then used as a titanium source for peroxotitanic acid formation (direct-addition method). Particle size, phase, crystallinity and surface charge were analysed by PXRD, SEM, DLS and zeta potential measurements.

Acetic acid binds readily to $TiO_2$ *via* the carboxylate group, and was shown to direct growth towards anatase nanorods that aggregated strongly in solution due to low absolute zeta potential. Fluorine substitution of hydrogen groups on methyl "tail" of the SMA resulted in more elongated "needles" of rutile titania, which showed a considerably more positive zeta potential and as a result did not aggregate as readily in solution. The change in phase and shape was attributed to the more acidic nature of the reaction solution,[278] a result of the choice of SMA. Under standard synthetic method conditions, $CF_2HCOOH$, $CF_3COOH$ and PFBA all produced particles of similar shape and with similar dimensions. As SMA tail length grew beyond this point, particles lost their needle-like shape and become more irregular, with their zeta potentials dropping and aggregation once again occurring. The reason for this change is not known but is theorised to be due either to the micellar nature of long-chain perfluorinated carboxylic acids in aqueous solution, or due to steric effects. In addition, the presence of amorphous material in these products suggests that SMA is strongly bound to $TiO_2$ and resistant to post-synthetic washing.

Use of the direct-addition method ($dTiO_2$) had a clear effect upon the nature of the $TiO_2$ product. $CH_3COOH{-}dTiO_2$ exhibited less anatase than its $sTiO_2$ counterpart, and SEM images showed a structure closer resembled the elongated rutile needles observed for $CF_2HCOOH{-}sTiO_2$. Fluoride-modified acetic acid appears to promote the formation of anatase compared to its $sTiO_2$ equivalents, counter to the trend for $CH_3COOH$ and the expectation that strongly acidic media generally promote the formation of rutile.[278] The reason for this effect is as yet unknown. Use of the direct-addition method appears to favour larger particles, especially for longer-tail SMAs. The onset of particle irregularity noted above persists in the direct addition method.

Finally, $sTiO_2$ synthesised using a 0.1:1 SMA:Ti molar ratio with longer-tail SMAs were investigated. These were generally more monodisperse and well-shaped than similar materials synthesised using a 1:1 SMA:Ti ratio, suggesting that such large concentrations of SMA are not needed to have an effect on particle properties. $TiO_2$ synthesised in this manner using PFBA and PFPA as surface modifying agents resembled those particles synthesised in the presence of $CH_3COOH$, *i.e.* at reduced concentration, these fluoride-modified carboxylic acids act in a manner similar to weaker carboxylic acids. This suggests that the main way these SMAs influence particle properties is still through the carboxylate group, rather than the long fluorine tail.

This current study indicates that more detailed investigations are required to understand the role of fluorine-modified carboxylic acids as surface modifying agents for $TiO_2$. Specifically, there is as yet no concrete evidence that the fluorinated tail of these carboxylic acids greatly affects particle properties — *i.e.* , the main director of particle shape may simply be the pH of the reaction mixture. In addition, a number of samples studied in this chapter appeared to exhibit thick coatings of bound SMA, despite post-synthetic washing procedures. This layer of SMA may obscure the synthesised $TiO_2$ particles, making it difficult to determine their properties. Further studies may focus on reducing the ratio of SMA to Ti as well as detailed washing studies of materials made using higher SMA ratios. Further characterisation of these materials using techniques such as energy-dispersive X-ray spectroscopy (EDS) and X-ray photoelectron spectroscopy (XPS) will also allow exploration of the binding of SMAs to the titania surface.

# Chapter VII

# Synthesis of $Au@TiO_2$ catalysts

## *7.1 Introduction*

Gold has until very recently been considered an inert or near-inert metal. While Bond *et al.* discovered in 1973 that it was possible to catalyse hydrogenation reactions on the surface of the bulk material,[282] its low activity relegated it to a mere curiosity rather than a viable catalyst. However, studies in the 1980s on the hydrochlorination of ethylene and low-temperature oxidation of CO over supported gold nanoparticles, reported by Hutchings and Haruta *et al.* respectively, demonstrated the remarkable catalytic properties of nanoscale gold particles and revolutionised the field of heterogeneous catalysis.[283,284] Since the publication of these articles the area of gold catalysis has grown drastically, and now represents one of the most active areas of catalysis.[285]

Liquid-phase chemical synthesis of metal clusters allows for excellent control over particle composition and size, while maintaining scalability.[286] However, stabilising ligands must be used to control particle growth, prevent aggregation, and ensure solubility in the reaction media. Once nanoparticles are deposited on support, these ligands are often[287,288] (although not always[289]) detrimental to catalytic activity, by preventing either the approach of substrate or the absorption of light.[287] Thermal (calcination) and oxidative (ozonolysis) treatments are often used to remove stabilising ligands and also help anchor the particles to the support,[290,291] minimising cluster sintering during catalysis. It has generally been found that ozonolysis is superior to thermal treatment for ligand removal, and in addition catalysts which have been subjected to ozonolysis tend to show increased resistance to further sintering.[291,292] However, it has been shown that both of these treatment

methods will encourage gold nanoparticles to sinter and aggregate due to the relatively weak gold-oxide interaction.[292] Since gold nanoparticle catalytic activity is closely linked to particle size,[293] any and all aggregation will affect their performance. The ready sintering of gold nanoparticles is one of the major issues preventing widespread commercialisation of such catalysts as compared to platinum-based catalysts,[285,294] which are less effective at high concentrations of subtrate and generally require temperatures of 100°C or higher to function efficiently.[283]

Valden *et al.* have demonstrated that the catalytic ability of supported gold clusters decreases drastically with increasing size, and suggested that pre-treatment of support should be used to remedy this.[295] Since then a number of groups have explored different methods of support pre-treatment and their effect on gold cluster aggregation. For example, Hidalgo *et al.* have demonstrated that sulfuric acid pre-treatment of $TiO_2$ leads to the fixation of sulfate groups on the particle surface, resulting in a much stronger support-nanoparticle interaction.[296] Veith *et al.* have reported that pre-treatment of $TiO_2$ with both acid and base may help prevent gold aggregation,[297] so the modification of the $TiO_2$ surface by $H^+$ in sulfuric acid pre-treatment may also play a role in improving the metal-support interaction. In addition, further studies have shown that hydrolxylation of the $TiO_2$ surface results in a drastic improvement to gold cluster catalytic activity while negligibly affecting aggregation.[298] Meanwhile, Zhong *et al.* showed in 2007 that the addition of $Sn^{2+}$ to the surface of titanium dioxide improved the dispersion of Pd, Pt, Au and Ag nanoparticles, as well as mixed-metal nanoparticles composed of these elements.[299] Similar systems prepared in the absence of tin experienced aggregation, and it was proposed that strong tin-hydroxyl chelating bonds were responsible for the high dispersion of the nanoparticles. Matthey *et al.* have explored the nucleation of small ($< 20$ atoms) gold clusters on oxidised, reduced and hydrated $TiO_2$ surfaces.[300] They found that the gold-oxide bond is strongest in the case of oxidised support, while hydrated $TiO_2$ surfaces readily allowed for gold particle aggregation. This is in strong contrast to larger ($\sim$1.5 nm) gold nanoparticles, which aggregate readily on oxidised support,[285] especially at higher temperatures.[301]

While the above reports demonstrate the importance of surface pre-

treatment, they are not ideally suited to direct comparison due to the variations in individual approaches towards material fabrication. To our knowledge there has been no comprehensive comparative report on the effect of popular pre-treatments on the gold-support interaction. Ideally, one would aim to focus on the effect of support treatment only, but in order to do so it is important to eliminate interference caused by other factors (*e.g.* type and synthetic method of gold cluster and support) to isolate the effect of treatment methods.

In this chapter, the effects of a number of pre-treatment methods on the deposition and activation of atomically-precise gold clusters were investigated. We have selected a number of pre-treatment methods (discussed above) which have been proven to affect gold cluster aggregation on metal oxide supports.[296–300] These pre-treatment methods were applied to the commercially-available Aeorixde P-25 $TiO_2$ support (a NIST standard).[302] The as-treated materials were used as supports for the $[Au_9(PPh_3)_8](NO_3)_3$ cluster ("$Au_9$"), and the resultant materials were subject to two post-deposition treatments (calcination and ozonolysis). Detailed investigation of these materials was carried out *via* synchrotron XPS at the soft X-ray beamline of the Australian Synchrotron. As the binding energy of XPS peaks is dependent on both particle size and environment, UV-vis diffuse reflectance spectroscopy (UV-vis DRS) was used to confirm the findings and give a detailed picture of gold particle aggregation on the support surface. Using these techniques in conjunction, we demonstrate the effects of pre-treatment on the behaviour of the gold clusters during deposition and activation. By using the exact same support material for each pre-treatment, we eliminate any interference due to variability in the support synthetic method or source. The use of the commercially-available P-25 as a support allows the results of this study to be widely applicable, benefitting numerous researchers working in the area by providing a comprehensive reference point.

This chapter builds on our recent studies on a series of atomically-precise clusters deposited and activated on titania.[303,304] Importantly, our earlier studies have also highlighted the important role support pre-treatment plays in the aggregation of gold clusters. By using atomically-precise $Au_9$ clusters as a target for this study, we have been able to focus on exactly how vari-

ous pre-treatment methods of the same, popular support affect nanoparticle aggregation, both during deposition and upon post-deposition treatment.

## *7.2 Experimental*

$AuPPh_3(NO_3)$ gold cluster precursor was synthesised from 99.99% pure gold following a procedure described previously.[303] P-25 titania "Aeroxide" was manufactured by Evonik Degussa GmbH. Titania particles are 80:20 anatase to rutile phase, with a quoted average particle size of 30 nm and surface area of 50 $m^2\ g^{-1}$. Sodium borohydride (synthetic grade, Merck), potassium hydroxide ($\geq$ 85%, Merck), hydrogen peroxide (50% w/w solution, Jasol), sulfuric acid (99%, Orica Chemnet), and tin chloride hydrate ($\geq$ 98%, Sigma-Aldrich) were used as received.

### *7.2.1 Gold cluster synthesis*

$Au_9$ clusters were synthesised by a method described by Wen *et al.* ,[305] and used extensively by our group.[303,304] Briefly, a solution of $NaBH_4$ (0.072 g, 1.92 mmol) in ethanol (92 mL) was added to a solution of $AuPPh_3NO_3$ (4.000 g, 7.6 mmol) in ethanol (160 mL). After stirring for two hours, the solution became deep red, and was filtered to remove impurities. The filtrate was dried under reduced pressure and the resultant solid dissolved in $CH_2Cl_2$ (20 mL) and filtered through a sintered glass funnel. Solvent was once again removed under reduced pressure, and the resultant black precipitate was washed with THF (4 $\times$ 50 mL) and then hexanes (3 $\times$ 50 mL). The precipitate was crystallized from methanol solution by slow diffusion of diethyl ether at 4°C over approximately 5 days.

Gold clusters were stored at 4°C in the dark prior to deposition.

### *7.2.2 Titanium dioxide pretreatment*

P-25 titanium dioxide was pretreated in a number of ways, as described below. Unless otherwise stated, following treatment all samples were washed three times with Milli-Q water and once with ethanol, and dried under reduced pressure.

- **Potassium hydroxide wash:** KOH aqueous solution (2M) was added dropwise to a mixture of P-25 (1.000 g) and Milli-Q water (90 mL) until the pH reached 10. The mixture was stirred at 60°C for two hours. The product was removed by centrifugation.[297]

- **Sonication in hydrogen peroxide:** P-25 (1.000 g) was added to $H_2O_2$ solution (10 mL, 50% w/w) and sonicated for thirty minutes at 30°C.

- **Calcination under hydrogen:** P-25 (1.000 g) was placed in a quartz boat in a sealed tube furnace (MTI OTF-1200X). The system was purged with argon (MKS 647C multi-gas controller, Ar flow rate 100 $cm^3\ min^{-1}$) and heated to 450°C. At this point, hydrogen was added to the argon flow ($H_2$ flow rate 100 $cm^3\ min^{-1}$). Gas flow was maintained for three hours, after which the hydrogen flow was stopped and the sample allowed to cool to room temperature under argon flow. The sample was not washed prior to deposition.

- **Calcination under static air:** P-25 (1.000 g) was placed in a quartz boat in a tube furnace, left open to atmosphere. The sample was heated to 400°C for two hours. The sample was not washed prior to deposition.

- **Ozone/UV treatment:** P-25 (1.000 g) was placed in a quartz tube and stirred under ozone flow and UV exposure (provided by a 500 W Ushio UXL-500D-O broad-spectrum Xe lamp) for two hours. The sample was not washed prior to deposition.

- **Sulfuric acid wash:** P-25 (1.000 g) was added to sulfuric acid solution (10 mL, 1 M) and stirred for five hours.

- **Tin chloride wash:** Tin chloride solution ([Sn] = 26.4 mM) was formed by adding $SnCl_2 \cdot 2\,H_2O$ (1.19 g ) to HCl (200 mL, 0.02 M). P-25 (1.000 g) was dispersed in Milli-Q water (200 mL) before being added to the tin chloride solution. The pale yellow suspension was stirred for 10 minutes, removed from the tin chloride solution by centrifugation, and washed with HCl solution (1 M) five times to remove SnClOH (insoluble at pH 7) formed on its surface.

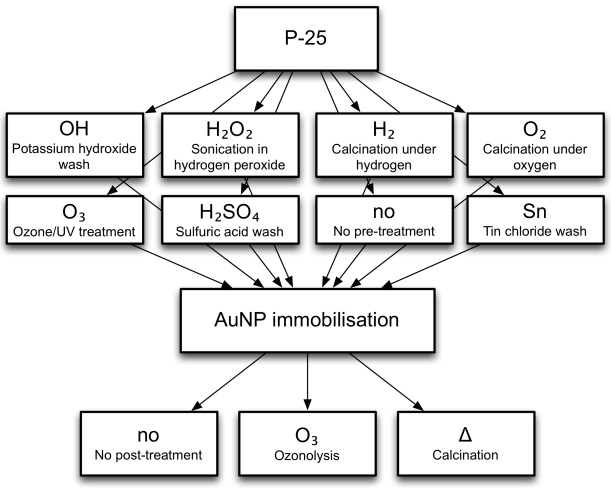


**Figure 7.1.** A total of eight pre-deposition and three post-deposition treatment methods were used, for a total of twenty-four products. Details of specific treatments are given in the main text.

### *7.2.3 Gold cluster deposition*

Gold clusters were deposited on as-treated P-25 titanium dioxide supports to give a 0.17% metal loading (by mass of Au). In a typical preparation, 1.000 g of titania was dispersed in dichloromethane (20 mL) with stirring. $Au_9$ clusters (3.9 mg) were dissolved in dichloromethane (5 mL) and added to the suspension, and the mixture was stirred for one hour. Following this, the solvent was removed under reduced pressure. Au@$TiO_2$ products were stored and processed in the absence of light, as this has previously been shown to encourage cluster aggregation.[297]

Portions of each material were then treated using one of the two different post-deposition treatments (see Figure 7.1). Details of post-deposition treatment methods follow:

- **Ozonolysis:** 200 mg of sample was stirred under constant ozone flow (provided using a Yanco Industries OL100DS generator) for 90 minutes, before being washed twice with ethanol and dried under vacuum.

- **Calcination:** 100 mg of sample was heated in a Schlenk tube to 200°C under vacuum with stirring for one hour.

In both cases, care was taken to prevent product exposure to light. Materials in this report will be denoted "<pre>−$TiO_2$−<post>": *e.g.* $O_3$/UV−$TiO_2$−$\Delta$ indicates the the support was ozonolysed prior to gold cluster deposition, and subjected to calcination after the deposition.

### *7.2.4 Characterisation*

X-ray photoelectron spectroscopy (XPS) was performed at the Australian Synchrotron's soft X-ray beamline[230] using a SPECS Phoibos 150 hemispherical electron analyser. XPS measurements were performed with an excitation energy of 625 eV and a pass energy of 20 eV. The background was fitted using a combination Shirley background/polynomial function. Peaks were fit using pseudo-Voigt peaks fixed at 30% Cauchy (Lorentz) character and 70% Gaussian character. Due to the low gold cluster loading, gold and phosphorus XP spectra were measured ten times and averaged to remove noise, while other signals of interest were measured twice and averaged.

UV-vis diffuse reflectance spectroscopy (UV-vis DRS) was performed using an Agilent Cary 4000 UV-vis spectrometer with diffuse reflectance sphere. Band gaps were calculated from a modified Kubelka-Munk plot, assuming a direct transition (see Figure 7.10 for a typical plot). Background under SPR peaks was approximated using a quadratic function, and peaks were fitted with Gaussian functions and parameters determined by non-linear least squares fitting. Peak intensity was measured as the area under the curve. Full width at half maximum values for these peaks were approximately 110 nm, with a standard deviation of 17 nm.

## *7.3 Results*

Materials in this report will be denoted "<pre-treatment>−$TiO_2$−<post-treatment>": *e.g.* $O_3$/UV−$TiO_2$−$\Delta$ indicates the the support was ozonolysed prior to gold cluster deposition, and subjected to calcination after the deposition.

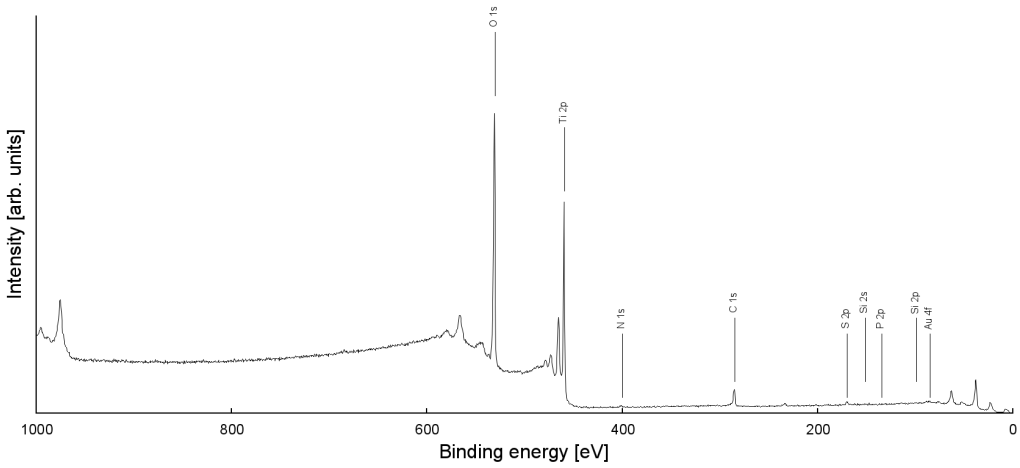


**Figure 7.2.** A typical XP survey spectrum for Au@$TiO_2$ material (here: $H_2SO_4$−$TiO_2$−None).

### *7.3.1 X-ray photoelectron spectroscopy*

X-ray photoelectron spectroscopy (XPS) survey scans revealed the presence of titanium, oxygen, carbon, phosphorus and gold for all samples (Figure 7.2). Further high-resolution XP spectra were recorded for the Ti 2p, O 1s, C 1s, P 2p and Au 4f peaks of each sample. $TiO_2$−Sn samples were also analysed at the Sn 3d peak. Sn-modified samples showed no evidence of bound chlorine from the $SnCl_2$ precursor; $H_2SO_4$-modified samples showed very small amounts ($< 0.5\%$ of Ti signal intensity) of residual sulfate ($E_B \approx$ 170 eV, Figure 7.3),[244] which has previously been shown to bind strongly to the titanium dioxide surface.[306]

Exact binding energies in all spectra were obtained by normalisation using the C 1s adventitious carbon peak at 285 eV.[167] No samples required major correction, indicative of little or no sample charging. Unless otherwise noted, peak intensities are reported as a fraction of the titanium total peak intensity.

*Effects of pre- and post-deposition treatments on Ti-XPS*

Relative intensities for all Ti populations are tabulated in Table 7.1, and $Ti^{3+}$ populations are shown in Figure 7.7 (fitting of a typical Ti XPS peak is shown in Figure 7.4). In all cases, the Ti 2*p* region displayed two distinct

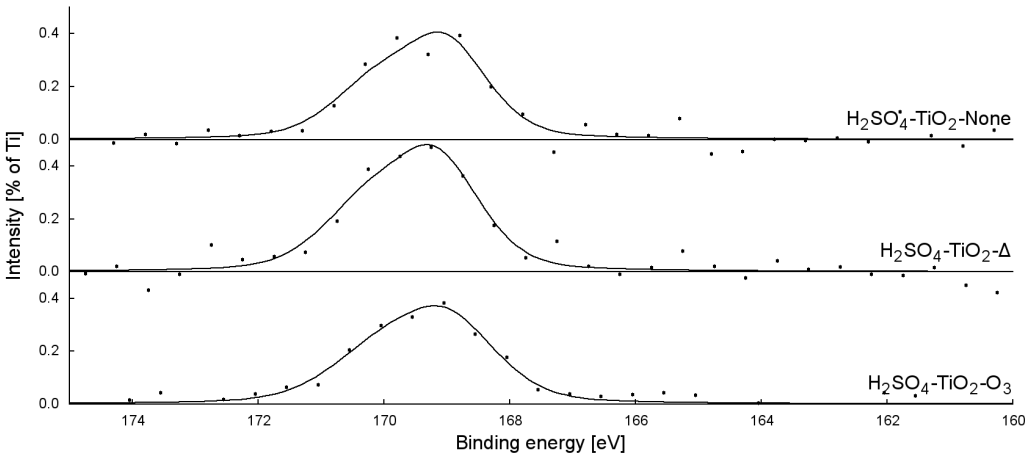


**Figure 7.3.** XP spectrum of the sulfur 2p peak for $H_2SO_4$−$TiO_2$ samples.

peaks at ∼459.2 eV and ∼457.6 eV, which correspond to $Ti^{4+}$ and $Ti^{3+}$ respectively.[307] In addition, $SnCl_2$ pre-treated materials exhibited a third Ti peak at ∼460.1 eV (Figure 7.5). Upon ozonolysis, both the Sn XPS peak (Figure 7.6) and this additional Ti peak disappear, suggesting that:

1. ozonolysis/ethanol washing was effective at removing tin from the surface of the support (although the mechanism is not known), and

2. this third Ti peak ($E_B \approx 460$ eV) was caused by interaction with surface-bound tin.

This Ti XPS peak observed at high binding energy is likely due to titanium-oxygen-tin atom interactions on the sample surface, in which tin centres withdraw electron density from titanium.[308]

$Ti^{3+}$ ions in $TiO_2$ have been known to extend the photoresponse of the material into the visible light spectrum,[88] but thermal treatment is known to reduce the $Ti^{3+}$ population of $TiO_2$ materials.[90] The $Ti^{3+}$ population of supports in this study was found to depend on both pre- and post-deposition treatment methods.

Untreated P-25 shows the highest recorded $Ti^{3+}$ concentration of all analysed samples. However, upon calcination the $Ti^{3+}$ population of untreated P-25 support drops drastically, presumably due to thermally-induced reorder-

**Table 7.1.** $Ti^{3+}$ surface populations of Au@$TiO_2$ materials, as determined by fitting of Ti 2p XP spectra.

| **Pre-treatment** | **Post-treatment** | **% Ti population** | | |
|---|---|---|---|---|
| | | $Ti^{3+}$ | $Ti^{4+}$ | Other* |
| | None | 6.71 | 93.29 | – |
| None | Δ | 3.10 | 96.90 | – |
| | $O_3$ | 5.78 | 94.22 | – |
| | None | 4.52 | 95.48 | – |
| $H_2(\Delta)$ | Δ | 2.73 | 97.27 | – |
| | $O_3$ | 4.48 | 95.52 | – |
| | None | 4.23 | 95.77 | – |
| $O_2(\Delta)$ | Δ | 5.11 | 94.89 | – |
| | $O_3$ | 4.70 | 95.30 | – |
| | None | – | 79.97 | 20.03 |
| $SnCl_2$ | Δ | 0.18 | 85.15 | 14.67 |
| | $O_3$ | 4.45 | 95.55 | – |
| | None | 4.26 | 95.74 | – |
| $O_3$/UV | Δ | 4.28 | 95.72 | – |
| | $O_3$ | 3.68 | 96.32 | – |
| | None | 4.22 | 95.78 | – |
| $H_2O_2$ | Δ | 4.07 | 95.93 | – |
| | $O_3$ | 5.10 | 94.90 | – |
| | None | 3.85 | 96.15 | – |
| KOH | Δ | 3.66 | 96.34 | – |
| | $O_3$ | 2.33 | 97.67 | – |
| | None | 1.14 | 98.86 | – |
| $H_2SO_4$ | Δ | 3.10 | 96.90 | – |
| | $O_3$ | 5.19 | 94.81 | – |

*See main text for discussion of these peaks.

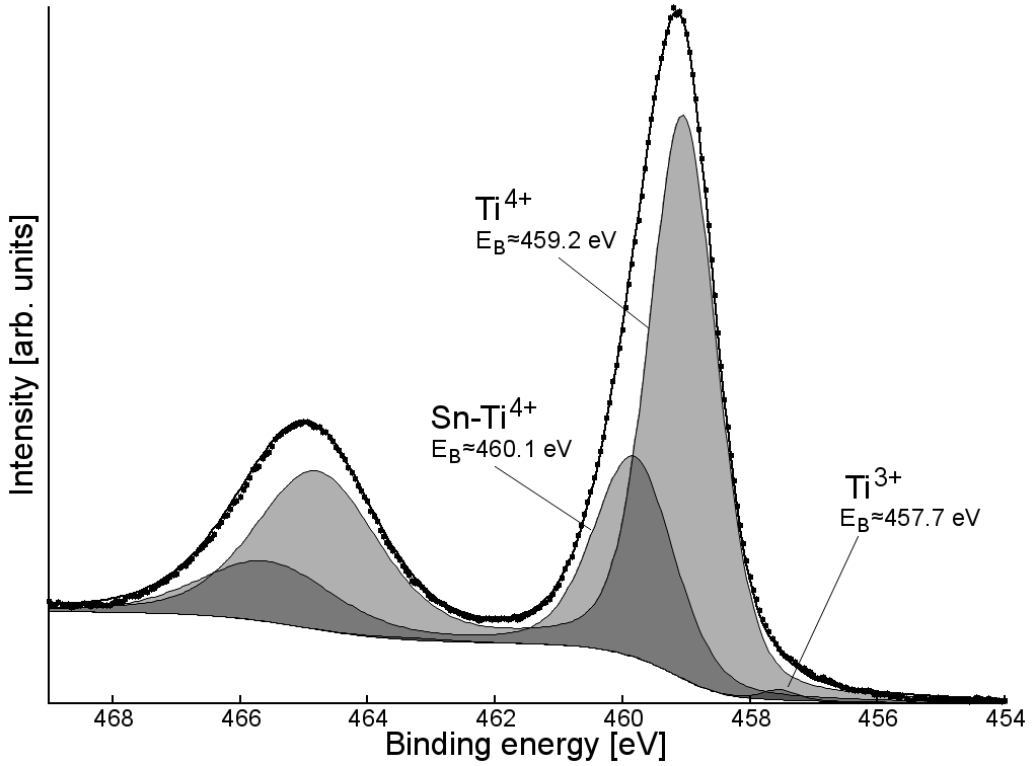


**Figure 7.4.** Fitting of a typical Ti 2p XPS peak (shown here: $SnCl_2-TiO_2-\Delta$). In this sample, all three Ti XPS peaks reported in this paper can be observed. Points show raw data.

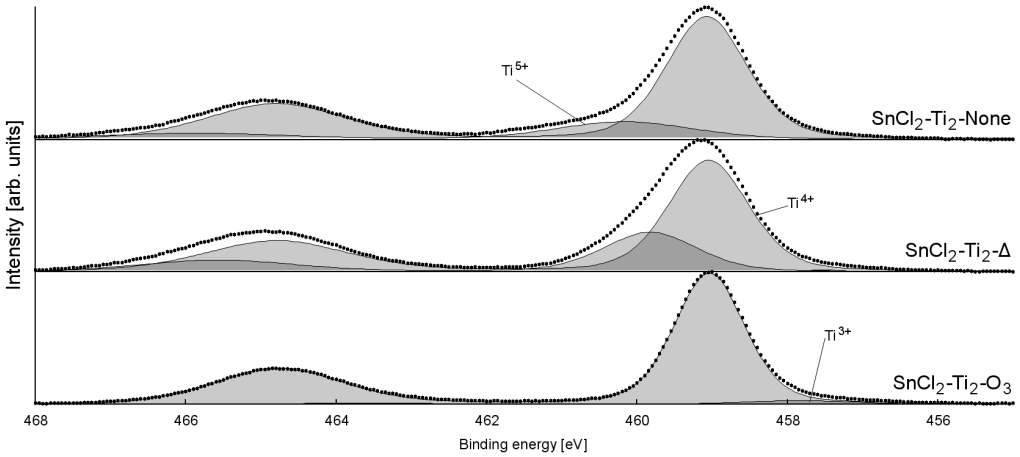


**Figure 7.5.** The presence of a shoulder on the main $Ti^{4+}$ peak reveals a third Ti peak with its centre around 460.6 eV for $SnCl_2-TiO_2$. This peak disappears upon post-treatment, most notably through ozonolysis.

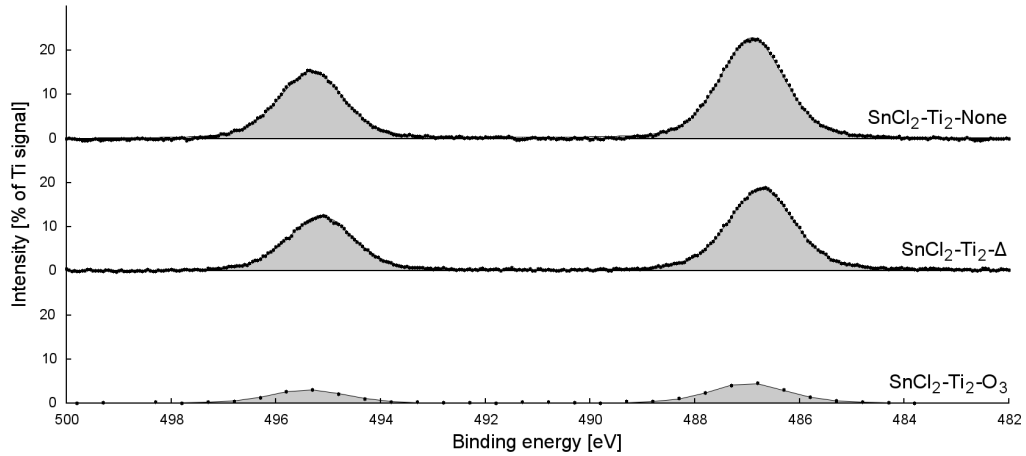


**Figure 7.6.** Effect of post-deposition treatment on the Sn 3d XPS peak of Sn−$TiO_2$. Peak intensities normalised based on Ti peak intensity.

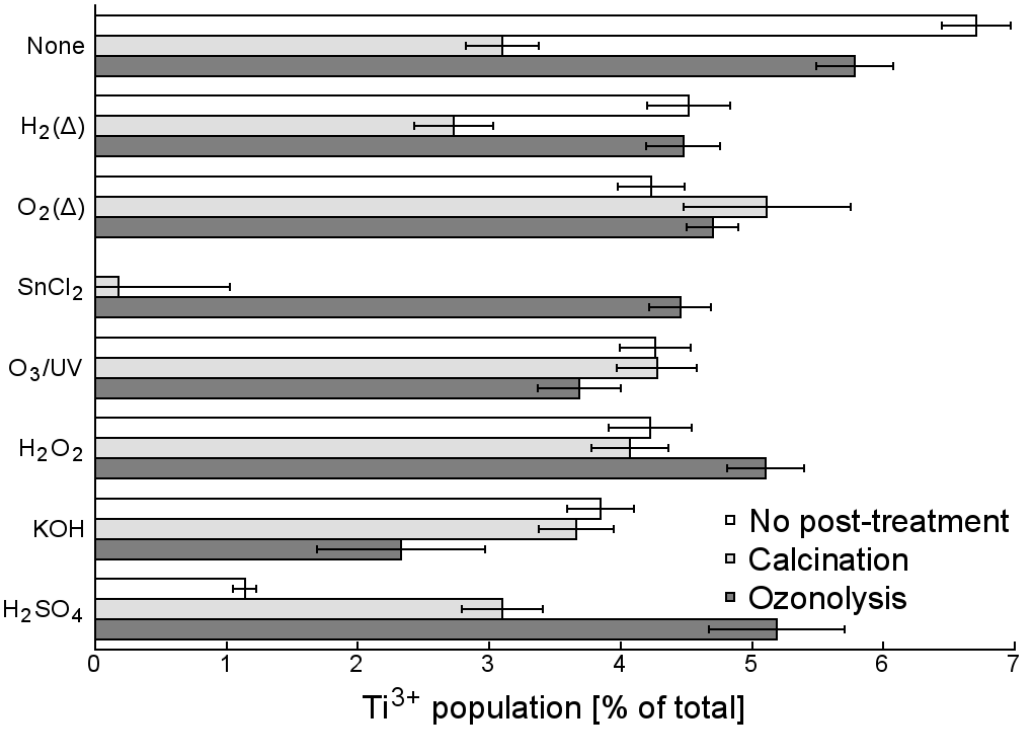


**Figure 7.7.** Effect of pre-deposition and post-deposition treatment method on the percentage of Ti observed in the $Ti^{3+}$ state. Error bars indicate 95% C.I.

ing of the $TiO_2$ surface. Ozonolysis, on the other hand, only causes a minor drop in $Ti^{3+}$ population.

Pretreatment of support at elevated temperature under both hydrogen (reducing) and static air (oxidising) conditions resulted in reduced $Ti^{3+}$ populations, as has previously been reported[309] (and as was seen for calcination of P-25 under vacuum above). This is likely due to thermal reordering and the removal of surface defect cites that could lead to the formation of $Ti^{3+}$ centres. Post-treatment by ozonolysis has little to no effect on the $Ti^{3+}$ populations of these samples, however, the effect of calcination is varied. The $Ti^{3+}$ population observed for $H_2(\Delta)-TiO_2-\Delta$ is similar to that of None$-TiO_2-\Delta$, but it appears that static air pre-treatment produces a support whose $Ti^{3+}$ population is resistant to calcination.

Tin-modified $TiO_2$ initially displays no $Ti^{3+}$ character, likely due to electron-withdrawing nature of surface-bound Sn (as detailed above). As tin was removed *via* post-deposition treatment, the $Ti^{3+}$ population was regenerated. $Sn-TiO_2-O_3$, which has the lowest concentration of surface Sn, exhibits a $Ti^{3+}$ population comparable to other samples.

Ozonolysis and hydrogen peroxide pre-treatments were both used in an attempt to form oxide or peroxo species on the surface of the support. Ozonolysis pre-treatment resulted in a decrease in the support $Ti^{3+}$ population which was not regenerated by either calcination or ozonolysis post-deposition treatments: in fact, ozonolysis post-treatment served only to further decrease the $Ti^{3+}$ population. It is likely that $O_3$, being a strong oxidising agent, is able to oxidise a number of surface $Ti^{3+}$ sites, thus reducing the overall population. Following $O_3$ pre-treatment, calcination has little effect on the $Ti^{3+}$ population of the material: this suggests that those $Ti^{3+}$ sites oxidised by pre-desposition ozonolysis treatment are the same sites that would be removed upon calcination. $H_2O_2$ pre-treatment resulted in a $Ti^{3+}$ population comparable to $O_3/UV-TiO_2$, and post-deposition calcination again had little effect on the $Ti^{3+}$ population, suggesting that both $H_2O_2$ and $O_3/UV$ pretreatment methods alter the $TiO_2$ surface in a similar manner. While further ozonolysis on $O_3/UV-TiO_2$ results in a drop in $Ti^{3+}$ population, $H_2O_2-TiO_2-O_3$ exhibits an appreciably larger $Ti^{3+}$ population than $H_2O_2-TiO_2-$None.

Acid and base treatments vary considerably in both their initial $Ti^{3+}$ populations and their reactions to post-deposition treatments. $H_2SO_4$−$TiO_2$ exhibits a remarkably low $Ti^{3+}$ population, but post-treatment by calcination and ozonolysis both result in considerable recovery. Of note, $H_2SO_4$−$TiO_2$−$O_3$ shows a considerably higher $Ti^{3+}$ population than its non-post-treated analogue, a trend mirrored by $H_2O_2$−$TiO_2$ as discussed above. KOH−$TiO_2$, however, has a much higher $Ti^{3+}$ content which drops significantly upon either post-treatment.

*Effects of pre- and post-deposition treatment on Au-XPS*

Gold clusters were analysed by XPS, with data normalised and corrected as detailed above. Full gold peak data (intensity and position) is given in Figure 7.8 (tabulated data shown in Table 7.2, fitting of a typical Au XPS spectrum given in Figure 7.9).

XPS peaks of gold clusters on support can be broadly divided into "high binding-energy" peaks (HPB), attributed to small discrete gold clusters, and "low binding-energy" peaks (LBP) that result from larger aggregates.[303,304] Gold clusters exhibit peaks with higher binding energies due to positive surface-atom oxidation states and size effects.[310] While larger aggregates may also contain oxidised gold surface atoms, the ratio of surface to bulk is much lower than for small clusters. While bulk centres in large gold nanoparticles are effectively "invisible" to XPS (in this study $594 < E_{kin} < 610$; $d_{\text{escape}} \approx 20$ Å),[311] for smaller ($\leq 3$ nm) gold nanoparticles the influence of these bulk gold atoms is expected to be observable. In addition, the wide variety of oxidation states and chemical environments exhibited by gold atoms in $Au_9$ (which can all be considered "surface" atoms) result in a broad XPS peak and large full-width at half maximum (FWHM). As particles become larger, they start to consist chiefly of "bulk" gold atoms, with similar chemical environments, oxidation states, and thus binding energies. This results in a much narrower gold XPS peak and a much lower FWHM (see also the fitting shown in Figure 7.9).[303,312]

Gold XPS peak positions may also be affected by the nature of the support upon which the gold is deposited: large ($> 3$ nm) gold nanopar-

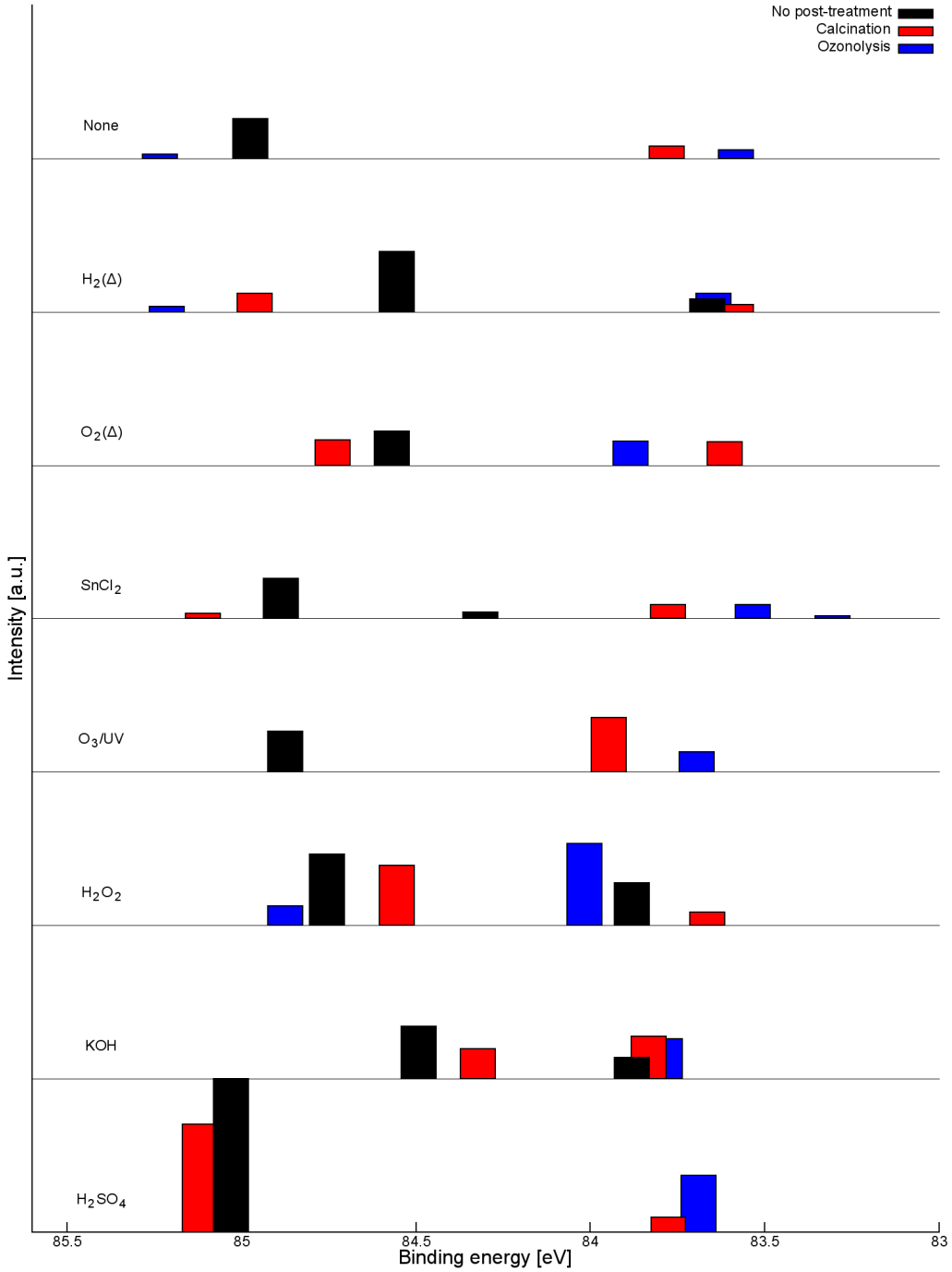


**Figure 7.8.** Binding energy and intensity of Au $4f_{7/2}$ XPS peaks for analysed materials. Intensity is normalised so that peak heights for different samples are comparable.

**Table 7.2.** Table of Au $4f_{7/2}$ XPS

peak position, intensity and full-width at half maximum by sample. Peaks are categorised as HBP, LBP, or aggregate by binding energy. Intensity is reported as percentage of total Ti 2p XPS peak intensity.

| **Pre-treatment** | **Post-treatment** | **HBP** | | | **Agg.** | | | **LBP** | | |
|---|---|---|---|---|---|---|---|---|---|---|
| | | Pos. | Int. | FWHM | Pos. | Int. | FWHM | Pos. | Int. | FWHM |
| None | None | 84.97 | 0.40 | 2.07 | – | – | – | – | – | – |
| | Heat | – | – | – | – | – | – | 83.78 | 0.13 | 0.85 |
| | $O_3$ | 85.23 | 0.04 | 1.80 | – | – | – | 83.58 | 0.09 | 1.10 |
| $H_2(\Delta)$ | None | – | – | – | 84.56 | 0.60 | 1.80 | 83.67 | 0.13 | 1.00 |
| | Heat | 84.96 | 0.19 | 2.72 | – | – | – | 83.58 | 0.07 | 0.83 |
| | $O_3$ | 85.21 | 0.05 | 1.89 | – | – | – | 83.65 | 0.18 | 0.97 |
| $O_2(\Delta)$ | None | – | – | – | 84.57 | 0.34 | 2.19 | – | – | – |
| | Heat | – | – | – | 84.74 | 0.25 | 2.30 | 83.61 | 0.23 | 0.83 |
| | $O_3$ | 83.88 | 0.24 | 2.62 | – | – | – | – | – | – |
| $SnCl_2$ | None | 84.89 | 0.40 | 2.06 | – | – | – | 84.32 | 0.06 | 0.92 |
| | Heat | 85.11 | 0.05 | 1.21 | – | – | – | 83.78 | 0.14 | 0.93 |
| | $O_3$ | – | – | – | – | – | – | 83.53 | 0.14 | 0.74 |
| $O_3$/UV | None | 84.87 | 0.41 | 2.12 | – | – | – | – | – | – |
| | Heat | – | – | – | – | – | – | 83.95 | 0.54 | 1.14 |
| | $O_3$ | – | – | – | – | – | – | 83.70 | 0.20 | 0.96 |
| $H_2O_2$ | None | 84.75 | 0.71 | 2.26 | – | – | – | 83.88 | 0.42 | 1.02 |
| | Heat | 84.87 | 0.20 | 1.73 | – | – | – | 84.02 | 0.81 | 1.20 |
| | $O_3$ | – | – | – | – | – | – | 83.76 | 0.38 | 0.90 |
| KOH | None | – | – | – | 84.49 | 0.52 | 1.92 | 83.88 | 0.21 | 0.95 |
| | Heat | – | – | – | 84.32 | 0.30 | 2.05 | 83.83 | 0.42 | 0.94 |
| | $O_3$ | – | – | – | – | – | – | 83.79 | 0.40 | 1.04 |
| $H_2SO_4$ | None | 85.03 | 1.52 | 1.76 | – | – | – | – | – | – |
| | Heat | 85.12 | 1.07 | 1.83 | – | – | – | 83.78 | 0.15 | 1.01 |
| | $O_3$ | – | – | – | – | – | – | 83.69 | 0.56 | 0.95 |

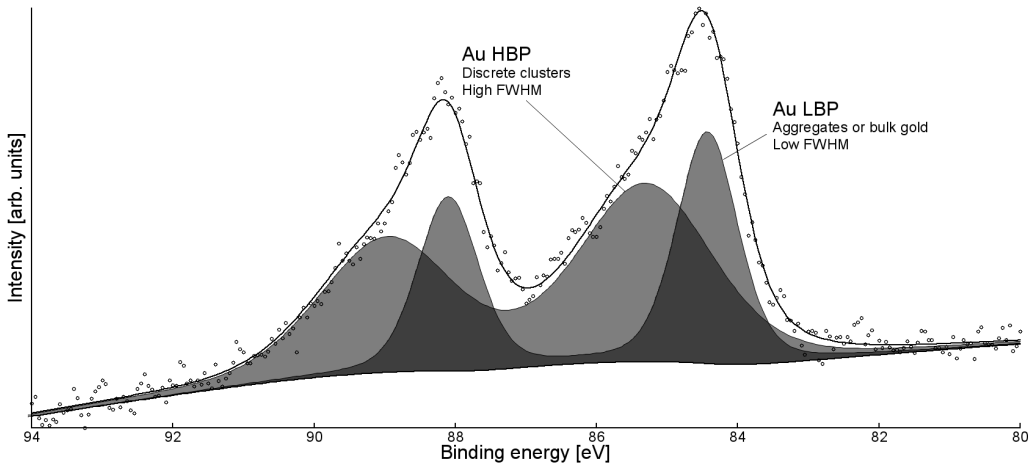


**Figure 7.9.** Fitting of a typical Au 4f XP spectrum (shown here: $H_2O_2$−$TiO_2$−None). Points show raw data.

ticles on titanium dioxide, for example, have been reported to have binding energies of anywhere from 82.7–84 eV.[47,167,312–316] In contrast, small (*i.e.* sub-nanometre) gold clusters exhibit binding energies around 84.5–85 eV.[303,312,316] While it is tempting to assign cluster and nanoparticle sizes based on the observed XPS peak binding energies, care must be taken as gold XPS binding energies can be affected by a number of size-independent factors. For example, Lee *et al.* found that Au@$TiO_2$ materials exposed to indoor light over the course of five months did not appreciably grow in size (as measured by HRTEM), but *did* show a binding energy shift of −0.5 eV.[313] Meanwhile Radnik *et al.* have reported that post-deposition heating under hydrogen gas results in a peak shift of −0.3 eV. The phenomenon was reversed by calcination in air, implying that the change in binding energy was due at least in part to ligand (rather than size) effects.[317]

In this study, all "as-deposited" samples (*i.e.* no post-deposition treatment) exhibited a distinct XPS peak around 84.5–85 eV. This peak was assigned to discrete $Au_9$ clusters, although for lower binding energies (*e.g.* $H_2(\Delta)$−$TiO_2$−None, $O_2(\Delta)$−$TiO_2$−None, KOH−$TiO_2$−None) these may also be due to small aggregates. The variation in binding energy is attributed to the effect of support. Peaks at lower binding energies were attributed to larger gold nanoparticles formed by aggregation of clusters, approaching

"bulk" gold as the binding energy decreased.

Without pre-treatment (None−$TiO_2$), gold quickly aggregates upon either heating or ozonolysis, as has been previously established.[304] None−$TiO_2$−$\Delta$ shows a very low-intensity HBP around 85.3 eV, approximately 0.5 eV higher than for None−$TiO_2$−No. This may be due to a number of different effects. First, ligands may be removed by the post-deposition treatment, resulting in a slight oxidation of the gold core and a resultant rise in binding energy. Second, the treatment may encourage the oxidation of surface gold, thus increasing the binding energy.[303] No similar peak is seen for None−$TiO_2$−$O_3$, which indicates complete or near-complete aggregation of gold clusters. LBP intensities are much lower after post-deposition treatments than their equivalent pre-treatment HBPs. Comparison of peak intensities is imprecise as the relatively low photoelectron escape depth means that large aggregates are under-represented in XPS (as "buried" Au atoms are effectively invisible to the technique).

Both elevated-temperature pre-treatments (under $H_2$ and static air) result in a significant decrease in HBP binding energy compared to clusters on untreated $TiO_2$. Radnik *et al.* have shown that hydrogen *post*-treatment of Au@$TiO_2$ can lower Au $4f$ electron binding energy,[317] however the technique outlined in their paper uses considerably higher temperature than was used here. While a similar effect may be postulated for $H_2$-pretreated materials, the relative mildness of the technique suggests that the downward shift observed here is not solely due to support effects. Crucially, no similar effect has been observed for oxidised surfaces, suggesting that the drop in HBP binding energy for $O_2(\Delta)$−$TiO_2$ is due to aggregation on the support surface as has previously been reported for oxygenated surfaces.[300] For both $H_2(\Delta)$−$TiO_2$ and $O_2(\Delta)$−$TiO_2$, post-deposition treatments result in the growth of an Au LBP and the shift of the HBP to higher binding energies. This shift in HBP is indicative of considerable cluster deprotection and oxidation. Of note, $H_2(\Delta)$−$TiO_2$−$O_3$ is the only ozonolysed sample to show an Au HBP, suggesting that hydrogen pre-treatment is effective toward immobilisation of Au clusters. $O_2(\Delta)$−$TiO_2$−$O_3$ appears somewhat resistant toward aggregation as well: the Au LBP has a binding energy approximately 0.4 eV higher than for $O_2(\Delta)$−$TiO_2$−$\Delta$, indicative of reduced aggregation.

Pre-treatment of titania support with tin appears to have little effect on the nature of deposited Au clusters. Sn−$TiO_2$−No shows a small peak at $\sim$ 84.4 eV, which may be due to gold-tin interactions on the support surface. Gold-tin interactions would also explain the relatively high binding energy ($\sim$ 487 eV *vs.* 485 eV for metallic tin) of observed Sn 3*d* XPS peaks (Figure 7.6). The Au XPS peak at 84.4 eV disappears upon post-treatment, indicative of the loss of Au-Sn clusters. Peak positions and intensities after post-deposition treatment look very similar to those observed for $TiO_2$−No, suggesting that tin deposition does very little to affect gold cluster aggregation. The one exception is a small peak observed at very low binding energy upon ozonolysis, which may be indicative of large gold nanoparticles.

Support pre-treatment by $O_3$/UV does not drastically affect gold aggregation for "as deposited" samples: as is the case for None−$TiO_2$, the only Au-XPS peak appears in the HBP region. However, Au-XPS peaks for both calcined and ozonolysed samples appeared at higher binding-energy and with higher relative intensity than their None−$TiO_2$ counterparts, indicating that ozonolysis pre-treatment was effective at limiting the extent of gold cluster aggregation. While hydrogen peroxide pre-treatment results in an initial Au LBP, this material retains its HBP after both calcination and ozonolysis, indicative of discrete gold clusters remaining on the sample. This suggests that $H_2O_2$ pre-treatment improves gold cluster resistance to aggregation upon heating. Neither sample exhibits additional oxygen XPS peaks (*e.g.* due to Ti−OOH surface bonds). Interestingly, $H_2O_2$−$TiO_2$ also shows greater resistance to cluster aggregation than $O_3$/UV−$TiO_2$, which may suggest that the formation of peroxo groups on the support surface prevents aggregation of larger Au nanoparticles.

Pretreatment by KOH washing results in an immediate decrease in the binding energy of Au HBPs. However, the presence of electron-rich surface Ti−OH groups is likely to lower the binding energy of deposited Au clusters.[317] An Au LBP is observed for KOH−$TiO_2$−No, indicating that base-treatment encourages gold particle aggregation for this particular system, contrary to what is expected based on previous reports.[300] Overall, this pre-treatment method does not seem to offer a significant advantage in controlling the aggregation of clusters according to the XPS observations of

post-treated samples.

Finally, pre-treatment with $H_2SO_4$ gives rise to a remarkably intense HBP (the most intense HBP peak observed in this report), whose binding energy is comparable to $Au_9$ deposited on untreated support. This binding energy is comparable to that of the pure, intact cluster in its solid-state micro-crystalline powder form,[303] indicating that the clusters deposited on $H_2SO_4$−$TiO_2$ remain intact. Calcination shifts this HBP to a higher binding energy, which is explained by ligand removal and partial oxidation of the cluster, and may also be due to a better interaction with the oxide support. A relatively low-intensity LBP is also observed for the calcined sample, indicative of a small population of aggregates. Nonetheless it is noteworthy that the intensity of the HBP of $H_2SO_4$−$TiO_2$−$\Delta$ is the highest in the series, indicating that support pre-treatment by washing in sulfuric acid is the best for preventing aggregation of clusters.

Ozonolysis, however, results in more extensive aggregation, as evidenced by the disappearance of the HBP and the concomitant appearance of an LBP. However, the high relative intensity of the LBP suggests that these aggregates are still relatively small, as a high proportion of Au atoms remains detectable by XPS (compared with other samples in the series).

*Effects of pre- and post-deposition treatments on P-XPS*

Triphenylphosphine ligands bound to the Au cluster core display a P-XPS peak with binding energy of 131–132 eV.[303] $H_2SO_4$−$TiO_2$−No and $H_2SO_4$−$TiO_2$−$\Delta$ both exhibited P-XPS peaks in this region, which suggests that $H_2SO_4$ pre-treatment is effective at stabilising discrete gold clusters on the $TiO_2$ surface. $H_2O_2$−$TiO_2$ also exhibited this P-XPS peak after deposition, although it disappeared upon either calcination or ozonolysis, indicating that while peroxide treatment helped prevent gold aggregation, the effect was not as strong as for sulfate pre-treatment. No other samples showed evidence of this P XPS peak, suggesting that in all other cases, extensive ligand removal had occurred. Additionally, P-XPS peaks were observed at 133–134 eV for all samples, which is attributed to oxidised phosphorus bound to the support surface.[244]

It is believed that the processes of aggregation and ligand removal are concurrent: this has been observed previously in XPS studies of phosphine-protected gold clusters deposited on titanium dioxide.[303,304] Of particular note, these studies show that gold clusters deposited on untreated commercial P-25 undergo deprotection and aggregation even without specific post-deposition treatment, confirming previous findings.[304]

### *7.3.2 UV-vis DRS Analysis*

All samples were subject to UV-vis Diffuse Reflectance Spectroscopy (UV-vis DRS) analysis. $TiO_2$ exhibits a strong absorption band for $\lambda < 400$ nm, and the band gap of the material can be approximated from the position and shape of this band using the Kubelka-Munk plot. In addition, gold nanoparticles of diameter 2 nm or greater[318] exhibit a broad peak around 400–700 nm[319] due to surface plasmon resonance. The position and intensity of this peak depends on the size and shape of the gold nanoparticles, with larger particles generally giving more intense peaks at higher wavelengths.[100,319,320] Peak intensity is also a function of gold concentration. Finally, individual $Au_9$ clusters show a much narrower peak around 480-500 nm due to their electronic structure.[305]

The optical absorption coefficient $\alpha$ of a semiconductor around the band-gap can be modelled by the equation:[164–166]

$$\alpha = B\frac{(h\nu - E_g)^{m/2}}{h\nu} \tag{7.1}$$

where $B$ is a constant, $h\nu$ is the energy of the incident radiation, $E_g$ is the energy of the band gap, and $m$ is a constant set to 1 for direct transitions.[165] By plotting $(\alpha h\nu)^2$ against $h\upsilon$ is it possible to find the direct band gap, as when $h\nu = E_g$, $\alpha = 0$. Using this method (a typical graph is shown in Figure 7.10), direct band gap energies were determined for all samples as well as P-25 (Figure 7.11).

P-25, being mainly anatase, has a band gap of approximately 3.2 eV.[4] Au@$TiO_2$ samples all show a significantly smaller band gap than pure P-25, indicative of visible-light sensitisation due to Au nanoparticles on the support surface.[100] The effect of gold nanoparticle deposition on P-25 can be

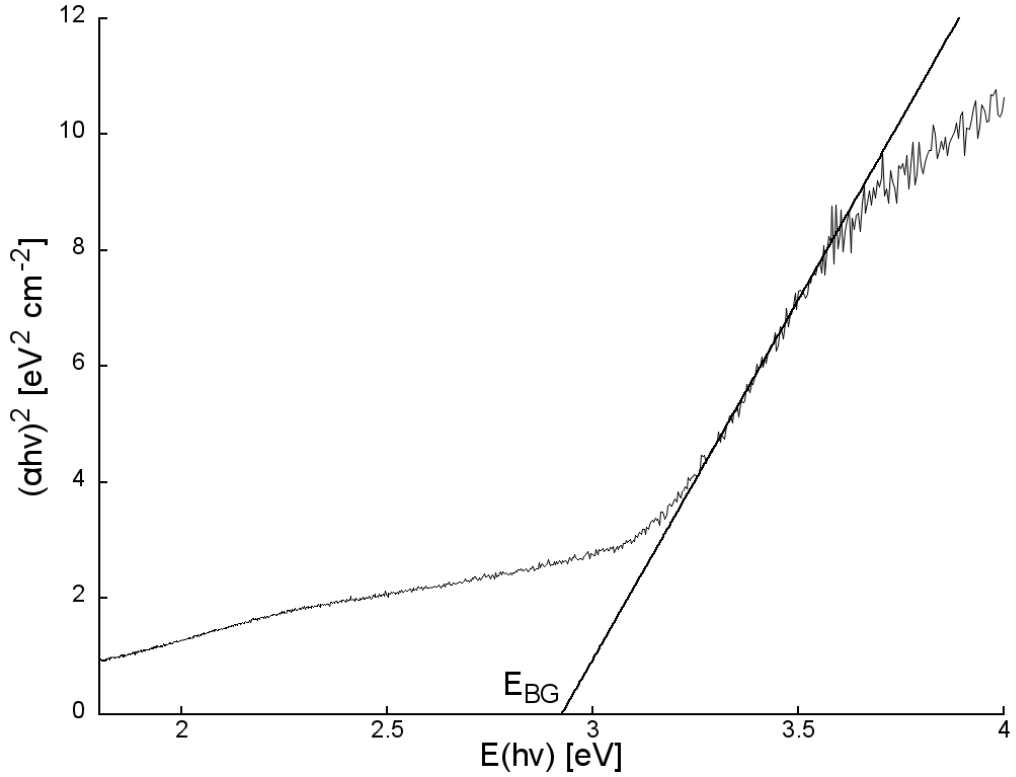


**Figure 7.10.** A typical Kubelka-Munk plot for Au@$TiO_2$ sample. The band gap energy is determined by taking the tangent to the linear section of the curve and extrapolating to $(\alpha h/nu)^2 = 0$.

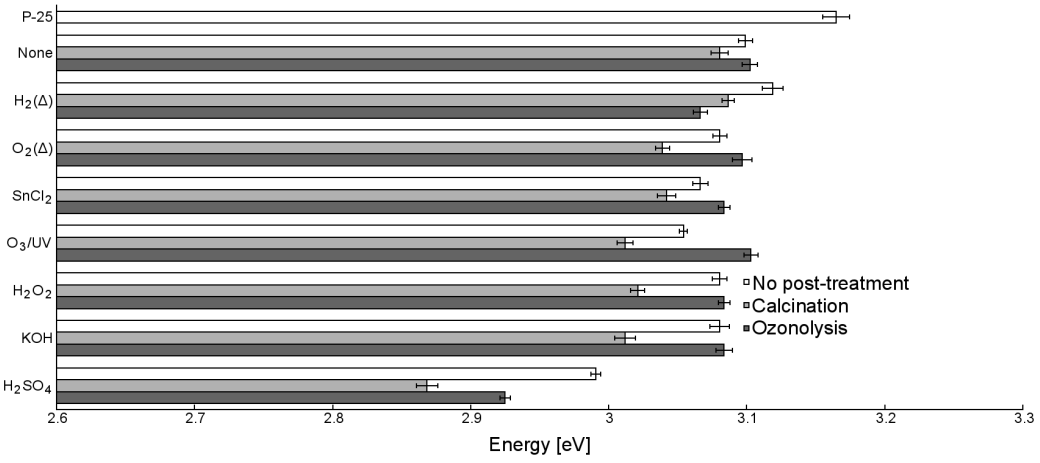


**Figure 7.11.** Direct transition bandgap energies for Au@$TiO_2$ materials, with P-25 shown for comparison. Error bars show 95% C.I.

observed by comparing the band gaps for P-25 and None−$TiO_2$−None. It is observed that while calcination further reduces the band gap of materials, ozonolysis either has no effect ($H_2O_2$−$TiO_2$, KOH−$TiO_2$, $O_2(\Delta)$−$TiO_2$) or widens the band gap (Sn−$TiO_2$, $O_3$/UV−$TiO_2$). There are two exceptions to this: $H_2(\Delta)$−$TiO_2$ and $H_2SO_4$−$TiO_2$ both show band gap narrowing upon ozonolysis. The reason for this narrowing effect is unknown, but the fact that such a phenomenon is *not* observed for $H_2O_2$−$TiO_2$−$O_3$ (which displays a prominent Au XPS HBP) suggests that band-gap narrowing is merely due to the presence discrete gold clusters. Tian *et al.* have previously reported that there is a finite size regime in which gold nanoparticles may affect the photoresponse of $TiO_2$,[100] and this may partially explain the band-gap narrowing effect. However, other factors (such as *e.g.* surface modification by pre- and post-treatment) cannot be ruled out at this stage.

$H_2SO_4$−$TiO_2$ materials systematically exhibit the smallest band gaps of the those studied. This is apparently *not* due to the lack of Au cluster aggregation, as $H_2O_2$−$TiO_2$ (which according to XPS studies above, is resistant to aggregation) has a band gap comparable to other samples which exhibited greater aggregation. It may be that the formation of sulfate species on the surface enhances visible-light activity, as has been previously reported in the literature,[321,322] although these studies only report a significant visible-light response after calcination. Upon calcination, the band gap of $H_2SO_4$−$TiO_2$ narrows considerably, however, the small change observed in sulfur XPS peak binding energy ($\sim$ 0.2 eV) is not indicative of Ti−S formation.[322]

SPR peaks and intensities are shown in Figure 7.12. Initial (*i.e.* before post-treatment) SPR peaks are observed for $H_2O_2$−$TiO_2$, $H_2(\Delta)$−$TiO_2$, $O_2(\Delta)$−$TiO_2$, and KOH−$TiO_2$. This correlates with XPS measurements, which show that these samples exhibit relatively intense LBPs (indicative of large nanoparticles) and/or HBPs at low binding energies (which suggests that the majority of the gold is present as aggregates). It is interesting that Sn−$TiO_2$−No displays no SPR peak, despite having a small Au XPS LBP at $\sim$ 84.3 eV. In contrast, $O_2(\Delta)$−$TiO_2$−No displays an SPR peak despite showing no Au XPS LBP at all. One factor that may influence the presence of SPR peaks is the age of the materials. The materials studied in this report were stored in the dark for three months between synthesis and UV-vis DRS

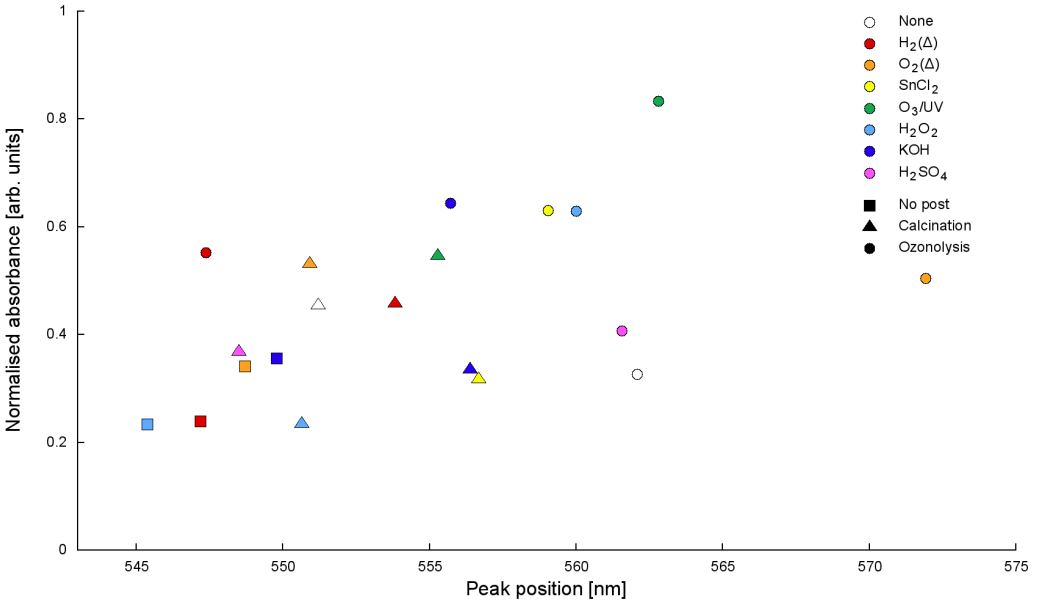


**Figure 7.12.** UV-vis DRS surface plasmon resonance peaks of Au@$TiO_2$ samples. SPR peak wavelength is shown on the abscissa, peak intensity on the ordinate. Absence of a point indicates that this sample exhibited no SPR peak.

study, and it may be that even these conditions were enough to result in mild aggregation on support.[297]

In all cases, the SPR peak becomes more intense and/or shifts to a higher wavelength upon post-deposition treatment, confirming that these treatments result in aggregation. The shift is generally more dramatic upon ozonolysis than calcination, with the exception being $H_2(\Delta)-TiO_2$. This agrees with what was observed using XPS: thermal pre-treatment under hydrogen enables some of the $Au_9$ clusters to survive harsh, aggregation-inducing ozone treatment. The lowest SPR peak position after calcination is observed for $H_2SO_4-TiO_2$ (∼548 nm), which confirms above XPS findings that $TiO_2-H_2SO_4$ samples were resistant to aggregation upon calcination.

## *7.4 Conclusion*

A number of Au@$TiO_2$ catalysts were synthesised, covering a broad range of pre- and post-immobilisation treatment conditions. These materials were analysed by X-ray photoelectron spectroscopy and UV-vis diffused reflectance

spectroscopy, which both revealed evidence of both discrete gold clusters and aggregated gold nanoparticles. While XPS can detect both individual clusters and aggregates, the binding energy of the gold peak may be influenced not only by particle size, but also by ligand and support effects. On the other hand, the observed UV-vis DRS signals were a result of gold surface plasmon resonance and thus independent of ligand and support effects, but did not reveal the presence of clusters of size $< \sim 2$ nm (which do not exhibit surface plasmon resonance).

# Chapter VIII

# Photodegradation of Reactive Blue 19 on $TiO_2$

*The work described in this chapter was performed with Ida Nuramdhani and Faridah Abu Bakar.*

## *8.1 Introduction*

Industrial dye wastewater is one of the most prominent pollutants of the modern world.[323] Modern reactive dyes in solution can be toxic[324] and mutagenic,[325] posing environmental and health problems even at low concentrations.[326] Such dyes are often near-impossible to biodegrade and are resistant to fading when exposed to light, hot water or various chemicals.[327] Therefore, it is imperative to fully explore more effective, efficient and environmentally benign methods of dye degradation.

Titanium dioxide has been used for photocatalytic applications ever since Fujishima and Honda's seminal work demonstrated its water-splitting capability,[3] and the degradation of dye in water under broad-spectrum (*i.e.* mimicking solar) light is a popular method of gauging $TiO_2$ nanomaterial photocatalytic activity.[16,328–331] While many researchers use simple dyes such as methylene blue (currently an ISO standard for measuring photocatalytic activity[332]), such dyes decolourise easily in comparison to those currently used by industry,[194,333] and are therefore do not necessarily model industrial dye degradation.

Reactive dyes represent about 20-30% of the total dye market, and are amongst the most popular substances for colouring cellulosic fibres.[334] These dyes usually contain reactive functional groups tailored to undergo addition or substitution reactions with textile fibres, producing covalent bonds that enhance stability and provide greater colour-fastness.[327] The anthraquinone-

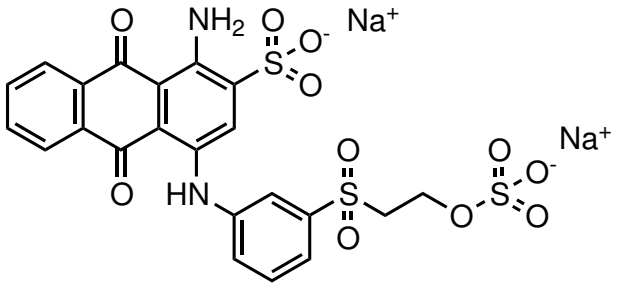


**Figure 8.1.** The chemical structure of the dye Reactive Blue 19 (RB19).

based reactive dye C.I. Reactive Blue 19 (RB19, Figure 8.1) is one of the most widely used reactive dyes.[335,336] It maintains colour under both acidic and basic conditions and can chemically bind to substrate fibres *via* a vinyl sulfone "anchor" group.[335,337,338] Despite these features, the degree of fixation of RB19 to cotton rarely exceeds 80%, with 20–25% of the dye emerging as chemical waste. The half-life of RB19 under natural conditions (pH 7, 25°C) has been estimated in excess of forty years,[339] so RB19-containing wastewater may still have a significant impact on the environment long after it has been discharged.

In this chapter, a number of previously-synthesised $TiO_2$ nanomaterials (see Chapters 4, 5, and 7) are trialled as photocatalysts, using the degradation of the dye Reactive Blue 19 as a model reaction. Initial studies use Aeroxide P-25 by Evonik, a commercially-available titanium dioxide nanomaterial and NIST standard,[302] to examine how conditions affect photocatalytic acitivty. Following from this, the effect of specific variations in the synthetic method on photocatalytic activity is explored, with $TiO_2$ synthesised by hydrolysis in ethanol, thermal degradation of peroxotitanic acid, and arc discharge being trialled. Finally, two more detailed studies, on fluoride-modified $TiO_2$ and on Au@$TiO_2$ materials were performed. In all cases a broad-spectrum light designed to mimic natural sunlight was used to evaluate photocatalytic activity, although this could also be filtered to block out the UV component. Hydrogen peroxide was used in sub-stoichiometric (1:10 molar ratio of $H_2O_2$:dye) amounts as an electron acceptor: at this concentration it has been shown to accelerate the photocatalytic reaction without causing appreciable photodegradation of the chemical dye on its own.[340]

**Table 8.1.** List of conditions used in photocatalysis.

| Label | Description |
|---|---|
| 2 | pH adjusted to 2 using HCl. |
| 3 | pH adjusted to 3 using HCl. |
| 3 (buffer A) | pH buffered at 3 using 50 mmol potassium hydrogen phthalate + 22.3 mmol HCl. |
| 3 (buffer B) | pH buffered at 3 using 98.23 mmol $CH_3COOH$ + 1.77 mmol $CH_3COONa$. |
| N | no pH adjustment. |
| 7 | pH adjusted to 7 using NaOH. |
| 7 (buffer A) | pH buffered at 7 using 50 mmol $KH_2PO_4$ + 29.1 mmol NaOH. |
| 7 (buffer B) | pH buffered at 7 using 75.6 mmol $Na_2HPO_4$ + 24.4 mmol HCl. |
| 9 | pH adjusted to 9 using NaOH. |
| 10 | pH adjusted to 10 using NaOH. |
| 10 (buffer A) | pH buffered at 10 using 96.64 mmol $Na_2HPO_4$ + 3.36 mmol NaOH. |
| 10 (buffer B) | pH buffered at 10 using 12.5 mmol $Na_2B_4O_7 \cdot 10\,H_2O$ + 18.3 mmol NaOH. |

## *8.2 Experimental*

Photocatalytic studies were performed by monitoring the degradation of the industrial dye Reactive Blue 19 (RB19). General methodology was developed,[340] and is described below.

Dye stock solutions were prepared by dissolving 0.08 g of RB19 powder in 1 L of Milli-Q purified water. A slurry of dye solution (100 mL) and the catalyst to be studied (30 mg) was placed in a clean, dry quartz tube (total volume 160 mL). The slurry was stirred for five minutes and sonicated for fifteen minutes to ensure that the catalyst was homogeneously dispersed prior to the start of the reaction. Initial pH was set using either hydrochloric acid and sodium hydroxide, or a range of buffers to provide a constant pH during the reaction. A list of buffers and pH adjustments are given in Table 8.1.

Hydrogen peroxide was typically used in sub-stoichiometric amounts to aid the photocatalytic reaction: when used, it was added subsequent to pH adjustment. It should be noted that the amount of hydrogen peroxide required to totally degrade 1 mol of RB19 dye is estimated at approximately 40 moles, and thus even a 1:1 molar ratio of dye to peroxide is insufficient to cause significant mineralisation.

Photocatalytic reactions were conducted in an optically sealed photolysis chamber equipped with an Ushio UXL-500D-O 500 W broad spectrum Xe lamp, designed to mimic the spectrum of natural sunlight as observed at ground level. When determining visible-light photocatalytic activity, an Ocean Optics high pass filter was used to block all light of wavelength $\lambda < 395$ nm. The light flux was monitored to ensure that it was constant across all experiments.

The dye-catalyst slurry in the quartz tube was placed into the chamber and stirred magnetically for fifteen minutes without illumination. Following this, a 3 mL sample was withdrawn *via* syringe and the lamp was turned on. Further samples were withdrawn at 15, 30, 40, 60, 90, and 120 minutes after the start of irradiation. Each sample was centrifuged for three minutes at 13000 RPM and then decanted, with the supernatant being centrifuged again under the same conditions to remove final traces of catalyst. This process was necessary as previous study had shown that one centrifugation treatment would not remove all traces of catalyst, resulting in light scattering and variation in subsequent UV-vis characterisation. The resultant solution was stored under refrigeration (4°C) in the dark prior to characterisation. In all cases characterisation occurred within eight hours of sample acquisition.

Photodegradation product solutions were characterised by UV-vis spectroscopy. UV-visible spectra were recorded between 400 and 700 nm using a Cary 100 Bio UV-vis spectrophotometer. The dye's absorption maximum occurs at $\lambda = 593$ nm (Figure 8.2), with a molar absorption coefficient of $\eta = 7270$ L mol$^{-1}$ cm$^{-1}$. In none of the experiments did the absorbance exceed 0.7.

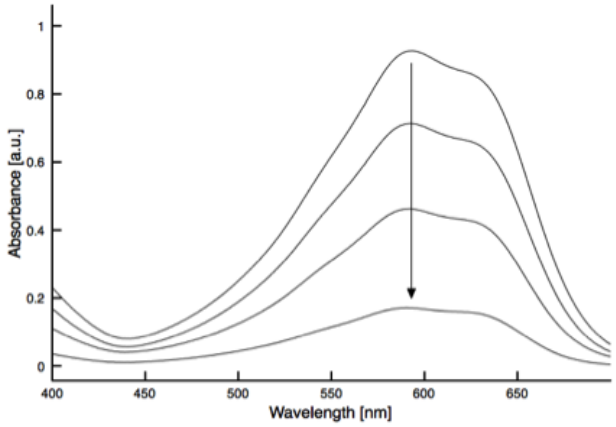


**Figure 8.2.** The UV-visible absorption spectrum of RB19 dye in water. The absorption maximum of the dye occurs at $\lambda = 593$ nm.

## *8.3 Results*

### *8.3.1 Blanks*

In order to minimise the extent of decolourisation due to non-photocatalytic processes, the amount of catalyst used was optimised in the range 100-500 mg $L^1$. Even at the highest catalyst loadings, the absorption decrease after eighty minutes was <0.5%, and was probably due to the adsorption of the dye onto the titania surface.[341] Such changes are insignificant in comparison to those observed upon illumination. In all further reactions, a catalyst loading of 300 mg $L^1$ was used. This loading showed minimal dye adsorption but was also large enough to eliminate errors in weighing of the catalyst.

### *8.3.2 Breakdown kinetics*

The breakdown of dye on a a heterogeneous catalyst surface is best modelled by Langmuir-Hinshelwood (L-H) kinetics.[16,341] For a surface-catalyzed, unimolecular reaction of a reactant on a solid surface, the rate $r$ is given by:

$$r = \frac{kKC}{1 + KC} \tag{8.1}$$

where $k$ is the rate coefficient of the reaction, $C$ the concentration of reactant solution and $K$ the equilibrium constant for the adsorption of the reactant

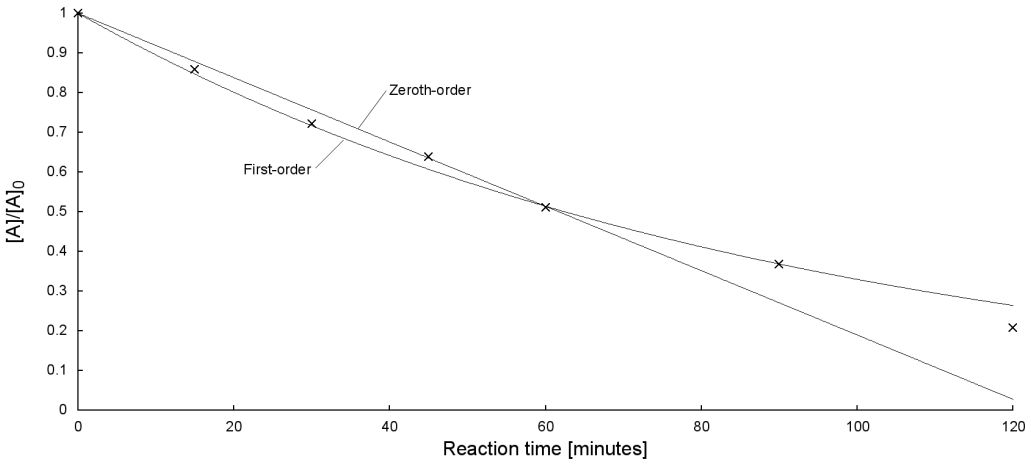


**Figure 8.3.** Zero- and first-order kinetic plots for the degradation of RB-19 on P-25 titanium dioxide. Crosses indicate experimental data. Performed at natural pH with 1:1 molar ratio of $H_2O_2$:dye.

onto the catalyst. Equation 8.1 simplifies to either zero- or first-order kinetics in the limiting cases of either very high ($C \gg 1$) or very low ($C \ll 1$) dye concentration, respectively. Thus, a number of studies of dye photodegradation model the rate as first-order with respect to the dye species.[17,342,343]

Initial studies were performed to determine if the photodegradation of RB19 on titanium dioxide at the concentrations used in this study followed either of the limiting L-H cases. In the case of zero-order and first-order reactions respectively, plots of $A_0 - A$ or $\ln(A_0/A)$ versus time should be linear, with slope $k$. It was found, however, that the reaction followed neither of these limiting cases (Figure 8.3), falling somewhere in between.

More generally, Equation 8.1 indicates that for a reaction obeying L-H kinetics, a plot of $1/r$ versus $1/C$ will give a straight line with slope $1/kK$ and intercept $1/k$. The instantaneous rate of the reaction was estimated by the change in concentration over a given period, but there was no strong linear correlation between $1/r$ and $1/C$, suggesting that this reaction does not obey the L-H model (Figure 8.4). This is possibly due to interference caused by the presence of photodegradation byproducts with absorption profiles closely matching that of RB19,[344] or due to the existence of multiple degradation mechanisms. The effect of changing pH on the rate of reaction cannot be

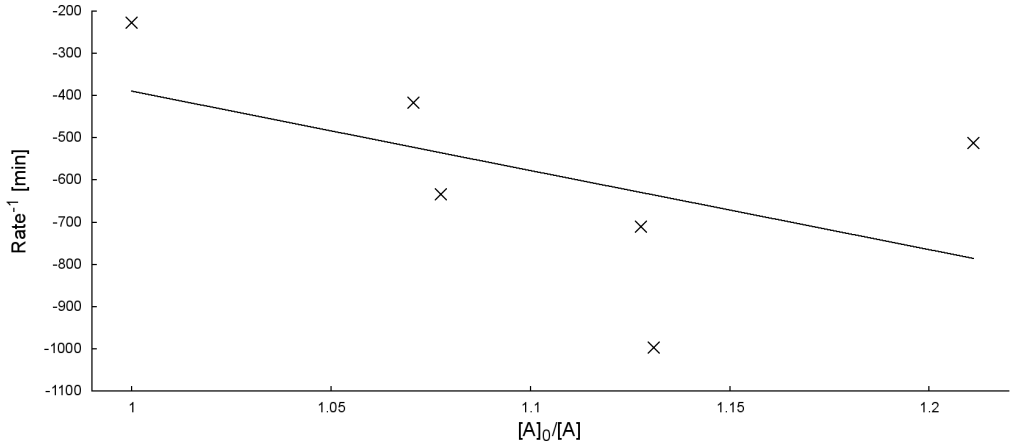


**Figure 8.4.** Attempted Langmuir-Hinschelwood fitting for the photodegradation of RB-19 on P-25 at natural pH using a 0.1:1 $[H_2O_2]$:[dye] ratio. Points show experimental data, line shows nearest fit of the L-H equation.

disregarded here either, as no buffer system was used in these initial studies.

While the above observations suggest that simple (pseudo-)first-order kinetics may not accurately reflect the mechanism of degradation for this dye, it can be seen that the rate of reaction can nonetheless be *approximated* to such kinetics. In this way the rate coefficient can be found, which is a more meaningful figure than a simple measure of percentage degradation over time. In the following chapter, the extent of degradation will be reported as both first-order rate coefficient $k$ and extent of degradation after two hours of irradiation.

### *8.3.3 Effect of pH and buffer on photodegradation using Aeroxide P-25 $TiO_2$*

The commercially-available titanium dioxide catalyst P-25 is commonly used as a standard in photocatalysis and photodegradation studies, and was recently recognised as such by the US National Institute of Standards and Technology.[302] In this study, P-25 titania was used as a model catalyst to determine the effect of pH, buffer and hydrogen peroxide concentration on the rate of photodegradation of RB-19. A series of photodegradation reactions were run with pH adjusted using methods described in Table 8.1, and $H_2O_2$ concentrations of 0, 0.1 and 1 mole equivalents compared to the dye.

Results are shown in Figure 8.5 and Table 8.2. It is interesting to note that uncertainty in the rate coefficient for these reactions does not appear to appreciably decrease when buffer is introduced to the system. This suggests that variations from first-order kinetics are due to effects other than that of varying pH.

In a number of cases an increase in $H_2O_2$ concentration is concomitant with an increase in the extent of photodegradation. Deviation from this pattern occurs in several neutral and basic systems, and above pH 9 the extent of degradation appears possibly independent of $H_2O_2$ concentration. Dye degradation in the presence of $TiO_2$ is known to occur by either *direct* photodegradation (in which the dye, adsorbed onto the $TiO_2$ surface, acts as an electron acceptor), or *indirect* photodegradation (in which radicals are formed on the $TiO_2$ surface, desorb, and attack the dye in solution (Figure 8.6).[345] Surface radical formation on $TiO_2$ is generally accepted to proceed *via* one of two mechanisms:[344,346]

$$H_2O_{surf} + h^+_{vb} \longrightarrow OH^{\cdot} + H^+ \tag{8.2}$$

$$OH^-_{surf} + h^+_{vb} \longrightarrow OH^{\cdot} \tag{8.3}$$

Equation 8.2 is independent of pH, and accounts for hydroxyl production in both acidic and basic media. Equation 8.3, however, depends on the concentration of hydroxide ions near the catalyst surface, and thus proceeds more efficiently in basic solution. As the pH increases, dye degradation may also occur *via* these photogenerated $OH^{\cdot}$ radicals, and is no longer reliant on solution $H_2O_2$. In addition, hydrogen peroxide has been shown to impede photocatalysis in the presence of hydroxyl radicals, as would be the case in a high-pH environment:[347]

$$H_2O_2 + OH^{\cdot} \longrightarrow H_2O + HO^{\cdot}_2 \tag{8.4}$$

$$HO^{\cdot}_2 + OH^{\cdot} \longrightarrow H_2O + O_2 \tag{8.5}$$

The rate of degradation shows dependence upon the pH of the solution,

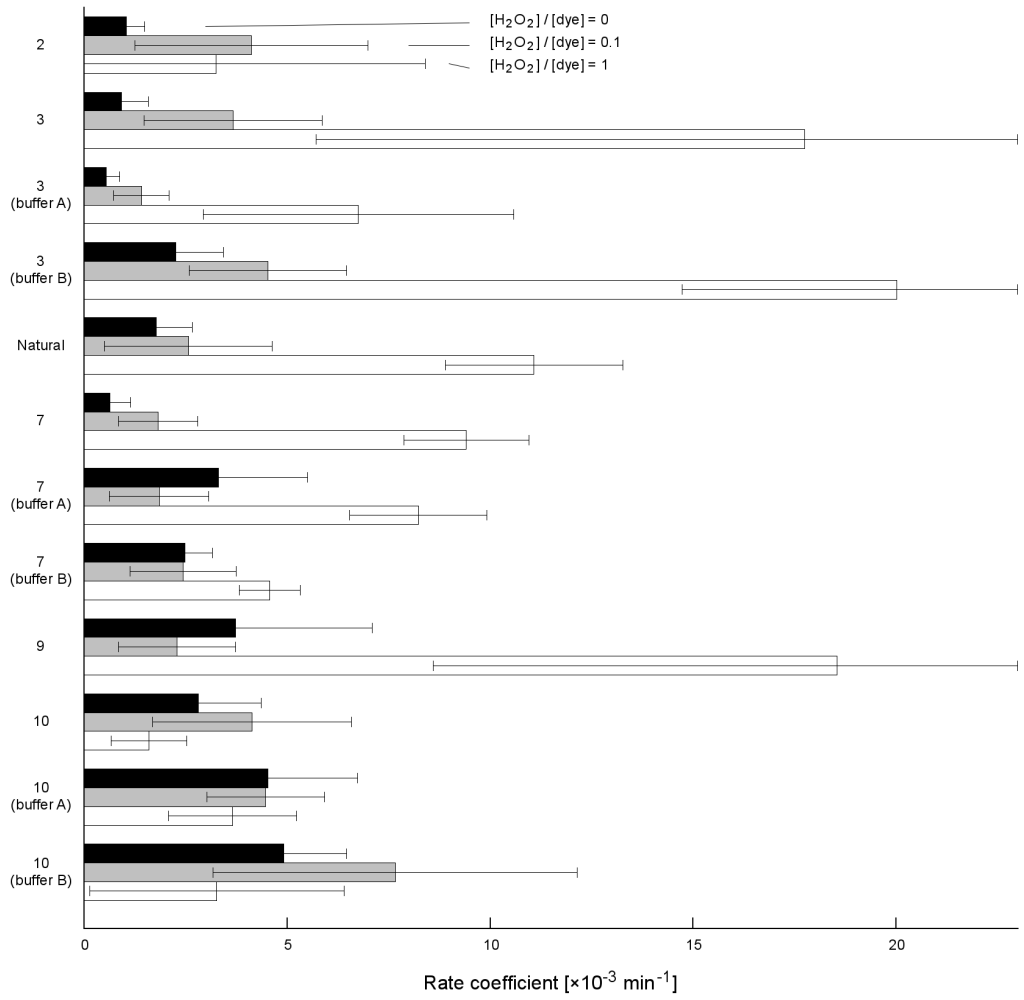


**Figure 8.5.** Effect of pH, buffer and $H_2O_2$ concentration on rate coefficient for the first-order degradation of RB-19 on P-25. Error bars show 95% CI.

**Table 8.2.** Table of (first-order) rate coefficients and % degradation (after 120 minutes) of RB-19 on P-25 under various pH and $H_2O_2$ conditions. Errors indicate 95% CI.

| pH | $[H_2O_2]$:[dye] | % deg. | $k$ [$\times 10^{-3}$ $min^{-1}$] |
|---|---|---|---|
| 2 | 0 | 10.7 | 1.06±0.44 |
| | 0.1 | 29.6 | 4.13±2.87 |
| | 1 | 58.7 | 3.26±5.15 |
| 3 | 0 | 12.6 | 0.92±0.67 |
| | 0.1 | 26.5 | 3.68±2.19 |
| | 1 | 82.3 | 17.76±12.03 |
| 3 (buffer A) | 0 | 5.3 | 0.56±0.33 |
| | 0.1 | 11.9 | 1.42±0.68 |
| | 1 | 44 | 6.77±3.82 |
| 3 (buffer B) | 0 | 21 | 2.26±1.18 |
| | 0.1 | 32.6 | 4.53±1.94 |
| | 1 | 91 | 20.02±5.28 |
| N | 0 | 14.5 | 1.79±0.89 |
| | 0.1 | 17.5 | 2.58±2.07 |
| | 1 | 79.2 | 11.09±2.18 |
| 7 | 0 | 7.3 | 0.64±0.51 |
| | 0.1 | 14.9 | 1.83±0.98 |
| | 1 | 72 | 9.43±1.54 |
| 7 (buffer A) | 0 | 25.2 | 3.33±2.18 |
| | 0.1 | 12.8 | 1.86±1.22 |
| | 1 | 68.5 | 8.24±1.69 |
| 7 (buffer B) | 0 | 24.7 | 2.49±0.68 |
| | 0.1 | 27.8 | 2.45±1.31 |
| | 1 | 43.6 | 4.58±0.75 |
| 9 | 0 | 22.6 | 3.74±3.37 |
| | 0.1 | 17.1 | 2.3±1.44 |
| | 1 | 96.6 | 18.56±9.95 |
| 10 | 0 | 26.1 | 2.82±1.56 |
| | 0.1 | 26.6 | 4.15±2.45 |
| | 1 | 22.4 | 1.61±0.93 |
| 10 (buffer A) | 0 | 35.2 | 4.53±2.21 |
| | 0.1 | 38.7 | 4.48±1.45 |
| | 1 | 39.9 | 3.67±1.58 |
| 10 (buffer B) | 0 | 47.7 | 4.92±1.55 |
| | 0.1 | 48.9 | 7.67±4.48 |
| | 1 | 43.8 | 3.28±3.13 |

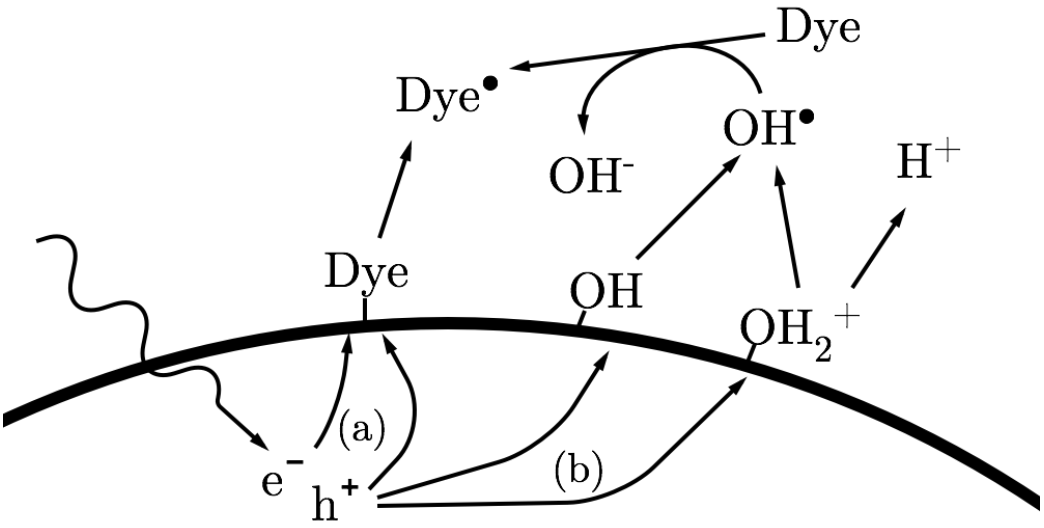


**Figure 8.6.** Possible means of dye photodegradation in the presence of $TiO_2$. Dye may degraded by the action of photogenerated electrons or holes on the surface of the catalyst (direct photodegradation, a) or in solution by hydroxyl radicals (indirect photodegradation, b).

proceeding the slowest in neutral or near-neutral conditions and the fastest under basic pH (although consistently rapid degradation is reported under acid conditions when a 1:1 $H_2O_2$:dye ratio is employed). These results are consistent with the assumption that degradation proceeds *via* two mechanisms: one which is pH-independent, and one which is dependent upon formation of photogenerated $OH^{\cdot}$ as described above, and thus becomes more prominent as pH increases, but is either minimally dependent or completely independent of $H_2O_2$ concentration. The decrease in degradation as pH approaches 7 can be explained by the tendancy of $TiO_2$ in solution to aggregate as the pH of the solution approaches the point of zero charge (pzc) of the material. At this point (generally agreed to be around 6[348–350]), the titania surface is uncharged, which encourages aggregation of the catalyst and reduces the effective surface area of the catalyst.

In order to better understand the link between pH and photocatalytic ability, these two variables are plotted together in Figure 8.7 with the initial $H_2O_2$:dye ratio kept constant at 0.1:1. This graph clearly demonstrates the link between extent of photodegradation and pH, but also illustrates how

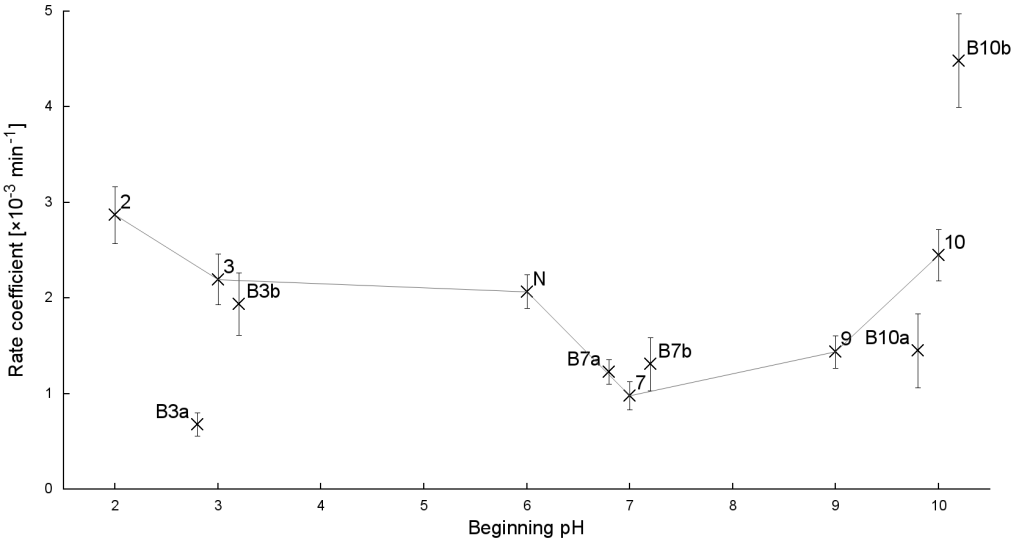


**Figure 8.7.** RB-19 photodegradation on P-25: first-order rate coefficient as a function of pH. The solid line shows the activity of adjusted (non-buffered) solutions. For all experiments shown, the initial $H_2O_2$:dye molar ratio was kept constant at 0.1:1. Buffered samples are offset from actual pH to aid in readability. Error bars show 95% CI.

buffer can drastically affect photodegradation. Importantly, the extent of photodegradation changes not only between buffered and adjusted cases, but also between different buffers at the same pH.

At pH 3, both buffers result in a drop in overall activity, possibly due to their pH-stabilising function. The phthalate buffer (3a) has a more significant inhibitory effect on the system than the acetic acid bufer (3b). It has previously been shown[351] that phthalate may bind to the titania surface (possibly helped by a combination of bidentate binding[352] and $\pi$-interactions[353]), an effect that cannot be reversed by UV irradiation. While acetic acid (3b) will also bind to the titania surface, it lacks the phthalate ion's aromatic system and is much easier to remove either by photodegradation or by water-aided dissociation.[4] While bound, acetic acid may improve the activity of the photocatalyst through either electronic alteration[351] or enhancement of electron transfer.[352]

The overall effect of buffer is minimal at pH 7, with both buffers having a very similar effect on the rate coefficient. This correlates well with the fact

that the two buffers ($KH_2PO_4$ and $Na_2HPO_4$) are chemically very similar.

At pH 10, both buffers had a significant effect on to the rate of degradation. At this pH, a decrease in the pH of the unbuffered system (due to acidic byproducts of photodegradation) would be detrimental to the overall rate of reaction: therefore, it is expected that the presence of buffer would improve the activity of the system. It has previously been shown that phosphate ions may poison $TiO_2$ catalysts by adsorbtion onto the catalyst surface.[306] While phosphate is relatively labile to sorption in alkaline media, it may still compete with RB19 dye for adsorption sites. This may explain why use of the phosphate buffer (10a) results in a drop in photocatalytic activity. The higher degradation efficiency of the system buffered using tetraborate (10b) could also be explained by the fact that under these conditions tetraborate reacts with hydrogen peroxide to form the perborate anion,[354] which is considered more effective in the oxidative degradation of dyes than hydrogen peroxide.[355]

### *8.3.4 Effect of catalyst fabrication method on photocatalytic ability.*

In previous chapters we have described the synthesis of titanium dioxide by a number of different methods. Here we examine and compare the photocatalytic ability of $TiO_2$ catalysts synthesised by the following distinct methods:

- Hydrolysis in ethanol (e-$TiO_2$: see Section 4.4.2, Figure 8.9)
- Hydrolysis in ethanol, followed by calcination at 500°C for 2 hours (c-$TiO_2$: Figure 8.10)
- Thermal degradation of peroxotitanic acid (p-$TiO_2$: see Section 4.4.2, Figure 8.11)
- Arc discharge synthesis (a-$TiO_2$: see Section 4.3, $TiO_2$-60-300R, Figure 8.12)

Characterisation of materials is detailed in the referenced sections, and SEM comparison of e-$TiO_2$ and c-$TiO_2$ is shown in Figure 8.8. In the first three cases, photocatalytic reactions were performed using $H_2O_2$:dye molar ratios of 0, 1:10 and 1:1. a-$TiO_2$ was initially trialled using a 1:10 $H_2O_2$:dye

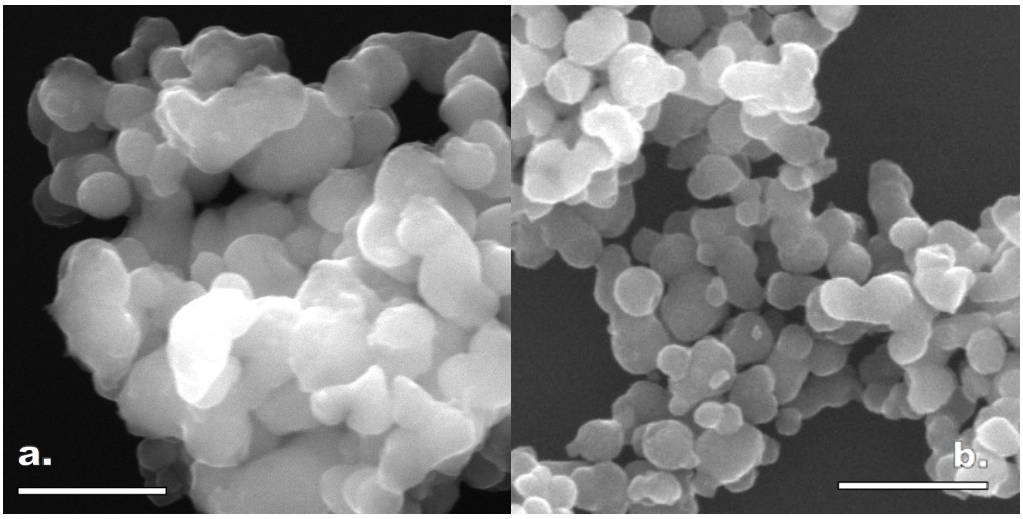


**Figure 8.8.** SEM images of (a) e-$TiO_2$ and (b) c-$TiO_2$. Scale bar indicates 500 nm.

molar ratio, and found to be particularly ineffective at photodegradation of RB19; further studies were not conducted. All catalysts were trialled at natural pH, as well as at pH values of 3, 7 and 10 (buffered using "b" series buffers, Table 8.1, to maintain pH throughout the reaction). In addition, p-$TiO_2$ and e-$TiO_2$ were trialled at pH 3, 7 and 10 adjusted by HCl/NaOH.

Figure 8.9 shows the rate coefficient for the photodegradtion of of RB19 on e$-TiO_2$ (data presented in Table 8.3). Similar to P-25, this catalyst is least active around the pzc of $TiO_2$, although it is more active under acidic than basic conditions. This suggests that hydroxyl production is less prevalent for e$-TiO_2$ than for P-25. In the majority of cases, an increase in $H_2O_2$ concentration results in an increase in degradation, although at pH 7 this is not always the case. It may be that the high concentration of $H_2O_2$ encourages the breakdown of surface-generated $OH^{\cdot}$ before it is able to react with dye molecules (see Equation 8.4): the low effective surface area at pH $\approx$ 6–7 results in a low rate of hydroxyl radical production, which means that such peroxide-mediated breakdown has a considerable effect on the overall hydroxyl population.

Figure 8.10 shows the rate of degradation of RB19 on c$-TiO_2$ (data presented in Table 8.4). Similar to e$-TiO_2$, activity was highest at pH 3

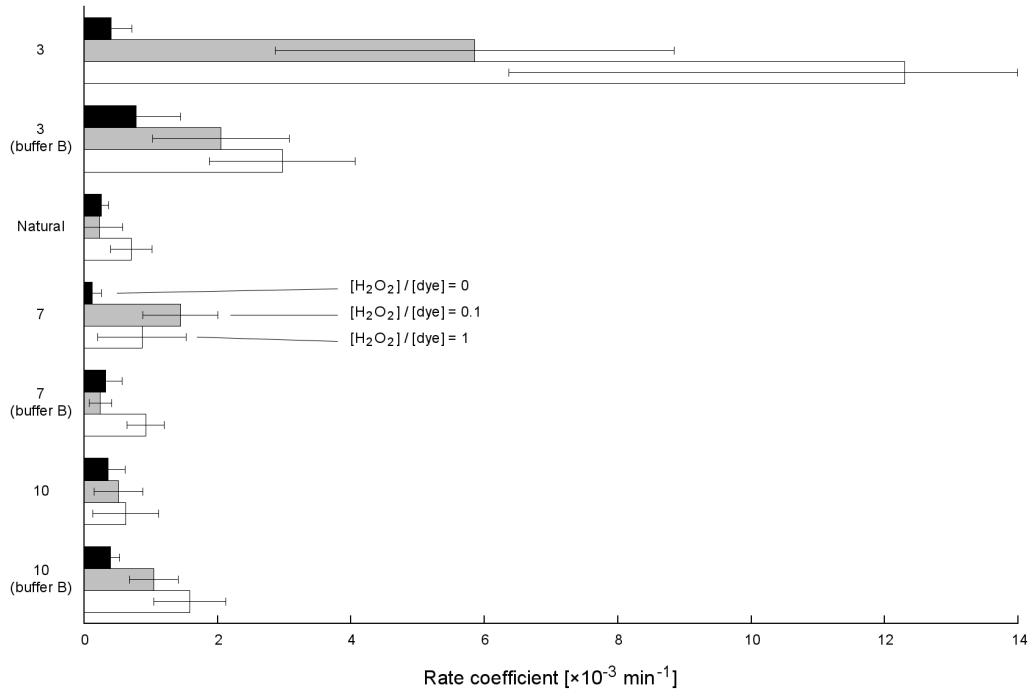


**Figure 8.9.** First-order rate coefficients for the photodegradation of RB19 on e-$TiO_2$. Error bars indicate 95% CI.

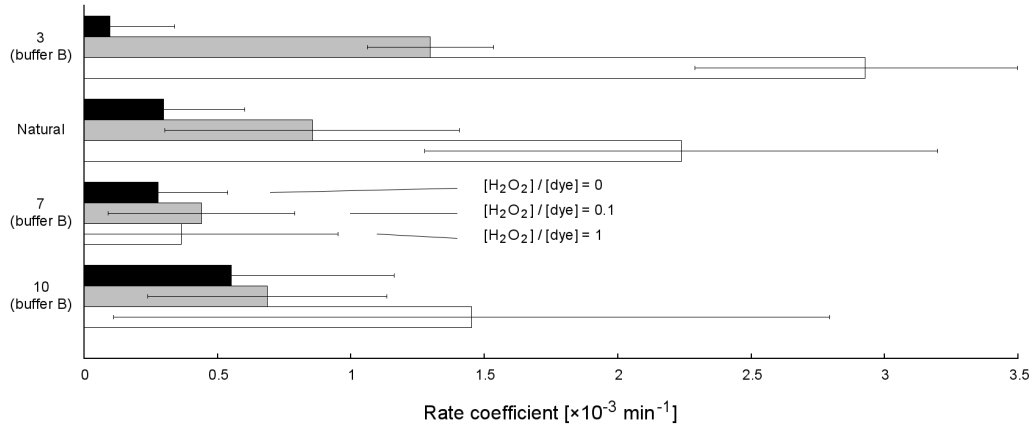


**Figure 8.10.** First-order rate coefficients for the photodegradation of RB19 on c-$TiO_2$. Error bars indicate 95% CI.

**Table 8.3.** Table of (first-order) rate coefficients and % degradation (after 120 minutes) of RB-19 on e-$TiO_2$. Errors indicate 95% CI.

| pH | $[H_2O_2]$:[dye] | % deg. | $k$ [$\times 10^{-3}$ $min^{-1}$] |
|---|---|---|---|
| 3 | 0 | 5.6 | 0.41±0.32 |
| | 0.1 | 41.5 | 5.86±2.99 |
| | 1 | 85.6 | 12.31±5.93 |
| 3 (buffer B) | 0 | 13.1 | 0.79±0.66 |
| | 0.1 | 22.6 | 2.06±1.03 |
| | 1 | 32.5 | 2.98±1.09 |
| N | 0 | 2.5 | 0.27±0.11 |
| | 0.1 | 2.6 | 0.24±0.35 |
| | 1 | 8.4 | 0.71±0.31 |
| 7 | 0 | 2.7 | 0.13±0.14 |
| | 0.1 | 18.5 | 1.45±0.56 |
| | 1 | 12.1 | 0.87±0.66 |
| 7 (buffer B) | 0 | 3.9 | 0.33±0.24 |
| | 0.1 | 2.4 | 0.25±0.17 |
| | 1 | 10.8 | 0.93±0.28 |
| 10 | 0 | 5.1 | 0.37±0.26 |
| | 0.1 | 5.9 | 0.52±0.37 |
| | 1 | 9.8 | 0.63±0.49 |
| 10 (buffer B) | 0 | 5.6 | 0.4±0.13 |
| | 0.1 | 9.5 | 1.05±0.37 |
| | 1 | 18.4 | 1.59±0.54 |

**Table 8.4.** Table of (first-order) rate coefficients and % degradation (after 120 minutes) of RB-19 on c-$TiO_2$. Errors indicate 95% CI.

| pH | $[H_2O_2]$:[dye] | % deg. | $k$ [$\times 10^{-3}$ $min^{-1}$] |
|---|---|---|---|
| 3 (buffer B) | 0 | 2.8 | 0.1±0.24 |
| | 0.1 | 16.4 | 1.3±0.24 |
| | 1 | 29.2 | 2.93±0.64 |
| N | 0 | 3.1 | 0.3±0.3 |
| | 0.1 | 7 | 0.86±0.55 |
| | 1 | 20.4 | 2.24±0.96 |
| 7 (buffer B) | 0 | 4.4 | 0.28±0.26 |
| | 0.1 | 4.2 | 0.44±0.35 |
| | 1 | 9.2 | 0.37±0.59 |
| 10 (buffer B) | 0 | 7.4 | 0.55±0.61 |
| | 0.1 | 8.8 | 0.69±0.45 |
| | 1 | 21.7 | 1.45±1.34 |

and lowest around the pzc of $TiO_2$. As with e$-TiO_2$, activity is generally proportional to $H_2O_2$ concentration except around pH 7. Of note, c$-TiO_2$ is slightly less active than e$-TiO_2$ at low pH.

Figure 8.11 shows the rate of degradation of RB19 on p$-TiO_2$ (data presented in Table 8.5). p$-TiO_2$ is most active at low pH, much like other materials studied in this section, although it is consistently more active than either e$-TiO_2$ or c$-TiO_2$.

Figure 8.12 shows the extent of degradation of RB19 when using a$-TiO_2$ as a catalyst (data presented in Table 8.6). Initial studies showed that this catalyst was considerably less active than other materials studied in this section, and further studies were not attempted.

In order to better compare these catalysts, a composite graph of rate coefficients ($H_2O_2$:dye molar ratio kept constant at 1:10) is shown in Figure 8.13. Once again it is clearly shown that extent of photodegradation is strongly dependent upon pH, although in this case activity is highest at pH 3 for most catalysts. Buffer also has a significant effect, increasing activity at pH 10 and decreasing it at pH 7. The effect is more complex at pH 3: buffering increases the activity of p-$TiO_2$, but decreases that of e-$TiO_2$. It is unknown why buffer inhibits degradation on e-$TiO_2$ at pH 3, but the effect is observed when an $H_2O_2$:dye molar ratio of 1:1 is used as well (Figure 8.9).

p-$TiO_2$ is generally the most active of the trialled catalysts, and a-$TiO_2$ the least active. SEM studies (details in relevant chapters as referred to above) show that p-$TiO_2$ is considerably smaller than other $TiO_2$ materials studied here, resulting in a higher surface area for this material. a-$TiO_2$ was the only catalyst which was synthesised in a non-aqueous environment: it was generally found that this material was difficult to disperse in water, and this could lead to irreversible aggregation and precipitation during the experiment.

Calcination of e-$TiO_2$ to form c-$TiO_2$ results in smaller and more crystalline particles, but this does not necessarily improve the activity of the catalyst. At pH 3, e-$TiO_2$ is still the more active of the two, while at pH 6 and 7 c-$TiO_2$ appears slightly more active and at pH 10 the two are very similar in activity. Similar hydrolytic methods[356] have reported the formation of mesopores in the product: it may be that e-$TiO_2$ contains such pores,

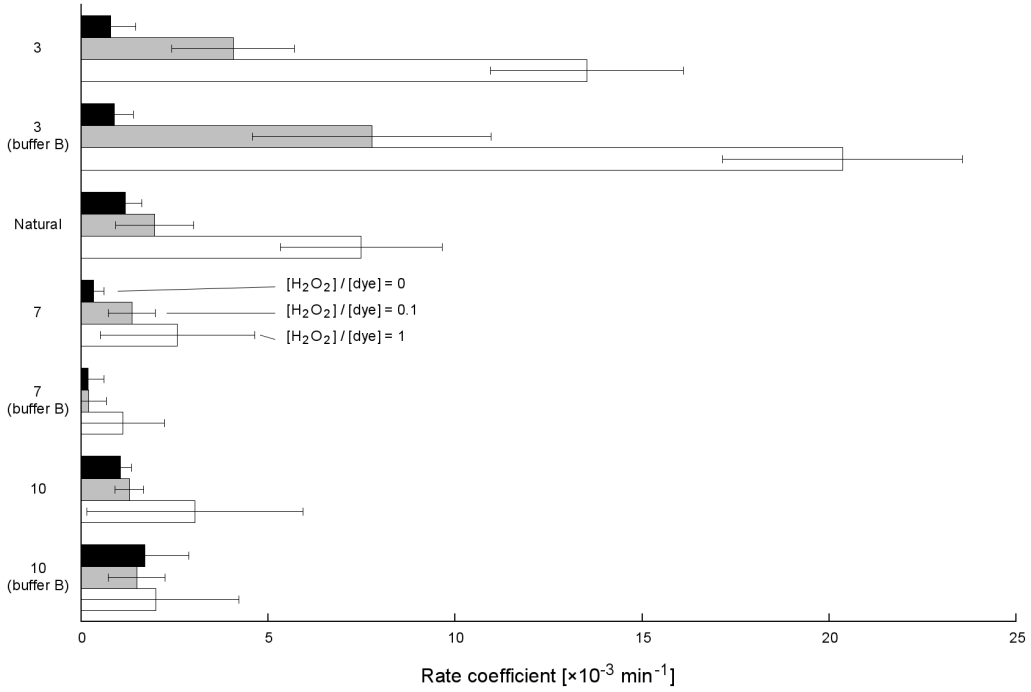


**Figure 8.11.** First-order rate coefficients for the photodegradation of RB19 on p-$TiO_2$. Error bars indicate 95% CI.

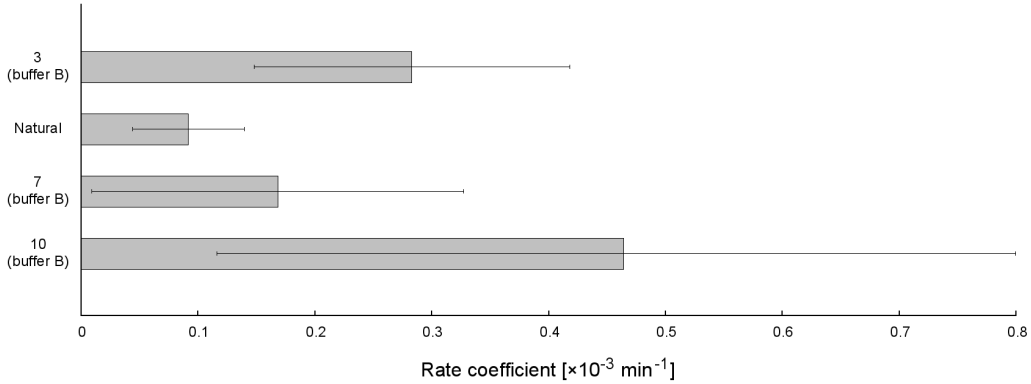


**Figure 8.12.** First-order rate coefficients for the photodegradation of RB19 on a-$TiO_2$. $H_2O_2$ was used in a 0.1:1 molar ratio with dye. Error bars indicate 95% CI.

**Table 8.5.** Table of (first-order) rate coefficients and % degradation (after 120 minutes) of RB-19 on p-$TiO_2$. Errors indicate 95% CI.

| pH | $[H_2O_2]$:[dye] | % deg. | $k$ [$\times 10^{-3}$ $min^{-1}$] |
|---|---|---|---|
| 2 | 0 | 7 | 0.8±0.67 |
| | 0.1 | 32.6 | 4.08±1.64 |
| | 1 | 79.1 | 13.54±2.58 |
| 3 | 0 | 12.6 | 0.89±0.51 |
| | 0.1 | 49.4 | 7.78±3.19 |
| | 1 | 90.8 | 20.38±3.21 |
| 3 (buffer A) | 0 | 12.2 | 1.19±0.43 |
| | 0.1 | 16.5 | 1.97±1.04 |
| | 1 | 64.6 | 7.5±2.17 |
| 3 (buffer B) | 0 | 4.2 | 0.35±0.27 |
| | 0.1 | 14.5 | 1.37±0.63 |
| | 1 | 17.5 | 2.58±2.07 |
| N | 0 | 3.5 | 0.2±0.42 |
| | 0.1 | 5.1 | 0.21±0.47 |
| | 1 | 16.5 | 1.12±1.11 |
| 7 | 0 | 11.8 | 1.06±0.29 |
| | 0.1 | 11.4 | 1.3±0.38 |
| | 1 | 38.7 | 3.06±2.89 |
| 7 (buffer A) | 0 | 14.1 | 1.71±1.19 |
| | 0.1 | 16.9 | 1.5±0.76 |
| | 1 | 29.1 | 2.01±2.21 |

**Table 8.6.** Table of first-order rate coefficients and % degradation (after 120 minutes) of RB-19 on a-$TiO_2$. Errors indicate 95% CI.

| pH | $[H_2O_2]$:[dye] | % deg. | $k$ [$\times 10^{-3}$ $min^{-1}$] |
|---|---|---|---|
| 3 (buffer B) | 0.1 | 3.2 | 0.28±0.14 |
| N | 0.1 | 1.3 | 0.09±0.05 |
| 7 (buffer B) | 0.1 | 2.1 | 0.17±0.16 |
| 10 (buffer B) | 0.1 | 8.1 | 0.46±0.35 |

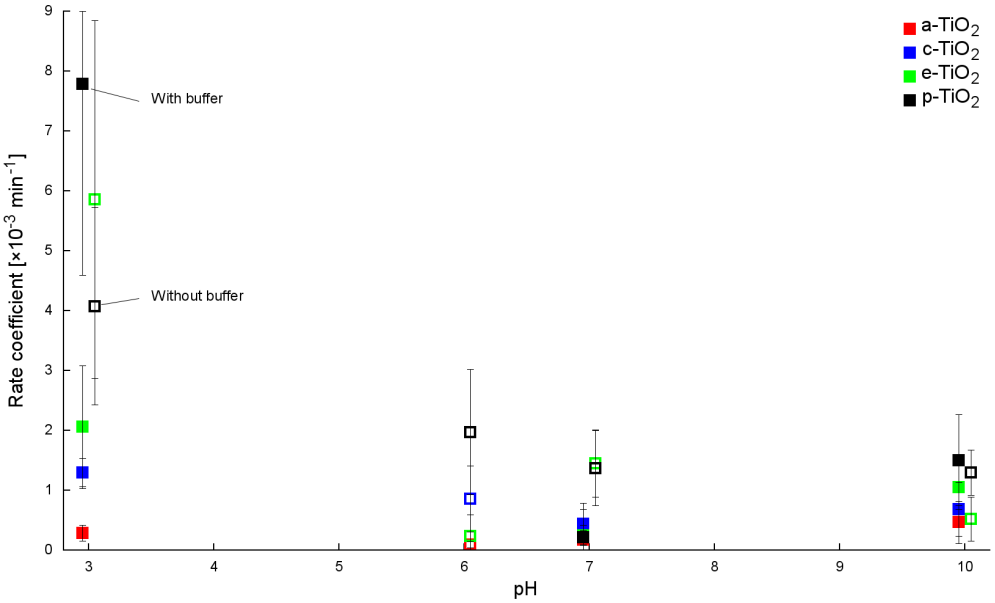


**Figure 8.13.** First-order rate coefficient for photodegradation of RB-19 on various forms of $TiO_2$. [H2O2]:[dye] is set at 0.1:1 for all points. Buffered systems are shown as solid points, unbuffered systems as hollow points, and both systems are slightly offset horizontally for legibility. Error bars show 95% CI.

which collapse upon calcination to give the smaller particles observed in c-$TiO_2$. While the c-$TiO_2$ particles would consequently have a lower surface area, their improved crystallinity would result in lowered electron-hole recombination (due to a decrease in the population of bulk defects) and thus higher activity. However, at pH 3 degradation is governed primarily by direct photodegradation, which requires the adsorption of dye to the catalyst surface. It may be that under these conditions, the reaction is limited by surface area, giving the advantage to the porous e-$TiO_2$. Nitrogen gas adsorption surface area analysis of these materials showed e-$TiO_2$ had a BET surface are of approximately 130 $m^2\ g^{-1}$, which dropped to approximately 30 $m^2\ g^{-1}$ upon calcination. This drastic reduction in surface area supports the above argument.

In conclusion, it was found that the four synthetic methods resulted in catalysts with considerably different activities towards the photodegradation of RB19. The catalysts also showed different responses to the changing initial pH of the system, and to the use of buffer. It is proposed that this is due to the

limiting factors of different photodegradation mechanisms, whose importance is a function of pH. It was found that titania synthesised *via* the thermal degradation of peroxotitanic acid was the most effective catalyst under the given conditions, and this is believed to be due to its high crystallinity and small size, which resulted in a large surface are while minimising exciton recombination.

### *8.3.5 Fluoride-modified $TiO_2$: effect of SMA on activity*

The photocatalytic activity of fluoride-modified $TiO_2$ materials as synthesised in Chapter 5 was measured using the photodegradation of RB19 as a model reaction. Photocatalytic ability was determined under both broad-spectrum (UV + visible) and visible ($\lambda > 395$ nm) light in the presence of two buffer solutions (buffers 3b and 10b, see Table 8.1) and without pH modification (pH $\sim$ 6), using a $[H_2O_2]$:[dye] ratio of 0.1:1. First-order rate coefficients for these reactions are shown in Figure 8.14.

P-25 outperforms fluoride-modified $TiO_2$ under both acidic and basic conditions, but under neutral conditions it is slightly less active than several fluoride-modified $TiO_2$ catalysts, *i.e.* $NH_4BF_4{-}TiO_2$, $NH_4PF_6{-}TiO_2$ and $NBu_4PF_6{-}TiO_2$. The use of fluoride in synthesis may result in a $TiO_2$ catalyst with a fluorinated surface: these fluorine groups will reduce the surface charge of the material and will result in a drop in the point of zero charge from $\sim$6.6 to as low as 3.[242] This will result in an improvement in activity at neutral pH as aggregation is minimised, while under acidic conditions aggregation of fluoride-modified $TiO_2$ is considerably more prevalent than for "naked" $TiO_2$.

There is a weak correlation between the size of the cation and the activity of the catalyst: $F^-$-modified catalysts (with the exception of $NH_4F{-}TiO_2$ at pH 3) show relatively poor activity as compared to $BF_4^-$- and $PF_6^-$-modified catalysts. This is believed to be because as cation size increases, particle size decreases. Thus, $BF_4^-$- and $PF_6^-$-modified $TiO_2$ particles are smaller, and the same mass of catalyst has a higher effective surface area than the equivalent mass of $F^-$-modified $TiO_2$. While the substitution of ammonium for tetrabutylammonium anion appears to have no *systematic* impact on the

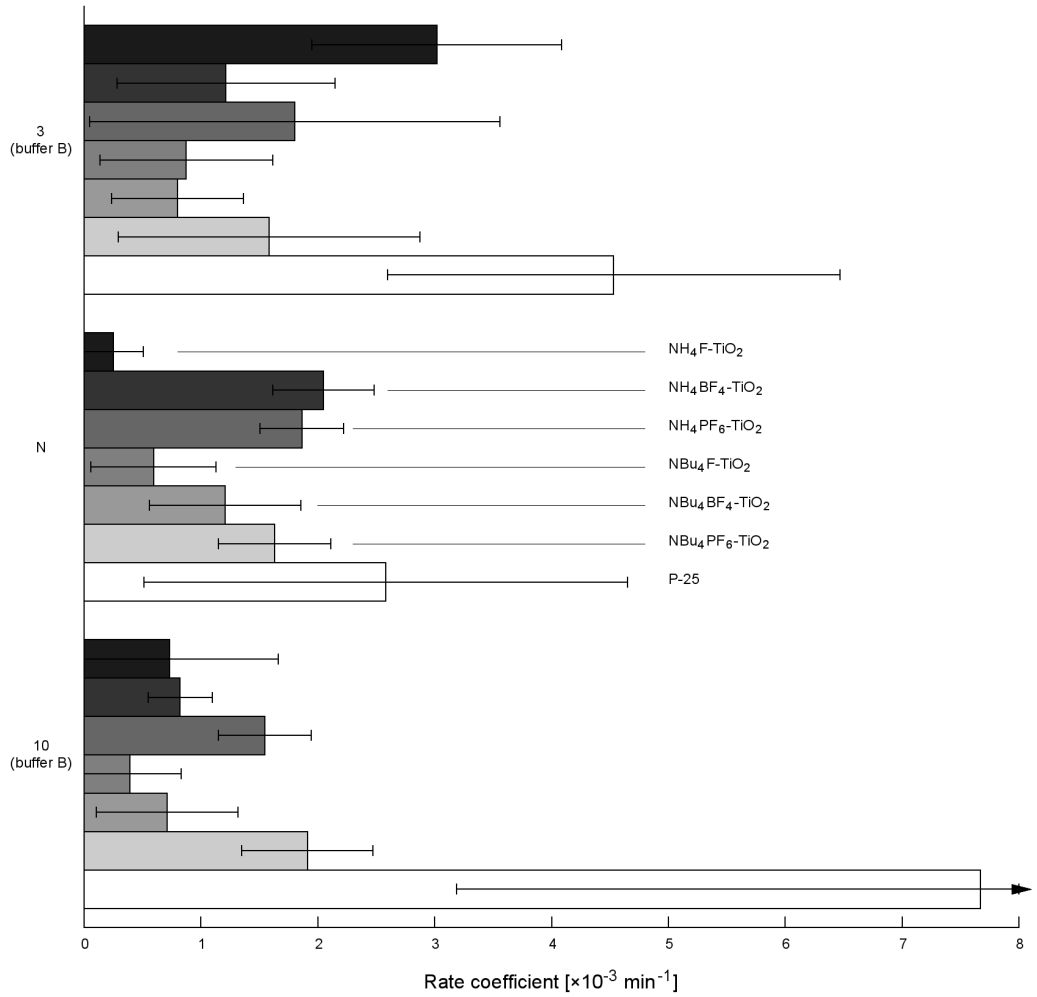


**Figure 8.14.** First-order rate coefficients for the photodegradation of RB-19 on fluoride-modified $TiO_2$ at differing buffer conditions. Error bars show 95% CI. A 0.1:1 $[H_2O_2]$:[dye] ratio was used in these reactions. Arrow indicates error bar proceeds off graph axis.

activity of the system, $NBu_4^+$-modified catalysts obey the given trend with less variation (*i.e.* catalytic activity progressively increases as cation size increases across all pH values, a trend that is not observed for ammonium-modified catalysts).

*Normalised photocatalytic activity*

In order to analyse degradation efficiency independent of surface area, the above measures of activity were normalised to catalyst surface area (Figure 8.15). The effectiveness of $PF_6^-$-modified $TiO_2$ is not as prominent as it is when surface are normalisation is not taken into account: instead, $BF_4^-$-modified catalysts are the most active. This trend is apparent for both ammonium- and tetrabutylammonium-modified $TiO_2$.

Data for the photocatalytic activity of fluoride-modified $TiO_2$ (both normalised for surface area, and non-normalised) are shown in Table 8.7.

*pH effect on photocatalytic activity*

The effect of pH change on the photocatalytic activity of P-25 has been discussed previously in this chapter. In order to better visualise the effect of pH on catalyst activity for fluoride-modified $TiO_2$, the data presented in this section is re-plotted in Figure 8.16.

The activity of fluoride-modified $TiO_2$ at low pH ($\sim$3) is dependent upon the state of the catalyst surface, as discussed above. The decrease in activity due to aggregation will be somewhat countered by the tendency of Ti$-$F groups to "trap" electrons, encouraging charge separation, although this may also make these electrons less accessible for direct photodegradation.[6,242] At higher pH ($\sim$6), the negative charge on the surface of fluoride-modified titania should prevent aggregation, but will also repel RB19 dye (which will also be negatively charged at this pH), preventing direct photodegradation. Indirect photodegradation *via* the production of $OH^{\cdot}$ is expected to proceed more rapidly on fluoride-modified $TiO_2$ as surface fluoride groups have been shown to aid in the production of free $OH^{\cdot}$.[242]

The photocatalytic activity of these materials appears to be linked to the nature of the anionic group of the SMA. $F^-$-modified $TiO_2$ catalysts show

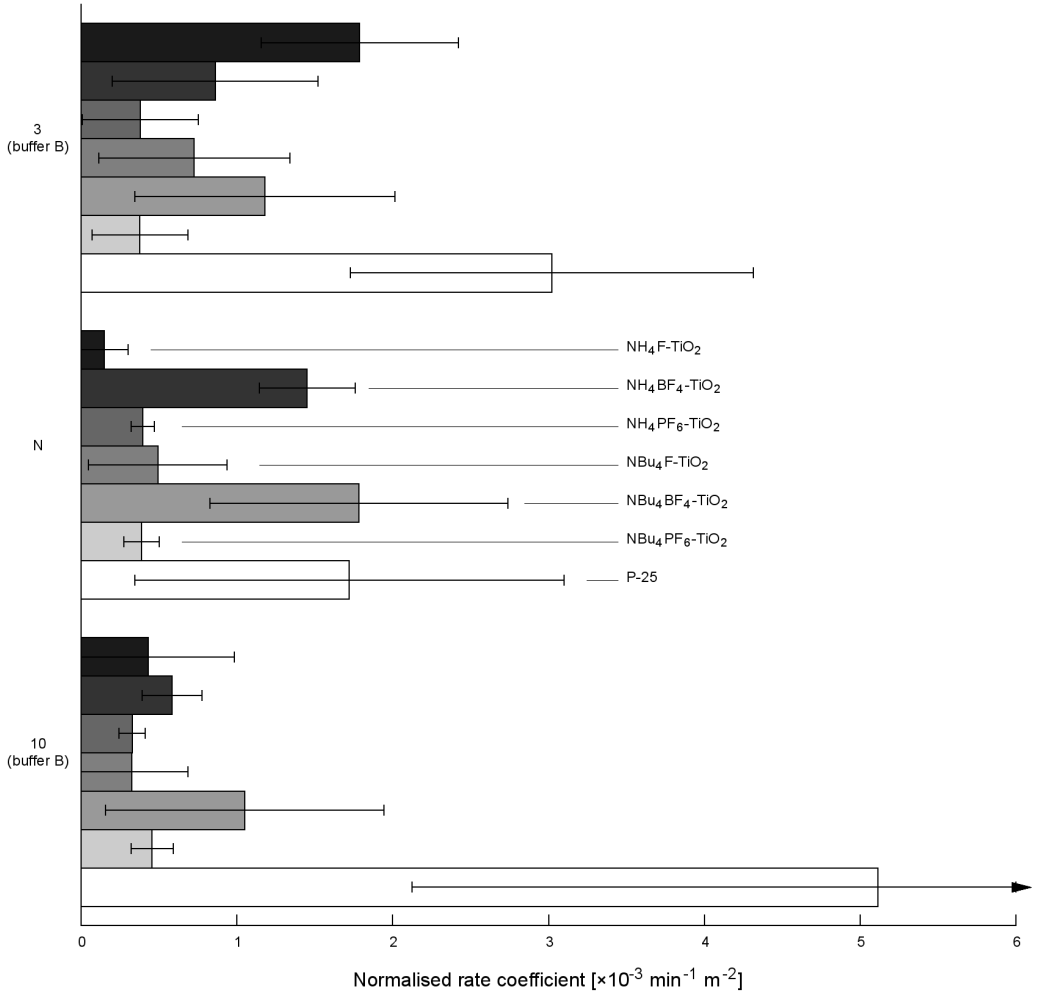


**Figure 8.15.** First-order rate coefficients for the photodegradation of RB-19 on fluoride-modified $TiO_2$ at differing pH and buffer conditions. Rate coefficients normalised by surface area; error bars show 95% CI. Arrow indicates error bar proceeds off graph axis.

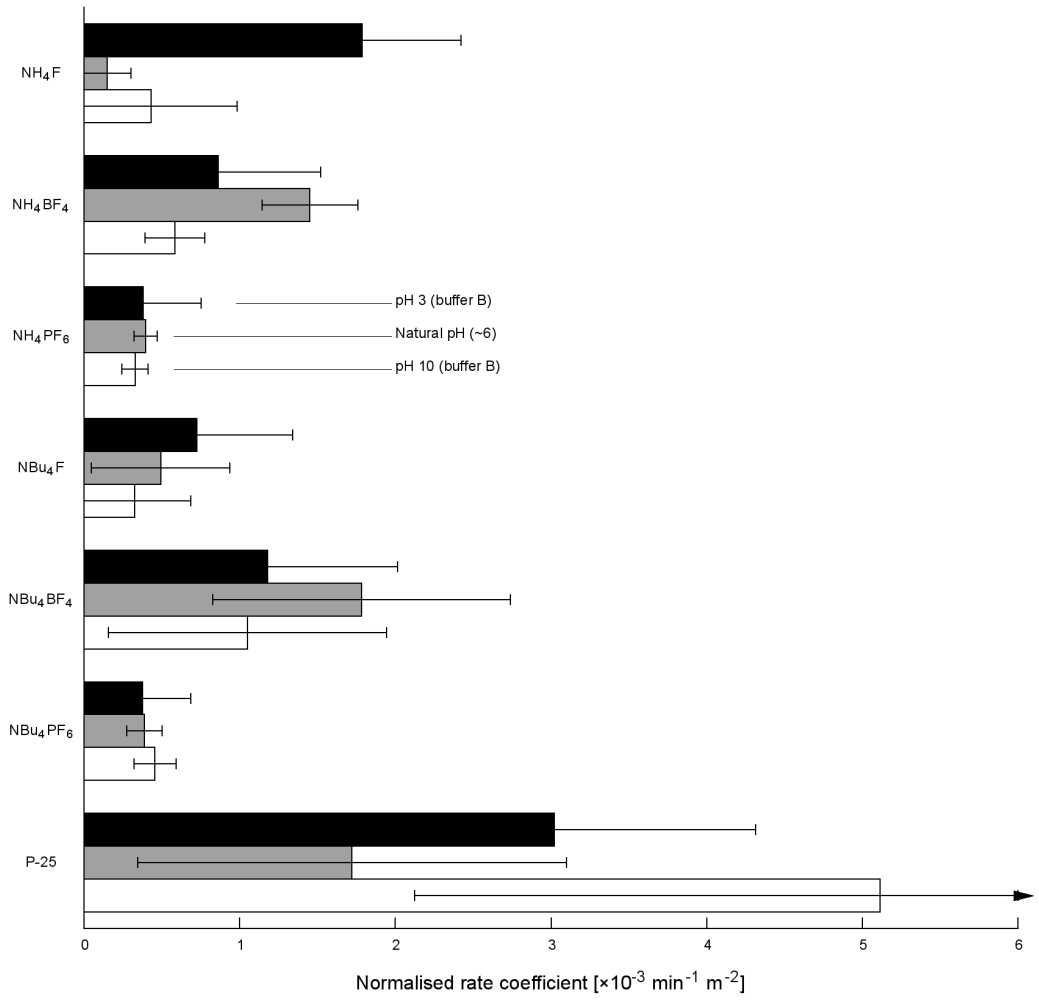


**Figure 8.16.** Dependence of photocatalytic activity on pH for fluoride-modified titania catalysts. Rate coefficients normalised by surface area; error bars show 95% CI. Arrow indicates error bar proceeds off graph axis.

**Table 8.7.** Table of first-order rate coefficients (both normalised for surface area, and non-normalised) and % degradation (after 120 minutes) of RB-19 on fluoride-modified $TiO_2$ under various buffer conditions. Errors indicate 95% CI.

| Material | pH | % deg.[a] | $k^b$ [$\times 10^{-3}$ $min^{-1}$] | $k_{SA}$ [$\times 10^{-3}$ $min^{-1}$ $m^{-2}$] |
|---|---|---|---|---|
| $NH_4F-TiO_2$ | 3 (buffer B) | 26.4 | 3.02±1.07 | 1.79±0.63 |
| | N | 3.7 | 0.25±0.26 | 0.15±0.15 |
| | 10 (buffer B) | 10.6 | 0.73±0.93 | 0.43±0.55 |
| $NH_4BF_4-TiO_2$ | 3 (buffer B) | 16.6 | 1.21±0.93 | 0.86±0.66 |
| | N | 18.8 | 2.05±0.43 | 1.45±0.31 |
| | 10 (buffer B) | 10.8 | 0.82±0.27 | 0.58±0.19 |
| $NH_4PF_6-TiO_2$ | 3 (buffer B) | 28.5 | 1.8±1.76 | 0.38±0.37 |
| | N | 18.9 | 1.86±0.36 | 0.39±0.08 |
| | 10 (buffer B) | 15 | 1.55±0.4 | 0.33±0.08 |
| $NBu_4F-TiO_2$ | 3 (buffer B) | 11.4 | 0.88±0.74 | 0.73±0.61 |
| | N | 5.8 | 0.59±0.54 | 0.49±0.45 |
| | 10 (buffer B) | 4.4 | 0.39±0.43 | 0.32±0.36 |
| $NBu_4BF_4-TiO_2$ | 3 (buffer B) | 12.9 | 0.8±0.57 | 1.18±0.84 |
| | N | 8.9 | 1.21±0.65 | 1.79±0.96 |
| | 10 (buffer B) | 8.4 | 0.71±0.6 | 1.05±0.89 |
| $NBu_4PF_6-TiO_2$ | 3 (buffer B) | 19.6 | 1.58±1.29 | 0.38±0.31 |
| | N | 18.8 | 1.63±0.48 | 0.39±0.11 |
| | 10 (buffer B) | 23.6 | 1.91±0.56 | 0.46±0.13 |
| P-25 | 3 (buffer B) | 32.6 | 4.53±1.94 | 3.02±1.29 |
| | N | 17.5 | 2.58±2.07 | 1.72±1.38 |
| | 10 (buffer B) | 48.9 | 7.67±4.48 | 5.11±2.99 |

high activity under acidic conditions, but are generally not so active under neutral or basic conditions. $BF_4^-$-modified $TiO_2$ is most active around its "natural" pH, without the use of pH modifying agents. The activity of $PF_6^-$-modified $TiO_2$ appears independent of pH, and is generally lower than that of other materials.

Fluoride-modified $TiO_2$ is expected to excel under basic conditions (pH = 10), as degradation *via* the indirect mechanism dominates: this is clearly not the case for the catalysts trialled here. The reason for this is unknown, but it is thought that the lack of activity at pH 10 may be due to excess SMA strongly bound to the catalyst surface. This observation is supported by the detection of multiple fluorine peaks under XPS (see Section 5.3.4), although no correlation is observed between XPS fluorine peak intensity and

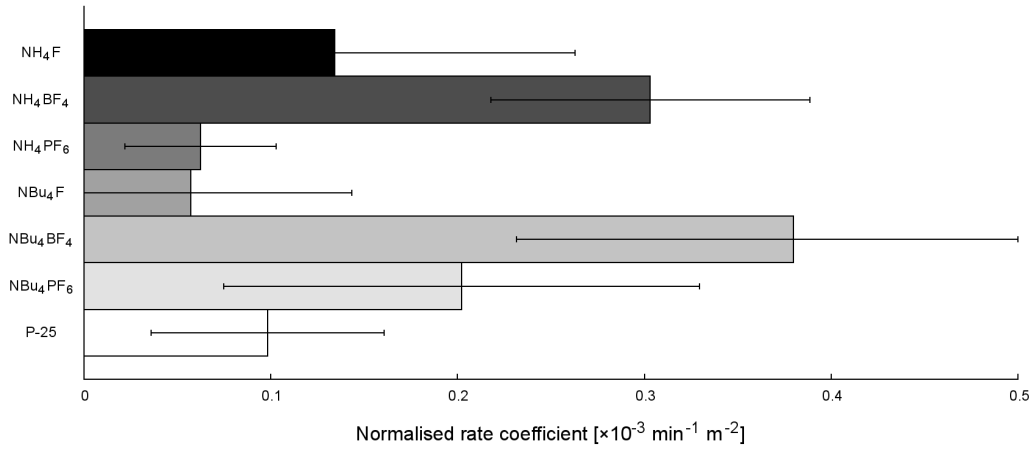


**Figure 8.17.** Visible-light activity of catalysts in the photodegradation of RB19. Rate coefficients normalised by surface area; error bars show 95% CI.

catalytic activity.

Initial fluoride removal studies suggest that repeated washes with NaOH solution (1 M) are able to remove the physisorbed layer of SMA from the catalyst: no such washing was attempted prior to XPS studies. It may be that under photocatalysis conditions (*i.e.* stirring, high-intensity broad-spectrum illumination) the surface of the catalyst is modified (*e.g.* by removal of physisorbed and possibly even chemisorbed fluoride), resulting in a change in activity.

*Visible-light activity*

The ideal photocatalyst should also be active under visible light, as UV light constitutes only a small fraction of the total photon flux from the sun. The visible light activity of these catalysts was measured (at natural pH, ∼6) by limiting incoming light to wavelengths $\lambda > 395$ nm. Results, normalised for surface area, are presented in Figure 8.17 and Table 8.8.

It is immediately apparent that the catalysts are considerably less active under visible light than UV light. The majority of light incident on the catalyst under visible light conditions is less energetic than the band gap of $TiO_2$ (∼3.2 eV, 387 nm) and therefore is not absorbed. Some activity

**Table 8.8.** Table of first-order rate coefficients (both normalised for surface area, and non-normalised) and % degradation (after 120 minutes) of RB-19 on fluoride-modified $TiO_2$ under visible light. Errors indicate 95% CI.

| Material | % deg. | $k$ [$\times 10^{-3}$ $min^{-1}$] | $k_{SA}$ [$\times 10^{-3}$ $min^{-1}$ $m^{-2}$] |
|---|---|---|---|
| $NH_4F-TiO_2$ | 2.7 | 0.23±0.22 | 0.14±0.13 |
| $NH_4BF_4-TiO_2$ | 5.4 | 0.43±0.12 | 0.31±0.09 |
| $NH_4PF_6-TiO_2$ | 4.1 | 0.29±0.19 | 0.06±0.04 |
| $NBu_4F-TiO_2$ | 2 | 0.07±0.1 | 0.06±0.08 |
| $NBu_4BF_4-TiO_2$ | 3 | 0.26±0.1 | 0.38±0.15 |
| $NBu_4PF_6-TiO_2$ | 6.9 | 0.85±0.53 | 0.2±0.13 |
| P-25 | 2.4 | 0.15±0.09 | 0.1±0.06 |

is observed, even on P-25, and this may be helped by sensitisation of the catalyst caused by adsorbed RB19 dye.

Almost all catalysts are as active as or more active than P-25 under visible light conditions. While the exact mechanism of visible-light activity is unknown, it may be due to a combination of sensitisation due to surface fluoride groups,[241,357] and stabilisation of surface $Ti^{3+}$ states, although in no case did any of the samples turn the blue colour reported for heavily-reduced $TiO_2$ materials.[151] Catalysts synthesised using $BF_4^-$-containing SMAs show considerably higher activity under visible light than P-25. The reason for the effectiveness of $BF_4^-$-modified $TiO_2$ has not been confirmed, but it is believed to be due to a "sweet spot" of factors including surface defect sites, $Ti^{3+}$ population, and crystallinity. The presence of boron was mentioned in Section 8.3.3 to aid in photocatalysis by formation perborate ions in solution: it may be that residual boron from SMAs is able to react with photogenerated hydroxyl radicals near the $TiO_2$ surface and further aid in photocatalysis.

In conclusion, fluorine-modified $TiO_2$ materials were trialled as photocatalysts using the degradation of RB19 as a model reaction under both broad-spectrum UV/visible and visible-only light. Materials did not consistently follows trends that could be related to their properties: this is believed to be due to a number of factors that change in a non-systematic fashion. Catalysts generally outperformed P-25 $TiO_2$ under visible-light conditions, with $NBu_4BF_4-TiO_2$ proving the most active by surface area.

Further work in this area should focus on removal of excess SMA on the

catalysts, as this material is not completely removed by cursory washing using water. Initial studies in this direction suggest that repeated washing with basic solution is sufficient to remove such SMA. It is expected that by thoroughly removing SMA from the surface of these catalysts, further trends in catalyst activity will be revealed, and that the results will prove useful in exploring the interaction between catalyst and dye.

### *8.3.6 Au@$TiO_2$ catalysts: effect of pre- and post-treatment method.*

The catalytic activity of Au@$TiO_2$ materials as synthesised in Chapter 7 was explored using the photodegradation of RB19 as a model reaction. The extent of degradation of RB19 under these conditions is shown in Figure 8.18 and Table 8.9. As all catalysts use P-25 as a support, it is assumed that surface area does not vary.

When no post-treatment method is applied, None$-TiO_2$ and $H_2O_2-TiO_2$ are the most active catalyst of those trialled. This suggests that while pre-treatment limits aggregation of gold clusters to some extent on the $TiO_2$ surface, it generally does not help in enhancing photocatalytic activity. However, upon post-deposition treatment several pre-treated catalysts show higher activity than the equivalent non-pre-treated catalyst. Upon calcination, $H_2(\Delta)$-, KOH- and $O_3$/UV$-TiO_2$ show considerable activity, with all outperforming None$-TiO_2-$None. Yet it must be pointed out that these samples are not as active as None$-TiO_2$ was without post-treatment.

It was found in Chapter 7 that ozonolysis was a considerably harsher post-treatment method than calcination with respect to particle aggregation. Ozonolysed samples are overall less active than either calcined or non-post-treated samples: this suggests that while *some* aggregation does not necessarily decrease the activity of a given catalyst, excessive aggregation is still detrimental. Under ozonolysis post-treatment, $O_3$/UV$-TiO_2$ is still the most active catalyst.

To further understand how post-treatment method affects catalytic activity, the change in activity upon post-treatment for each sample is shown in Figure 8.19.

This figure clearly separates the synthesised Au@$TiO_2$ catalysts into two

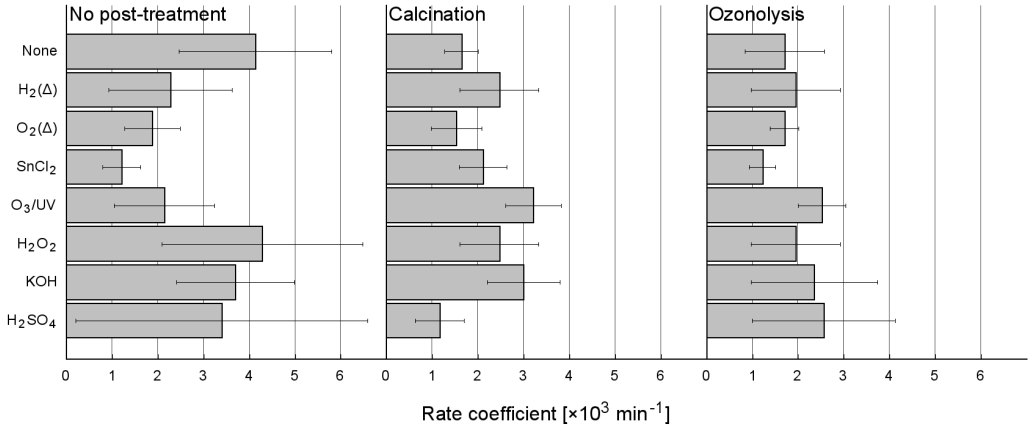


**Figure 8.18.** First-order rate coefficients for the photodegradation of RB-19 on Au@$TiO_2$ materials.

**Table 8.9.** Table of (first-order) rate coefficients and % degradation (after 120 minutes) of RB-19 on Au@$TiO_2$ materials. Errors indicate 95% CI.

| Pre-treatment | Post-treatment | % deg. | $k$ [$\times 10^{-3}$ min$^{-1}$] |
|---|---|---|---|
| None | None | 32.2 | 4.14±1.67 |
| | Δ | 15.9 | 1.65±0.37 |
| | $O_3$ | 14.2 | 1.71±0.87 |
| $H_2(\Delta)$ | None | 16.5 | 2.28±1.35 |
| | Δ | 21.2 | 2.47±0.86 |
| | $O_3$ | 18.2 | 1.96±0.98 |
| $O_2(\Delta)$ | None | 15.8 | 1.89±0.6 |
| | Δ | 14.2 | 1.54±0.55 |
| | $O_3$ | 17.9 | 1.71±0.31 |
| $SnCl_2$ | None | 12 | 1.21±0.42 |
| | Δ | 23 | 2.12±0.52 |
| | $O_3$ | 12.6 | 1.23±0.29 |
| $O_3$/UV | None | 17.3 | 2.14±1.09 |
| | Δ | 29.8 | 3.22±0.61 |
| | $O_3$ | 23.4 | 2.53±0.52 |
| $H_2O_2$ | None | 31.6 | 4.29±2.2 |
| | Δ | 21.2 | 2.47±0.86 |
| | $O_3$ | 18.2 | 1.96±0.98 |
| KOH | None | 30.3 | 3.7±1.29 |
| | Δ | 28.7 | 3±0.8 |
| | $O_3$ | 19 | 2.36±1.38 |
| $H_2SO_4$ | None | 20 | 3.4±3.19 |
| | Δ | 11.3 | 1.17±0.53 |
| | $O_3$ | 16.8 | 2.57±1.56 |

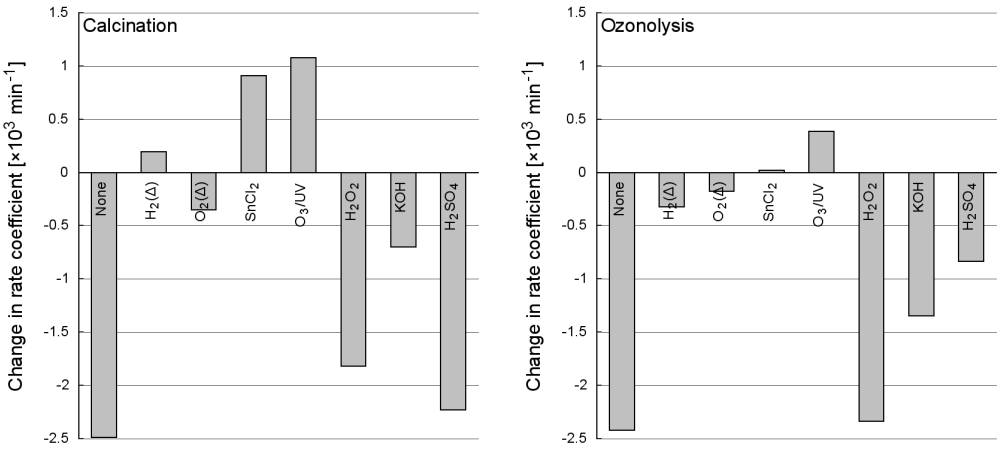


**Figure 8.19.** Change in photocatalytic activity as a result of calcination and ozonolysis post-treatment. Positive numbers indicate that post-treatment improved the activity of the catalyst.

groups:

- Those for which post-treatment results in an appreciable drop in activity (None$-TiO_2$, $H_2O_2-TiO_2$, KOH$-TiO_2$, $H_2SO_4-TiO_2$), and
- those for which post-treatment either does not affect activity or increases it significantly ($H_2(\Delta)-TiO_2$, $O_2(\Delta)-TiO_2$, $SnCl_2-TiO_2$, $O_3$/UV$-TiO_2$).

It is expected that comparison of Figures 8.18 (photocatalytic activity) and 7.8 (XPS spectra of gold for Au@$TiO_2$ catalysts) should demonstrate some form of correlation between (for example) gold peak intensity and position, and activity. However, no such pattern is readily apparent. Given the somewhat harsh conditions of photocatalysis (exposure to high-intensity broad-spectrum light) and the tendency for gold clusters on titanium dioxide to aggregate upon exposure to light,[297,358] it may be that photocatalysis induces further aggregation upon the $TiO_2$ surface. As samples were kept in the dark between synthesis and XPS characterisation it follows that light-induced aggregation would be minimised under those conditions. As a result, XPS spectra of Au@$TiO_2$ materials may not mirror the nature of systems during photocatalysis.

It has been noted that both calcination and ozonolysis may increase the activity of Au@$TiO_2$ catalysts, although calcination is generally more effective. It has also been noted that while both calcination and ozonolysis lead to deprotection and aggregation, ozonolysis is a much harsher method: clusters undergo more rigorous ligand removal by this method, but also aggregate more readily. Pre-treatment alters the surface of the support material and thus the support-cluster interaction, which may weaken the overall bond between the two. Under photocatalytic conditions, this would lead to increased aggregation as gold clusters will more readily migrate across the support surface. Post-treatment may be effective in increasing the affinity between cluster and support: while it also leads to aggregation, this aggregation will occur under photocatalytic conditions whether post-treatment was performed or not. Thus, it may be that post-treatment can increase catalyst activity by anchoring some clusters more firmly to the support surface, preventing (or at least inhibiting) aggregation under photocatalytic conditions.

*Aging studies*

Unless suitably treated, Au@$TiO_2$ catalysts are susceptible to aggregation when exposed to light or high temperatures.[297] The photocatalytic reactions performed in this chapter expose catalysts to intense UV light, which may change the nature (and activity) of these materials as the reaction progresses. In addition, factors such as age of catalyst and storage conditions may result in mild aggregation, which may in turn affect catalytic activity.

In order to determine the effect of catalyst ageing, a select number of the synthesised catalysts were stored at room temperature in the dark (wrapped in foil, in a dark cabinet) for two months, after which a second reaction was undertaken. The results of this study are shown in Figure 8.20.

In most cases ageing resulted in a drop in activity, although $KOH{-}TiO_2{-}O_3$ shows a slight increase in activity (which may be due to error), and $O_2(\Delta){-}TiO_2{-}O_3$ and $H_2SO_4{-}TiO_2{-}\Delta$ show a more marked increase after ageing. While a decrease in activity can be explained by aggregation over time (leading to large, catalytically inactive gold particles), the reason for the increase in activity for some samples is unknown. Impor-

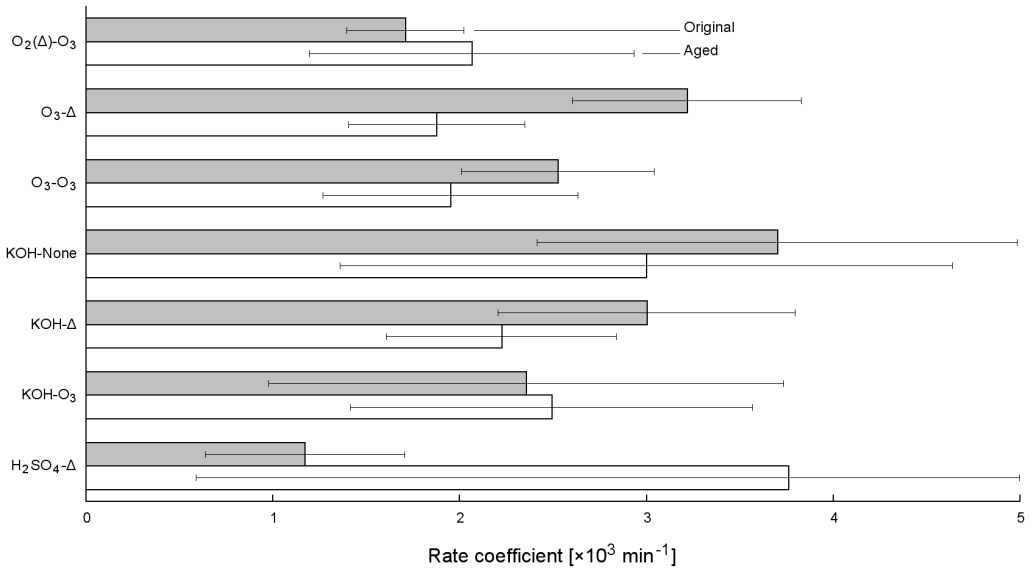


**Figure 8.20.** Effect of catalyst aging on selected Au@$TiO_2$ catalysts.

tantly, this study shows that catalyst activity changes with storage time. In order to fully characterise these catalysts, further work is required, focussing on the effect of storage conditions and times. Techniques such as UV-vis DRS may in future be used to monitor aggregation that occurs with storage.

*Support-only studies*

Alteration of the support surface may in turn alter the activity of the support as a catalyst in its own right, regardless of gold cluster deposition. In order to further understand the effect of support pre-treatment methods, a number of pre-treated supports were trialled in the degradation of RB19. The results of these trials, compared to similar catalysts with gold clusters deposited on them, are shown in Figure 8.21. It is interesting to note that in some cases (*e.g.* $H_2SO_4$−$TiO_2$) the support on its own is a better catalyst than when gold is deposited on it. In others, gold deposition enhances activity even after ozonolysis post-treatment. Previous studies on metal nanoparticles deposited on $TiO_2$ have reported that excessive metal load can harm the activity of the catalyst either by shielding it from incoming photons, deforming the potential field and encouraging electron-hole recombination, or

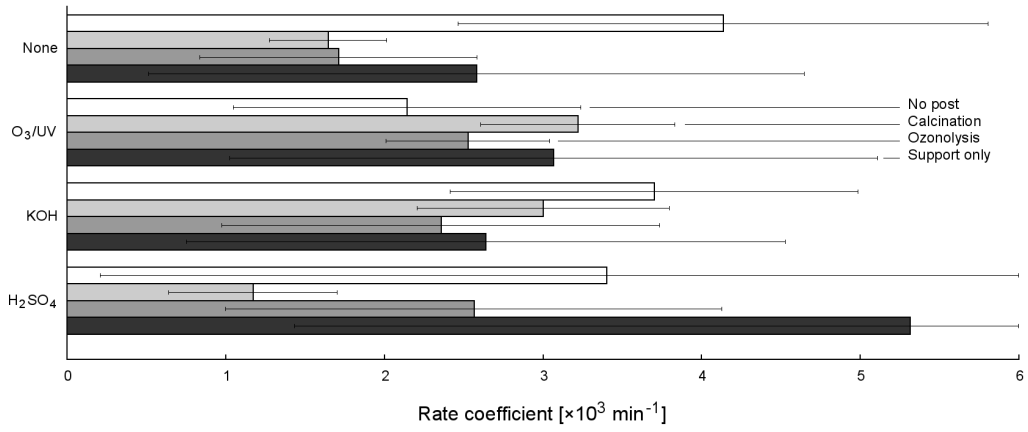


**Figure 8.21.** Comparison of photocatalytic activity of pretreated support-only catalysts, and gold-on-support catalysts.

by preventing the formation of reactive titanol groups on the catalyst surface.[26,36] While these factors generally become an issue once metal loading exceeds 1%, previous literature has demonstrated similar results for 0.4% loadings of gold nanoparticles on $TiO_2$ and $TiO_2/SiO_2$ hybrids.[359] This suggests that even at low loadings, if gold particles are allowed to aggregate they may have a considerable detrimental effect on the activity of the material.

It is interesting to note that $H_2SO_4-TiO_2$, which demonstrated the highest population of discrete gold clusters by XPS, is a much better catalyst when used on its own than when used as a support for gold. This reinforces the finding that there is no clear and direct correlation between the presence of discrete gold clusters under XPS and their photocatalytic activity.

## *8.4 Conclusion*

The photocatalytic activity of several titanium dioxide materials was evaluated using the photodegradation of the dye Reactive Blue 19 (RB19) as a model reaction. Initial studies demonstrated that when using UV-vis spectroscopy as a measure of dye degradation, the system did not obey 0th-order, 1st-order or Langmuir-Hinschelwood kinetics. Thus, the extent of degradation in all cases was determined by comparing the absorbance of the initial ($t = 0$) and final ($t = 2$ hours) solutions at the absorption maximum of the

dye.

Initial studies using Aeroxide P-25 as a catalyst were undertaken to determine the effect of pH and buffer on photocatalytic ability. It was found that activity was highest at low and high pH, but activity decreased as pH approached the point of zero charge of the catalyst. The use of buffer rather than pH had a significant effect on catalyst activity, even when the initial pH remained the same. More importantly, it was observed that choice of buffer had an effect on activity, presumably due to each buffer's chemical properties.

Studies were performed on $TiO_2$ synthesised in a number of methods, including hydrolysis in ethanol, thermal degradation of peroxotitanic acid, and arc discharge. Arc discharge-synthesised titania proved only sparing active in the photodegradation of RB19, and this was believed to be due to its method of synthesis coupled with a relatively large particle size, leading to difficulties in forming and maintaining a homogenous catalyst suspension. Peroxotitanic acid titania was the most active of those trialled, which is attributed to its small particle size, high crystallinity, and synthesis in aqueous conditions which allows for improved dispersion. Titania synthesised by hydrolysis in ethanol was amorphous in nature but high surface-area, and showed middling activity compared to other catalysts. Upon calcination, the material became crystalline but surface area dropped drastically, which is attributed to the collapse of particle mesopores in the material. This resulted in an overall drop in catalytic activity, especially at low pH where dye adsorption onto the catalyst surface is critical for degradation.

Titanium dioxide materials synthesised by the degradation of peroxotitanic acid in the presence of fluoride-containing surface modifying agents (SMAs, see Chapter 5) were also trialled as photocatalysts. Results suggested that photocatalytic activity was modified by surface-bound SMA, which may reduce the apparent activity of the catalysts. However, the majority of these materials outperformed P-25 under visible-light-only photocatalysis, with $BF_4^-$-modified materials being the most active (when activity was normalised to account for surface area).

Finally, Au@$TiO_2$ materials (Chapter 7) were trialled as photocatalysts by this technique. It was found that a high proportion of discrete gold clusters

(as reported by XPS) does not necessarily result in a good catalyst, and it was proposed that photocatalytic conditions promote cluster aggregation, especially if post-deposition treatment to "anchor" gold clusters was not performed. While some materials show a decrease in activity after post-treatment, a number show a significant increase in activity as a result. It is thought that this can be attributed to the combined anchoring/ligand removal effects of post-treatment. Ozonolysis is generally not as effective as calcination at "activating" these catalysts, and this is believed to be due to excessive aggregation. Ageing studies showed that these materials' activity generally deteriorated upon storage for a period of several months, even in the dark. Further, photocatalytic trials on selected pre-treated pure supports (absent of gold clusters) provides examples of both beneficial and detrimental effects from gold cluster deposition, hinting at the complex nature of these systems.

While initial studies on P-25 and "basic" $TiO_2$ materials provided a good foundation for further synthetic and photocatalytic studies, several observations for both fluoride-modified $TiO_2$ and Au@$TiO_2$ materials indicate that further, more comprehensive study must be performed in order to better understand the material and its interaction with the environment. In particular, further studies on fluoride-modified $TiO_2$ will focus on removal of excess SMA in an attempt to monitor trends in the synthesised materials. Meanwhile, further work on Au@$TiO_2$ materials will focus on the effect of photocatalytic testing conditions on gold cluster aggregation, as well as improvements in storage or synthesis to prevent aggregation both over time and during said photocatalytic tests. Such research will hopefully lead to a more thorough understanding of the gold-support-dye interaction. While initial studies on P-25 and "basic" $TiO_2$ materials provided a good foundation for further synthetic and photocatalytic studies, several observations for both fluoride-modified $TiO_2$ and Au@$TiO_2$ materials indicate that further, more comprehensive study must be performed in order to better understand the material and its interaction with the environment. In particular, further studies on fluoride-modified $TiO_2$ will focus on removal of excess SMA in an attempt to monitor trends in the synthesised materials. Meanwhile, further work on Au@$TiO_2$ materials will focus on the effect of

testing conditions on gold cluster aggregation, as well as improvements in storage or synthesis to prevent aggregation both over time and during said photocatalytic tests. Such research will hopefully lead to a more thorough understanding of the gold-support-dye interaction.

# Chapter IX

# Conclusion

## *9.1 Summary of work*

In this thesis I have reported on the synthesis of titanium dioxide by a number of (generally solution-based) chemical methods. Following these investigations, titanium dioxide nanomaterials were synthesised in the presence of a number of fluoride-containing surface modifying agents, to determine the effect of these agents on particle growth, shape and crystallinity. Further studies investigated modification of the surface of a commercially-available $TiO_2$ material, Aeroxide P-25 by a number of treatment methods, and the effect of these surface modifications on gold deposition and aggregation. Finally, several of these materials were trialled as photocatalysts, using as a model reaction the photodegradation of the industrial dye Reactive Blue 19.

Initial studies focussed on developing several synthetic methods as a foundation for future work. Titanium dioxide nanomaterials were synthesised using a number of different routes, including simple sol-gel synthesis, solvothermal synthesis in benzyl alcohol, thermal degradation of peroxotitanic acid, plasma arc discharge synthesis, and hydrothermal synthesis in the presence of oxalic acid. The formation of $TiO_2$ nanoparticles was monitored *in situ* using small-angle X-ray scattering, demonstrating the usefulness of this technique to probe the mechanism of synthesis and evolution of nanomaterial properties over time. Obtained materials were also characterised to determine particle crystallinity (powder X-ray diffraction, high-resolution transmission electron microscopy) and particle and crystallite size and shape (powder X-ray diffraction, dynamic light scattering, scanning and transmission electron microscopy).

The above constitutes a broad but shallow investigation into synthetic

methods. Following this study, two further systems were selected to study in more depth.

The first of these was the modification of $TiO_2$ by fluoride-containing surface modifying agents (SMAs). Thermal degradation of peroxotitanic acid was chosen as the synthetic method for this study as the relatively slow formation of $TiO_2$ (compared to common hydrolytic methods) allowed for SMA binding and influence on particle growth. It was found that the use of these SMAs resulted in the formation of ellipsoid particles with extended {010} facets, and that the use of different cationic and anionic groups in the SMA may alter particle size. Following this, the effect of a number of fluorine-containing carboxylic acids (of varying tail length) on particle size, shape and crystallinity was investigated, with acetic acid-modified $TiO_2$ also synthesised to explore the effect of fluorine in these systems. It was found that the nature of the SMA in this case strongly affected the crystalline phase of particles, with increasing fluorine substitution of acetic acid resulting in the formation of rutile over anatase titania. Longer-tail carboxylic acids were less effective as SMAs, and this was believed to be either due to the formation of micelles in solution, a result of the particles' hydrophilic/hydrophobic nature, or due to steric hindrance as the overall size of the SMA increased. When the SMA was added directly to the titanium precursor (as opposed to being added after initial hydrolysis), the overall crystallinity and size of the particles changed, indicating that addition order has a marked effect on the formation of $TiO_2$. The above studies were conducted using a SMA:Ti molar ratio of 1:1. A series of materials synthesised using 0.1:1 SMA:Ti ratios suggested that this level of SMA was enough to control nanoparticle morphology, and also that materials synthesised using 1:1 ratios may still retain significant concentrations of SMA on the particle surface.

The second study investigated the effect of pre- and post-deposition treatment on atomically precise gold clusters immobilised on P-25 $TiO_2$. A number of chemical techniques were applied to P-25 titanium dioxide nanopowders to alter their surface chemistry prior to gold cluster deposition, and the resultant $Au@TiO_2$ materials were then either subjected to post-treatment or investigated as-is. Materials were characterised by synchrotron X-ray electron spectroscopy and UV-vis diffuse reflectance spectroscopy. It was found

that on the majority of supports, gold clusters lost their protecting phosphine ligand shell upon deposition (*i.e.* even without post-deposition treatment). Out of the two post-treatments trialled, ozonolysis was a more harsh treatment (in terms of both ligand removal and aggregation) than calcination under vacuum for the studied system. Out of all surface pre-treatments, washing with sulfuric acid and washing with hydrogen peroxide were both effective at decreasing the magnitude of gold cluster aggregation, and sulfated $TiO_2$ also decreased aggregation under calcination. Samples for which the support was pre-treated by heating under hydrogen were unique in the studies series in that a distinct population of unaggregated clusters was detectable by XPS after $O_3$ post-treatment.

Finally, several of the materials synthesised in previous chapters were trialled as photocatalysts, using the degradation of the industrial dye Reactive Blue 19 (RB19) as a model reaction. First, several studies were performed to determine the effect of pH, buffer and $H_2O_2$ concentration on the efficiency of dye degradation, using P-25 as a catalyst. It was found that not only does the presence of buffer affect the rate of the reaction, but the *chemical nature* of the buffer plays an important part, with considerable differences observed when using different buffers at the same pH. Following this, a number of the $TiO_2$ materials synthesised in the initial section of this project were trialled as photocatalysts. $TiO_2$ synthesised by thermal degradation of peroxotitanic acid was found to be the most active of those materials trialled. Studies on fluoride-modified $TiO_2$ were unable to elicit an overall trend relating photocatalytic activity to SMA, even when normalised for surface area. Under visible-light irradiation these materials showed greater photoactivity than P-25, which may be due to the presence of fluoride on the surface of the particles. The variation in activity is not systematic, which suggests that it may be due to the interplay of several key factors, such as crystallite and particle size, surface area, zeta potential, populations of surface species, and even radical transfer reactions mediated by residual SMA. Au@$TiO_2$ materials were also tested for photocatalytic activity, although it should be noted that exposure to intense broad-spectrum light likely results in near-immediate aggregation of clusters on the $TiO_2$ support. Of note, there was no correlation between the presence of discrete, unaggregated gold clusters (as suggested by

XPS) and activity, and in a number of cases the gold-modified material was actually less active than the support *sans* clusters. These signs are all indicative of gold cluster aggregation. Significant differences in photocatalytic activity between stored and fresh catalysts suggest that the materials are not stable over the long-term.

## *9.2 Future work*

Of the materials investigated in Chapter 4, several displayed interesting properties. For example, $TiO_2$ synthesised in benzyl alcohol showed remarkable crystallinity and small size (and thus high surface area). Studies also showed that particle shape and crystallinity were dependent upon both surface modifying agents (SMAs) used, and pressure. Further work in this area could focus on alteration of the solvent or modifying agents, use of differing temperature or pressure, or use of different atmosphere in an attempt to influence the properties of the resultant particles. For example, fluorine-containing SMAs have been effective in controlling particle size, shape and crystallinity in other studies reported herein, and may be effective in this method either in concert with or instead of oleylamine and water. It may even be possible to use fluorinated derivatives of benzyl alcohol as solvents, which may further alter the properties of synthesised materials. In addition, these particles' catalytic ability have not yet been investigated: their high crystallinity and surface area suggests that they would function well in this role, however being synthesised in non-aqueous media, they may aggregate when dispersed in water. This suggests that future investigations may also explore post-synthesis surface treatment of these materials to aid dispersion in aqueous media.

Plasma arc-discharge synthesised $TiO_2$ was very polydisperse, although highly crystalline. While initial studies briefly looked at the effect of different atmosphere on the morphology of these particles, the presence of leaks in the system (evident in the formation of $TiO_2$ even under supposedly oxygen-free atmosphere) means that the actual makeup of the atmosphere during synthesis cannot be estimated. At the time of writing the apparatus at GNS Science has been upgraded, and the new setup is much more suited to

such experiments. This would allow for better investigation on the effect of pressure and gas type on synthesis. However, arc-discharge $TiO_2$ materials showed low activity in the photodegradation of RB19: unless they show promise in other applications, or can be modified to improve their activity (*e.g.* by surface treatment) it may be that "wet chemistry" methods are more applicable to this research.

The work described on synthesis of $TiO_2$ in the presence of oxalic acid currently focusses on synthesis and immediate structural properties. No attempt has been made to explore the photocatalytic activity of these materials for dye degradation, although they prove effective in breakdown of oxalic acid under weak UV light. Of particular interest, the gradual transition between phases observed on hydrothermal treatment suggests that it may be possible to engineer mixed-phase catalysts (similar to or outperforming commercial products such as P-25) *via* this method. These catalysts may exhibit increased efficiency due to charge separation along grain boundaries. It is expected that further work be informed by the results of photocatalytic tests.

Initial SAXS studies confirmed that the formation of $TiO_2$ particles could be monitored *in situ*, although the limitations of a laboratory instrument suggest that synchrotron SAXS may be a better candidate for in-depth studies. While the research reported here does shed light on the formation of $TiO_2$ from peroxotitanic acid, it also acts as a proof of concept. SAXS studies could be applied to any system where the reaction occurs over the course of hours and the exact course of particle nucleation and growth are unknown: for example, SAXs studies could be used in future to probe the formation of $TiO_2$ from peroxotitanic acid in the presence of fluorine-containing surface-modifying agents, to investigate how different SMA affect particle growth. With the use of synchrotron SAXS even rapid events like $TiO_2$ hydrolysis may be studied.

Chapters 5 and 6 focus on the synthesis of $TiO_2$ in the presence of fluorine-containing SMAs. While detailed analysis of fluorine salts was performed, the form of the modifying agent physisorbed on the surface is still not known. In addition, the shape of these particles is reminiscent of similar particles synthesised in low concentrations of HF.[239] Further studies may investigate how

increased fluoride concentration affects particle shape, particularly in regard to which crystal faces dominate. There may also be merit in exploring pressurised (*i.e.* in sealed containers, as compared to reflux conditions) synthesis, as this may increase the crystallinity of particles and bring to light any differences in the behaviour of SMAs. Photocatalytic studies (Chapter 8) suggest that the physisorbed SMA layer may adversely affect activity on the titania surface: as it is strongly bound, exposure to UV light may not be enough to dislodge it (as compared with other SMAs studied in this thesis, *e.g.* oxalic acid). Further photocatalytic studies hinge on the removal of this layer, which it is hoped will result in a more reliable and reproducible catalyst. It is also worth exploring the effect of pH on these systems, particularly in the case of $TiO_2$ synthesised in the presence of fluorinated carboxylic acids. It may be that for some of these systems, shape and phase are affected more by the pH of the system than by the modifying agents themselves.

Chapter 7 reports on the stability of more complex Au@$TiO_2$ materials, particularly regarding gold cluster aggregation. While the majority of this thesis reports on the synthesis of $TiO_2$, this chapter focuses instead on modification of titania post-synthesis, and opens up a vast array of future work. There are a virtually limitless number of ways in which $TiO_2$ materials may be pre-treated, and the results reported here could be used to select new methods for pre-treatment. Given the conditions encountered in catalytic systems, it may be useful to perform analysis of these materials both before and after catalysis, as severe aggregation may occur under UV light. The overall goal of this would work be to synthesise a Au@$TiO_2$ material that was stable to both ageing and UV light, to be used as a recyclable catalyst.

Overall this work has laid a strong foundation for further research on $TiO_2$ nanomaterials. Several synthetic methods for $TiO_2$ have been trialled and the resultant products characterised in order to understand the differing mechanisms of formation. Several advanced $TiO_2$ nanomaterials have been made, with a focus on fluorine-containing SMAs and gold cluster decoration. While the studies reported above have shed some light on these systems, there still remains much work to do to achieve the optimal photocatalyst.

# Appendix A

# PXRD data integration

Data acquired using the Bruker APEXII X-ray diffraction instrument was stored as two-dimensional data in Bruker's SFRM file format. Each file is made up of:

- Metadata (including the dimensions and density (in pixels per centimetre) of the CCD and wavelength of radiation). Each metadata item is 80 characters long, with no newline separating it and the next metadata item.
- Two lines made up of the nonprinting ASCII characters 26 ("<SUB>") and 4 ("<EOT>") followed by 78 period characters.
- The intensity map of the pattern, stored as binary data.

Each pixel of the CCD records intensity as a value between 0 and 255, and this intensity is stored as one ASCII character (*i.e.* one byte of binary data). If this data is read and converted to integer values, it is a trivial task to re-form the diffraction pattern given the CCD width and height in pixels (stored in the metadata section of the file).

Given the resolution of the detector and distance between sample and CCD (both provided in file metadata), and assuming that the CCD is centred on the transmitted beam, it is possible to find a value $2\theta$ for any point given its coordinates on the CCD:

$$2\theta = \tan^{-1}\left(\frac{d}{D}\right) \tag{A.1}$$

where $d$ is the distance between the CCD centre and the point in question, and $D$ is the distance between the sample and the CCD. This assumes that the angle between the incident beam and the centre of the CCD, $\Theta$, is zero.

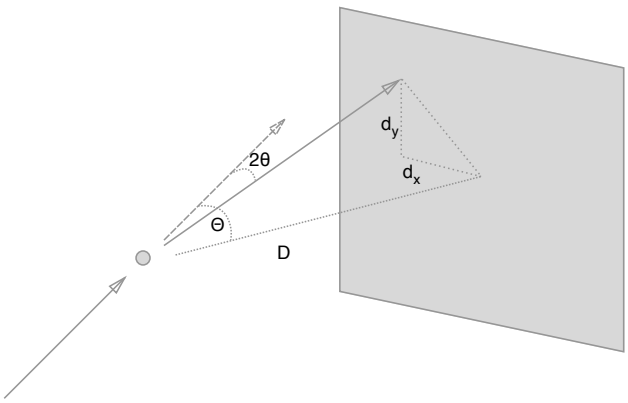


**Figure A.1.** X-ray diffraction setup for off-axis data collection. The CCD is offset from the transmitted beam by an angle $\Theta$ in the horizontal plane, and the centre of the CCD is a distance $D$ from the diffraction source. The angle between the transmitted beam and a beam of diffracted radiation landing on the point $(d_x, d_y)$ is marked as $2\theta$.

It is somewhat more difficult to calculate the diffraction angle if the CCD is off-centre. In a number of cases the CCD was offset from the transmitted beam by an angle $\Theta$ in the horizontal plane, in order to collect higher-resolution data at higher $2\theta$ than would normally be possible (see A.1).

In order to determine $2\theta$ for a given peak we must first find:

1. The distance between the point where the transmitted beam ($2\theta = 0$) strikes the CCD plane ($d_t$) and the point where the diffracted light hits the CCD plane ($d_\gamma$).

2. The distance between the sample and the point $d_t$.

3. The distance between the sample and the point $d_\gamma$

This relationship is shown in A.2.

The transmitted beam will strike the plane of the CCD at a point $d_t$ in the horizontal plane. The offset of $d_t$ from the centre of the CCD can be calculated given the fact that a line between the sample and the centre of the CCD will be normal to the plane of the CCD:

$$d_t = D \tan \Theta \tag{A.2}$$

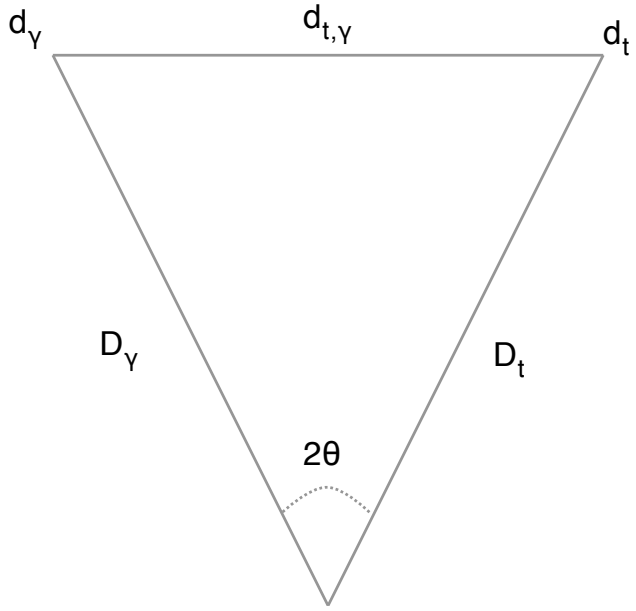


**Figure A.2.** Determination of $2\theta$ when the CCD is offset from the transmitted beam.

Given that this offset is entirely in the horizontal plane, it is relatively simple to find the distance between a given point $(d_x, d_y)$ on the CCD and the point $d_t$. We define this distance between the *transmitted beam* and the *diffracted radiation* to be $d_{t,\gamma}$:

$$d_{t,\gamma} = \sqrt{(d_t - d_x)^2 + d_y^2} \tag{A.3}$$

The distance travelled by the transmitted beam $D_t$ is simple given the previous calculation of the distance between the CCD centre and the point $d_t$:

$$D_t = \sqrt{d_t^2 + D^2} \tag{A.4}$$

The distance travelled by the diffracted beam is similarly trivial:

$$D_\gamma = \sqrt{D^2 + d_x^2 + d_y^2} \tag{A.5}$$

Given these values, the diffraction angle $2\theta$ can be determined using the cosine law:

$$2\theta = \cos^{-1}\left(\frac{d_{t,\gamma}^2 - D_\gamma^2 - D_t^2}{2D_\gamma D_t}\right) \tag{A.6}$$

$$= \cos^{-1}\left(\frac{(d_t - d_x)^2 + d_y^2 - D^2 - d_x^2 - d_y^2 - D^2 - d_t^2}{2D_\gamma D_t}\right) \tag{A.7}$$

$$= \cos^{-1}\left(\frac{d_t d_x - D^2}{D_\gamma D_t}\right) \tag{A.8}$$

## References


[1] *Ullmann's Encyclopedia of Industrial Chemistry*, ed. F. Ullmann, John Wiley & Sons, Inc., 2006.

[2] A. T. Bell, *Science*, 2003, **299**, 1688.

[3] A. Fujishima and K. Honda, *Nature*, 1972, **238**, 37–38.

[4] U. Diebold, *Surface Science Reports*, 2003, **48**, 53–229.

[5] S. Bingham and W. A. Daoud, *Journal of Materials Chemistry*, 2011, **21**, 2041–2050.

[6] L. G. Devi and S. G. Kumar, *Central European Journal of Chemistry*, 2011, **9**, 959–961.

[7] S. M. Gupta and M. Tripathi, *Chinese Science Bulletin*, 2011, **56**, 1639–1657.

[8] A. Fujishima, X. Zhang and D. Tryk, *Surface Science Reports*, 2008, **63**, 515–582.

[9] Y. M. Evtushenko, S. V. Romashkin and V. V. Davydov, *Nanotech. Nanomat.*, 2011, **45**, 731–738.

[10] S. Liu, J. Yu and M. Jaroniec, *Chemistry of Materials*, 2011, **23**, 4085–4093.

[11] S. Polarz, *Advanced Functional Materials*, 2011, **21**, 3214–3230.

[12] C. Z. Wen, H. B. Jiang, S. Z. Qiao, H. G. Yang and G. Q. M. Lu, *Journal of Materials Chemistry*, 2011, **21**, 7052–7061.

[13] D. P. Macwan, P. N. Dave and S. Chaturvedi, *Journal of Materials Science*, 2011, **46**, 3669–3686.

[14] X. Chen and S. S. Mao, *Chemical Reviews*, 2007, **107**, 2891–2959.

[15] O. T. Can, M. Kobya and E. Demirbas, *Chemosphere*, 2006, **62**, 181–187.

[16] D. Chen, M. Sivakumar and A. K. Ray, *Developments in Chemical Engineering and Mineral Processing*, 2000, **8**, 505–550.

[17] S. Ahmed, M. G. Rasul, R. Brown and M. A. Hashib, *Journal of Environmental Management*, 2011, **92**, 311–330.

[18] H. He, C. Liu, K. D. Dubois, T. Jin, M. E. Louis and G. Li, *Industrial & Engineering Chemistry Research*, 2012, **51**, 11841–11849.

[19] P. Mutin and A. Vioux, *Chemistry of Materials*, 2009, **21**, 582–596.

[20] *Handbook of Heterogeneous Catalysis*, ed. G. Ertl, H. Knözinger, F. Schüth and J. Weitkamp, Wiley-VCH, Weinheim, 2nd edn., 2008, vol. 1.

[21] *Nanoscale Materials in Chemistry*, ed. K. J. Klabunde, John Wiley and Sons Ltd., New York, 2001.

[22] E. Barborini, I. N. Kholmanov, P. Piseri, C. Ducati, C. E. Bottani and P. Milani, *Applied Physics Letters*, 2002, **81**, 3052.

[23] A. Mills and S. Le Hunte, *Journal of Photochemistry & Photobiology, A: Chemistry*, 1997, **108**, 1–35.

[24] J. Gong, *Chemical Reviews*, 2012, **112**, 2987–3054.

[25] W. Doerffler and K. Hauffe, *Journal of Catalysis*, 1964, **3**, 156–170.

[26] D. Y. C. Leung, X. Fu, C. Wang, M. Ni, M. K. H. Leung, X. Wang and X. Fu, *ChemSusChem*, 2010, **3**, 681–694.

[27] S. Yu, S. Ahmadi, C. Sun, P. Palmgren, F. Hennies, M. Zuleta and M. Göthelid, *Journal of Physical Chemistry, C*, 2010, **114**, 2315–2320.

[28] J. L. Giocondi, P. A. Salvador and G. S. Rohrer, *Top. Catal.*, 2007, **44**, 529–533.

[29] N. Roy, Y. Sohn and D. Pradhan, *ACS Nano*, 2013, **7**, 2532–2540.

[30] W. P. Dumke, *Physical Review*, 1957, **105**, 139–144.

[31] S. M. Sze and M. K. Lee, *Semiconductor Devices: Physics and Technology*, John Wiley & Sons, Inc., New York, 3rd edn., 2012.

[32] H. Tong, S. Ouyang, Y. Bi, N. Umezawa, M. Oshikiri and J. Ye, *Advanced Materials*, 2012, **24**, 229–251.

[33] J.-P. Jolivet, M. Henry and J. Livage, *Metal oxide chemistry and synthesis*, John Wiley and Sons Ltd., Chippenham, 2000.

[34] J.-M. Herrmann, *Environ. Sci. Pollut. Res.*, 2012, **19**, 3655–3665.

[35] M. Pelaez, N. T. Nolan, S. C. Pillai, M. K. Seery, P. Falaras, A. G. Kontos, P. S. M. Dunlop, J. W. J. Hamilton, J. A. Byrne, K. O'Shea, M. H. Entezari and D. D. Dionysiou, *Applied Catalysis B, Environmental*, 2012, **125**, 331–349.

[36] A. Primo, A. Corma and H. Garcia, *Physical Chemistry Chemical Physics*, 2011, **13**, 886–910.

[37] D. C. Hurum, A. G. Agrios, K. A. Gray, T. Rajh and M. C. Thurnauer, *Journal of Physical Chemistry, B*, 2003, **107**, 4545–4549.

[38] C. Colbeau-Justin, M. Kunst and D. Huguenin, *Journal of Materials Science*, 2003, **38**, 2429–2437.

[39] N. Sakai, Y. Ebina, K. Takada and T. Sasaki, *Journal of the American Chemical Society*, 2004, **126**, 5851–5858.

[40] J. Livage, M. Henry and C. Sanchez, *Progress in Solid State Chemistry*, 1988, **18**, 259–341.

[41] H. Kominami, Y. Takada, H. Yamagiwa, Y. Kera and M. I. T. Inui, *Journal of Materials Science Letters*, 1996, **15**, 197–200.

[42] N. Sasirekha, B. Rajesh and Y.-W. Chen, *Thin Solid Films*, 2009, **518**, 43–48.

[43] W. Y. Teoh, J. A. Scott and R. Amal, *Physical Chemistry Letters*, 2012, **3**, 629–639.

[44] F. Amano, O.-O. Prieto-Mahaney, Y. Terada, T. Yasumoto, T. Shibayama and B. Ohtani, *Chemistry of Materials*, 2009, **21**, 2601–2603.

[45] S.-K. Joung, T. Amemiya, M. Murabayashi and K. Itoh, *Chemistry: A European Journal*, 2006, **12**, 5526–5534.

[46] M. A. Henderson, *Surface Science Reports*, 2011, **66**, 185–297.

[47] B. Cojocaru, Ş. Neaţu, E. Sacaliuc-Pârvulescu, F. Lévy, V. I. Pârvulescu and H. Garcia, *Applied Catalysis B, Environmental*, 2011, **107**, 140–149.

[48] V. R. de Mendonc and C. Ribeiro, *Applied Catalysis B, Environmental*, 2011, **105**, 298–305.

[49] G. Yang, Z. Yan, T. Xiao and B. Yang, *Journal of Alloys and Compounds*, 2013, **580**, 15–22.

[50] S. Tieng, R. Azouani, K. Chhor and A. Kanaev, *Journal of Physical Chemistry, C*, 2011, **115**, 5244–5250.

[51] L. Liu, S. Chen, W. Sun and J. Xin, *J. Mol. Struct.*, 2011, **1001**, 23–28.

[52] Y. Li, W. Wang, X. Qiu, L. Song, H. M. Meyer III, M. P. Paranthaman, G. Eres, Z. Zhang and B. Gu, *Applied Catalysis B, Environmental*, 2011, **110**, 148–153.

[53] M. P. Seabra, I. M. M. Salvado and J. A. Labrincha, *Ceramics International*, 2011, 3317–3322.

[54] S. Buddee, S. Wongnawa, U. Sirimahachai and W. Puetpaibool, *Materials Chemistry and Physics*, 2011, **126**, 167–177.

[55] C.-C. Yen, D.-Y. Wang, L.-S. Chang and H. C. Shih, *Journal of Solid State Chemistry*, 2011, **184**, 2053–2060.

[56] S. Bzdon, J. Góralski, W. Maniukiewicz, J. Perkowski, J. Rogowski and M. Szadkowska-Nicze, *Rad. Phys. Chem.*, 2012, **81**, 322–330.

[57] L. Laokiat, P. Khemthong, N. Grisdanurak, P. Sreearunothai, W. Pattanasiriwisawa and W. Klysubun, *Korean J. Chem. Eng.*, 2012, **329**, 377–383.

[58] S. Murcia-López, M. C. Hidalgo and J. A. Navío, *Applied Catalysis A, General*, 2011, **404**, 59–67.

[59] R. M. Mohamed and E. S. Aazam, *Journal of Alloys and Compounds*, 2011, **509**, 10132–10138.

[60] W. S. Tung and W. A. Daoud, *Journal of the American Ceramic Society*, 2012, **95**, 2330–2338.

[61] D. Wang, L. Xiao, Q. Luo, X. Li, J. An and Y. Duan, *Journal of Hazardous Materials*, 2011, **192**, 150–159.

[62] D. Ma, Y. Xin, M. Gao and J. Wu, *Applied Catalysis B, Environmental*, 2014, **147**, 49–57.

[63] N. Aman, P. K. Satapathy, T. Mishra, M. Mahato and N. N. Das, *Materials Research Bulletin*, 2012, **47**, 179–183.

[64] C. R. Tubio, F. Guitian and A. Gil, *Journal of Sol-Gel Science and Technology*, 2012, **64**, 436–441.

[65] D. M. Tobaldi, A. S. Škapin, R. C. Pullar, M. P. Seabra and J. A. Labrincha, *Ceramics International*, 2012, **39**, 2619–2629.

[66] A. V. Manole, M. Dobromir, M. Gîrtan, R. Mallet, G. Rusu and D. Luca, *Ceramics International*, 2012, **39**, 4771–4776.

[67] F. E. Oropeza, B. Mei, I. Sinev, A. E. Becerikli, M. Muhler and J. Strunk, *Applied Catalysis B, Environmental*, 2013, **140-141**, 51–59.

[68] R. Asahi, T. Morikawa, T. Ohwaki, K. Aoki and Y. Taga, *Science*, 2001, **293**, 269–271.

[69] C. Di Valentin, G. Pacchioni and A. Selloni, *Physical Review B*, 2004, **70**, 085116.

[70] B. Viswanathan and K. R. Krishanmurthy, *International Journal of Photoenergy*, 2012, **2012**, 1–10.

[71] C. Di Valentin, E. Finazzi, G. Pacchioni, A. Selloni, S. Livraghi, M. C. Paganini and E. Giamello, *Chemical Physics*, 2007, **339**, 44–56.

[72] R. M. Mohamed and E. Aazam, *Chinese Journal of Catalysis*, 2013, **34**, 1267–1273.

[73] S. Guo, S. Han, M. Haifeng, C. Zeng, Y. Sun, B. Chi, J. Pu and J. Li, *Materials Research Bulletin*, 2013, **48**, 3032–3036.

[74] M. Iwase, K. Yamada, T. Kurisaki, O.-O. Prieto-Mahaney, B. Ohtani and H. Wakita, *Applied Catalysis B, Environmental*, 2013, **132-133**, 39–44.

[75] L. n. Djafer, A. Ayral, B. Boury and R. M. Laine, *Journal of Colloid and Interface Science*, 2012, 1–5.

[76] M. Jalalah, M. Faisal, H. Bouzid, A. A. Ismail and S. A. Al-Sayari, *Materials Research Bulletin*, 2013, **48**, 3351–3356.

[77] M. Wu, A. Zheng, F. Deng and B.-L. Su, *Applied Catalysis B, Environmental*, 2013, **138-139**, 219–228.

[78] M. V. Dozzi, S. Livraghi, E. Giamello and E. Selli, *Photochemical & photobiological sciences : Official journal of the European Photochemistry Association and the European Society for Photobiology*, 2011, **10**, 343–349.

[79] Q. Hou, Y. Zheng, J.-F. Chen, W. Zhou, J. Denga and X. Tao, *Journal of Materials Chemistry*, 2011, **21**, 3877–3883.

[80] X. Hong, Z. Luo and J. D. Batteas, *Journal of Solid State Chemistry*, 2011, **184**, 2244–2249.

[81] H.-t. Gao, Y.-y. Liu, C.-h. Ding, D.-m. Dai and G.-j. Liu, *Int. J. Min. Met. Mat.*, 2011, **18**, 606.

[82] Y. Niu, M. Xing, J. Zhang and B. Tian, *Catalysis Today*, 2013, **201**, 159–166.

[83] N. C. Tolosa, M.-C. Lu, H. D. Mendoza and A. P. Rollon, *Applied Catalysis A, General*, 2011, **401**, 233–238.

[84] U. G. Akpan and B. H. Hameed, *Desalination and Water Treatment*, 2013, 1–13.

[85] W. Shi, *Catalysis Letters*, 2013, **143**, 732–738.

[86] G. Zhang, Y. C. Zhang, M. Nadagouda, C. Han, K. O'Shea, S. M. El-Sheikh, A. A. Ismail and D. D. Dionysiou, *Applied Catalysis B, Environmental*, 2014, **144**, 614–621.

[87] F.-t. Li, X.-j. Wang, Y. Zhao, J.-x. Liu, Y.-j. Hao, R.-h. Liu and D.-s. Zhao, *Applied Catalysis B, Environmental*, 2014, **144**, 442–453.

[88] F. Zuo, L. Wang, T. Wu, Z. Zhang, D. Borchardt and P. Feng, *Journal of the American Chemical Society*, 2010, **132**, 11856–11857.

[89] X. Zhang, H. Tian, X. Wang, G. Xue, Z. Tian, J. Zhang, S. Yuan, T. Yu and Z. Zou, *Materials Letters*, 2013, **100**, 51–53.

[90] F. Amano, M. Nakata, K. Asami and A. Yamakata, *Chemical Physics Letters*, 2013, **579**, 111–113.

[91] M. Grätzel, *Current Opinion in Colloid & Interface Science*, 1999, **4**, 314–321.

[92] M. Anpo, *Bulletin of the Chemical Society of Japan*, 2004, **77**, 1427–1442.

[93] S. Sakthivel, M. V. Shankar, M. Palanichamy, B. Arabindoo, D. W. Bahnemann and V. Murugesan, *Water Research*, 2004, **38**, 3001–3008.

[94] G. Li, L. Chen, M. E. Graham and K. A. Gray, *Journal of Molecular Catalysis A: Chemical*, 2007, **275**, 30–35.

[95] J. A. O. Méndez, C. R. López, E. P. Melián, O. G. Díaz, J. M. D. Rodríguez, D. F. Hevia and M. Macías, *Applied Catalysis B, Environmental*, 2014, **147**, 439–452.

[96] D. Astruc, F. Lu and J. R. Aranzaes, *Angewandte Chemie International Edition*, 2005, **44**, 7852–7872.

[97] M. V. Dozzi, L. Prati, P. Canton and E. Selli, *Physical Chemistry Chemical Physics*, 2009, **11**, 7171–7180.

[98] W. Hou, Z. Liu, P. Pavaskar, W. H. Hung and S. B. Cronin, *Journal of Catalysis*, 2011, 149–153.

[99] S. Mubeen, G. Hernandez-Sosa, D. Moses, J. Lee and M. Moskovits, *Nano Lett*, 2011, **11**, 5548–5552.

[100] B. Tian, J. Zhang, T. Tong and F. Chen, *Applied Catalysis B, Environmental*, 2008, **79**, 394–401.

[101] M. Sadeghi, W. Liu, T. G. Zhang, P. Stavropoulos and B. Levy, *Journal of Physical Chemistry*, 1996, **100**, 19466–19474.

[102] T. Ohno, K. Sarukawa, K. Tokieda and M. Matsumura, *Journal of Catalysis*, 2001, **203**, 82–86.

[103] R. I. Bickley, T. Gonzalez-Carreno, J. S. Lees, L. Palmisano and R. J. Tilley, *Journal of Solid State Chemistry*, 1991, **92**, 178–190.

[104] X. Shen, J. Zhang and B. Tian, *Journal of Hazardous Materials*, 2011, **192**, 651–657.

[105] M. Yan, F. Chen, J. Zhang and M. Anpo, *Journal of Physical Chemistry, B*, 2005, **109**, 8673–8678.

[106] R. Su, R. Bechstein, L. Sø, R. T. Vang, M. Sillassen, B. Esbjörnsson, A. Palmqvist and F. Besenbacher, *Journal of Physical Chemistry, C*, 2011, **115**, 24287–24292.

[107] R. Boppella, P. Basak and S. V. Manorama, *ACS Applied Materials: Interfaces*, 2012, **4**, 1239–1246.

[108] A. Iwaszuk and M. Nolan, *Journal of Materials Chemistry A*, 2013, **1**, 6670.

[109] X. Luo, F. Liu, X. Li, H. Gao and G. Liu, *Materials Science in Semiconductor Processing*, 2013, **16**, 1613–1618.

[110] M. Grätzel, *Nature*, 2001, **414**, 338–344.

[111] C.-C. Wang and J. Y. Ying, *Chemistry of Materials*, 1999, **11**, 3113–3120.

[112] T. Hanley, Y. Krisnandi, A. Eldewik, V. Luca and R. Howe, *Ionics*, 2001, **7**, 319–326.

[113] J. Zhao, Z. Wang, L. Wang, H. Yang and M. Zhao, *Materials Chemistry and Physics*, 2000, **63**, 9–12.

[114] J. Yu, J. C. Yu, M. K. P. Leung, W. Ho, B. Cheng, X. Zhao and J. Zhao, *Journal of Catalysis*, 2003, **217**, 69–78.

[115] C.-h. Zhou, S. Xu, Y. Yang, B.-c. Yang, H. Hu, Z.-c. Quan, B. Sebo, B.-l. Chen, Q.-d. Tai, Z.-h. Sun and X.-z. Zhao, *Electrochim. Acta*, 2011, **56**, 4308–4314.

[116] Z. Zheng, B. Huang, J. Lu, X. Qin, X. Zhang and Y. Dai, *Chemistry: A European Journal*, 2011, **17**, 15032–15038.

[117] Z. Zhao, Z. Sun, H. Zhao, M. Zheng, P. Du, J. Zhao and H. Fan, *Journal of Materials Chemistry*, 2012, **22**, 21965.

[118] C. Herring, *Physical Review*, 1951, **82**, 87–93.

[119] G. Liu, J. C. Yu, G. Q. M. Lu and H.-M. Cheng, *Chemical Communications*, 2011, **47**, 6763.

[120] H. G. Yang, C. H. Sun, S. Z. Qiao, J. Zou, G. Liu, S. C. Smith, H.-M. Cheng and G. Q. Lu, *Nature*, 2008, **453**, 638–641.

[121] P. T. Dawson and D. A. Haydon, *Kolloid-Zeitschrift und Zeitschrift für Polymere*, 1965, **203**, 133–138.

[122] A. A. Isirikyan, S. S. Mikhailova and I. A. Polunina, *Bulletin of the Academy of Sciences of the USSR, Division of chemical science*, 1978, **27**, 1041–1043.

[123] A. A. Isirikyan, S. S. Mikhailova, I. A. Polunina and S. N. Tolstaya, *Bulletin of the Academy of Sciences of the USSR, Division of chemical science*, 1983, **32**, 12–16.

[124] L. P. Podmore, P. W. Smith and R. Stoessiger, *Journal of the Chemical Society, Dalton Transactions*, 1973, 209.

[125] Y. C. Zhu and C. X. Ding, *Nanostructured Materials*, 1999, **11**, 427–431.

[126] P. Cozzoli, A. Kornowski and H. Weller, *Journal of the American Chemical Society*, 2003, **125**, 14539–14548.

[127] X.-L. Li, Q. Peng, J.-X. Yi, X. Wang and Y. Li, *Chemistry: A European Journal*, 2006, **12**, 2383–2391.

[128] R. Parra, M. S. Góes, M. S. Castro, E. Longo, P. R. Bueno and J. A. Varela, *Chemistry of Materials*, 2008, **20**, 143–150.

[129] J. A. Chang, M. Vithal, I. C. Baek and S. Il Seok, *Journal of Solid State Chemistry*, 2009, **182**, 749–756.

[130] J.-W. Seo, H. Chung, M.-Y. Kim, J. Lee, I.-H. Choi and J. Cheon, *Small*, 2007, **3**, 850–853.

[131] C.-T. Dinh, T.-D. Nguyen, F. Kleitz and T.-O. Do, *ACS Nano*, 2009, **3**, 3737–3743.

[132] U. Schubert, *Journal of Materials Chemistry*, 2005, **15**, 3701.

[133] T. Kemmitt, N. I. Al-Salim, J. Lian, V. B. Golovko and J.-Y. Ruzicka, *Current Applied Physics*, 2013, **13**, 142–147.

[134] H. G. Yang, G. Liu, S. Z. Qiao, C. H. Sun, Y. G. Jin, S. C. Smith, J. Zou, H.-M. Cheng and G. Q. M. Lu, *Journal of the American Chemical Society*, 2009, **131**, 4078–4083.

[135] X. Han, Q. Kuang, M. Jin, Z. Xie and L. Zheng, *Journal of the American Chemical Society*, 2009, **131**, 3152–3153.

[136] D. Zhang, G. Li, X. Yang and J. C. Yu, *Chemical Communications*, 2009, 4381–4383.

[137] M. Liu, L. Piao, L. Zhao, S. Ju, Z. Yan, T. He, C. Zhoua and W. Wang, *Chemical Communications*, 2010, **46**, 1664–1666.

[138] G. Liu, C. Sun, H. G. Yang, S. C. Smith, L. Wang, G. Q. M. Lu and H.-M. Cheng, *Chemical Communications*, 2010, **46**, 755–757.

[139] K. Lv, Q. Xiang and J. Yu, *Applied Catalysis B, Environmental*, 2011, **104**, 275–281.

[140] H. Zhang, Y. Wang, P. Liu, Y. Han, X. Yao, J. Zou, H. Cheng and H. Zhao, *ACS Applied Materials: Interfaces*, 2011, **3**, 2472–2478.

[141] C. K. Nguyen, H. G. Cha and Y. S. Kang, *Crystal Growth and Design*, 2011, **11**, 3947–3953.

[142] J.-M. Wu, X.-M. Song, L.-Y. Ma and X.-D. Wei, *Journal of Crystal Growth*, 2011, **319**, 57–63.

[143] X. H. Yang, Z. Li, G. Liu, J. Xing, C. Sun, H. G. Yang and C. Li, *CrystEngComm*, 2011, **13**, 1378–1383.

[144] Q. Xiang, J. Yu and M. Jaroniec, *Physical Chemistry Chemical Physics*, 2011, **13**, 4853–4861.

[145] J.-M. Wu and M.-L. Tang, *Journal of Hazardous Materials*, 2011, **190**, 566–573.

[146] Z. He, Q. Cai, F. Hong, Z. Jiang, J. Chen and S. Song, *Industrial & Engineering Chemistry Research*, 2012, **51**, 5662–5668.

[147] L. Pan, J.-J. Zou, S. Wang, X.-Y. Liu, X. Zhang and L. Wang, *ACS Applied Materials: Interfaces*, 2012, **4**, 1650–1655.

[148] X. Wang, H. He, Y. Chen, J. Zhao and X. Zhang, *Applied Surface Science*, 2012, **258**, 5863–5868.

[149] W. Wei, L. Chunhua, S. Mingxing, N. Yaru and X. Zhongzi, *Chinese Journal of Catalysis*, 2012, **33**, 629–636.

[150] B. Liu, Y. Huang, Y. Wen, L. Du, W. Zeng, Y. Shi, F. Zhang, G. Zhu, X. Xua and Y. Wang, *Journal of Materials Chemistry*, 2012, **22**, 7484.

[151] T. R. Gordon, M. Cargnello, T. Paik, F. Mangolini, R. T. Weber, P. Fornasiero and C. B. Murray, *Journal of the American Chemical Society*, 2012, **134**, 6751–6761.

[152] A. S. Ichimura, B. M. Mack, S. M. Usmani and D. G. Mars, *Chemistry of Materials*, 2012, **24**, 2324–2329.

[153] C. Cai, J. Wang, F. Cao, H. Li and J. Zhu, *Chinese Journal of Catalysis*, 2011, **32**, 862–781.

[154] K. Lv, J. Yu, J. Fana and M. Jaroniec, *CrystEngComm*, 2011, **13**, 7044–7048.

[155] Z. Lai, F. Peng, Y. Wang, H. Wang, H. Yu, P. Liu and H. Zhao, *Journal of Materials Chemistry*, 2012, **22**, 23906.

[156] X. Zhou, F. Peng, H. Wang, H. Yu and Y. Fang, *Chemical Communications*, 2012, **48**, 600–602.

[157] W. Wang, C. Lu, Y. Ni, F. Peng and Z. Xu, *Applied Surface Science*, 2012, 1–5.

[158] R. A. Spurr and H. Myers, *Analytical Chemistry*, 1957, **29**, 760–762.

[159] A. L. Patterson, *Physical Review*, 1939, **56**, 978–982.

[160] R. Jenkins and R. Snyder, *Introduction to X-ray powder diffractometry*, Wiley-Interscience, New York, 1996.

[161] W. S. Rasband, *ImageJ*, `http://imagej.nih.gov/ij/`.

[162] P. J. Goodhew and F. J. Humphreys, *Electron Microscopy and Analysis*, Taylor & Francis, London, 2nd edn., 1992.

[163] C. A. Schneider, W. S. Rasband and W. K. Eliceiri, *Nature Methods*, 2012, **9**, 671–675.

[164] N. Serpone, D. Lawless and R. Khairutdinov, *Journal of Physical Chemistry*, 1995, **99**, 16646–16654.

[165] E. Sanchez and T. Lopez, *Materials Letters*, 1995, **25**, 271–275.

[166] J. Xu, Q. Liu, S. Lin and W. Cao, *Res. Chem. Intermed.*, 2012, **39**, 1655–1664.

[167] L. Armelao and D. Barreca, *Surf. Sci. Spec.*, 2003, **10**, 1–7.

[168] D. A. Shirley, *Physical Review B*, 1972, **5**, 4709.

[169] J. Stöhr, *NEXAFS Spectroscopy*, Springer, Berlin, 1st edn., 2003.

[170] J. J. Yeh and I. Lindau, *Atomic data and nuclear data tables*, 1985, **32**, 1–155.

[171] F. De Groot, M. O. Figueiredo, M. J. Basto, M. Abbate, H. Petersen and J. C. Fuggle, *Physics and Chemistry of Minerals*, 1992, **19**, 140–147.

[172] J. P. Crocombette and F. Jollet, *Journal of Physics: Condensed Matter*, 1994, **6**, 10811–10821.

[173] M. Cheynet, S. Pokrant, S. Irsen and P. Krüger, *Ultramicroscopy*, 2010, **110**, 1046–1053.

[174] X. Chen, P.-A. Glans, X. Qiu, S. Dayal, W. D. Jennings, K. E. Smith, C. Burda and J. Guo, *Journal of Electron Spectroscopy and Related Phenomena*, 2008, **162**, 67–73.

[175] S. J. Stewart, M. Fernández-García, C. Belver, B. S. Mun and F. G. Requejo, *Journal of Physical Chemistry, B*, 2006, **110**, 16482–16486.

[176] D. Mardare, V. Nica, C.-M. Teodorescu and D. Macovei, *Surface Science*, 2007, **601**, 4479–4483.

[177] R. Pärna, U. Joost, E. Nõmmiste, T. Käämbre, A. Kikas, I. Kuusik, M. Hirsimäki, I. Kink and V. Kisand, *Applied Surface Science*, 2011, **257**, 6897–6907.

[178] S. Kumar, S. Gautam, G. W. Kim, F. Ahmed, M. S. Anwar, K. H. Chae, H. K. Choi, H. Chung and B. H. Koo, *Applied Surface Science*, 2011, **257**, 10557–10561.

[179] D. Mardare, V. Nica, V. Pohoata, D. Macovei, N. Gheorghe, D. Luca and C.-M. Teodorescu, *Thin Solid Films*, 2011, **520**, 1348–1352.

[180] A. Fahmi, C. Minot, P. Fourré and P. Nortier, *Surface Science*, 1995, **343**, 261–272.

[181] T. Lopez, E. Sanchez, P. Bosch, Y. Meas and R. Gomez, *Materials Chemistry and Physics*, 1992, **32**, 141–152.

[182] R. Campostrini, M. Ischia and L. Palmisano, *Journal of thermal analysis and calorimetry*, 2003, **71**, 1011–1022.

[183] B. Wu, C. Guo, N. Zheng, Z. Xie and G. Stucky, *Journal of the American Chemical Society*, 2008, **130**, 17563–17567.

[184] J. C. Taylor and T. M. Sabine, *Acta Crystallographica B*, 1972, **28**, 3340–3351.

[185] P. Arnal, R. J. P. Corriu, D. Leclercq, P. H. Mutin and A. Vioux, *Journal of Materials Chemistry*, 1996, **6**, 1925–1932.

[186] M. Niederberger, G. Garnweitner, N. Pinna and G. Neri, *Progress in Solid State Chemistry*, 2005, **33**, 59–70.

[187] M. Niederberger, M. Bartl and G. Stucky, *Chemistry of Materials*, 2002, **14**, 4364–4370.

[188] M. Niederberger, G. Garnweitner, F. Krumeich, R. Nesper, H. Cölfen and M. Antonietti, *Chemistry of Materials*, 2004, **16**, 1202–1208.

[189] M. Niederberger, M. H. Bartl and G. D. Stucky, *Journal of the American Chemical Society*, 2002, **124**, 13642–13960.

[190] D. Koziej, F. Fischer, N. Kränzlin, W. R. Caseri and M. Niederberger, *ACS Applied Materials: Interfaces*, 2009, **1**, 1097–1104.

[191] J. Ba, J. Polleux, M. Antonietti and M. Niederberger, *Advanced Materials*, 2005, **17**, 2509–2512.

[192] J. Zhu, J. Yang, Z.-F. Bian, J. Ren, Y.-M. Liu, Y. Cao, H.-X. Li, H.-Y. He and K.-N. Fan, *Applied Catalysis B, Environmental*, 2007, **76**, 82–91.

[193] A. Mitra, A. Bhaumik and B. K. Paul, *Microporous and Mesoporous Materials*, 2008, **109**, 66–72.

[194] Y. C. Hsu, H. C. Lin, C. W. Lue, Y. T. Liao and C. M. Yang, *Applied Catalysis B, Environmental*, 2009, **89**, 309–314.

[195] M.-G. Willinger, G. Clavel, W. Di and N. Pinna, *J. Ind. Eng. Chem.*, 2009, **15**, 883–887.

[196] Y.-C. Hsu, H.-C. Lin, C.-H. Chen, Y.-T. Liao and C.-M. Yang, *Journal of Solid State Chemistry*, 2010, **183**, 1917–1924.

[197] G. Melcarne, L. De Marco, E. Carlino, F. Martina, M. Manca, R. Cingolani, G. Gigli and G. Ciccarella, *Journal of Materials Chemistry*, 2010, **20**, 7248–7254.

[198] G. V. Jensen, M. Bremholm, N. Lock, G. R. Deen, T. R. Jensen, B. B. Iversen, M. Niederberger, J. S. Pedersen and H. Birkedal, *Chemistry of Materials*, 2010, **22**, 6044–6055.

[199] H. Tong, N. Umezawa and J. Ye, *Chemical Communications*, 2011, **47**, 4219–4221.

[200] C.-T. Dinh, T.-D. Nguyen, F. Kleitz and T.-O. Do, *Canadian Journal of Chemical Engineering*, 2012, **90**, 8–17.

[201] C.-H. Chen, C.-H. Liu, Y.-C. Su and C.-M. Yang, *Applied Catalysis B, Environmental*, 2012, **123-124**, 36–42.

[202] H. G. Cordes, *Physical Review*, 1920, **16**, 179–201.

[203] S. Iijima, *Nature*, 1991, **354**, 56–58.

[204] M. Keidar, *Journal of Physics D: Applied Physics*, 2007, **40**, 2388–2393.

[205] A. A. Ashkarran, M. Kavianipour, S. M. Aghigh, S. A. A. Afshar, S. Saviz and A. I. Zad, *Journal of Cluster Science*, 2010, **21**, 753–766.

[206] N. Tanaka, D. L. Peng, K. Sumiyama and T. Hihara, *Thin Solid Films*, 2008, **516**, 1677–1682.

[207] Y. Guo, K. Ono, N. Murata and T. Okazaki, *Journal of Crystal Growth*, 2005, **275**, 2031–2036.

[208] S.-M. Oh and T. Ishigaki, *Thin Solid Films*, 2004, **457**, 186–191.

[209] T. Hihara and K. Sumiyama, *Journal of Applied Physics*, 1998, **84**, 5270–5276.

[210] S. M. Aghigh, M. Kavianipour, S. A. A. Afshar and A. A. Ashkarran, *2010 International Conference on Enabling Science and Nanotechnology*, 2010.

[211] I. Banerjee, S. Karmakar, N. V. Kulkarni, A. B. Nawale, V. L. Mathe, A. K. Das and S. V. Bhoraskar, *Journal of Nanoparticle Research*, 2010, **12**, 581–590.

[212] S. Yamamuro, K. Sumiyama and K. Suzuki, *Journal of Applied Physics*, 1999, **85**, 483.

[213] S. Yamamuro, K. Sumiyama, M. Sakurai and K. Suzuki, *Supramol. Sci.*, 1998, **5**, 239–245.

[214] A. Guinier and G. Fournet, *Small-Angle Scattering of X-rays*, John Wiley and Sons Ltd., New York, 1955.

[215] P. Krishnamurti, *Indian Journal of Physics*, 1930, **5**, 473–500.

[216] B. E. Warren, *The Journal of Chemical Physics*, 1934, **2**, 551.

[217] H. Boukari, J. S. Lin and M. T. Harris, *Journal of Colloid and Interface Science*, 1997, **194**, 311–318.

[218] N. V. Golubko, M. I. Yanovskaya and I. P. Romm, *Journal of Sol-Gel Science and Technology*, 2001, **20**, 245–262.

[219] C. Boissiere, D. Grosso, H. Amenitsch, A. Gibaud, A. Coupé, N. Baccilea and C. Sanchez, *Chemical Communications*, 2003, 2798–2799.

[220] D. L. Green, J. S. Lin, Y.-F. Lam, M. Z.-C. Hu, D. W. Schaefer and M. T. Harris, *Journal of Colloid and Interface Science*, 2003, **266**, 346–358.

[221] H. Jensen, M. Bremholm, R. P. Nielsen, K. D. Joensen, J. S. Pedersen, H. Birkedal, Y.-S. Chen, J. Almer, E. G. Søgaard, S. B. Iversen and B. B. Iversen, *Angewandte Chemie International Edition*, 2007, **46**, 1113–1116.

[222] V. Luca, W. K. Bertram, G. D. Sizgek, B. Yang and D. Cookson, *Langmuir*, 2008, **24**, 10737–10745.

[223] L. C. McKenzie, P. M. Haben, S. D. Kevan and J. E. Hutchison, *Journal of Physical Chemistry, C*, 2010, **114**, 22055–22063.

[224] J. Ilavsky and P. R. Jemian, *J. Appl. Cryst (2009). 42, 347-353 [doi:10.1107/S0021889809002222]*, 2009, 1–7.

[225] G. Beaucage, *Journal of Applied Crystallography*, 1995, **28**, 717–728.

[226] J. S. Chen and X. W. Lou, *Electrochem. Commun.*, 2009, **11**, 2332–2335.

[227] G. Liu, H. G. Yang, X. Wang, L. Cheng, H. Lu, L. Wang, G. Q. Lu and H.-M. Cheng, *Journal of Physical Chemistry, C*, 2009, **113**, 21784–21788.

[228] J. Zhang, J. Xi and Z. Ji, *Journal of Materials Chemistry*, 2012, **22**, 17700.

[229] D. Balzar, in *Microstructure Analysis from Diffraction*, ed. R. L. Snyder, H. J. Bunge and J. Fiala, International Union of Crystallography, 1999.

[230] B. C. C. Cowie, A. Tadic and L. Thomsen, *AIP Conference Proceedings*, 2010, **1234**, 307–310.

[231] J. Aguado-Serrano and M. L. Rojas-Cervantes, *Microporous and Mesoporous Materials*, 2006, **88**, 205–213.

[232] P. A. Webb and C. Orr, *Analytical Methods in Fine Particle Technology*, Micromeritics Instrument Corporation, Norcross, 1997.

[233] J. C. Yu, J. Yu, W. Ho, Z. Jiang and L. Zhang, *Chemistry of Materials*, 2002, **174**, 3808–3816.

[234] X. Y. Wang, Z. Liu, H. Liao, D. Klein and C. Coddet, *Thin Solid Films*, 2005, **473**, 177–184.

[235] B. A. Morales, O. Novaro, T. Lopez, E. Sanchez and R. Gomez, *Journal of Materials Research*, 1995, **10**, 2788–2796.

[236] A. A. Ramadan, M. R. Ebeid, S. K. Abdelraheem and E. M. Abdel-Minem, *Egypt. J. Solids*, 2005, **28**, 205–216.

[237] C. Ribeiro, C. Vila, D. B. Stroppa, V. R. Mastelaro, J. Bettini, E. Longo and E. R. Leite, *Journal of Physical Chemistry, C*, 2007, **111**, 5871–5875.

[238] W.-J. Li, E.-W. Shi and Z.-W. Yin, *Journal of Crystal Growth*, 2000, **208**, 546–554.

[239] J. Pan, G. Liu, G. Q. M. Lu and H.-M. Cheng, *Angewandte Chemie International Edition*, 2011, **50**, 2133–2137.

[240] Q. Wang, C. Chen, D. Zhao, W. Ma and J. Zhao, *Langmuir*, 2008, **24**, 7338–7345.

[241] T. K. Le, D. Flahaut, H. Martinez, T. Pigot, H. K. H. Nguyen and T. K. X. Huynh, *Applied Catalysis B, Environmental*, 2014, **144**, 1–11.

[242] H. Park and W. Choi, *Journal of Physical Chemistry, B*, 2004, **108**, 4086–4093.

[243] D. Li, H. Haneda, S. Hishita and N. Ohashi, *Chemistry of Materials*, 2005, **17**, 2588–2595.

[244] J. F. Moulder, W. F. Stickle, P. E. Sobol and K. D. Bomben, *Handbook of X-ray Photoelectron Spectroscopy*, Physical Electronics Limited, Minnesota, 1995.

[245] T. Kako, N. Umezawa, K. Xie and J. Ye, *Journal of Materials Science*, 2013, **48**, 108–114.

[246] G. S. Henderson, X. Liu and M. E. Fleet, *Physics and Chemistry of Minerals*, 2002, **29**, 32–42.

[247] M. A. Marcus and A. Manceau, *Overabsorption ("Self-absorption"), Thickness and Hole Effects in EXAFS*, Advanced light source, lawrence berkeley national laboratory technical report, 2005.

[248] K. Nakanishi and T. Ohta, *Installation of Fluorescence X-ray Detectors for Upgrade of BL-10*, The sr center, ritsumeikan university technical report, 2008.

[249] Z. Miao, Z. Liu, K. Ding, B. Han, S. Miao and G. An, *Nanotechnology*, 2007, **18**, 125605.

[250] P. J. Dyson and T. J. Geldbach, *Metal Catalysed Reactions in Ionic Liquids*, Springer, Dordrecht, 2005.

[251] D. S. Jacob, L. Bitton, J. Grinblat, I. Felner, Y. Koltypin and A. Gedanken, *Chemistry of Materials*, 2006, **18**, 3162–3168.

[252] S. Doeuff, M. Henry, C. Sanchez and J. Livage, *Journal of Non-crystalline Solids*, 1987, **89**, 206–216.

[253] C. Sanchez, J. Livage, M. Henry and F. Babonneau, *Journal of Non-crystalline Solids*, 1988, **100**, 65–76.

[254] P. I. Laaziz, A. Larbot, C. Guizard, J. Durand, L. Cot and J. Joffre, *Acta Crystallographica C*, 1990, **46**, 2332–2334.

[255] M. J. Muñoz-Aguado, M. Gregorkiewitz and A. Larbot, *Materials Research Bulletin*, 1992, **27**, 87–97.

[256] S. Barboux-Doeuff and C. Sanchez, *Materials Research Bulletin*, 1994, **29**, 1–13.

[257] C. Suresh, V. Biju, P. Mukundan and K. G. K. Warrier, *Polyhedron*, 1998, **17**, 3131–3135.

[258] S. Rajesh Kumar, S. C. Pillai, U. S. Hareesh, P. Mukundan and K. Warrier, *Materials Letters*, 2000, **43**, 286–290.

[259] P. A. Venz, R. L. Frost and J. T. Kloprogge, *Journal of Non-crystalline Solids*, 2000, **276**, 95–112.

[260] D. P. Birnie, III and N. J. Bendzko, *Materials Chemistry and Physics*, 1999, **59**, 26–35.

[261] D. P. Birnie, III, *Journal of Materials Science*, 2000, **35**, 367–374.

[262] C. Wang, Z.-X. Deng and Y. Li, *Inorganic Chemistry*, 2001, **40**, 5210–5214.

[263] H. Choi, E. Stathatos and D. D. Dionysiou, *Applied Catalysis B, Environmental*, 2006, **63**, 60–67.

[264] D. Reyes-Coronado, G. Rodríguez-Gattorno, M. E. Espinosa-Pesqueira, C. Cab, R. de Coss and G. Oskam, *Nanotechnology*, 2008, **19**, 145605.

[265] M. B. Fisher, D. A. Keane, P. Fernández-Ibáñez, J. Colreavy, S. J. Hinder, K. G. McGuigan and S. C. Pillai, *Applied Catalysis B, Environmental*, 2013, **130-131**, 8–13.

[266] S. Bagwasi, Y. Niu, M. Nasir, B. Tian and J. Zhang, *Applied Surface Science*, 2013, **264**, 139–147.

[267] L.-X. Du, Z.-T. Jiang and R. Li, *Materials Letters*, 2013, **95**, 17–20.

[268] U. Schubert, E. Arpac, W. Glaubitt, A. Helmerich and C. Chau, *Chemistry of Materials*, 1992, **4**, 291–295.

[269] R. Takahashi, S. Takenaka, S. Sato, T. Sodesawa, K. Ogura and K. Nakanishi, *Journal of the Chemical Society, Faraday Transactions*, 1998, **94**, 3161–3168.

[270] Q. D. Truong, M. Kobayashi, H. Kato and M. Kakihana, *Journal of the Ceramic Society of Japan*, 2011, **19**, 513–516.

[271] H.-T. Ren, S.-Y. Jia, S.-H. Wu, Y. Liu and X. Han, *Materials Letters*, 2013, 1–3.

[272] Y. Dai, C. M. Cobley, J. Zeng, Y. Sun and Y. Xia, *Nano Lett*, 2009, **9**, 2455–2459.

[273] C. Campbell, S. G. Bott, R. Larsen and W. G. Van Der Sluys, *Inorganic Chemistry*, 1994, **33**, 4950–4958.

[274] H. Fric, M. Puchberger and U. Schubert, *Journal of Sol-Gel Science and Technology*, 2006, **40**, 155–162.

[275] A. Pandey, V. D. Gupta and H. Nöth, *European Journal of Inorganic Chemistry*, 2000, 1351–1357.

[276] *Handbook of Sol-Gel Science and Technology*, ed. S. Sakka, Kluwer Academic Publishers, Boston, 2005, vol. 1.

[277] J. Muhlebach, K. Muller and G. Schwarzenbach, *Inorganic Chemistry*, 1970, **9**, 2381–2390.

[278] W. Zhang, S. Chen, S. Yu and Y. Yin, *Journal of Crystal Growth*, 2007, **308**, 122–129.

[279] K.-U. Goss, *Environmental Science & Technology*, 2008, **42**, 456–458.

[280] D. C. Burns, D. A. Ellis, H. Li, C. J. McMurdo and E. Webster, *Environmental Science & Technology*, 2008, **42**, 9283–9288.

[281] Y. B. Ryu, M. S. Lee, E. D. Jeong, H. G. Kim, W. Y. Jung, S. H. Baek, G.-D. Lee, S. S. Park and S.-S. Hong, *Catalysis Today*, 2007, **124**, 88–93.

[282] G. C. Bond, P. A. Sermon, G. Webb, D. A. Buchanan and P. B. Wells, *Journal of the Chemical Society, Chemical Communications*, 1973, 444b.

[283] M. Haruta, T. Kobayashi, H. Sano and N. Yamada, *Chemistry Letters*, 1987, 405–408.

[284] G. J. Hutchings, *Journal of Catalysis*, 1985, **96**, 292–295.

[285] M. Chen and D. W. Goodman, *Chemical Society Reviews*, 2008, **37**, 1860–1870.

[286] H. Bönnemann and R. M. Richards, *Euro. J. Inorg. Chem.*, 2001, 2455–2480.

[287] J. A. Lopez-Sanchez, N. Dimitratos, C. Hammond, G. L. Brett, L. Kesavan, S. White, P. Miedziak, R. Tiruvalam, R. L. Jenkins, A. F. Carley, D. Knight, C. J. Kiely and G. J. Hutchings, *Nature Chemistry*, 2011, **3**, 551–556.

[288] M. Turner, V. B. Golovko, O. P. H. Vaughan, P. Abdulkin, A. Berenguer-Murcia, M. S. Tikhov, B. F. G. Johnson and R. M. Lambert, *Nature*, 2008, **454**, 981–983.

[289] Y. Zhu, H. Qian, M. Zhu and R. Jin, *Advanced Materials*, 2010, **22**, 1915–1920.

[290] Y. Liu, H. Tsunoyama, T. Akita and T. Tsukuda, *Journal of Physical Chemistry, C*, 2009, **113**, 13457–13461.

[291] K. Ho and K. Yeung, *Journal of Catalysis*, 2006, **242**, 131–141.

[292] L. Menard, F. Xu, R. Nuzzo and J. Yang, *Journal of Catalysis*, 2006, **243**, 64–73.

[293] F. Boccuzzi, *Journal of Catalysis*, 2001, **202**, 256–267.

[294] W. Yan, S. M. Mahurin, Z. Pan, S. H. Overbury and S. Dai, *Journal of the American Chemical Society*, 2005, **127**, 10480–10481.

[295] M. Valden, X. Lai and D. W. Goodman, *Science*, 1998, **281**, 1647–1650.

[296] M. C. Hidalgo, M. Maicu, J. A. Navío and G. Colón, *Journal of Physical Chemistry, C*, 2009, **113**, 12840–12847.

[297] G. M. Veith, A. R. Lupini and N. J. Dudney, *Journal of Physical Chemistry, C*, 2009, **113**, 269–280.

[298] G. M. Veith, A. R. Lupini, S. J. Pennycook and N. J. Dudney, *ChemCatChem*, 2010, **2**, 281–286.

[299] L.-S. Zhong, J.-S. Hu, Z.-M. Cui, L.-J. Wan and W.-G. Song, *Chemistry of Materials*, 2007, **19**, 4557–4562.

[300] D. Matthey, J. G. Wang, S. Wendt, J. Matthiesen, R. Schaub, E. Laegsgaard, B. Hammer and F. Besenbacher, *Science*, 2007, **315**, 1692–1696.

[301] J. Biener, A. Wittstock, M. M. Biener, T. Nowitzki, A. V. Hamza and M. Baeumer, *Langmuir*, 2010, **26**, 13736–13740.

[302] B. Thinnes, *New nanoscale reference material to be known as P25*, 2012, `http://www.hydrocarbonprocessing.com/Article/3096210/Search/New-nanoscale-reference-material-to-be-known-as-P25.html`.

[303] D. P. Anderson, J. F. Alvino, A. Gentleman, H. A. Qahtani, L. Thomsen, M. I. J. Polson, G. F. Metha, V. B. Golovko and G. G. Andersson, *Physical Chemistry Chemical Physics*, 2013, **15**, 3917.

[304] D. P. Anderson, R. H. Adnan, J. F. Alvino, O. Shipper, B. Donoeva, J.-Y. Ruzicka, H. Al Qahtani, H. H. Harris, B. Cowie, J. B. Aitken,

V. B. Golovko, G. F. Metha and G. G. Andersson, *Physical Chemistry Chemical Physics*, 2013.

[305] F. Wen, U. Englert, B. Gutrath and U. Simon, *European Journal of Inorganic Chemistry*, 2008, **2008**, 106–111.

[306] M. Abdullah, G. K. Low and R. W. Matthews, *Journal of Physical Chemistry*, 1990, **94**, 6820–6825.

[307] T. C. Jagadale, S. P. Takale, R. S. Sonawane, H. M. Joshi, S. I. Patil, B. B. Kale and S. B. Ogale, *Journal of Physical Chemistry, C*, 2008, **112**, 14595–14602.

[308] Y. Duan, N. Fu, Q. Zhang, Y. Fang, X. Zhou and Y. Lin, *Electrochimica Acta*, 2013, **107**, 473–480.

[309] R. Sanjinés, H. Tang, H. Berger, F. Gozzo, G. Margaritondo and F. Lévy, *Journal of Applied Physics*, 1994, **75**, 2945.

[310] A. K. Santra and D. W. Goodman, *Journal of Physics: Condensed Matter*, 2003, **15**, R31.

[311] S. Hüfner, *Photoelectron spectroscopy*, Springer, Berlin, 2nd edn., 1996.

[312] N. Bogdanchikova, A. Pestryakov, M. H. Farias, J. A. Diaz, M. Avalos and J. Navarrete, *Solid State Sciences*, 2008, **10**, 908–914.

[313] W.-S. Lee, B.-Z. Wan, C.-N. Kuo, W.-C. Lee and S. Cheng, *Catalysis Communications*, 2007, **8**, 1604–1608.

[314] P. Lignier, M. Comotti, F. Schüth, J.-L. Rousset and V. Caps, *Catalysis Today*, 2009, **141**, 355–360.

[315] A. Naldoni, M. D'Arienzo, M. Altomare, M. Marelli, R. Scotti, F. Morazzoni, E. Selli and V. D. Santo, *Applied Catalysis B, Environmental*, 2013, **130-131**, 239–248.

[316] M. Ousmane, L. F. Liotta, G. Di Carlo, G. Pantaleo, A. M. Venezia, G. Deganello, L. Retailleau, A. Boreave and A. Giroir-Fendler, *Applied Catalysis B, Environmental*, 2011, **101**, 629–637.

[317] J. Radnik, C. Mohr and P. Claus, *Physical Chemistry Chemical Physics*, 2002, **5**, 172–177.

[318] K. Esumi, S. Sarashina and T. Yoshimura, *Langmuir*, 2004, **20**, 5189–5191.

[319] E. Kowalska, O. O. P. Mahaney, R. Abe and B. Ohtani, *Physical Chemistry Chemical Physics*, 2010, **12**, 2344.

[320] R. S. Sonawane and M. K. Dongare, *Journal of Molecular Catalysis A: Chemical*, 2006, **243**, 68–76.

[321] G. Colón, M. C. Hidalgo, G. Munuera, I. Ferino, M. G. Cutrufello and J. A. Navío, *Applied Catalysis B, Environmental*, 2006, **63**, 45–59.

[322] Q. Yang, C. Xie, Z. Xu, Z. Gao and Y. Du, *Journal of Physical Chemistry, B*, 2005, **109**, 5554–5560.

[323] A. B. dos Santos, F. J. Cervantes and J. B. van Lier, *Bioresource Technology*, 2007, **98**, 2369–2385.

[324] Č. Novotný, N. Dias, A. Kapanen, K. Malachová, M. Vándrovcová, M. Itävaara and N. Lima, *Chemosphere*, 2006, **63**, 1436–1442.

[325] J. H. Weisburger, *Mutation Research*, 2002, **506**, 9.

[326] P. P. Champagne, M. E. Nesheim and J. A. Ramsay, *Enzyme and Microbial Technology*, 2010, **46**, 147–152.

[327] A. Özcan, Ç. Ömeroglu, Y. Erdogan and A. S. Ozcan, *Journal of Hazardous Materials*, 2007, **140**, 173–179.

[328] M. A. Fox and M. T. Dulay, *Chemical Reviews*, 1993, **93**, 341–357.

[329] A. L. Linsebigler, G. Lu and J. T. Yates, Jr, *Chemical Reviews*, 1995, **95**, 735–758.

[330] J. Herrmann, *Catalysis Today*, 1995, **24**, 157–164.

[331] M. Anpo, *Catalysis Surveys from Japan*, 1997, **1**, 169–179.

[332] A. Mills, C. Hill and P. Robertson, *Journal of Photochemistry & Photobiology, A: Chemistry*, 2012, **237**, 7–23.

[333] K. B. Jaimy, K. V. Baiju, S. Ghosh and K. Warrier, *Journal of Solid State Chemistry*, 2012, **186**, 149–157.

[334] Y. He, G. Li, Z. Jiang, H. Wang, J. Zhao and H. Su, *Desalination*, 2011, **279**, 235–242.

[335] E. K. Dafnopatidou and G. P. Gallios, *Industrial & Engineering Chemistry Research*, 2007, **46**, 2125–2132.

[336] J. E. B. McCallum, A. Stephen, S. Alkan, R. L. Depinto and R. U. R. Wahl, *Environmental Science & Technology*, 2000, **34**, 5157–5164.

[337] W. J. Epolito, Y. H. Lee and L. A. Bottomley, *Dyes and Pigments*, 2005, **67**, 35–46.

[338] M. Constapel, M. Schellenträger and J. M. Marzinkowski, *Water Research*, 2009, **43**, 733–743.

[339] O. J. Hao, H. Kim and P.-C. Chiang, *Critical Reviews in Environmental Science and Technology*, 2000, **30**, 449–505.

[340] F. Abu Bakar, J.-Y. Ruzicka, I. Nuramdhani, B. Williamson, M. Holzenkaempfer and V. B. Golovko, *In submission*, 2013.

[341] J. M. Herrmann, *Applied Catalysis B, Environmental*, 2010, **99**, 461–468.

[342] M. Y. Ghaly, T. S. Jamil, I. E. El-Seesy, E. R. Souaya and R. A. Nasr, *Chemical Engineering Journal*, 2011, **168**, 446–454.

[343] N. T. Nolan, D. W. Synnott, M. K. Seery, S. J. Hinder, A. Van Wassenhoven and S. C. Pillai, *Journal of Hazardous Materials*, 2012, **211**, 88–94.

[344] F. Herrera, A. Lopez, G. Mascolo, P. Albers and J. Kiwi, *Water Research*, 2001, **35**, 750–760.

[345] M. Abu Tariq, M. Faisal, M. Saquib and M. Muneer, *Dyes and Pigments*, 2008, **76**, 358–365.

[346] M. Muruganandham, *Dyes and Pigments*, 2006, **68**, 133–142.

[347] D. E. Kritikos, N. P. Xekoukoulotakis, E. Psillakis and D. Mantzavinos, *Water Research*, 2007, **41**, 2236–2246.

[348] M. Saquib, M. Abu Tariq, M. M. Haque and M. Muneer, *Journal of Environmental Management*, 2008, **88**, 300.

[349] C. Hachem, F. Bocquillon, O. Zahraa and M. Bouchy, *Dyes and Pigments*, 2001, **49**, 117–125.

[350] M. Qamar, M. Saquib and M. Muneer, *Dyes and Pigments*, 2005, **65**, 1–9.

[351] V. G. Gandhi, M. K. Mishra and P. A. Joshi, *Journal of Industrial and Engineering Chemistry*, 2012, 1–6.

[352] J. Moser, S. Punchihewa, P. P. Infelta and M. Graetzel, *Langmuir*, 1991, **7**, 3012–3018.

[353] A. G. Thomas and K. L. Syres, *Chemical Society Reviews*, 2012, **41**, 4207–4217.

[354] B. J. Brotherton, in *Encyclopedia of Inorganic Chemistry*, ed. R. B. King, John Wiley and Sons Ltd., Chichister, 1994.

[355] C. Karunakaran and R. Kamalam, *Synthesis and Reactivity in Inorganic and Metal-Organic Chemistry*, 1999, **29**, 1463–1474.

[356] D. Chen, F. Huang, Y.-B. Cheng and R. A. Caruso, *Advanced Materials*, 2009, **21**, 2206–2210.

[357] K. Lv, B. Cheng, J. Yu and G. Liu, *Physical Chemistry Chemical Physics*, 2012, **14**, 5349–5362.

[358] R. Kydd, J. Scott, W. Y. Teoh, K. Chiang and R. Amal, *Langmuir*, 2010, **26**, 2099–2106.

[359] L. Matějová, K. Kočí, M. Reli, L. Čapek, V. Matějka, O. Šolcová and L. Obalová, *Applied Surface Science*, 2013, 1–9.